Radiation effects on the structure of chromosomes

By

Archana Bhartiya

Submitted in partial fulfilment of the requirements for the degree of Doctor of Engineering at the University College London

Supervisors
Prof Ian K. Robinson
Prof Stan W. Botchway

Department of Chemistry and London Centre for Nanotechnology
University College London

May 2022

Declaration

I, Archana Bhartiya, confirm that the work presented in this thesis is my own. Where information has been derived from other sources, I confirm that this has been indicated in the thesis.

Archana Bhartiya
May 2022

Abstract

The study aims to investigate the effect of ionising radiation on the structure of the chromosomes after lose-dose X-ray irradiation. The first aim was to investigate the changes that occurred in the molecular environment of the chromosomes after radiation exposure using Fluorescence Lifetime Imaging Microscopy (FLIM). The study's second aim was to measure the mass of the human chromosomes and produce 'X-ray karyotypes' of each spread, plotting the measured mass against the number of base pairs using the X-ray ptychography technique. The purpose was to observe the changes in the mass of the X-ray induced chromosomes.

A complete set of 46 human metaphase chromosomes in one frame is known as 'spread'. Exponentially growing cells were irradiated with X-ray doses at 0.1 Gy (Gray), 0.5 Gy and 1 Gy, followed by chromosome preparation from the irradiated as well as non-irradiated cells. DNA specific stain, 4',6-diamidino-2-phenylindole (DAPI), was used to stain the chromosomes during the analysis.

Using FLIM, a significant reduction in the DAPI lifetime values (2.8 ± 0.03 ns) was observed in the heterochromatin region of heteromorphic chromosomes 1, 9, 15, and 16 compared to the non-heterochromatin region of the chromosomes (2.88 ± 0.02 ns) present in the non-irradiated chromosome spreads. Furthermore, in the case of irradiated chromosomes, the heterochromatic regions of chromosomes showed statistically significant reduced lifetime values, with the difference ranging between ~260 picoseconds (ps) to ~290 ps compared to the non-irradiated chromosomes. This indicates that chromosomes might have undergone chemical perturbations. However, DAPI lifetime values were not significantly different between low-dose radiations. Therefore, low-dose irradiation is thought to induce an adaptive or hermetic response under certain conditions. However, the sensitivity of the FLIM could assist in the early detection of epigenetic variations that occur in the structure of chromosomes due to radiation/diseases.

Key results were obtained from the Diamond Light Source (Harwell), I-13-coherence beamline by imaging metal-stained and unstained human chromosome spreads at room temperature to determine the gain or loss of genetic material upon low-level X-ray irradiation doses due to radiation damage. The obtained better resolution phase-contrast images of chromosome spreads gave the distribution of electron density which correlates with the mass of the chromosomes. The masses of non-irradiated and irradiated chromosomes were karyotyped to observe the difference in the masses. Therefore, the mass of the human genome can be determined using phase-contrast X-ray ptychography.

The X-ray ptychography results are fascinating. The importance of this research lies in developing a new and improved technique to image and weigh individual chromosomes that will benefit medicine in diagnosing cancer and other health problems from patient samples.

Impact statement

Chromosomes are bundles of tightly packed DNA and proteins stored in the nucleus of almost every cell. Chromosomes contain hereditary information and help to ensure the appropriate distribution of genetic material during cell division. Chromosome karyotypes detect chromosomal abnormalities to diagnose genetic diseases.

The work in this thesis has focussed on investigating the effect of ionising radiation on the structure of human chromosomes after lose-dose X-ray irradiation. The FLIM technique has been used to investigate the microenvironment along the length of DAPI stained metaphase chromosomes. Also, the phase-contrast X-ray ptychography has been used to measure the mass of individual metaphase chromosomes and build an 'X-ray karyotype'. The significant results obtained are variation in DAPI lifetime between i) irradiated and non-irradiated chromosomes, ii) heterochromatin and non-heterochromatin regions of the chromosome in a different cell type, iii) DNA oligomers (each containing ten bases of DNA) and metaphase chromosomes and iv) lifetime variation was also observed in a different passage of the cell culture. In addition, for the first time, the masses of 46 individual chromosomes have been obtained using phase contrast X-ray ptychography (Bhartiya *et al.*, 2021).

FLIM is independent of probe concentration; it avoids photobleaching and is cost-effective. X-ray ptychography provides quantitative information used to build an X-ray karyotype based on the amount of matter present in each chromosome. Linear regression was found between masses of chromosomes and the number of DNA base pairs present in each chromosome. X-ray ptychography was successfully applied to image unstained chromosome spreads.

Ultimately, in the future, the X-ray imaging technique can be used to identify inter and intrachromosomal aberrations with immunolabelling and using cryo preservatives to image weak scattering biological samples without any invasive

staining. FLIM has enormous potential to investigate the early changes in the structure and the chemistry of biological samples. The importance of this research lies in the development of a valuable tool for radiation biology and an improved technique to image and weigh individual chromosomes that will benefit medicine in diagnosing cancer and other health problems from patient samples.

Acknowledgement

First and foremost, I want to express my sincere gratitude to my academic supervisors, Prof Ian K. Robinson, Prof Stanley W. Botchway (Science and Technology Facilities Council) and Dr Mohammed Yusuf (UCL), for their continuous guidance throughout PhD research and thesis writing, for their motivations, enthusiasm, and immense knowledge which I will apply in future life.

I would like to acknowledge UCL's industrial training centre in Molecular Modelling and Material Science and the PhD sponsor ERC. It also gives me great pleasure to thank Dr Zhimei Du (UCL) for her administrative guidance throughout the academic year.

I would also like to thank Research Complex at Harwell, Octopus group of Central Laser Facility and I-13-coherence beamline, Diamond Light Source, UK. For allowing me to perform all the research experiments. I also appreciate the support of Dr Darren Batey and Dr Xiaowen Shi for helping during the beamtime and ptychographic reconstructions. My heartiest thanks to Dr Ken Raj and Dr Sylwia Kabacik from Public Health England for offering T-lymphocytes cells for the experiments, group discussions and support.

My efforts will remain incomplete if I don't express my love and deep gratitude to my parents, Mrs Anarkali Bhartiya and Mr Phul Chandra Bhartiya and my siblings Arpana and Akhilesh Bhartiya for their never-ending affection and untiring efforts for bringing my dreams and ambitions to a proper shape. I would also like to thank my husband, Mr Pankaj Kumar, for his immense support, inspiration, and love throughout my PhD research.

Publications, conferences and articles

- **A. Bhartiya**, M.Yusuf, S.W. Botchway and I.K. Robinson. "**Application of Fluorescence Lifetime Imaging Microscopy for assessment of chromosomal aberrations in X-ray induced chromosomes**". (*In preparation*).

- 4 April 2022|Article in 'Research Outreach'| **X-ray ptychography: Seeing chromosome abnormalities in a new light|**Link: Research Outreach.

- 29 May 2021| Press release in 'The Telegraph'| **The secrets of human chromosomes have not yet been cracked by scientists, study suggests** | UCL | UK. Links: *The Telegraph*, *UCL*, *LCN*, *Technology Networks*, *Technology*.

- Presented a **poster + flash talk** in the Joint Meeting of the 23rd International Chromosome Conference (ICC) and the 24th International Colloquium in Animal Cytogenetics and Genomics (ICACG), 2021. The poster titled: **"X-ray Ptychography Imaging of Human Chromosomes after Low-dose Irradiation".**

- Presented a **poster + flash talk** in Microscience Microscopy Congress 2021: International scientific virtual conference. The poster titled: **"X-ray Ptychography Imaging of Human Chromosomes after Low-dose Irradiation".**

- Atiqa Sajid, El-Nasir Lalani, Bo Chen, Teruo Hashimoto, Darren K Griffin, **Archana Bhartiya**, George Thompson, Ian K Robinson and Mohammed Yusuf. **Ultra-structural imaging provides a 3D fingerprint of 46 chromosomes of a human prophase nucleus,** International Journal of Molecular Sciences, 2021, ***22***(11), 5987. doi.org/10.3390/ijms22115987.

- **A. Bhartiya**, I. Robinson, M. Yusuf and S. W. Botchway, **Combining Multicolor FISH (M-FISH) with Fluorescence lifetime imaging (FLIM) for chromosomal identification and chromosomal sub structure investigation,** Frontiers in Molecular Biosciences, 2021, 8:631774. doi.org/10.3389/fmolb.2021.631774.

- **A. Bhartiya**, D. Batey, S. Cipiccia, X. Shi, C. Rau, S.W. Botchway, M. Yusuf, and I.K. Robinson, **X-ray Ptychography Imaging of Human Chromosomes after Low-dose Irradiation**, Chromosome Research, 2021, **29**, 107-126.

- **A. Bhartiya**, K. Madi, C. M. Disney, L. Courtois, A. Jupe, F. Zhang, A. Bodey, P. Lee, C. Rau, I.K. Robinson and M. Yusuf, **Phase contrast**

3D tomography of HeLa cells grown in PLLA polymer electrospun scaffolds using synchrotron X-ray, J. Synchrotron Rad, 2020, **27**, 1-6. doi.org/10.1107/S1600577519015583.

- Presented a **poster** in a Coherence 2018: International workshop on phase retrieval and coherent scattering conference, New York, USA. The poster titled: **"X-ray ptychography on a human chromosome spread".**

- M. Yusuf, F. Zhang, B. Chen, **A. Bhartiya**, K. Cunnea, U. Wagner, F. Cacho-Nerin, J. Schwenke and I. K. Robinson, **Procedures for Cryogenic X-ray Ptychographic Imaging of Biological Samples,** *IUCrJ*, 2017, **4**, 147– 151. doi.org/10.1107/S2052252516020029.

- **Talk** in UK-Japan workshop, 2016, Osaka University, Japan. Talk titled: **"Cryo-sample preparation and hard X-ray imaging at I-13-1(Diamond Light Source)".**

Table of Contents

List of Figures

List of Tables

Chapter 1

1. Introduction

1.1. Chromosome structure

Chromatin is composed of DNA-protein complexes present in nucleated cells. They form a thread-like structure during interphase and become condensed at the metaphase stage during cell division. DNA acquires different levels of packaging to fit within the approximately 10 μm (micrometer) nucleus of the cell. A 2 meter (m) long DNA is wrapped around octamer histone proteins (H2A, H2B, H3 and H4) to form 11 nanometer (nm) nucleosomes referred to as “beads on a string” (Olins and Olins, 1974). Nucleosomes are the building blocks of chromosomes. The X-ray crystal structure of nucleosomes confirmed the assembly of histone proteins and 146 DNA base pairs (bp) at a resolution of 2.8 Angstrom (Å) (Figure 1.1) (Luger *et al.*, 1997).

The best-known model of a 30 nm structure is solenoid/one-start-helix (Finch and Klug, 1976). This model represents the stacking of nucleosomes with their consecutive neighbours. This was identified from chromatin fibre after treatment with a low concentration of cations. The other model is zigzag/two-start-helix (Woodcock, Frado and Rattner, 1984). This model agrees with observing the crystal structure of the tetranucleosome at a resolution of 9 Å (Schalch *et al.*, 2005). The other model of the two-start-helix is cross-link chromatin fibre of diameter ~25 nm and 5 to 6 nucleosomes per ~11 nm nucleosomes (Dorigo *et al.*, 2004). However, the folding of the 30 nm structure is controversial (Maeshima, Hihara and Eltsov, 2010). Histone H1 proteins are DNA linkers that link nucleosomes together, giving chromatin stability (Thoma, Koller and Klug, 1979) (Maeshima and Eltsov, 2008). The linker histone (H1 and H5)

binds to the nucleosome that determines the geometry of the nucleosomes (Robinson *et al.*, 2006).

Figure 1.1: Structure of nucleosome core particle: the brown and turquoise ribbon depict the 146 DNA bp which wraps octamer histone proteins (blue: H3; green: H4; yellow: H2A; red: H2B). The images depict the views down the DNA superhelix axis for the left particle and perpendicular to it for the right particle. For both particles, the pseudo-twofold axis is aligned vertically with the DNA centre at the top (Luger *et al.*, 1997).

Understanding the organisation of chromatin into higher-order structures and its condensation process represents one of the key challenges in structural biology. The ratio of compaction for the nucleosome is 1:6, that for the 30 nm chromatin is 1:36 and for a mitotic chromosome is >1:10000 (Figure 1.2) (Strachan and Read, 2004) (Ou *et al.*, 2017).

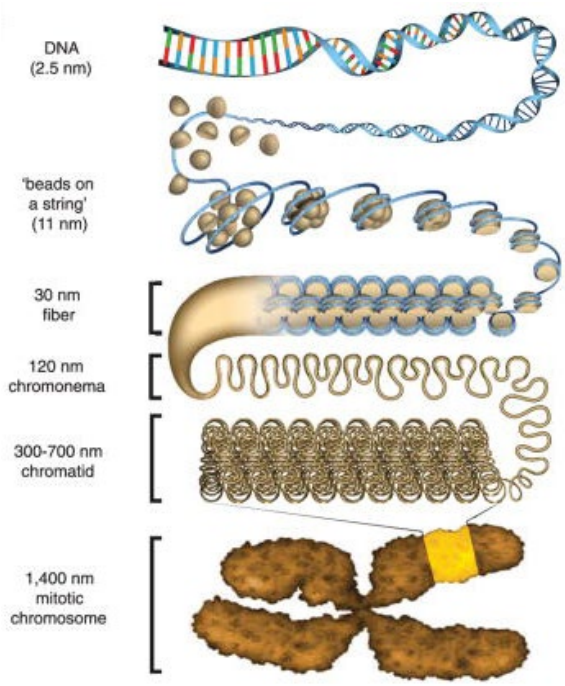

Figure 1.2: Packaging levels of the human genome, starting from 2.5 nm double-helix DNA to 1400 nm thick mitotic chromosome to fit into a 10 µm nucleus (Ou *et al.*, 2017).

Other factors such as monovalent and divalent cations play essential roles in regulating the high-order structures of chromosomes. The concentration of monovalent Na^+/K^+ and divalent Ca^{2+}/Mg^{2+} cations increase from interphase to metaphase in the cell cycle (Maeshima and Eltsov, 2008).

In 1956, Tjio and Levan successfully counted the correct number of human chromosomes, 46 (Figure 1.3). The human genome consists of 22 pairs of autosomes and a pair of sex chromosomes (Tjio and Levan, 1956). Chromosome 1 is the largest and contains 248,956,422 bp, whereas chromosome 21 is the smallest and has 46,709,983 bp of DNA sequences. Table 1.1 lists the length, DNA base pair sequences, GC-content, and weight of all the 46 human chromosomes that make up the human genome.

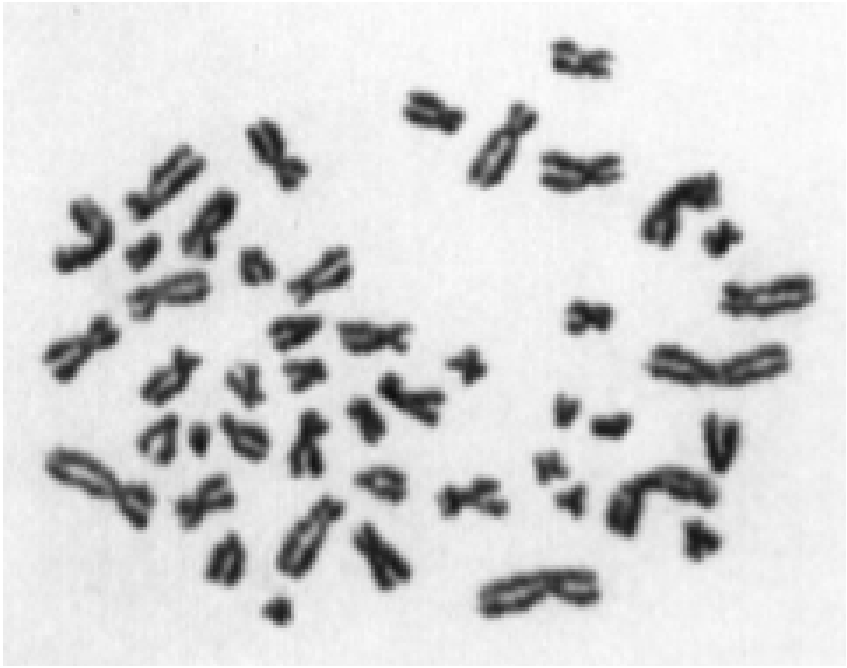

Figure 1.3: Metaphase plate of human chromosomes obtained from human embryonic lung fibroblast, showing all 46 human chromosomes (Tjio and Levan, 1956).

Chromosome	Length (bp)	Length (cm)	Weight (pg)	GC%
1	*249,250,621*	*8.15 ± 0.08*	*0.25*	41.74
2	243,199,373	7.95 ± 0.08	*0.25*	40.24
3	198,022,430	6.47 ± 0.06	0.20	39.69
4	191,154,276	6.25 ± 0.06	0.20	*38.25*
5	180,915,260	5.91 ± 0.06	0.18	39.52
6	171,115,067	5.59 ± 0.05	0.17	39.61
7	159,138,663	5.20 ± 0.05	0.16	40.75
8	146,364,022	4.78 ± 0.05	0.15	40.18
9	141,213,431	4.62 ± 0.04	0.14	41.32
10	135,534,747	4.43 ± 0.04	0.14	41.58
11	135,006,516	4.41 ± 0.04	0.14	41.57
12	133,851,895	4.38 ± 0.04	0.14	40.81
13	115,169,878	3.77 ± 0.04	0.12	38.53
14	107,349,540	3.51 ± 0.03	0.11	40.89
15	102,531,392	3.35 ± 0.03	0.10	42.20
16	90,354,753	2.95 ± 0.03	0.09	44.79
17	81,195,210	2.65 ± 0.03	0.08	45.54
18	78,077,248	2.55 ± 0.02	0.08	39.78
19	59,128,983	1.93 ± 0.02	0.06	*48.36*
20	63,025,520	2.06 ± 0.02	0.06	44.13
21	*48,129,895*	1.57 ± 0.02	*0.05*	40.83
22	51,304,566	1.68 ± 0.02	*0.05*	47.99
X	155,270,560	5.08 ± 0.05	0.16	39.50
Y	59,373,566	1.94 ± 0.02	0.06	39.97
Total (1-22, X, Y)	3,095,677,412	101.20 ± 0.97	3.17	40.90

Table 1.1: Indicates the length of the base pair (bp) and the GC- content of all 46 chromosomes. The length is indicated in bp and cm, while the weight is in picograms (pg) (Piovesan *et al.*, 2019).

1.2. Cell cycle and DNA content

In somatic cells, the cell cycle consists of two major phases: i) interphase that divides into G1- the first gap phase to prepare the cells for DNA replication, S-phase- where DNA is duplicated, G2- regulation of proteins and other essential processes required for forthcoming M-phase, ii) the M-phase further divides into mitosis and cytokinesis (Figure 1.4). The doubling time for eukaryotic cell cycle completion varies depending on the cell type. For example, the doubling time for lymphocytes cells is 20 hours (hrs) (Stewart, Cramer and Steward, 1975) and for a mammary epithelial cell is 22 hrs (Buehring and Williams, 1976). Approximately one cell division takes 24 hours, with G1 lasting around 11 hrs, S-phase for 8 hrs, G2 for 4 hrs and M-phase for about an hour (Cooper, 2000).

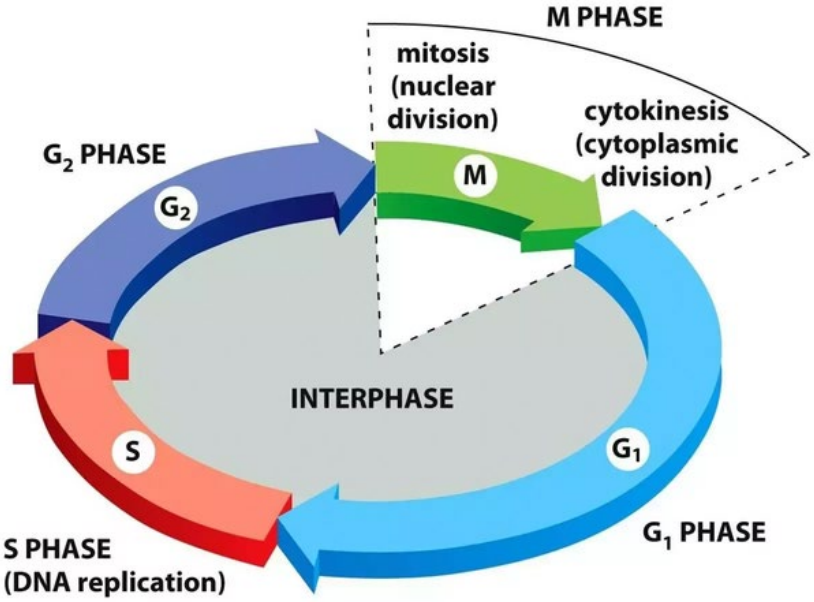

Figure 1.4: Schematic represent the somatic cell cycle phases (Alberts *et al.*, 2002)

Mitosis consists of four sub-phases; i) **prophase**-where the nucleolus disappears, and chromosomes condense, followed by nuclear membrane breakdown ii) **metaphase-** the chromosomes align to the equator of the cell, and

the chromosomes are at their most condensed state, iii) **anaphase-** the chromatids pull apart to opposite poles and iv) **telophase-** the nuclear membrane appears and the chromosome de-condenses. Eventually, the cell cleaves and divides into two daughter cells in **cytokinesis** (Morgan, 2007)**,** (Cooper, 2000)**.** After the cell division, the cells either enter the G0 stage (quiescent state) or the G1 stage for further division**.** In addition, there are three main checkpoints, i) G1/S point, to assure DNA replication and required growth factors ii) G2/M point, to ensure DNA damage and spindle attachment and iii) M-phase checkpoint, ensure spindle attachment and complete segregation of chromatids to the opposite poles (Morgan, 2007), (Schnerch *et al.*, 2012).

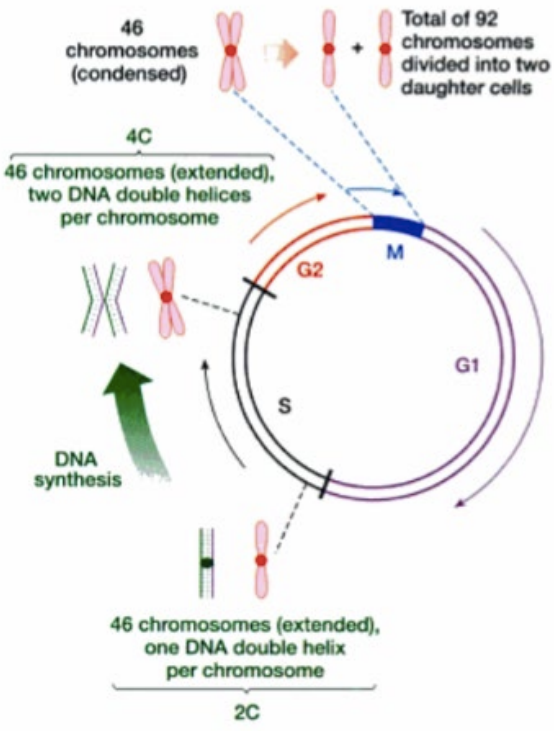

Figure 1.5: Chromosomal DNA content at different stages of the cell cycle. At G0 and G1 stage the DNA content is 2C and after synthesis of DNA at S-phase the DNA content gets doubled (4C) before the anaphase (Strachan and Read, 2004).

Furthermore, the DNA content varies at different stages of the cell cycle; at the growth phase (G1), the DNA content is 2C, where “C” is the amount of DNA contained by 2N chromosomes (“N”- number of unique chromosomes). When DNA replicates at S-phase, the amount of DNA is doubled to 4C, but the chromosome number remains 2N (Strachan and Read, 2004). Hence, in total,

there are 46 chromosomes with 92 chromatids that remain the same until the metaphase and anaphase. At the following telophase, the sister chromatids separate into two daughter cells, whereby the DNA content again reduces to 2C (Cooper, 2000), going into the 'rest' phase (G0) until the subsequent cell division. Consequently, a human nucleus will always consist of 46 chromatids, but after replication at S-phase, the DNA doubles to 92 chromatids before the separation of the daughter cells (Figure 1.5). During cell division, the relative chromosomal proteins (mainly scaffold proteins) also vary (Gookin *et al.*, 2017).

1.3. Karyotyping

A karyotype shows the arrangement of chromosomes and their pairs (except for males as they have X and Y chromosomes) from a single cell. Chromosomes in a karyotype are arranged according to many parameters that include their size, shape, and amount of genetic material (Figure 1.6)

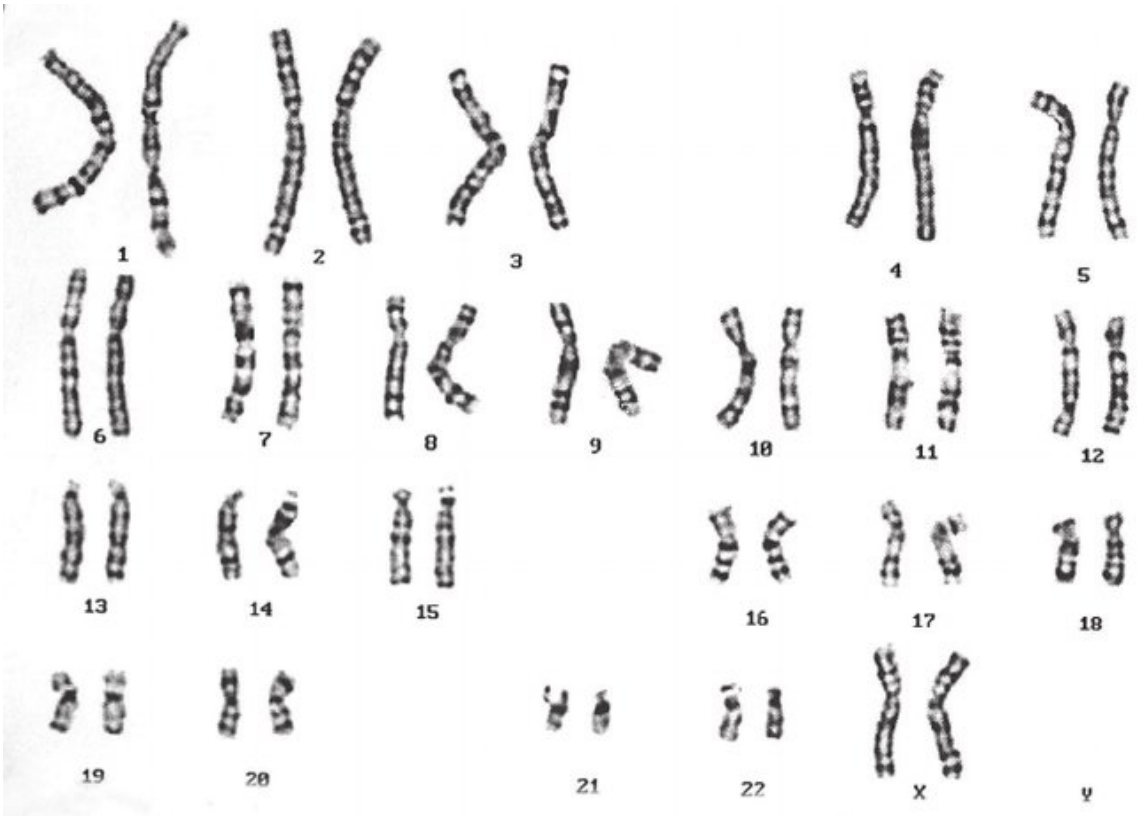

Figure 1.6: Karyogram showing all 46 chromosomes from a normal human female cell after G-banding (Huang *et al.*, 2010).

A karyotype is the first stage of identifying any genetic aberrations that include structural and numerical aberrations in an organism. Typically, chromosomes at the metaphase/prometaphase stage of the cell cycle are arrested using a spindle inhibitor such as colchicine to stop the further division of cells by hindering the cell cycle entering anaphase of the cell cycle (Taylor, 1965) (Anderson, Stevens and Goodhead, 2002) (Yusuf *et al.*, 2011). Karyotypes can be built after staining the chromosomes using appropriate dyes such as Giemsa or DAPI (Huang *et al.*, 2010) (Dai *et al.*, 2006). Karyotypes producing G-banding are the gold standard used in clinical laboratories worldwide to diagnose genetic diseases (Cram *et al.*, 1988).

1.3.1. Classification of human chromosome according to centromeric positions

In 1960, the Denver conference proposed the 24-human chromosomes classification and divided them into seven cytogenetic groups according to their lengths and sizes (Figure 1.7a) (Gagula-Palalic and Can, 2013). Human chromosomes are classified based on their centromeric positions and were initially arranged into different groups: median, sub-median and acrocentric chromosomes (Figure 1.7b) (Levan, Fredga and Sandberg, 1964). These are now classified as metacentric with almost equal p- and q-arm lengths, sub-metacentric having short p-arm and long q-arm and acrocentric-chromosomes almost with no p-arms with the centromere located near the end of the chromosomes. Nevertheless, Madian and Jayanthi (2014) proposed a fourth type, “very submetacentric,” in chromosome 5 (Madian and Jayanthi, 2014).

a)

Chromosome Class	Denver Group
#1-#3	Group A
#4-#5	Group B
#6-#12,X	Group C
#13-#15	Group D
#16-#18	Group E
#19-#20	Group F
#21-#22,Y	Group G

b)

Denver report			
No.	r	d	Designation
1	1.1	0.5	median
2	1.6	2.3	"
3	1.2	0.9	"
4—5	2.7	4.6	submedian
X, 6—12	1.9	3.1	"
13—15	6.7	7.4	acrocentric
16	1.5	2.0	median
17—18	2.8	4.7	submedian
19—20	1.3	1.3	median
Y	(5.9)	7.1	acrocentric
21—22	3.4	5.1	"

Figure 1.7: Classification of human chromosomes: a) chromosomes are divided into seven groups according to Denver's group (Gagula-Palalic and Can, 2013), b) arranged based on their length of short p-arm and the long q-arm ratios (Levan, Fredga and Sandberg, 1964).

Patau measured the long q-arm and short p-arm of human chromosomes in 1965, and the table below (Table 1.2) illustrates the updated relative lengths of human chromosomes (Therman, 2012).

Chromosome		Average length (in % of autosomal genome) of:		Chromosome		Average length (in % of autosomal genome) of:	
Group	No.	Long arm	Short arm	Group	No.	Long arm	Short arm
	1	4.68	4.57		13	3.29	—
A	2	5.28	3.35	D	14	3.12	—
	3	3.80	3.32		15	2.89	—
	4	4.85	1.84		16	1.93	1.34
B	5	4.66	1.75	E	17	2.07	0.96
	6	3.87	2.36		18	2.04	0.76
	7	3.54	2.04	F	19	1.32	1.11
	8	3.45	1.63		20	1.30	1.05
C	9	3.23	1.72	G	21	1.26	—
	10	3.22	1.54		22	1.38	—
	11	2.90	1.88	Total autosomes		100.00	
	12	3.38	1.32				
					X	3.26	2.02
					Y	1.64	—

Table 1.2: Depicts the list of average lengths of p and q-arms of autosome +X+Y human chromosomes (Therman, 2012).

There are two types of constrictions, primary (centromere) and secondary. The primary constrictions are present in all the chromosomes, whilst the secondary constrictions are present only in a few chromosomes. The latter is more frequently observed in the proximal region of chromosomes 1 and 9 after treatment with the BrdU (5-bromodeoxyuridine) (Palmer and Funderburk, 1965). The secondary constrictions in acrocentric chromosomes 13, 14, 15, 21 and 22 are associated with the Nucleolar Organisation Regions (NORs). These NORs are present at the top of the p-arm and contain genes to produce ribosomal DNA that forms the nucleolus at the end of the mitosis stage of the cell cycle (Henderson, Warburton and Atwood, 1972) (Goodpasture and Bloom, 1975). The role of the primary constriction is to secure the two sister chromatids, while the centromere acts as a bending site during the separation of the sister chromatid at the anaphase. During anaphase, secondary constriction is useful for identifying the NOR-containing chromosome (Bhatnagar and Bansal, 2009).

1.3.2. Identification of chromosomes with banding techniques

Several differential staining techniques have been developed which allow the visualisation of “bands” on the structure of chromosomes. Caspersson *et al.* in (1971) discovered the quinacrine (Q) fluorescence banding (observed patterns of dark and light bands) technique for identifying metaphase chromosomes (Sumner, 1982). Furthermore, chromosomes at metaphase can be identified by certain banding techniques such as Giemsa (G) and Reverse (R). These banding techniques are common in clinical practice for cytogenetic analysis (Shaw, 1973) and are based on the use of stains and/or fluorescent dyes to produce a display of dark and light bands in the chromosomes (Figure 1.6).

The positive G-bands show a dark colour at the AT-rich regions and the negative G-bands show a light colour representing mainly GC-rich regions of DNA (Hozier, Furcht and Wendelshafer-grabb, 1981). The GC-rich regions are less densely packed and early replicating regions, whereas AT-rich regions are more tightly packed and late replicating (Sumner, 1982). Imaging has shown that the former mostly localises at the centre of the nucleus whereas the latter at the

periphery during interphase (Cooper, 2000) (Cremer and Cremer, 2010). The C-banding method only stains the constitutive heterochromatin-rich region present in chromosome 1qh (secondary constriction region present in the heterochromatic region of the long arm of chromosome 1), 9qh 16qh and Yqh. These regions consist of highly packed repetitive DNA (Verma *et al.*, 1993) (Sumner, Evans and Buckland, 1971) (Shaw, 1973).

1.4. Chromosome staining techniques

Live cell imaging is a powerful technique to study cellular organelles such as chromosomes. Due to resolution constraints, early investigations relied heavily on sample preservation before imaging, however super resolution imaging is now available. For their preservation, chromosomes can be dehydrated using ethanol/acetone/methanol (Barke *et al.*, 2015), followed by chemical fixation using aldehydes such as glutaraldehyde/osmium tetroxide (Wako *et al.*, 2020). Alternatively, they can also be cryopreserved (in vitrified ice) (Yusuf *et al.*, 2017) (Dillard *et al.*, 2018). For electron microscopy or X-ray imaging, contrast can be enhanced using heavy metals bound to chromosomes, such as platinum blue (Pt-blue) (Yusuf *et al.*, 2014) (Shemilt *et al.*, 2015), (Ou *et al.*, 2017) and uranyl acetate (UA) (Xu and Wu, 1983). The negative stains UA and Pt-blue have been utilised to give the highest electron density map, improving the contrast of the biological sample such as chromosomes after X-ray ptychography imaging (Derksen and Meekes, 1984) (Ou *et al.*, 2017) (Shemilt *et al.*, 2015).

Uranium acetate is present in the form of uranyl cation (UO_2^{2+}) when diluted in water and maintains the pH of 4.5, and when used as a stain, it repels the positively charged proteins (Hayat and Miller, 1990) and phosphate ions of nucleic acid enhancing the contrast (Derksen and Meekes, 1984). Uranyl ions bind to proteins and DNA of mitotic chromosomes (Ou *et al.*, 2017) and induce a conformational change in protein-protein or DNA-protein interactions (Lin, 2020). Pt-blue is an alternative to UA, and it holds the advantage of being safer to handle, easily synthesisable and useful to enhance the contrast for electron density mapping (Inaga *et al.*, 2007). Staining is not sufficient for ultrathin

sections, and the stain probably crystallises on the sample (Inaga *et al.*, 2007) (Yusuf *et al.*, 2019). Pt-blue stains the chromosome well when mounted on the glass slides to collect backscattering signals from electrons (Yusuf *et al.*, 2019).

1.4.1. DNA-DAPI binding of chromosomes

Chromosomes can be visualised using fluorescence microscopy after binding to 4',6-diamidino-2-phenylindole (DAPI), a popular nucleic acid stain that binds to AT-rich regions of DNA every 2-3 base pairs (Kapuscinski, 1995). It absorbs light at around 358 nm (peak absorption) wavelength and emits blue fluorescence at 461 nm wavelength (Karg and Golic, 2018). The quantum yield of DAPI is 0.92 when bound to DNA and 0.04 for unbound DAPI (Kapuscinski, 1995). When DAPI bounds to DNA, it significantly improves the contrast of the image since the quantum yield is much smaller for unbound dye in solution (Estandarte *et al.*, 2016) (Barcellona and Gratton, 1990).

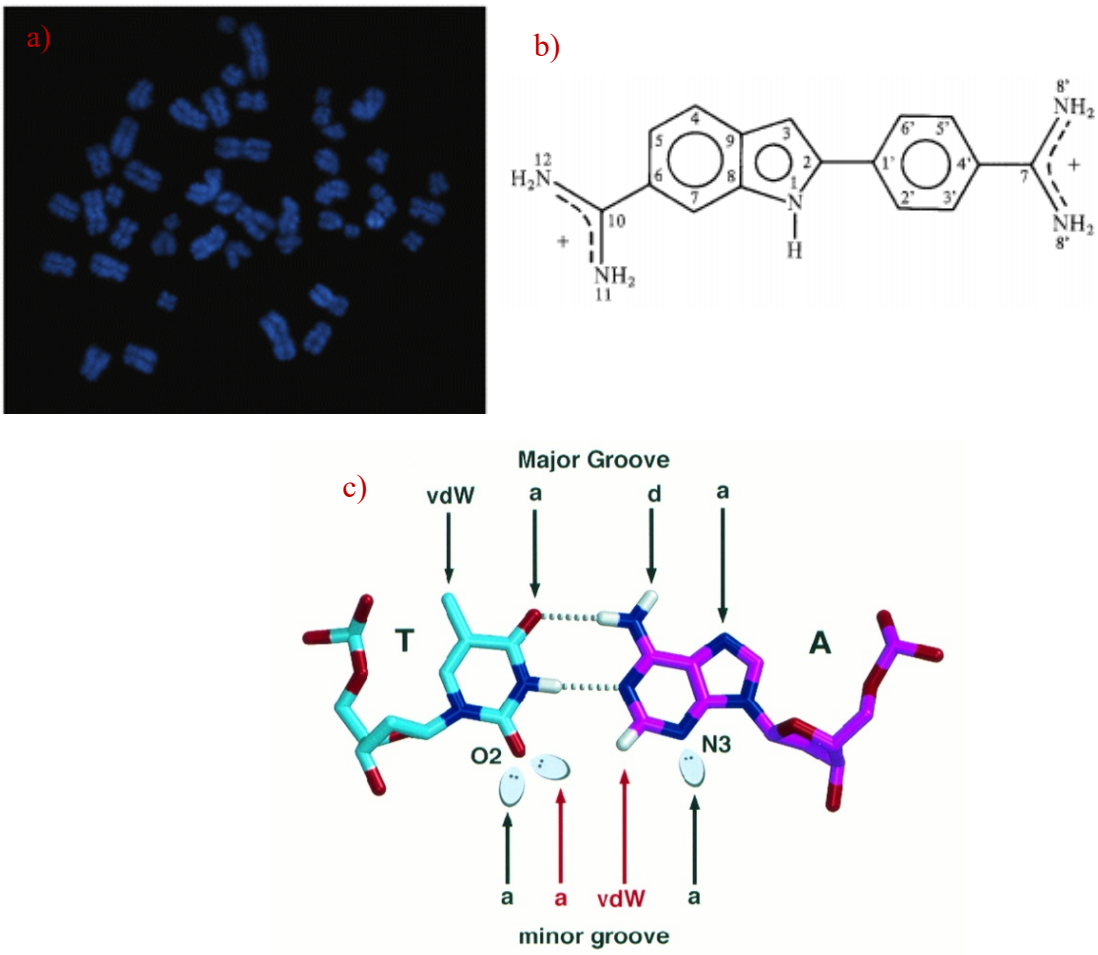

Figure 1.8: DNA-DAPI binding groove. a) DAPI stained chromosomes obtained from human induced pluripotent stem (hiPS) cells (Moralli *et al.*, 2011), b) chemical structure of DAPI (Barcellona and Gratton, 1990), and c) shows the minor groove region where DAPI binds to a DNA (Kielkopf *et al.*, 1998).

Figure 1.8a shows an example of a microscopy image of DAPI stained human chromosomes. Figure 1.8b represents the molecular structure of DAPI with three hydrogen donor groups, 2 amidino moieties at the end and one NH indole group carrying a positive charge. These positive charges strongly interact with the three hydrogen-bond acceptors of the minor grooves of the DNA AT-rich region (N3 of adenine and O2 of thymidine). The hydrogen bonding and van der Waals forces form the DNA-DAPI complex are shown labelled as “a” and “vdW” in Figure 1.8c (Kielkopf *et al.*, 1998).

DNA-DAPI complex depends on various factors such as i) the specificity of DAPI to bind to AT-rich regions of DNA at minor grooves rather than GC-rich regions because of the presence of an amino group at the position 2 of an adenine ii) the complex has low anisotropy because of the highly coiled structure of DNA iii) the proton transfer process is inhibited when DAPI binds to AT clusters rather than GC clusters which increase its lifetime. These properties of DAPI make it more specific to bind to DNA and assist in the structural determination of DNA and chromosomes. The excited-state lifetime varies substantially on binding: the DNA-DAPI complex has 2.8 ns (nanoseconds) when bound with AT-rich regions and 0.2 ns for unbound DAPI in solution (Barcellona and Gratton, 1990).

1.5. Chromosome sorting based on DNA content

Two-colour flow cytometry is a quantitative method of sorting chromosomes when stained with Hoechst 33258 and chromomycin A3 (Figure 1.9), with the sorting that occurs based on the amount of AT and GC content present in each chromosome, respectively (Langlois *et al.*, 1982). The positive correlation between the base ratio and the brightness from the fluorescence of Hoechst

33258 and chromomycin A3 is used to sort human chromosomes (Langlois *et al.*, 1982). However, the use of this method is uncertain because of the presence of an unequal proportion of base ratio in each chromosome.

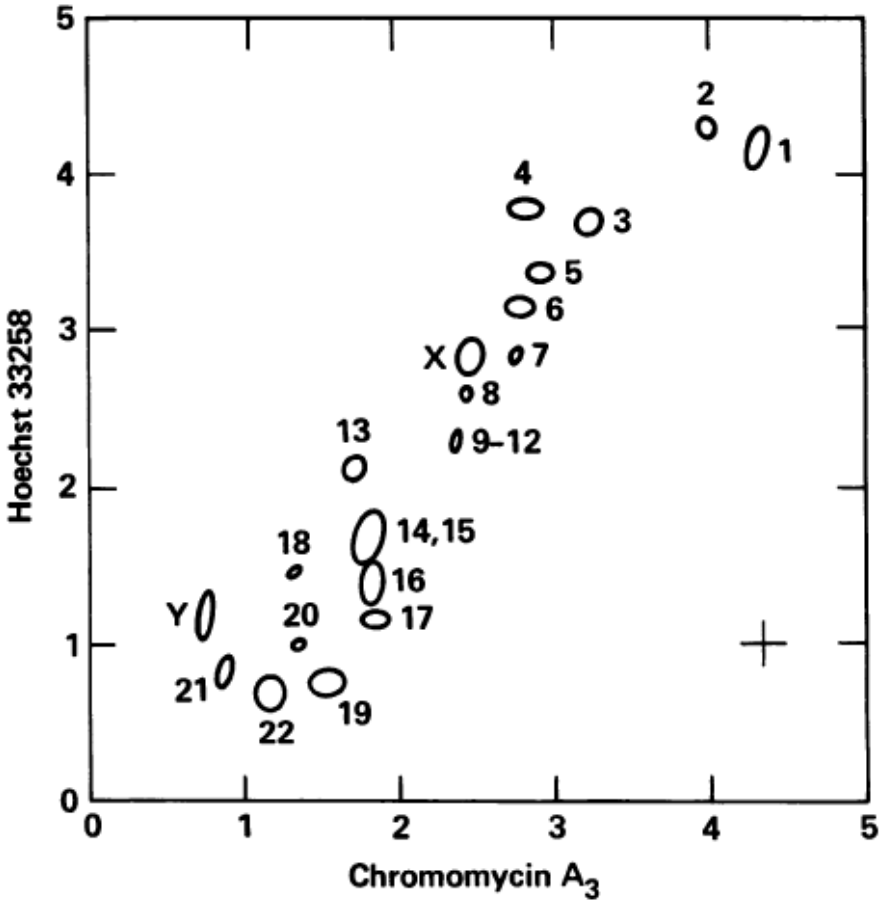

Figure 1.9: The bivariate flow cytometry shows the positive correlation between two dyes used for the karyotype. Ellipses indicates each chromosomes and the size of it corresponds to the variability of the base composition (Langlois *et al.*, 1982).

Chromosome sorting is based on the base pair composition and DNA content that is further classified in the following manner: i) The variability of the base ratio can be observed in a whole chromosome as well as within regions of a chromosome (Korenberg and Engels, 1978). ii) The larger chromosomes are more AT-rich than, the smaller ones examined by autoradiography. Moreover, they are late replicating in the cell cycle. In addition, the extent of AT base ratio is higher in larger chromosomes relative to smaller ones as determined by quinacrine-brightness (Korenberg and Engels, 1978), iii) A reasonable amount of

variation in DNA content has been observed between homologous pairs also within different donors volunteered, and the DNA content is measured by Cytophotometric Data Converter (CYDAC) (Mayall *et al.*, 1984).

The heteromorphic chromosomes 1, 9, 16, and Y showed more significant variability in the DNA content due to the presence of constitutive heterochromatin, followed by acrocentric chromosomes 13, 14, 15, 21 and 22 (Harris *et al.*, 1986). Among heteromorphic chromosomes, the Y chromosome showed the most significant variability, followed by chromosomes 1, 16, and 9 (Harris *et al.*, 1986) (Langlois *et al.*, 1982) (Mayall *et al.*, 1984). The sensitivity of flow cytometry has been unable to identify chromosomes 9-12, probably due to their same total DNA content (Langlois *et al.*, 1982).

1.6. Fluorescence lifetime Imaging Microscopy for assessment of the molecular environment of chromosomes

Fluorescence lifetime imaging microscopy (FLIM) is a technique that can map the molecular environment of fluorophore and can act as a reporter to photophysical events at a nanosecond time scale (Anthony, Guo and Berland, 2009) (see chapter 2 Materials and Methods section 1.5). Recently, regional chromosome compaction at nanometre length scales has been proposed along the length of chromosomes imaged using multiphoton FLIM following DAPI staining alone (Estandarte *et al.*, 2016). This was performed on a classical spread of chromosomes whereby excited-state lifetime measurements were obtained on all 46 chromosomes. Crucial for analysing the FLIM data is identifying each chromosome, whereby M-FISH plays an important role (Estandarte *et al.*, 2016).

M-FISH is a fluorescence technique that uses computer-generated pseudo colours from a coding scheme, which analyses the fluorescence from various combinations of five paints (probes) and uses DAPI as a counterstain (Speicher, Ballard and Ward, 1996). M-FISH is an invaluable karyotyping tool that provides a detailed analysis of structural rearrangements and marker chromosomes

(Yusuf *et al.*, 2013). Its use has been expanded into validating and karyotyping complex clinical cases after G-banding (Jalal and Law, 1999) on the same sample. Furthermore, its use has been demonstrated in identifying and karyotyping chromosomes based on phase contrast (Shemilt *et al.*, 2015) and fluorescence (Yusuf *et al.*, 2011) imaging methods.

1.6.1. Principle of FLIM

When a sample is exposed to electromagnetic radiation, absorption occurs, resulting in a transition of electrons from the ground state to an excited state. The subsequent relaxation to a lower energy state (possibly the ground state) through the emission of a lower energy photon is called fluorescence (singlet state transition). In addition to the fluorescence, the relaxation phenomenon can also occur by alternative mechanisms such as internal conversion and intersystem crossing, as described in the simplified Jablonski diagram in Figure 1.10. The fluorescence lifetime is the amount of time a fluorophore remains on average in its excited state before returning to the ground state by emitting a photon. The emission of a fluorescence photon from a fluorophore does not occur at a fixed time, i.e., probabilistic. Instead, a distribution of times is observed, which can be described by an exponential decay function (Lakowicza *et al.*, 1987).

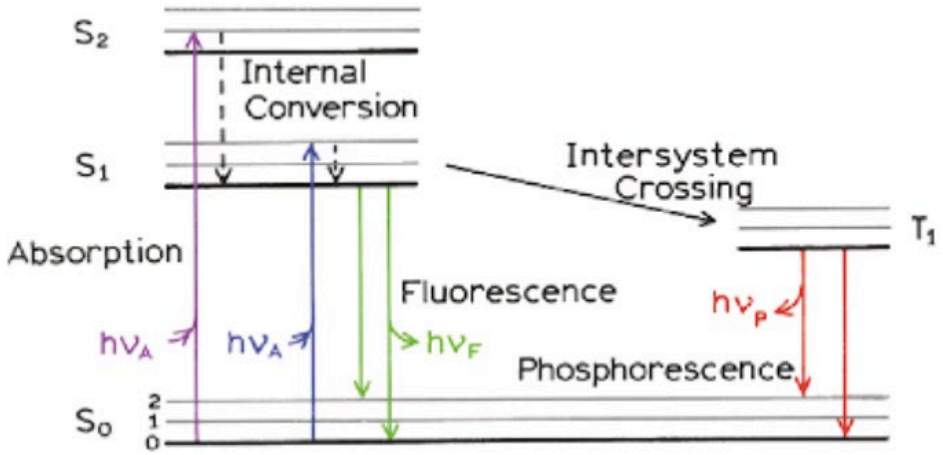

Figure 1.10: Jablonski diagram representing electronic energy levels (Lakowicz, 2006b).

The relaxation of an electron promoted to an electronic excited state can lose energy by vibration and molecular collision. These conversions are known as non-radiative decay. The absorption typically lasts for approximately 10^{-15} seconds (s), while fluorescence lasts for 10^{-9} s (Lakowicz, 2006b),(Wang and Bai, 2006). The time during which the molecules stay in their excited state is called the lifetime of the fluorophore, and it ranges from 10^{-8}-10^{-9} s (Lakowicz, 2006b). The fluorescence lifetime is defined by **Equation 1.1**:

$$\tau = \frac{1}{k_r + k_{nr}} \qquad \textbf{(1.1)}$$

The fluorescence lifetime (τ) is inversely proportional to the sum of radiated rate constant (K_r) and non-radiated rate constant (K_{nr}) (Suhling *et al.*, 2015). The single exponential fluorescence decay is obtained from an **Equation 1.2:**

$$\mathbf{F(t)= f_0 e^{-t\backslash\tau}} \qquad \textbf{(1.2)}$$

The lifetime value is generated from the fitted function model (equation 1.2). However, f_0 is the intensity at a time t = 0, t is the time after the absorption, and $\boldsymbol{\tau}$ is the fluorescence lifetime (Suhling *et al.*, 2015). As well as this, instrument response function (IRF) should also be considered during fluorescence decay calculations. IRF is used to determine the parameter that affects the measured lifetime from the instrumentation as a whole.

FLIM can distinguish two regions of an image with the same brightness (i.e. intensity) but different lifetime values (Lakowicz, 2006a). Therefore, the FLIM image can give more information than the intensity image alone. Besides, FLIM is rarely affected by photo-bleaching (which occurs due to the complete decayed of fluorophore) or by the auto-fluorescence-emission of light that naturally occurs within the biological structures (it affects only the intensity). Hence, FLIM has the potential for single molecule monitoring (Becker, 2012). Photo-bleaching and the signal to noise ratio can be reduced, unlike other fluorescence microscopy methods, by adjusting the scan time of the samples and altering laser power

according to the requirements to gain good resolution (Laptenok *et al.*, 2007). Another advantage of FLIM is that it is independent of the concentration of fluorophores. It calculates the lifetime from environmental change in the sample, such as pH, viscosity, temperature, refractive index, ion concentrations and quantum efficiency of the probes (Suhling *et al.*, 2015). The colour-coded images obtained from FLIM give information on lifetime values at each pixel level. Therefore, the spatial information of molecules can be obtained by FLIM on a nanometer (<100 nm) length scale (see chapter 2 Materials and Methods section 1.5.5).

The FLIM data are acquired when the samples are raster scanned in X and Y coordinates using high power Ti-sapphire laser pulses. In this work, the emitted photons are recorded by Time-Correlated Single Photon Counting (TCSPC) within each pixel with respect to time. Integrated photons were analysed using computer software to fit exponential decays at each pixel to get the lifetime of decayed fluorophores (Laptenok *et al.*, 2007) (see chapter 2, Materials and Methods).

1.6.2. Applications of FLIM

Fluorescence microscopy has contributed tremendously to elucidating the dynamic structure of chromosomes (Ried *et al.*, 1998) (Manders, Kimura and Cook, 1999) (Ishizuka *et al.*, 2016) and proteomic contribution to the chromosomes (Gassmann, Henzing and Earnshaw, 2005) (Rahman-Roblick *et al.*, 2008). One of the important uses of FLIM is the Forster Resonance Energy Transfer (FRET), used to study protein-protein interactions and conformational changes in life science (Suhling *et al.*, 2015) (Ahmed *et al.*, 2020). FRET measures intermolecular distances between chromophores on an angstrom scale. It has also been employed to measure the compaction of chromatin from interphase to telophase of the cell division (Llères *et al.*, 2009).

The combined FRET-FLIM technique has been applied to understanding the condensation and the de-condensation process of chromosomes, from prophase to prometaphase, following regulation of the amount of calcium (Ca^{2+}) divalent cations in the cells (Phengchat *et al.*, 2016). Recently, FLIM has been used to observe chromosomal structural changes such as compaction in DAPI-stained fixed methanol acetic acid metaphase human chromosomes (Estandarte *et al.*, 2016). According to Estandarte *et al.* (2016), FLIM, of non-irradiated fixed human metaphase chromosomes showed a shorter lifetime in chromosomes 1, 9, 15, 16 and Y at the heterochromatic regions in comparison to other chromosomes in the human genome (Estandarte *et al.*, 2016) as shown in Figure 1.11. The chromosomes are commonly known as heteromorphic (comprising of different sizes and shapes of heterochromatin regions present close to the pericentromeric region) chromosomes. FLIM provides a measure of the reduced lifetime values in condensed chromatin in human endothelial cell nuclei at different viscosity environments at every pixel forming an image (Spagnol and Dahl, 2016). From all three examples mentioned above, shorter lifetime values were observed in condensed chromatin than in de-condensed chromatin (Spagnol and Dahl, 2016) (Estandarte *et al.*, 2016) (Phengchat *et al.*, 2016).

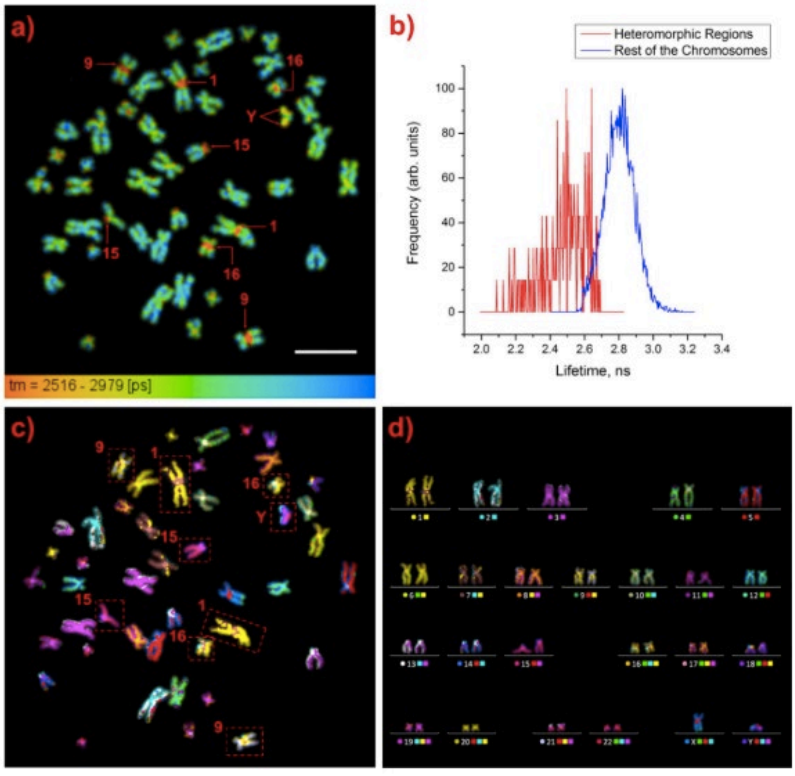

Figure 1.11: Identified heteromorphic human metaphase chromosomes from a spread; a) a human metaphase chromosome spread showing after FLIM. Red arrows show the heteromorphic chromosomes, scale bar = 10 µm b) normalised lifetime distribution of heteromorphic region and rest of the chromosomes and the former possess shorter DAPI lifetime relative to latter, c) M-FISH image of spread a) displaying 46 chromosomes that are all colour-coded in their respective pairs, d) the M-FISH karyotype of spread c) (Estandarte *et al.*, 2016).

Furthermore, FLIM can distinguish the change in affected to unaffected cells via lifetime changes. For example, chromosomes extracted from leukaemia affected cells showed a shorter lifetime compared to the unaffected chromosomes (Yahav *et al.*, 2016). In another approach, FLIM was used to record the de-condensation behaviour of Hoechst 34580 stained nuclei irradiated with a 10 Gy X-ray dose. The de-condensation nature was confirmed with the increased lifetime values from 1.3 ± 0.04 ns to 1.4 ± 0.05 ns in 10 Gy exposed nuclei (Abdollahi, Taucher-Scholz and Jakob, 2018). Further studies performed using FLIM to show the lifetime change in condensed and decondensed mitotic chromosomes as summarised in Table 1.3 below (Botchway *et al.*, 2021).

Microscopy approach	Sample	Cell type	Findings	Publication
FLIM	Human fixed metaphase chromosomes, DAPI and Hoechst 33258 stained	B-lymphocyte, HeLa, and CCD37/LU	Heteromorphic regions of chromosomes 1, 9, 15, 16, and Y displayed shorter lifetimes Variability in the lifetime amongst the heteromorphic region is due to structural changes	Estandarte et al. 2016
FLIM	Human fixed metaphase chromosome and cells, o-BMVC	CL1-0, MRC-5, BJ, and HeLa	Anti-HT can unfold telomeric G4 structures in fixed cells Metaphase chromosomes possess G4 structures formed by human telomeric TTAGGG repeats	Tseng et al. 2020
FLIM-FRET	Human live and permeabilized mitotic cells, EGFP/mCherry	Hela	Small molecules including cations and polyamines influence the conformation and compaction of chromatin within nuclei Condensation upon ATP depletion in interphase is distinctive from the mitotic chromatin condensation	Visvanathan et al. 2013
FLIM-FRET	Human live cells and metaphase chromosomes EGFP and mCherry	HeLa S3 cells, HeLaH1.2-EGFP, HeLaH2B-EGFP and HeLaH2B-2Fp	Ca^{2+} plays a crucial role in the mitotic progression and condensation of chromosomes Ca^{2+}-depleted chromosomes showed fibrous structure and $CaCl_2$-treated chromosomes had compact globular structure	Phengchat et al. 2016
FLIM-FRET	Human live cells interphase and mitotic chromosomes, H2B-EGFP, and H2B-mCherry-	HeLa	Chromatin compaction increases from prometaphase to late anaphase and decreases during telophase Heterogeneity in chromatin within individual chromosomes	Llères et al. 2009

Table 1.3: A list of selected FLIM studies performed to investigate the mitotic chromosome structure (Botchway *et al.*, 2021).

1.6.3. Constitutive heterochromatin

Heterochromatin was first expressed by Emil Heitz in 1928 in an interphase cell (Heitz, 1928) (Allshire and Madhani, 2018) (Berger, 2019). The heterochromatin can be of two types: constitutive and facultative. The constitutive heterochromatin remains compact, gene-poor and enriched with repetitive and late replicating DNA sequences. In contrast, the facultative heterochromatin shows temporal and spatial active and inactive behaviour of transcription (Woodcock and Ghosh, 2010). The compaction of the heterochromatin results from histone hypoacetylation and histone methylation (Bannister *et al.*, 2001). The constitutive heterochromatin is the cause of trimethylation of lysine 9 of histone H3 (H3K9me3) (Nicetto and Zaret, 2019) (Bannister *et al.*, 2001) and mono-methylation of lysine 27 of histone H3 (Figure 1.12a).

In contrast, the facultative heterochromatin is designed as H3 lysine 27 trimethylation (H3K27me3) (Saksouk, Simboeck and Déjardin, 2015). Some parts of the euchromatin are transcriptionally silenced mainly by mono-di-methylation of lysine 9 of H3 and to a lower extent by mono-di-tri-methylation of lysine 27 of H3 as shown in Figure 1.12b (Dillon, 2004). Heterochromatin protein 1 (HP1) binds with H3K9me3 sites, forming a bridge between nucleosomes, and plays an important role in gene silencing and packaging of pericentromeric heterochromatin (Lachner *et al.*, 2001) (Bannister *et al.*, 2001).

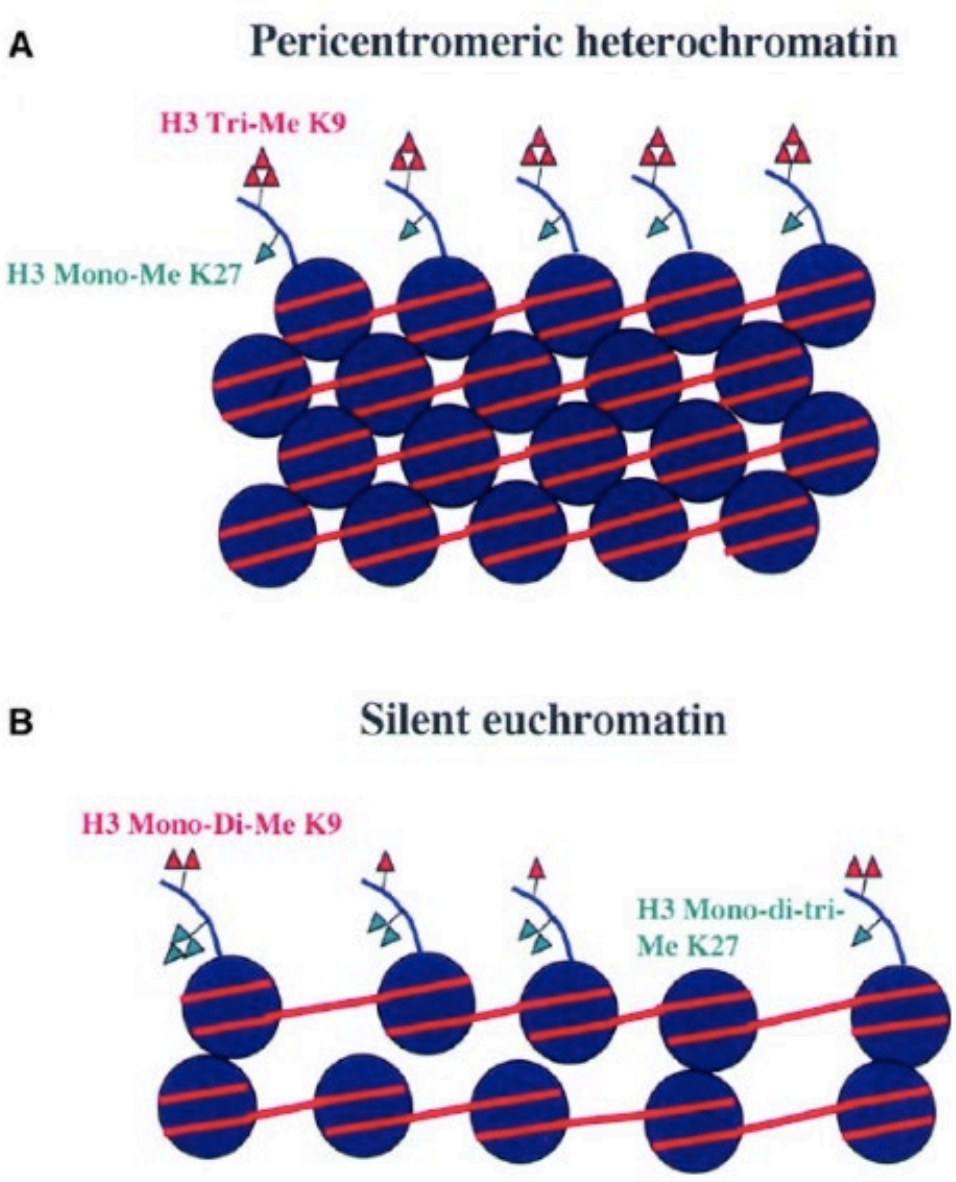

Figure 1.12: The arrangement of nucleosomes and the histone modifications determine the chromatin structure. (A) A regular array of nucleosomes promoting the highly condensed nature of pericentric heterochromatin (B) Irregular arrangement of nucleosomes causing silencing euchromatin by mono-di methylation of lysine 9 of histone 3 and mono-di-tri methylation of lysine 27 of histone 3 (Dillon, 2004).

The block of constitutive heterochromatin regions are located at the pericentric region of chromosome 1, 9 and 16 (Tagarro, Fernández-Peralta and González-Aguilera, 1994), short p-arm of chromosome 15 (Friedrich *et al.*, 1996) (Chen *et al.*, 1981), and distal region of chromosomes Y (Estandarte *et al.*, 2016) (Bachtrog, 2014) (Choo, 1997) (Meyne *et al.*, 1984). Chromosomes 1, 9, 15, 16 and Y were defined as heteromorphic chromosomes by visualisation using the C-banding technique (Sahin *et al.*, 2008). Heteromorphism was also identified in

the short arm of the acrocentric chromosomes 13, 14, 15, 21 and 22 with G-banding with regards to the presence of satellite and the stalk length (Arthur R Brothman *et al.*, 2006). It has been reported in the cytogenetics resource committee (of the College of American Pathologists and the American College of Medical Genetics) that chromosomes 1, 9, 16 and Y are considered more heteromorphic chromosomes as compared to other chromosomes in a genome (Arthur R. Brothman *et al.*, 2006). The heterochromatic chromosomes have also been identified using electron microscopy (Sanchez, Martinez and Goyanes, 1991), molecular cytogenetics (Speicher, Ballard and Ward, 1996) (Jalal and Law, 1999) (Estandarte *et al.*, 2016).

Furthermore, both pairs of chromosome 9 are structurally highly polymorphic containing the largest autosomal block of heterochromatin, making it heteromorphic in 6-8 % of the human genome 9 (Humphray *et al.*, 2004). Moreover, chromosome 9 contains some evolutionary conserved regions (ERCs) in their DNA sequence (Humphray *et al.*, 2004). Exceptionally, the pericentric inversion occurs at the heterochromatin region, which makes chromosome 9 differ morphologically (Akbas *et al.*, 2010) (Humphray *et al.*, 2004), and it is the most common (1-3 %) inversion noticed in the general population" (Akbas *et al.*, 2010). Additionally, the heteromorphic variants of chromosome 9 were more frequently observed in females than males by 1.4 times (Kosyakova *et al.*, 2013).

Constitutive heterochromatin of each chromosome is approximately size "5 Mb to a few hundred bp" (Saksouk, Simboeck and Déjardin, 2015), and these regions consist of varied satellite DNA defined as tandemly repeated sequences of DNA (Choo, 1997). The satellites are **α**-satellite DNA, DNA satellite I, II and III (Choo, 1997). Among them, Satellite II is not as conserved as satellite III (Tagarro, Fernández-Peralta and González-Aguilera, 1994). The centromere of all human chromosomes consists of AT-rich sequences; it contains 171 bp **α**-satellite repeats and comprises approximately "10 %" of the human genome (Sullivan, Chew and Sullivan, 2017). The **α**-satellites are regions of repetitive DNA sequences conserved from the primates to humans, and they are considered to be more evolutionary divergent than any other sequence type (Jackson *et al.*, 1999).

Satellite I is based on repetitive units of 42 bp, AT-rich DNA sequences (Prosser *et al.*, 1986) (Tagarro, Fernández-Peralta and González-Aguilera, 1994). In contrast, satellite II and III are considered to be heterogeneous in nature and are based on the 5 bp motif “GGAAT” (sense strand) and ATTCC (antisense strand) repeat DNA sequence (Figure 1.13) (Tagarro, Fernández-Peralta and González-Aguilera, 1994). To date, the functional role of satellite II and III is unclear. The chromosome 1 consists of satellite II (majority) and III (minority). Chromosome 9, 15 and Y have satellite III while chromosome 16 contains satellite II (Tagarro, Fernández-Peralta and González-Aguilera, 1994) (Figure 1.14).

The telomere, on the other hand, consists of repeats of hexanucleotide (TTAGGG) DNA sequences (Humphray *et al.*, 2004) (Saksouk, Simboeck and Déjardin, 2015) (Nishibuchi and Déjardin, 2017).

Satellite 2 ATTCCATTCG(A/G)G(A/T)CCATTCGATGAT

Satellite 3 $(ATTCC)_n$ ATTCCA(T/C)TCGGGTTGATTCC $(ATTCC)_n$

Figure 1.13: The consensus DNA sequence of satellite 2 and 3 and the underline sequences are the designed oligoprobes of each satellites, respectively (Tagarro, Fernández-Peralta and González-Aguilera, 1994).

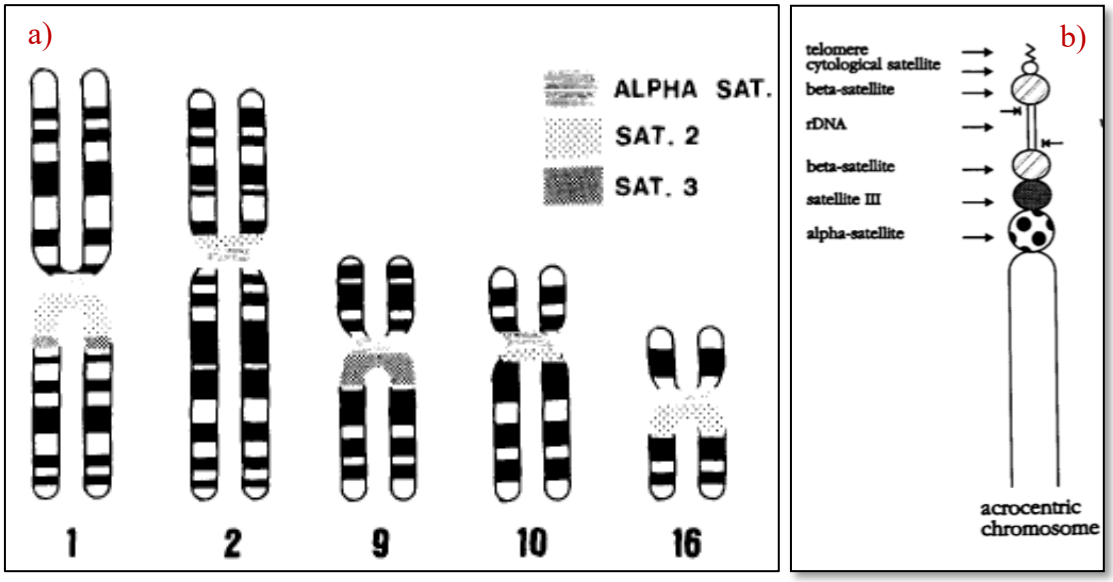

Figure 1.14: The proportional distribution of satellites at the pericentric centromere region of listed chromosomes; a) localisation of alpha satellite, satellite 2 and 3 (Tagarro, Fernández-Peralta and González-Aguilera, 1994), b) distribution of varied satellites, rDNA and telomere at the short p-arm of acrocentric chromosomes (Friedrich *et al.*, 1996).

Constitutive heterochromatin is inheritable and conserved (Allshire and Madhani, 2018), transcriptionally inactive (Bannister *et al.*, 2001) (Saksouk, Simboeck and Déjardin, 2015) and genetically inert (Allshire and Madhani, 2018) (Choo, 1997).

1.7. X-ray ptychography of chromosomes

For biological samples, the strength of X-ray penetration directly determines the choice of X-ray wavelength used for high-resolution imaging (Larabell and Nugent, 2010). Detailed information can be obtained from atomic to molecular level without any sample processing such as fixation, staining or sectioning (Robinson *et al.*, 2016). All forms of X-ray imaging, including X-ray microscopy, are sensitive to matter because a photon from an X-ray source interacts with the inner shell of each atom of the specimen through direct absorption or refraction (change of phase) (Howells *et al.*, 2006). The complex refractive index, n =1- $\boldsymbol{\delta}$ + iβ, describes the X-ray interaction with matter, with the real component ($\boldsymbol{\delta}$) describing the phase change and the imaginary component (β) denoting the absorption of the beam (Hémonnot and Köster, 2017).

There are three ways of interactions of X-rays with matter: i) photoelectric absorption, ii) elastic scattering and iii) inelastic scattering (Dendy and Heaton, 1999), (Martin, 2002). In photoelectric absorption, when light interacts with the matter, the electrons are ejected from the inner orbital of an atom; the energy of the incident light is completely absorbed, and the ejected electrons are known as photoelectrons. In elastic scattering, the energy of the incident light is conserved upon interaction with matter, while in inelastic scattering, such as Compton, energy loss occurs together with its deflection from its original path. For example, Rayleigh scattering is a form of elastic scattering (Young, 1981).

X-rays used for imaging biological samples can be divided into soft X-rays and hard X-rays, depending upon their wavelength and photon energy. The wavelength range for soft X-ray is 2 -5 nm, and it operates in the ‘water window’ of a spectral region between the carbon K-edge at 284 eV and the oxygen K-

edge at 540 eV (Maser *et al.*, 2000). The use of soft X-rays is advantageous over other conventional methods. For example, the sample mass loss during measurements with soft X-rays is minimal and morphological distortion effects are also limited even at a radiation dose of 10^{10} Gray (1Gy=1J/Kg). Soft X-rays also allow for imaging of frozen-hydrated biological samples, which maintains the sample structure close to its native state (Maser *et al.*, 2000). For example, soft X-ray tomography (SXT) was used for investigating the ultrastructure of cryopreserved female inactive X-chromosome, which in combination with cryogenic fluorescent microscopy (CFT), allowed for molecular localisation in a nucleus (Smith *et al.*, 2014). Moreover, a frozen-hydrated yeast cell was resolved at a resolution of ~ 25 nm using soft-X-ray diffraction imaging techniques (Huang *et al.*, 2009).

Due to their high penetrating capacity, the use of hard X-rays allows access to samples thicker than ~1 μm (Yamamoto and Shinohara, 2002). This means chromosomes can be imaged in a close to native state and does not require invasive staining. For hard-X-ray imaging, third-generation synchrotron radiation sources provide photon energies between 5 and 10 keV to study biological samples up to a thickness of the absorption length, which is 200 μm at 5 keV and 2.5 mm at 10 keV. This thickness significantly exceeds the 100 nm limit of transmission electron microscopy (TEM) (Guk et al., 2008). More importantly, “lensless” methods exploit the high coherence of third-generation synchrotron radiation sources to solve the “phase problem” to provide an electron density map by phase contrast (Nishino et al., 2009).

In short, soft X-rays tend to give absorption information (Shapiro et al., 2005), and although they are limited in resolution, they are claimed to prevent radiation damage effects (Kirz, Jacobsen and Howells, 1995). Hard X-rays allow better resolution, the stronger penetration of hard X-rays makes them suitable to study thick samples, like chromosomes, that are too thick for TEM imaging (Shemilt et al., 2015).

Scanning X-ray fluorescence microscopy has been used to map the signal of iron (Fe), phosphorus (P) and sulphur (S) in human nuclei, whereas P and S are presumed to be associated with DNA and protein components in the nuclei (Robinson *et al.*, 2016). The first ever attempt to image micron-sized details of the high order structure of the chromosome was made using SCALA X-ray Free Electron Laser (XFEL) facility in Japan using the MAXIC chamber (Robinson *et al.*, 2015), where 400,000 diffraction patterns were collected.

1.7.1. Coherent X-ray diffraction imaging (CXDI)

Coherence is a property of waves having a constant phase and frequency. Two waves interfere to form constructive (when two waves are in phase) and destructive (when two waves are out of phase) interference. Coherence has been applied in four different ways: i) plane wave coherent diffraction imaging (CDI) for fixed sample illumination, ii) ptychography CDI for non-periodic substances with a fixed illumination), iii) Bragg CDI for nanocrystal structures, and iv) curved wave CDI for a large field of view (Miao, Sandberg and Song, 2012) to investigate the internal and external structure of the samples for better understanding the molecule functions (Henry N Chapman *et al.*, 2006). CDI is a lensless method which uses computerised algorithms to reconstruct obtained diffraction patterns into high-resolution and better phase-contrast images (Robinson, 2015).

In addition, the Fresnel zone plate (FZP) is used to converge the planer incident beam onto the targeted positions (Schroer *et al.*, 2003). FZP is designed with concentric circles of different radii; these are divided into opaque and transparent rings so that the beam can only pass through alternative transparent rings to obtain a constructive interference point (Batey *et al.*, 2019) (Rau *et al.*, 2016). The FZP is the best option for lensless imaging as it diffracts the upcoming monochromatic beam to a converging point (Chapman and Nugent, 2010). Forward scattering CDI is a unique approach to image biological samples at a high resolution. This approach collects far field, scattered diffracted patterns once the incident beam hits the isolated sample to reconstruct into images (Chapman and Nugent, 2010).

An example of coherent X-ray imaging to study a human chromosome is the first attempt by Nishino *et al*. 2009, to image 3-D, ultra-structure of unstained human metaphase chromosome at a photon energy of 8 keV. The diffraction patterns were processed using a hybrid input output (HIO) phase retrieval algorithm (Nishino *et al.*, 2009). Although the axial chromosome structure was successfully resolved (Figure 1.15), the internal structure of the chromosome was not imaged (Nishino *et al.*, 2009).

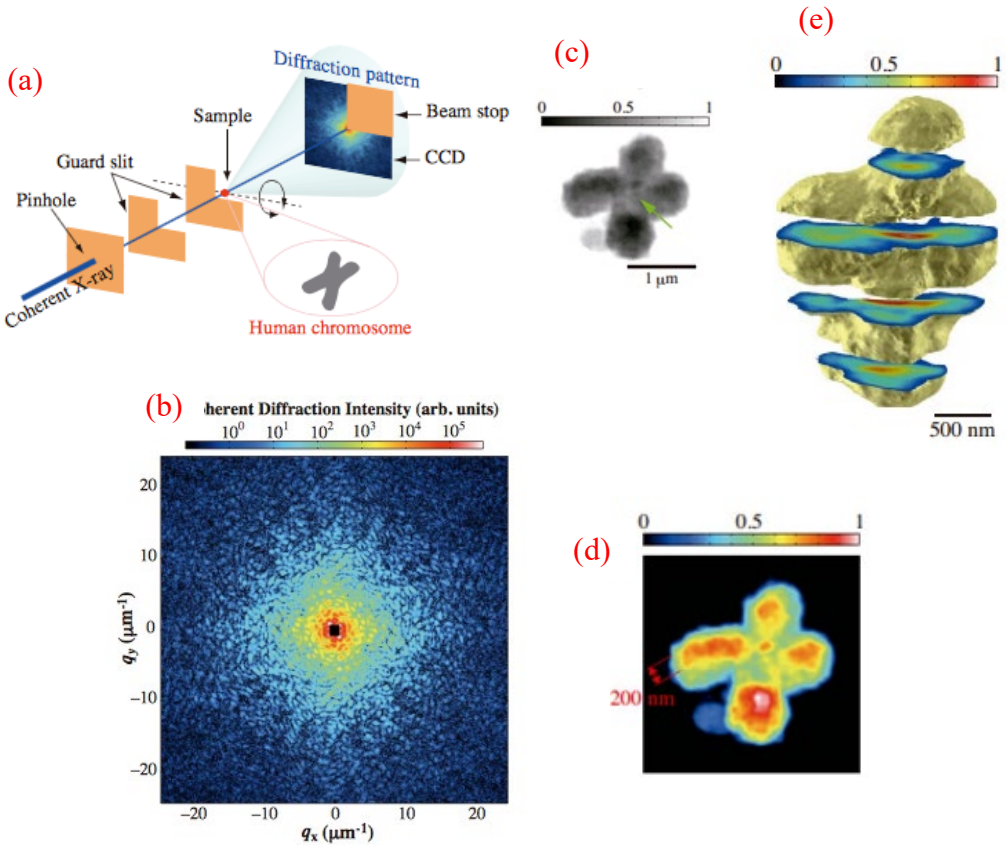

Figure 1.15: Hard-X-ray coherent diffraction imaging of an unstained human chromosome; a) schematic of the coherent X-ray setup, b) the obtained speckle pattern from the chromosome, c) gray scale image, green arrow indicate the centromere, d) indicate the axial structure at 200 nm resolution and e) cross-sectioned at a 409 nm intervals for 3D analysis (Nishino *et al.*, 2009).

Moreover, Yan *et al*. (2016) developed a new imaging technique by combining hard X-ray with a nano-focusing optic; this enabled the detection of a platinum blue (Pt-blue) stained human chromosome even without sectioning. With this technique, the nanoscale information was obtained from the absorption,

phase-contrast and fluorescence intensity simultaneously (Yan *et al.*, 2016) which allowed to resolve the ultra-structure of a thick chromosome.

1.7.2. Ptychography

In principle, ptychography CDI is a technique in which an object is illuminated and scanned in a stepwise fashion to produce an array of partially overlapped probe spots onto the object. The obtained diffraction patterns from each spot are run through complex inverse Fast Fourier Transform (FFT) algorithms (Figure 1.16) for reconstructing the patterns into images (Sidorenko and Cohen, 2016) (Rodenburg et al., 2007). The output is a pair of images containing information regarding: i) the amplitude, which measures the extent of light absorbed by the sample, and ii) the phase, which measures the phase delay introduced to the beam as it passes through the sample. Ptychography solves the phase problem by consistently combining the diffraction patterns of overlapping images (Robinson, 2015) (Stachnik, 2012).

The combination of high penetration power of hard-X-rays and sensitivity of CDI are the main benefits of ptychographic imaging. It has the capability for nanometre-scale resolution of three-dimensional structures with increased sensitivity to electron density changes (Dierolf *et al.*, 2010). The method gives phase information (electron density maps) across a large field of view (Rodenburg *et al.*, 2007). As with CDI, the ptychography method takes advantage of the “Nyquist-Shannon Theorem” of oversampling (Henry N. Chapman *et al.*, 2006) (Miao, Sayre and Chapman, 1997) in each diffraction pattern. Overlapping illumination spots provide additional information density, and ptychography tends to be more forgiving of experimental restrictions such as data noise than single-shot CDI.

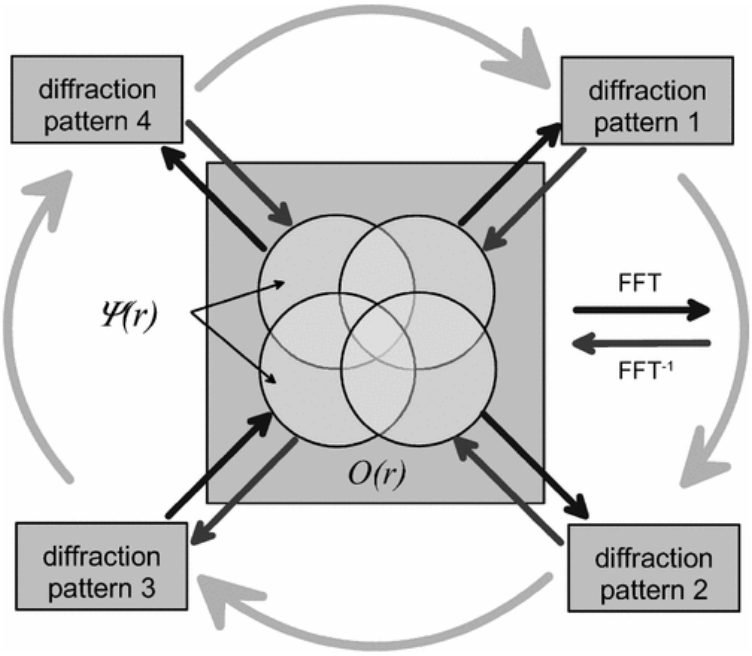

Figure 1.16: Ptychographic phase-retrieval algorithm used for reconstruction of diffraction patterns into relative images (Rodenburg *et al.*, 2007).

The reconstruction is a crucial step in retrieving an object's frame-by-frame information by using a basic ptychographic algorithm called Ptychographical Iterative Engine (PIE) to solve the phase problem; however, it has a drawback of the constant illumination function of the wavefront (Rodenburg *et al.*, 2007). The revised extended PIE (ePIE) algorithm considers both object function and complex illumination (probes) function (Maiden, Johnson and Li, 2017); this constrains the image leading to a better resolution. Furthermore, in ePIE, the obtained diffraction patterns are processed with inverse FFT to reconstruct into a high-resolution image and a decreased signal to noise ratio due to partial spatial coherence (Stachnik, 2012) (Robinson, 2015). The algorithms iterate between real and reciprocal spaces applying to constrain in both spaces until a solution is reached. It is a powerful tool for studying thick samples at a high spatial resolution.

Ptychography makes use of redundant information that occurs when there is sufficient overlap of multiple probe positions on the same region of the sample. In order to obtain a good reconstruction of an image from redundant scanning positions, certain parameters should be set prior, such as illumination probe function and translation steps; the former should be smaller than the latter (Zhang

et al., 2013). Oversampling of the object is taken into account by measuring the distance between the detector and the sample, sample thickness, aperture size, pixel size and the wavelength of an incident beam to obtain diffraction patterns from the object (Miao, Sandberg and Song, 2012). Ptychography improves the spatial resolution and provides the phase information without prior knowledge of the object (Howells *et al.*, 2009) (Rodenburg *et al.*, 2007).

Several biological samples have been imaged using ptychography. These includes freeze-dried diatoms at a resolution of 30 nm, bacteria at a 20 nm resolution, frozen-hydrated yeast at a 85 nm resolution and 3D nonporous glass at a resolution of 30 nm (Deng J. *et al.*, 2015). Corelative imaging of X-ray fluorescence microscopy (XRM) and X-ray ptychography has been used to image whole frozen-hydrated *C. reinhardtii* alga cells to map the elemental constituent by including tomography to obtain the 3-D view of the cells (Deng *et al.*, 2019). XRM and ptychography have also been used in algae cells to obtain fluorescence signals from available elements with a spatial resolution of ~ 2 μm. Soft X-rays ptychography has been applied to obtain chemical information from ~ 2 μm thick freeze-dried *Deinococcus radiodurans* without slicing and staining at a photon energy of 512 eV in the water window (Beckers *et al.*, 2011). Moreover, ptychography CDI allowed for the quantitative study of human metaphase chromosomes to build a karyotype based on mass (Shemilt *et al.*, 2015). Finally, ptychography CDI was used in the first attempt to image the human nucleus under cryogenic conditions (Yusuf *et al.*, 2017).

Serial block-face scanning electron microscopy (SBFSEM) is one of the imaging techniques in which a sample is embedded in resin. In this approach, the sample is embedded in resin which is polymerized at 60-70 °C to become hard plastic. The resin is then further sliced into an ultrathin sections for individual imaging (Yusuf *et al.*, 2014) (Chen *et al.*, 2017). In addition, the reliable and growing technique is plunge freezing for atomic to molecular level investigations. Plunge freezing maintains the native state of the biological specimen, and it protects it from radiation damage while imaging (Yusuf *et al.*, 2017). During plunge freezing, the samples get vitrified in liquid ethane and later stored in liquid nitrogen for future use.

1.7.3. Mass-based human karyotype

Ptychography provides the required resolution to karyotype chromosomes by their relative mass (Shemilt *et al.*, 2015). A partial karyotype was performed in 2015 from the quantitative information obtained from the measured mass of the chromosomes using the phase-shift hard X-ray ptychography technique (Shemilt *et al.*, 2015). This first attempt demonstrated that the phase-shift gives an accurate measure of the electron density map from the X-ray ptychography method along with the high spatial resolution of thick mitotic chromosomes (Shemilt *et al.*, 2015). The relative mass was calculated from the acquired largest chromosome 5 to build a partial karyotype (Figure 1.17), including chromosomes 5, 6, 7, 17, 18 and 20 *versus* known molecular weight from sequencing. Similarly, the mass of the human nuclei was obtained using quantitative phase-shift, hard X-ray ptychography and optimised ePIE algorithms which fall within range of hundreds of picograms (Schwenke *et al.*, no date), unpublished work). Both the X-ray ptychography experiments were performed at I-13-coherence branch, Diamond Light Source, Didcot, UK.

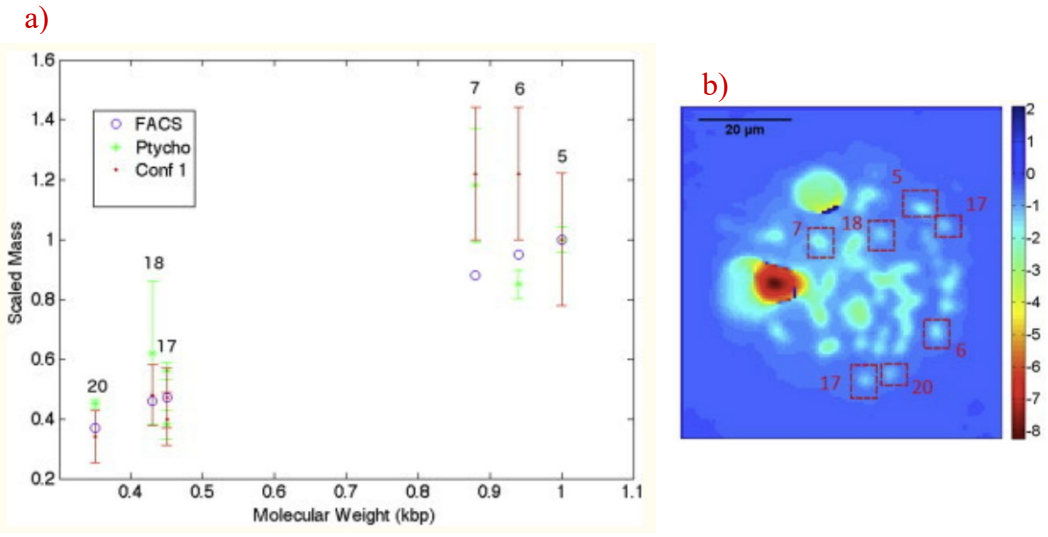

Figure 1.17: A first attempt to measure the mass of the human metaphase chromosomes using hard X-ray ptychography *versus* known molecular weight available from human genome sequence. a) Comparative partial karyotype using fluorescence-activated cell sorting (FACS), X-ray ptychography and confocal imaging b) phase image of human metaphase chromosomes spread obtained X-ray ptychography, scale bar= 20 μm (Shemilt *et al.*, 2015).

Moreover, quantitative 3-D structural information of 36 out of the 46 chromosomes was obtained from a prophase nucleus using the SBFSEM technique, from which the volume information was rendered to build a karyotype-from measured chromatid volume and the known DNA sequences (Figure 1.18) (Chen et al., 2017). The morphology and the localisation of chromosomes in the prophase nuclei were then used to extract the volume of each individual chromosome.

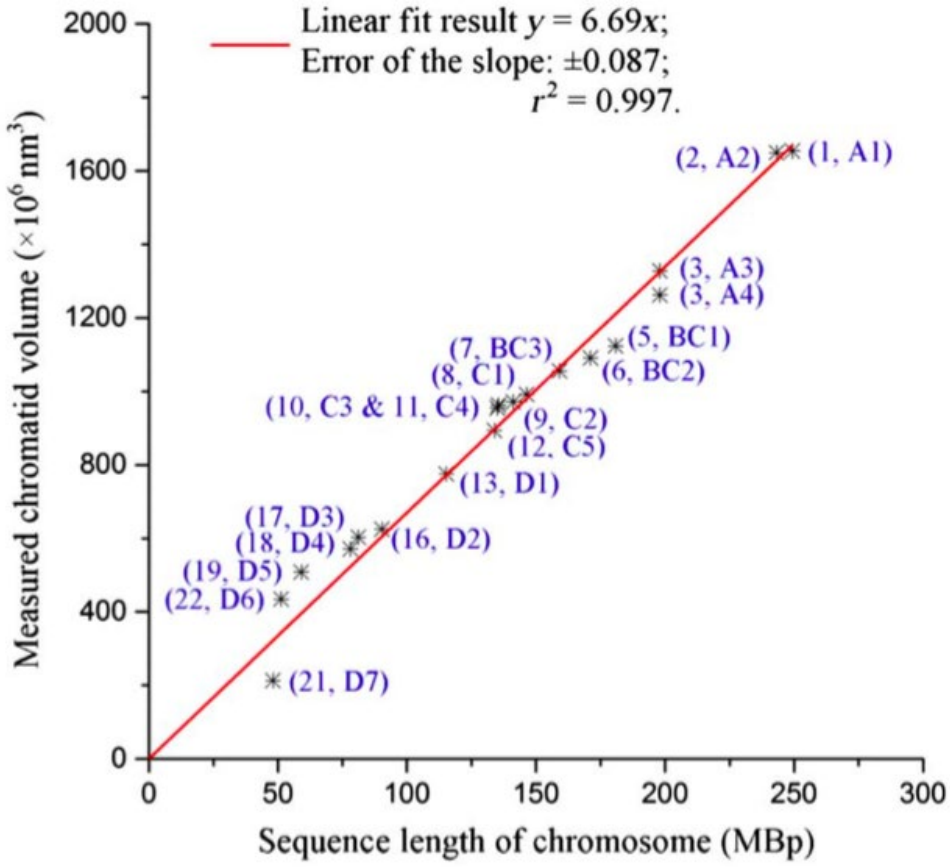

Figure 1.18: Volume karyotype of human chromosomes obtained from prophase nuclei against known DNA sequence length of chromosomes using SBFSEM technique. However, only 36/46 chromosomes were recovered. The linear fit supports the relation between measured chromatid volume versus sequence length (Chen et al., 2017).

1.7.3.1. Metaphase chromosomal proteins

The mass of a chromosome is composed of DNA and proteins (Maeshima and Eltsov, 2008) (Maeshima *et al.*, 2014). Both the DNA content and the cell cycle proteins (cyclins A-E) vary throughout the different stages of the cell cycle (Gookin *et al.*, 2017). Chromosomal proteins (histones and non-histones) are essential for maintaining the integrity and stability of the chromosomes. The histone provides structural stability, whereas the non-histones are responsible for accurate sister-chromatid segregation (Ono *et al.*, 2003) and condensation of chromosomes (Lohka and Masui, 1983). For example, two scaffold proteins, ScI (Scaffold component I) and ScII (scaffold component II) have been identified in nuclease-digested chromosomes after treatment with low ionic salt concentration (Earnshaw and Laemmli, 1983). The molecular weight of ScI (170 KDa) and ScII (135 KDa) contribute 40% to the total mass of the scaffold proteins (Lewis and Laemmli, 1982) (Earnshaw and Laemmli, 1983). These scaffold proteins locate around the kinetochore and the axial region of the chromosome. These scaffold proteins (SCI and SCII) are known as topoisomerase II that contribute to around 60%/80% of organising the overall chromatin structure (Gasser *et al.*, 1986) (Earnshaw and Mackay, 1994).

Other structural proteins are from the structural maintenance of the chromosome (SMC) family, including cohesion and condensin (Ono *et al.*, 2003). Cohesion activates at the S-phase of the cell cycle and glues the sister chromatids until early anaphase, where condensin removes cohesion and recoils the stretched chromatids before sister chromatid separation (Renshaw *et al.*, 2010), (Nasmyth, 2010). Both topoisomerase II and SMC proteins are involved in chromatin compaction and function (Gasser *et al.*, 1986) (Cuvier and Hirano, 2003) (Ono *et al.*, 2003). Out of 15 centromeric proteins colocalised at the centromere, 6 are categorized as kinetochore-associated proteins, whereas 9 are associated with heterochromatin (Craig *et al.*, 2003). The following proteins are involved in epigenetic modifications and transcriptional processes, but their individual role is unclear (Craig *et al.*, 2003).

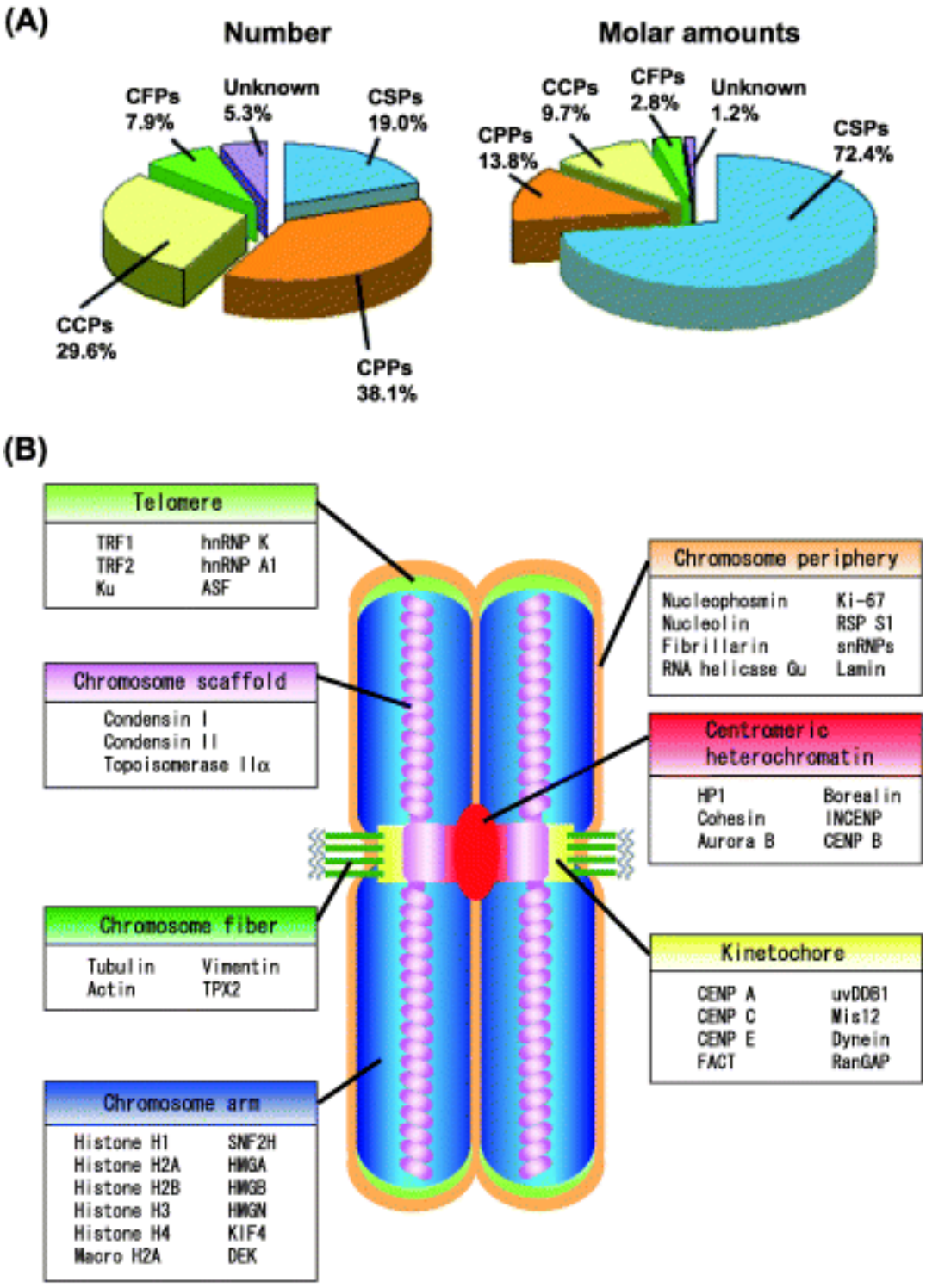

Figure 1.19: A list of isolated proteins obtained from polyamine treated metaphase chromosomes, classified into four groups: CSPs, CPPs, CCPs and CFPs. A) The pie charts show the four groups of chromosomal proteins and their relative sub-proteins, represented in numbers and molar amount, and B) represents the different proteins classified into seven sub-regions of a metaphase chromosome (Takata et al., 2007).

In 2007, Takata *et al*. identified more than 200 chromosomal proteins after isolating them from HeLa cells. This was achieved by using two proteomic analysis techniques: i) one-dimensional- sodium dodecyl sulphate–polyacrylamide gel electrophoresis (SDS-PAGE), and ii) radical-free and highly reducing two-dimensional electrophoresis (RFHR 2-DE) (Takata *et al.*, 2007). In this study, the chromosomal proteins were classified into four groups: “i) chromosome coating proteins (CCPs), ii) chromosome peripheral proteins (CPPs), iii) chromosome structural proteins (CSPs) and iv) chromosome fibrous proteins (CFPs)” (Takata et al., 2007) as shown in Figure 1.19a. Initially, 107 to 158 proteins were identified (Uchiyama et al., 2005) and they are classified according to where they are located in the sub-regions of a metaphase chromosome (Figure 1.19b). It was concluded that chromosomes suspended in polyamine buffer are more suitable for chromosome isolation as they exhibit reduced protein degradation and structural conformation distortion. This is essential as histone proteins contribute to 60% of the chromosome structure (Uchiyama et al., 2005) but can vary throughout the different stages of the cell cycle that remains to be determined.

1.8. Ionising effects on chromosomes

Ionising radiation (IR) causes a wide spectrum of lesions, including DNA single-strand breaks, double-strand breaks (DSBs), base damage and DNA–protein crosslinks (Balajee *et al.*, 2014) (Nakano *et al.*, 2017). Among these, DSBs are considered one of the most lethal and highly effective cell killing (A. S. W. Botchway *et al.*, 1997) (Schwer *et al.*, 2016). Most probably, the DSBs are least repairable or are mis-repaired leading to chromosomal aberrations (CAs); (Balajee *et al.*, 2014) (Ojima *et al.*, 2015). Aberrations can be caused by external factors such as ultraviolet (UV), sunlight exposure, ionising radiation (X-rays, gamma rays) and toxic chemicals. The aberrations also depend on the radiation quality (Durante and Formenti, 2018), dose (Touil *et al.*, 2000) and dose rate (Fujimichi and Hamada, 2014) (Lowe *et al.*, 2020). On the other hand, internal factors such as unequal cell divisions, replication errors and enzymatic reactions can also cause aberrations (Jain *et al.*, 2017). Radiation exposure can cause

simple or clustered DNA damage (Gulston *et al.*, 2004) (Magnander *et al.*, 2010). However, one or two aberrations per DNA helical turn leads to double DNA strand breaks (Lomax, Folkes and Neill, 2013). All these defects can produce large-scale rearrangements of the human genome and may cause major phenotypic and biological alterations, including mutations/cell death (Ojima *et al.*, 2015).

When traversing biomolecules, X-ray irradiation deposits part of the energy in the form of low or high 'Linear energy transfer' (LET). Chemical modifications in DNA are one of the results of such energy deposition (Lomax, Folkes and Neill, 2013) (Desouky, Ding and Zhou, 2015) via direct or indirect damage. The interaction with DNA directly releases electrons from the atoms and bonds and can break strands of DNA (Swarts et al., 2007). Energy absorbed by water content present in a biomolecule causes water radiolysis, which results in free radicals of H^+ and $\cdot OH$- (Azzam, E. Jay-Gerin, J. Pain, 2012), that can also damage DNA indirectly. Other free radicals, such as toxic superoxide, can lead to DNA damage (AbdulSalam, Thowfeik and Merino, 2017). There are two types of ionising radiation effects: i) deterministic/non-stochastic effect, this effect is dose-dependent and has a certain threshold, after which the effect occurs and ii) stochastic effect, this is a random effect and has no threshold but the damage correlate with the increasing dose (Leenhouts and Chadwick, 1989) (Marci et al., 2018).

A recent finding confirms that the nearby, non-irradiated cells also become affected apart from irradiated cells. This phenomenon is called the "Bystander effect" (Desouky, Ding and Zhou, 2015). Ionising radiation (IR)-induced DSBs can occur either in a random or non-random style (Balajee *et al.*, 2014); in either case, the resulting DSBs inhibit the replication and the transcription process (Schwer *et al.*, 2016) in upcoming cell divisions. Another critical factor is the phosphorylation of histone variant H2AX into *γ*-H2AX, introducing DSB breaks (Dickey *et al.*, 2009) in chromosomes. *γ*-H2AX is a typical aberration upon ionising radiation to identify DSB breaks by using the *γ*-H2AX foci assay (Dickey *et al.*, 2009) (Nair *et al.*, 2019).

Chromosomal aberrations can be classified as numerical or structural aberrations. Numerical aberrations consist of aneuploidy (occurring due to improper distribution of chromosomes at the anaphase stage of the cell cycle, for example, trisomy and monosomy) and triploidy (presence of an extra haploid chromosome set) (Tobias, 2011). These defects are known as non-dysjunction and take place at mitosis and later at the meiosis phase of the cell division (Tobias, 2011). Structural aberrations occur either due to breakage or irregular reunion, which is a consequence of exposure to mutagens and/or ionising radiations.

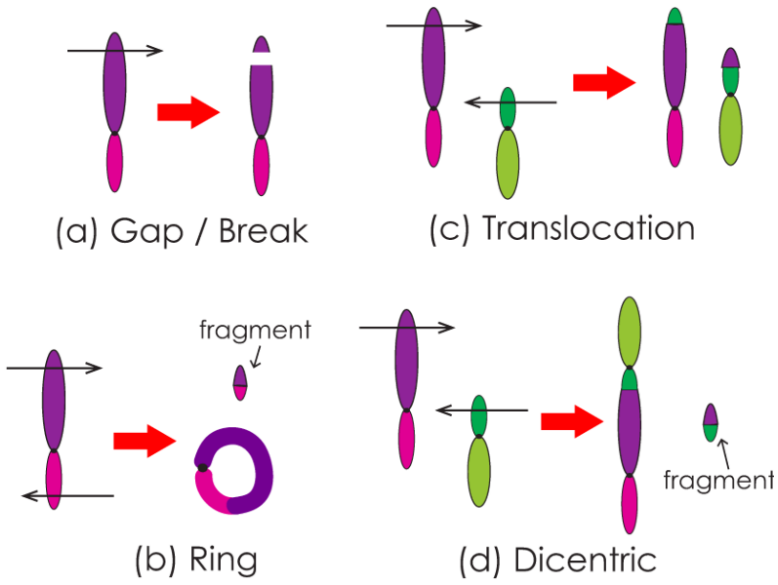

Figure 1.20: The four typical X-ray induced structural chromosomal aberrations (Ouchi, 2015).

The structural aberrations are classified as: i) deletion (loss of part of a chromosome), ii) translocation (transfer of DNA contents between homologous or non-homologous chromosome pairs), iii) ring chromosomes (joining of two broken ends together), iv) dicentrics (presence of two centromeres in a chromosome; mentioned in Figure 1.20, v) Isochromosomes (deletion of one arm with an addition of other), vi) duplication (gain of an extra segment from another chromosome) and vii) inversion (rotation of gene sequence by 180 degrees) (Tobias, 2011) (Ouchi, 2015). Cells containing deletion, ring, and dicentrics chromosomal aberrations die soon in upcoming cell division because of instability and loss of genetic material; on the other hand, translocation is heritable (Ellard

et al., 1996). Chromosome aberrations induce “sticky” breakpoint ends, which become repaired by mechanisms such as Non-Homologous End Joining (NHEJ) and Homologous Recombination (HR); (Blanpain et al., 2011) with the help of specific enzymes (Figure 1.21). Subsequently, failure of the repair process can produce large-scale rearrangements and recombination of the human genome and eventually causes disease such as cancer (Aparicio, Baer and Gautier, 2015). It was observed in chicken cells that the NHEJ pathway acts more dominantly in the G1 stage of the cell cycle, whereas the HR pathway comes into play in the S and G2 phases of the cell cycle to repair DSB (Takata et al., 1998). Cells which contain dicentric, ring chromosomes or deletion aberrations are generally unstable, and such cells are likely to die within the next few generations.

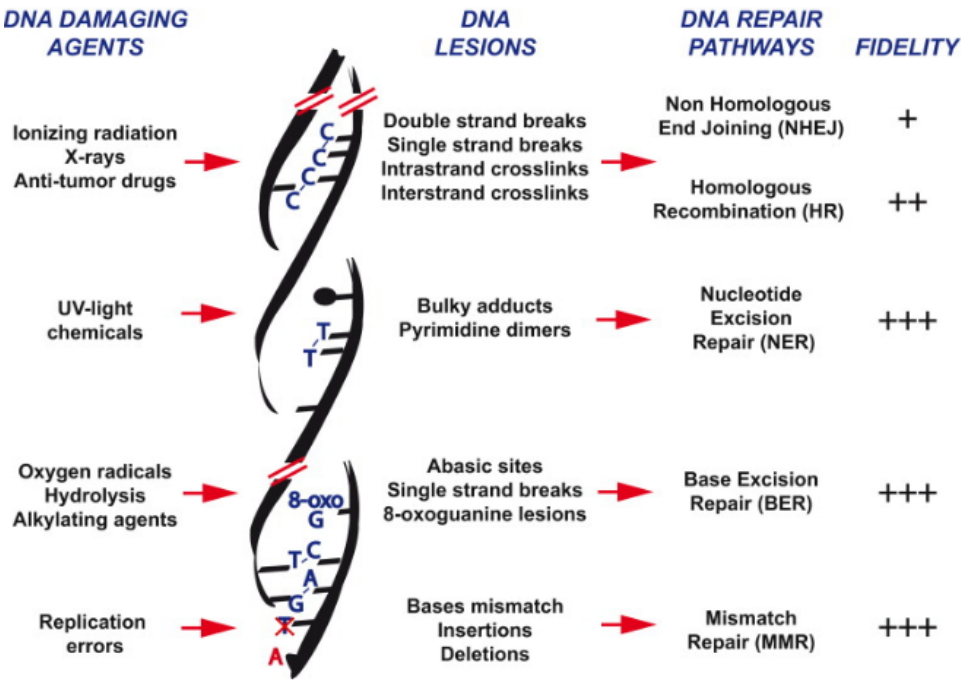

Figure 1.21: Potential regions prone to DNA damage and the response repair mechanism in mammalian cells (Blanpain *et al.*, 2011).

Cells irradiated with 1 to 2 Gy show slow cell division and DNA damage repair mechanisms. Subsequently, they decrease cell viability and can have acute levels of DNA damage such as exchanges and deletion of segments of chromosomes. Nonetheless, this does not affect the transcription process (Borràs-fresneda *et al.*, 2016). Major aberrations usually occur with higher radiation doses starting from 1 to 5 Gy. This leads to a decrease in metaphase

chromosome numbers and to an increase in the frequencies of dicentric, acentric (with no centromere) and ring chromosomes (Ryu, Kim and Kim, 2016).

Furthermore, the number of dicentric chromosomes decreases from the first, to the second and to the third mitotic cell division. The number of acentric and the centric aberrations, which occurred due to the deletion of telomeres, are found to increases from one mitotic cell division to another (Kaddour *et al.*, 2017). Acentric and the centric could be the reason for CAs transmission from subsequent mitotic cell cycles rather than dicentrics which leads to genomic instability.

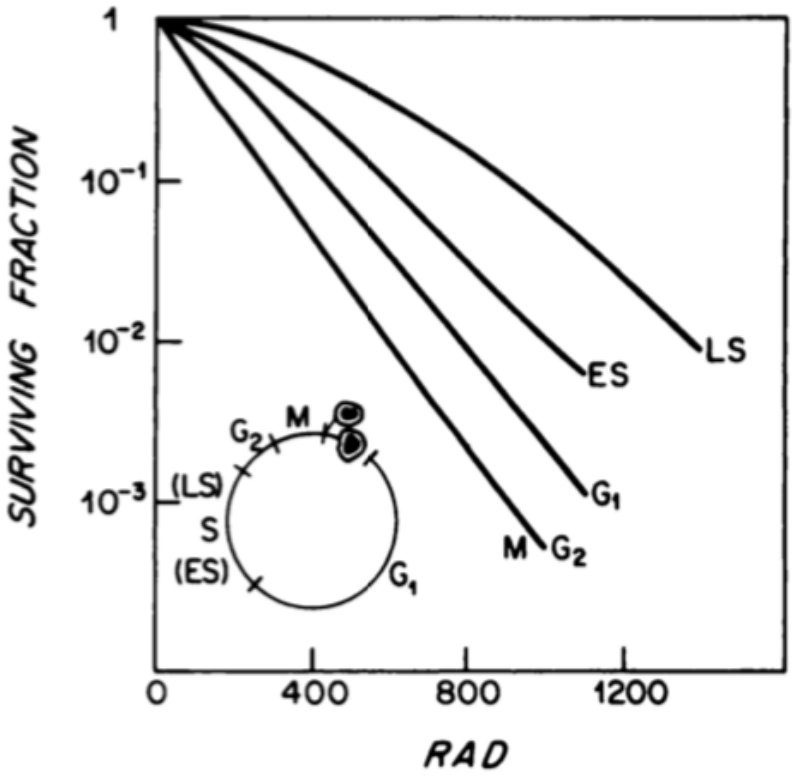

Figure 1.22: The surviving fraction of the mammalian cells at a different stage of the cell cycle upon low ionising radiation (x-axis). Interphases consist of G1, S and G2 phase, M=mitosis, LS= late synthesis and ES=early synthesis. The inset defines the duration of each stage of cycle and the two daughter cells separated during cytokinesis (Bloomer and Adelstein, 1982).

Figure 1.22 indicates that at low dose ionising radiation, mammalian cells in S-phase are more resistant to irradiation, especially at the late synthesis (LS) phase, whereas G2 phase cells are more susceptible to radiation (Bloomer and Adelstein, 1982). Considerable data show a relationship between cell killing and the induction of chromosome aberrations. The frequency of inter-chromosomal aberrations calculated in chromosomes 1, 2 and 4 during the G0 phase of the cell cycle at X-ray doses of, 2 Gy and 4 Gy '(mean ± SE; 0.02 ± 0.02 for 0.75 ± 0.21 for 2 Gy and 2.10 ± 0.48 for 4 Gy)' (Ryan *et al.*, 2019). Moreover, it was also shown that the q-arm is 10x times more prone to breaks than the p-arm (Ryan *et al.*, 2019). Henceforth, the frequency of chromosome aberrations is a linear function of radiation dose. Long-term exposure to low-level ionising radiation raises the risk of chromosomal abnormality compared to haematological alterations (Rozgaj *et al.*, 1999).

Biological dosimetry (BD) from dicentrics and micronuclei are the gold standard for the determination of the radiation doses (Marshall *et al.*, 1996) (Voisin, 2015) (Gil, Martins and Rosário, 2020). Probes used in BD are centromeric probes for dicentrics and telomeric probes for acentric (M'Kacher *et al.*, 2015). Giemsa staining is one of the techniques for CAs analysis (Sumner, 1982) that is used for the detection of symmetrical CAs like familial translocation, but it is a labour-intensive and time-consuming banding technique (del Amo and Gullón, 1972) (Natarajan and Boei, 2003). Translocation is also a type of BD that has been analysed by the Fluorescence *In Situ* Hybridisation (FISH) technique in human-hamster hybrid cells (Pinkel, Straume and Gray, 1986). In this technique, specific DNA probes hybridise with the targeted metaphase/interphase chromosomes, and it is limited to the number of probes that can be used simultaneously (Pinkel, Straume and Gray, 1986) (Bishop, 2010).

The combined effect of centromeric and FISH probes enhances and increases the sensitivity of identifying dicentrics and translocations, respectively in the cells, also has a sensitivity to detect aneuploidy (Marshall *et al.*, 1996). Routinely in clinics, quantitative fluorescent polymerase chain reaction (QF-PCR) has been used in practice to detect aneuploidies in a foetus (Atef *et al.*, 2011). Although, QF-PCR is limited to only a few chromosomes like 13, 18, 21, X and Y

(Atef *et al.*, 2011). The FISH technique is helpful for locating specific DNA sequences, whereas 24-colour multiplex Fluorescence *In Situ* Hybridisation (M-FISH) (Anderson, 2010) paints the whole genome, which makes it easier to identify accidental CAs. These techniques have their limitations. For example, Giemsa metaphases can mislead the results if the procedure of Giemsa staining alters the duration of staining, pH variation, or trypsin treatment (before staining) is imbalanced (Duijn, Prooijen-Knegt and Ploeg, 1985). FISH and M-FISH are insufficient to identify minor changes within chromosomes (Bishop, 2010) (Anderson, 2010), such as intrachromosomal arrangements. Flow cytometry is only significant for detecting numerical aberrations (Muehlbauer and Schuler, 2005).

The other method for karyotyping and detecting chromosomal abnormalities is spectral karyotyping, that is based on the emission spectra of labelled chromosomes after hybridisation (Schröck *et al.*, 1996). Comparative genomic hybridisation (CGH) is a method to determine DNA copy number variations, like duplication or deletion of DNA content from the genome (Spelcher *et al.*, 1993). In this technique, two different sets of genomes are compared, control and a defected/tumour, DNA from two genomes hybridised to metaphase chromosomes. In an advanced CGH, the control and tumour affected DNA is hybridised with the DNA probes present on the microarray chip, commonly known as microarray based-CGH (Redon and Carter, 2009). Microarray-CGH has been applied to many cancer studies and diseases like Downs syndrome and Cri du Chat syndrome, that is based on gain and loss of DNA copy number variation (CNV), respectively (Pinkel *et al.*, 1998). Next generation sequencing (NGS) is an emerging tool used for single nucleotide variations (SNV) and DNA CNV (Fan *et al.*, 2019) (Lee *et al.*, 2016).

In this thesis, FLIM and X-ray ptychography has been used to investigate CAs in cells irradiated by low-level doses of X-ray irradiation. The studies have been done using chromosomes from B and T-lymphocytes at different time points of cell culture (see chapter 2, Materials and Methods). The use of FLIM has allowed observation of the molecular environmental changes, while X-ray

ptychography has been used to measure the mass of the chromosomes after the radiation process.

The survival of cells from radiation and repair mechanisms are fundamental for life. Besides, while some DNA mutations are harmful, some are the driving force in evolution. The work presented in this thesis aims to understand better the DNA damage induced by X-ray radiation. A low-level dose of X-ray irradiation has been used in this study since it is a valuable tool for radiation biology and therapy in cancer treatment.

1.9. Aims and objectives of this thesis

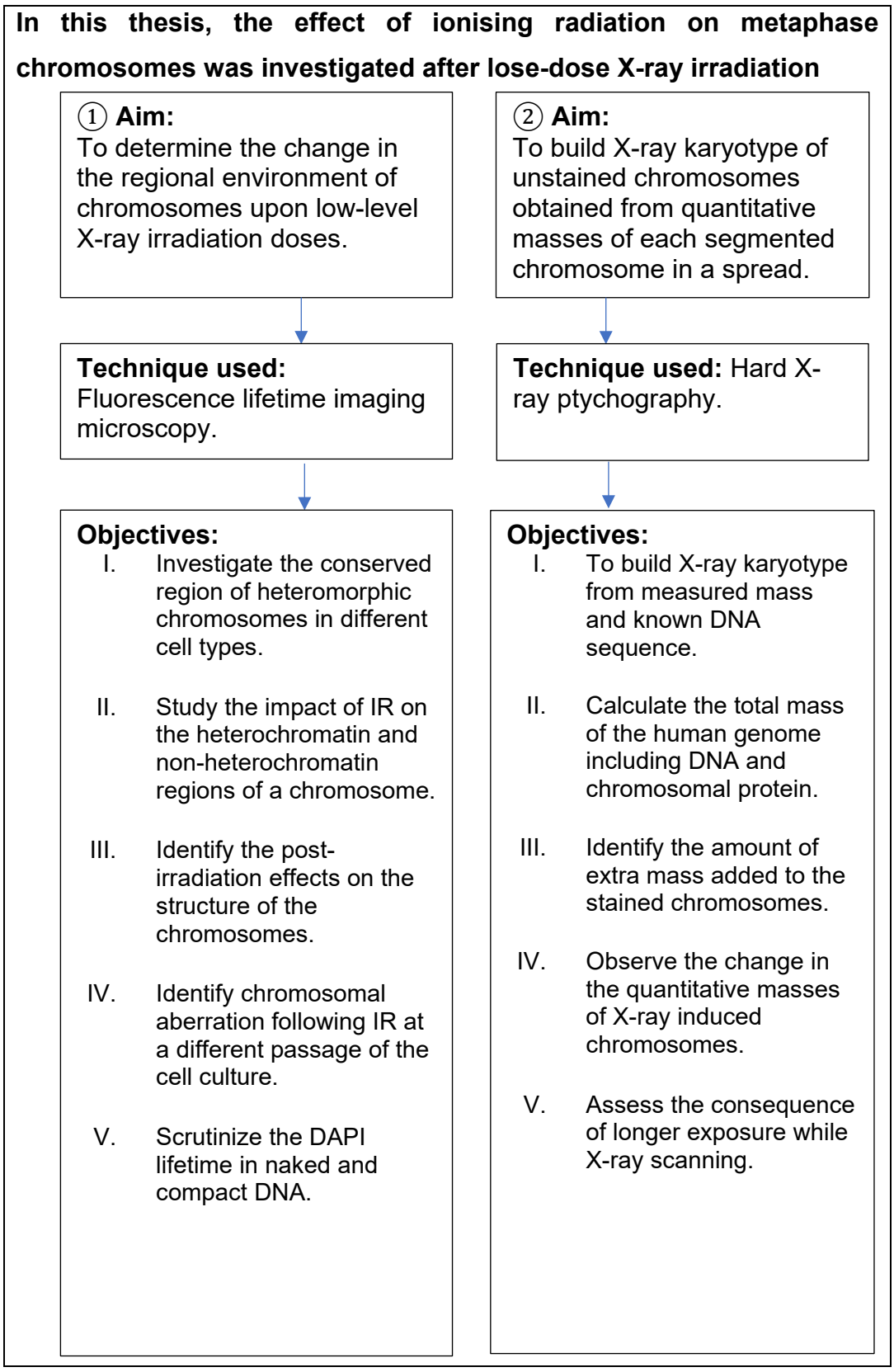

Figure 1.23: The outline of this thesis.

Chapter 2

2. Materials and Methods

All solutions were prepared using milliQ Millipore water (prepared by purifying deionised water, to attain a sensitivity of 18 MΩ -cm at 25 °C). Though chemical compounds described were purchased from Sigma Aldrich, UK, unless otherwise stated. All cell culture processes were performed inside a Laminar Air Flow (LAF) under a sterile condition.

Primary T- lymphocytes cells were donated by a 22-year-old female, provided by Dr Ken Raj's group, Public Health England (PHE), Oxford, UK. Additionally, lethally irradiated lymphoblastoid cells (GM1899A, provided by PHE) were used as feeder cells. The feeder's cells are the antigen-presenting cells needed for T-lymphocytes growth. The primary T-cells were cultured in the laboratory of PHE and maintained by Dr Ken Raj's group (Dr Sylwia Kabacik, PHE). The T-cells are suspension cells and at passages 3, 4 and 5 in a current investigation.

2.1. Primary T-lymphocytes cell culture

2.1.1. Lymphoblastoid cell line culture

3 x 10^6 cells were thawed at 37 °C in a water bath for two minutes and then transferred in a 15 ml conical bottom tube containing 10 ml of lymphoblastoid cell growth medium (LCGM), consisting of Roswell Park Memorial Institute (RPMI-1640 (1X)) medium supplemented with 20% heat-inactivated foetal bovine serum (FBS), 1 mM sodium pyruvate, 2 mM L-glutamine, 100 U/ml penicillin, 100 µg/ml streptomycin (all from Invitrogen/Life Technologies). Cells were mixed by inverting the tube (until the solution was homogeneous) and centrifuged for 5

mins at 1200 revolutions per minute (rpm). The supernatant was aspirated, followed by the cell pellet resuspended in 10 ml of LCGM and transferred in a vented 25 cm^2 culturing flask. Flasks of cells were incubated at 37 °C with 5 % CO_2 in the upright position for 3 days. At this stage, cells were disaggregated by vigorous shaking and counted at daily intervals using an ADAM cell counter (see section 2.1.5.). When cell numbers reached 0.8 x 10^6, 10 ml of fresh LCGM was added, and the cells were transferred to a 75 cm^2 flask. The cell number was maintained between 0.6 to 0.8 x 10^6 per ml by adding a fresh LCGM medium.

2.1.2. Feeder cell preparation

Lethally irradiated lymphoblastoid GM1899A cells were used as feeder cells for human T-lymphocytes. The culturing conditions for this lymphoblastoid cell line are described in section 2.1.1. The feeder cells were prepared as follows: when the culture reached 5 x 10^7 cells, the cells were transferred in one or two 50 ml conical bottom tubes (depending on the volume) and centrifuged at room temperature for 5 mins at 1200 rpm. The supernatant was aspirated, and cell pellets were resuspended in 5 ml of LCGM. The cells were lethally irradiated with X-rays at room temperature with a 40 Gray (Gy) dose, at a of 1.7 Gy/min dose rate. The lethally irradiated cells were mixed with freeze mix consisting of 10 % dimethyl sulfoxide (DMSO, Sigma-Aldrich Company Ltd., Gillingham, UK) and 90 % of FBS (Life Technologies) to 3 x 10^6 cells per ml. One millilitre of aliquots of the mixture was transferred to cryovials and frozen at -80 °C in Mr. Frosty™ (Thermo Scientific) containers allowing cooling at a rate of 1 °C per minute. The vials were transferred to the liquid nitrogen container for long-term storage the next day.

2.1.3. Preparation of human T-lymphocytes

The human T-lymphocytes were prepared as follows: 10 ml of blood from a 22-year-old female donor was collected into BD Vacutainer® lithium heparin tubes (Becton Dickinson). 5 ml of Histopaque-1077 (Sigma-Aldrich) pre-warmed to room temperature was aliquoted into four 15 ml conical bottom centrifuge tubes.

10 ml of blood was mixed with 10 ml of Hank's Balanced Salt Solution (HBSS, Life Technologies) pre-warmed to room temperature in a 50 ml conical bottom tube (Figure 2.1). 5 ml of diluted blood was layered slowly onto each of the four tubes containing Histopaque-1077 using a sterile pastette (Alpha Laboratories, Eastleigh, UK). Tubes were centrifuged at room temperature at 1600 rpm for 20 min. Following phase separation, the top serum layer was aspirated from each tube, leaving around 0.5 cm of liquid above the buffy coat cell layer. The buffy coats from sample tubes were collected and transferred into fresh 15 ml tube containing 10 ml of HBSS and mixed by inverting 5 - 6 times. The tubes were centrifuged at room temperature at 1200 rpm for 5 mins. The supernatant was aspirated, followed by resuspending cell pellet in 5 ml of HBSS. Suspended cells were combined into one tube and centrifuged again at room temperature at 1200 rpm for 5 mins. After the supernatant was aspirated, the cells were washed twice with 10 ml of HBSS, and a 20 µl aliquot of cell suspension was taken for cell counting. The tube was centrifuged at room temperature at 1200 rpm for 5 mins, and the supernatant was aspirated. Next, the cells were resuspended at a concentration of 3 x 10^6 cells per ml in freeze mix, then transferred to cryogenic vials in Mr. Frosty^{TM} container and frozen at -80 °C. The following day vials were transferred to a liquid nitrogen container for long-term storage.

2.1.4. Culturing conditions of T-lymphocytes

A cryovial containing 3 x 10^6 cells, passage 5, was thawed at 37 °C in a water bath for two minutes. The cells were transferred to a 15 ml conical bottom tube containing 10 ml of stimulating growth medium (SR10) containing RPMI 1640 (Dutch modification) supplemented with 10 % heat-inactivated FBS, 1 mM sodium pyruvate, 2 mM L-glutamine, 100 U/ml penicillin, 100 µg/ml streptomycin, 50 µM 2-mercaptoethanol (GIBCO/Life Technologies), 20 U/ml recombinant interleukin-2 (IL2; Sigma-Aldrich) and 0.4 µg/ml phytohaemagglutinin (PHA; Sigma-Aldrich). Cells were mixed by inverting the tube and centrifuged at room temperature for 5 mins at 1200 rpm. The supernatant was aspirated, the cell pellet was resuspended in 10 ml of SR10 and centrifuged at room temperature for 5 mins at 1200 rpm.

Prior to mixing feeder cells into T-lymphocytes, a cryovial of feeder cells was thawed in the water bath at 37 °C for two minutes. The supernatant from T-lymphocytes was aspirated, and the cells were resuspended in 10 ml of SR10 (Figure 2.1). The feeder cells were transferred into a 15 ml conical bottom tube containing T-lymphocytes, mixed by inverting the tube several times and centrifuged at room temperature for 5 mins at 1200 rpm. The supernatant was aspirated, and the cell pellet was resuspended in 10 ml of SR10. The cell suspension was transferred to a vented 25 cm^2 flask and incubated at 37 °C with 5 % CO_2 at an angle of about 10° from the horizontal. Cells were left undisturbed for 4 days, and thereafter they were disaggregated and counted daily using an ADAM cell counter (see section 2.1.5.). When the cells reached a density of 0.8 x 10^5 cells per ml, they were diluted 1:2 with a growth medium (GR10) that contained SR10 without PHA.

2.1.5. Cell viability assay

For cell counting and viability, the ADAM cell counter (Labtech International Ltd., Uckfield, UK) was used. Briefly, for every cell count, two 0.5 ml Eppendorfs were prepared. 20 µl of “T” solution (accuStain T for total cell count with a propidium iodide dye) was aliquoted into one, and 20 µl of “N” solution (for counting non-viable cells with fluorescent dye) into a second Eppendorf. Cells for counting were disaggregated by vigorous shaking, then two 20 µl aliquots were taken and mixed in tubes containing N and T solutions, respectively, and samples were incubated for 2 min at room temperature. After incubation, the samples were loaded into the cartridge’s appropriate T and N positions and loaded into the counter. The cell counter provides a value for total cell number (T), viable cell number (N) and percentage of viable cells.

2.1.6. Exposure to ionising radiation

Confluent T-lymphocytes cells, 5 x 10^6 cells per ml in a T75 vented cell culture flask, were transported to PHE for X-ray irradiation. Briefly, the PHE's AGO X-ray setup, model CP160/1 (AGO X-RAY Ltd, Martock, UK), was used with X-rays energy kept set at 250 KVp (maximum voltage applied across an X-ray tube during the creation of X-rays within the X-ray system) with a half-value layer of 2 mm of copper and aluminium compound filters and 13 mA current, giving a dose rate of 0.5 Gy/min. The flask containing cells was held flat inside the X-ray system chamber while irradiating, which exposed practically every cell to radiation. Three out of four flasks with 11 ml cell media, keeping one flask as a control, were irradiated with different radiation doses such as 0.1 Gy, 0.5 Gy and 1 Gy for 12 seconds (secs), one min, two mins, respectively. After irradiation, 9 ml of fresh SR10 media was added to each flask and mixed well by shaking manually. Thereafter, to arrest chromosomes at their mitotic (most condensed) stage, colcemid (Karyomax, Gibco by Life technologies (10 µg/ml)) was added at the final concentration of 0.2 µg/ml into each flask. The flask was kept for 16 hours in the incubator at 37 °C with 5% of CO_2 before harvesting.

To attain metaphase chromosomes at their first (40 hrs), second (64 hrs) and the third (88 hrs) passage of the cell culture, the T-lymphocytes cells were irradiated with a radiation dose of 0.5 Gy at a dose rate of 0.5 Gy/min. After irradiation, the cells were kept for 40 hrs, 64 hrs and 88 hrs in the incubator at 37 °C with 5% of CO_2 before adding colcemid (0.2 µg/ml). The cells were incubated with colcemid at 37 °C with 5% of CO_2 for 16 hrs before harvesting. The cell media was replaced with fresh media for flasks left for 64 hrs and 88 hrs.

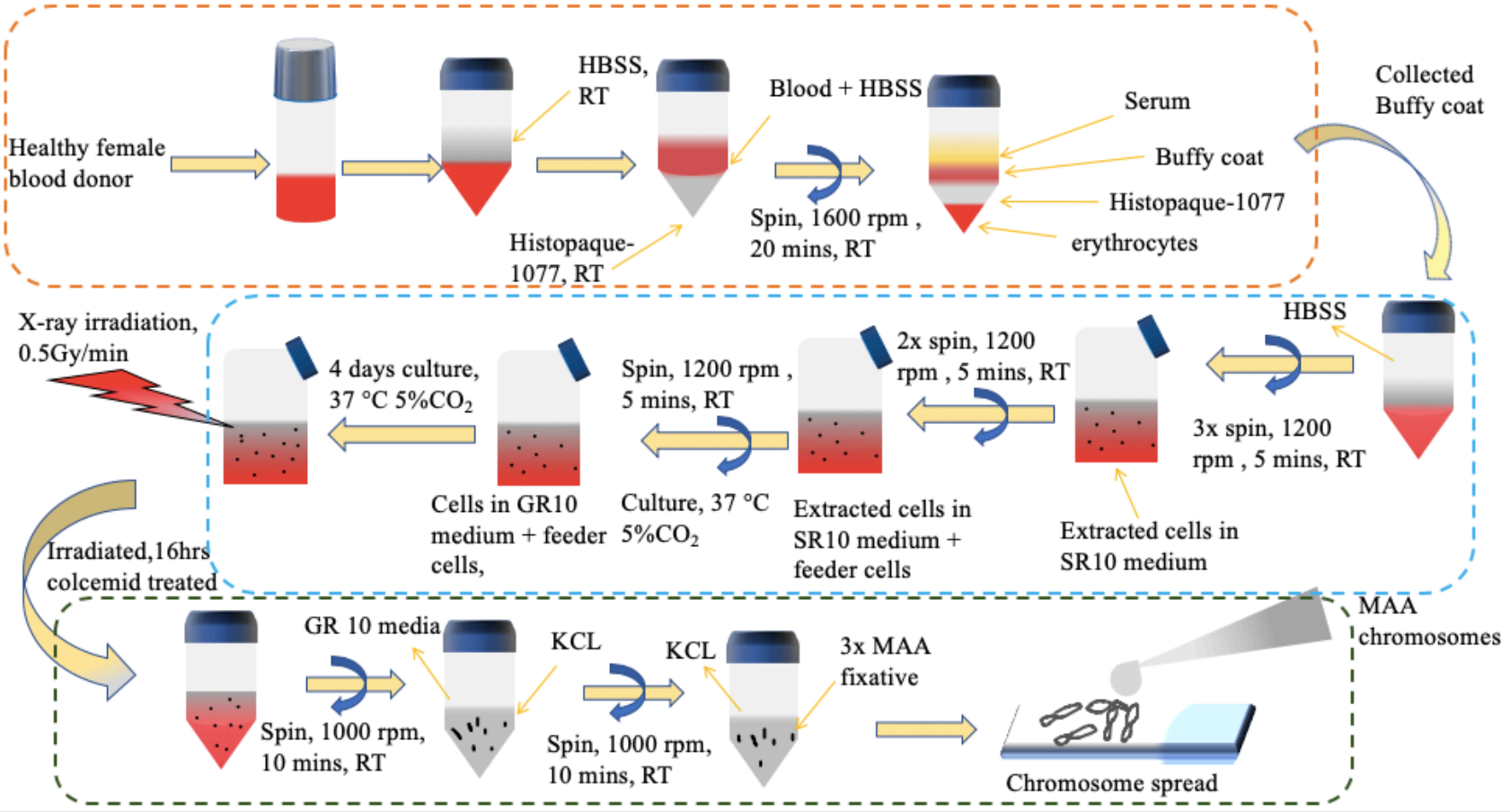

Figure 2.1: Preparation of X-ray irradiated chromosomes from donor's blood. The top panel (orange dotted rectangle) shows the process of extracting T-lymphocytes from the donor's blood. The middle panel (blue dotted rectangle) represents the process of purifying T-lymphocytes, culturing cells and then irradiating with x-ray doses at the rate of 0.5 Gy/min. The bottom panel (green dotted rectangle) represents the process of chromosomes extraction from the obtained cells, fixation with methanol acetic acid (MAA) followed by preparing chromosome spreads for FLIM imaging.

2.2. Yoruba cell line (B-lymphocytes)

2.2.1. Cell culture condition for Yoruba cell line

The B-lymphocytes cells from the Yoruba male cell line (GM18507, International HapMap Project) were used for the chromosome studies (Yusuf, Chen, *et al.*, 2014) (Yusuf, Parmar, *et al.*, 2014) (Shemilt *et al.*, 2014) (Estandarte *et al.*, 2016). The B-cells are suspension cells used at passage 15 in this study.

The reagents, 100 ml of thawed FBS (product code- 12103C), 5 ml of penicillin (100 U/ml), streptomycin (100 µg/ml) (product code- P0781), 5ml of L-glutamine (2mM) (product code- 56-85-9) and a 500 ml bottle of RPMI-1640 (1X, product code- R6504) in 37 °C water bath, were mixed well with RPMI-1640 medium. The media was prepared and stored in a 4°C fridge for further use. All reagents are from Sigma-Aldrich, UK.

A cryovial containing 2.6 x 10^6 cells /ml, passage-15, was thawed for one minute at 37 °C in a water bath. The cells were transferred to a 15 ml tube containing 5 ml of pre-warmed fresh media. The tube was centrifuged at 1000 rpm for 3 mins, and the supernatant aspirated, followed by re-suspension of the pellet in 5 ml of fresh media. The cell media was transferred to a vented T25 cell culture flask and left in the incubator at 37 °C for 2-3 days. After 3 days, the cells were transferred into a 15 ml tube and centrifuged at 1200 rpm for 10 mins, then aspirated supernatant, and the pellet was resuspended with 5 ml of fresh media and transferred to a vented T75 cell culture flask. An extra 15 ml of fresh media was added and allowed to grow with sub-culturing every 2 days.

The density of the cells was determined by performing a cell count. 10 µl of media containing cells and 10 µl of Trypan blue dye (0.4%, Life Technology) were mixed in an Eppendorf tube, and 10 µl of the mixture was loaded into the

cell counting cartridge of the cell counter (BIO-RAD), and a measurement was taken.

2.2.2. X-ray exposure for Yoruba cell line

Confluent B-lymphocytes cells, 7.55 x 105 cells per ml in a T25 vented cell culture flask, were transported to PHE for x-ray irradiation using the AGO X-ray setup (described in section 2.1.6.). The cells were shaken well before the irradiation process to achieve a monolayer, but not during the process (though the irradiation process lasts only for a couple of minutes). Four of five flasks with 5 ml cell media, keeping one flask as a control, were irradiated with different radiation doses such as 0.1 Gy, 0.5 Gy and 1 Gy with a duration of 12 secs, 1 min, 2 mins, respectively. After irradiation, cells were allowed to stand in the incubator at 37 °C with 5% of CO_2 until the first (40 hrs), second (64 hrs) and third (88 hrs) passage of the cell culture. Afterwards, to arrest chromosomes at their mitotic stage at a different cell cycle, colcemid (Karyomax, Gibco by Life technologies (10 µg/ml)) was added for 16 hrs at the final concentration of 0.2 µg/ml in each flask before harvesting. The cell media was replaced with fresh media in case of 64 hrs and 88 hrs of the passage of the cell culture.

2.3. Chromosome preparation from irradiated T and B lymphocytes

Following the process of irradiation and arresting chromosomes at the mitotic stage for both T and B lymphocytes, the cell media from the vented culture flasks were transferred to 50 ml falcon tubes and centrifuged at 1000 rpm for 10 mins. Prior to this, 20 µl of cell media from each flask was used to count the cells using an ADAM cell counter. The cell count ranged from 0.32 - 0.35 x 10^6 cells per ml in each flask for T lymphocytes.

The supernatant from each centrifuged tubes was aspirated, followed by the addition of 6 ml pre-warmed (37 °C), hypotonic solution (KCl ,75 mM) was slowly added in the falcon tubes (Figure 2.1). The tubes were immediately transferred to the pre-warmed water bath at 37 °C for 8-10 mins and then spun at 1000 rpm for 10 mins. Meanwhile, fresh methanol: acetic acid solution (MAA) was prepared in the ratio of 3:1 to fix the extracted chromosomes. After the supernatant was aspirated, 6 ml of MAA were quickly added dropwise and shaken immediately to dislodge the pellet in each tube. The tubes were spun at 1000 rpm for 10 mins, and then the supernatant was aspirated. The washing procedure with MAA was repeated three times to get clear solutions of chromosomes from both T and B lymphocytes. The prepared chromosome solutions were stored at -20 °C for future use.

2.4. Chromosome preparation

Glass slides (SuperFrost, VWR^{TM}) were first cleaned by soaking overnight in a 70% ethanol solution that effectively removes grease. The slides were wiped with soft tissues and placed in the freezer for 30 mins for later use for mounting chromosomes on them. Chromosome spreads were prepared on cleaned slides initially stored in a freezer at -20°C and blown on to create local humidity. 20 µl to 30 µl (depending upon the concentration of chromosomes in the solution) of methanol: acetic acid fixed chromosomes were then dropped from a height of around 40 cm (Figure 2.1). This is an established procedure known to obtain enough well-spread 46 chromosomes on glass slides.

The prepared slides were immediately transferred onto the hot plate (45 °C) to dry for 5 mins to 10 mins. Once the slides were dried, they were stained with 4', 6-Diamidine-2'-phenylindole dihydrochloride (DAPI, Sigma, H-1200, 5 µg/ml) and then covered with a 22 x 50 sized cover slip. The slides were incubated for 10 mins and observed under the fluorescence microscope (Zeiss Z2Axioimager with Isis software). A 10x objective was used to locate the chromosomes and observe the quality (maximum number of chromosome spreads on the glass slides) of the prepared chromosome spreads. A 63x

objective (with immersion oil) was used to observe the magnified views of DAPI stained chromosomes. Some chromosomes spread slides were left unstained for FLIM imaging.

2.5. Fluorescence lifetime imaging microscopy

FLIM is an imaging technique that records the decay lifetime of a fluorophore from its excited state (Suhling *et al.*, 2012) (see chapter 1, Introduction).

2.5.1. Preparation of DAPI

4', 6-Diamidine-2'-phenylindole dihydrochloride (DAPI, product code-D1306, ThermoFisher Scientific) is a DNA-specific dye used as a chromosome counterstain. DAPI was prepared from powder as follows: a stock solution was prepared by dissolving 5 mg of DAPI in 1 ml of milliQ millipore water to achieve a final concentration of 14.3 mM as a stock solution. For thorough mixing the solution was sonicated for 10 mins then wrapped in aluminium foil and stored in a -20 °C freezer for up to a year. The required 4 µM DAPI for chromosome staining was prepared from the stock solution, also wrapped in aluminium foil and stored at -20 °C for up to a year.

2.5.2. Staining chromosomes with DAPI

The chromosomes spreads were prepared according to section 2.3. and 2.4 prior to lifetime measurement. Spreads on the slides were stained with a freshly prepared 4 µM DAPI (see section 2.5.1.) and incubated at room temperature for 20 mins in the dark. Following the incubation, the stained slides were soaked in 1x phosphate buffered saline (PBS, pH-7.4, Sigma-Aldrich) for 4 mins. Afterwards, the slides were rinsed with milliQ Millipore water, mounted with 3 µl of PBS and covered with a coverslip (22 x 50 mm^2, No.1 or 1.5 depending on the cover glass thickness specifications of the imaging objective).

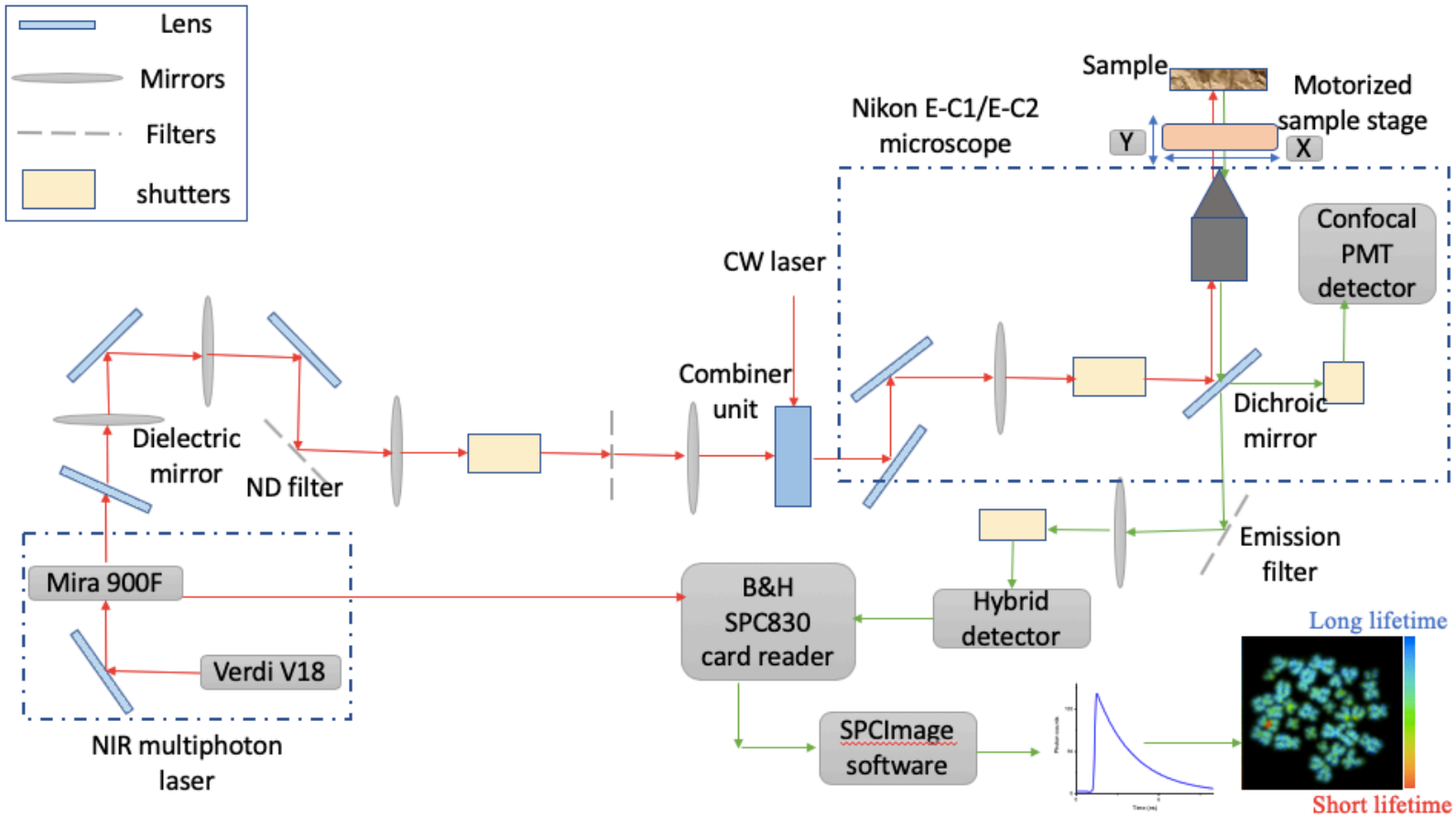

Figure 2.2: Schematic of multiphoton excitation FLIM with a confocal laser scanning microscopy setup. Excitation sources for the multiphoton FLIM were from a Mira 900F (Ti-sapphire laser (Coherent Ltd., UK, Tunable 700-980 nm, pulse length 180-200 fs) pumped by a Verdi V18, operating at 532 nm with a CW outputs. In this study, the laser was tuned to 760 nm. Photons were detected by a hybrid detector HPM 100-40, connected to a time correlated single photon counting PC module, SPC830 (Becker and Hickl). The data were then analysed using SPCImage that calculates the decay curve of the fluorophores and generates a lifetime value at each pixel of the image.

2.5.3. Calibration of the sample stage to correlate the FLIM and the epifluorescence microscope

Since the steady state epifluorescence and FLIM microscopes are separate instruments, there is a need to correlate the Field of View (FOV) and region of interest. A step-by-step procedure combining FLIM for investigating chromosome substructure and M-FISH for chromosome identification and karyotyping has been described. Following are the steps for correlative imaging:

1) A reference glass slide, “The England Finder”, also known as a graticule (Pyser-SGI Ltd.), was used to correlate chromosome images between the two microscopes. The graticule is 3” x 1” in size is the same as a standard glass slide. This has marked square grids at 1 mm intervals. Approximately 20 x, y coordinates on the graticules using both microscopes were recorded. Then calculated a linear equation for both X and Y directions from the obtained coordinates and then applied the same linear equation to transfer the locations of the chromosome spreads from the FLIM to the Zeiss epifluorescence microscope. This allowed identification of the same chromosome spreads imaged from the inverted-configuration multiphoton confocal to the upright-configuration epifluorescence microscope.

2) The first step in FLIM data acquisition is to measure the instrument response function (IRF) of the FLIM setup prior to any data acquisition to check the excitation pulse profile of the instrument. The IRF peak should be at least up to 100 photon counts to check the IRF response, and depending on the laser pulse width, this should not be larger than the detector response so long as the laser width is narrower. Potassium dihydrogen phosphate (KDP) crystals w used to determine the IRF. The NIR laser is tuned to 740-760 nm to excite the crystal, and the second harmonic signal is detected. With our instrument, it appears the IRF is mostly defined by the detector response. So, we obtained 20 ps for a detector with a 25 ps response and 110 ps for a detector with a 110 ps

response. A BG39 band filter is then used to remove the NIR laser light and transmit the DAPI fluorescence signal.

3) Calibrated the setup with standard fluorophores such as 100 μM rhodamine B, 100 μM erythrosin B and fluorescein, all prepared in water. 50 μl aliquots of the required fluorophore solution were placed on round glass coverslips with thickness number -1 or 1.5 (VWR international). The fluorophore standards were placed on the multiphoton confocal microscope stage and raster-scanned using NIR light, in the dark to avoid damage to the detector. The excited fluorescence signals were detected by a hybrid detector HPM 100-40. The lifetime value of the fluorophores, 1.65 ns, 0.12 ns and 3.7 ns, were obtained, respectively. This is within 5% of the standard literature values and in line with our daily calibration operation values. Once an instrument test and calibration were completed, the coordinates of the chromosome spreads on which FLIM measurements were taken were recorded and then located at the same coordinates on the Zeiss epifluorescence microscope.

2.5.4. Collection of FLIM data

Chromosomes on prepared slides, stained with 4 μM DAPI (see section 2.5.2.), were initially located by their x, y coordinates using the epifluorescence microscope, followed by the multiphoton FLIM microscope imaging. This was, at the time, done in reverse. In the multiphoton microscope, it was found to be easier to use a 405 nm excitation wavelength initially before using the multiphoton mode to identify the region of interest. Prior to multiphoton imaging mode, it was necessary to ensure the 405 nm laser was switched off. Due to chromatic aberration in our microscope, there is a need to adjust the focus for the 760 nm multiphoton excitation wavelength compared to that at 405 nm. Optimal excitation average power was chosen to avoid fluorescence decay of the DAPI during scanning. Using the software SPCM (version 9.80, 64 bit), we set out parameters such

as the number of cycles and the resolution of the image, 512 x 512, to acquire a clear set of FLIM data with each chromatid visible.

2.5.5. Processing steps for the FLIM data

1) Import raw FLIM data files from the TCSPC into the SPCImage software for further processing.

2) In the SPCImage software, decays containing photons with poor signal-to-noise ratio can be discarded using a threshold function. Photon counts of less than 100 in the initial rise channel are not analysed by adjusting the threshold between 25-35 in the present data sets. It is worth noting that 100 photons in the initial rise channel for a 3 ns decay profile give rise to 1000-1500 photons overall in the exponential decay. Analysing photon counts more than 1500 reduces error in the lifetime values obtained. It was found that analysing photon counts below this leads to around 20-30% error in the lifetime values calculated.

3) Choose the “Incomplete Multiexponential” decay model as a fitting model to calculate the accurate fluorescence lifetime of a fluorophore (under “Option - Model-Incomplete Multiexponential”) due to our laser operating at 80 MHz and the lifetime of DAPI does not decay to the baseline before the next pulse.

4) The reliability of the single or double lifetime components during analysis is determined by the goodness of fit, Chi square ($\chi 2$). The Chi square is used as a measure of whether the data fit to one or more components. For example, where fitting to one component the Chi square is >1.4, it is likely that there are other lifetimes present within the decay curve. If two components are applied and the Chi square reduces to between 1 to 1.3, the two lifetimes are taken as the correct lifetime values. A Chi square value of unity therefore indicates a good decay curve fitting that is desirable.

5) Set appropriate “scatter” and “shift” values, then run the decay matrix (under “calculate – Decay Matrix”), for the whole image to get the lifetime distribution of the whole image. BH software converts intensity images to false–coloured image to generate lifetime values of each pixel (Becker, 2012).

6) Set the false-colour range from “Minimum” and “Maximum” (continuous colour mode) (under “Option – Colour”) according to our expectation of the lifetime map of the chromosome.

7) Pseudo coloured histogram denotes the range of short and long lifetime of the fluorophore-stained chromosomes. Here, we consider red to represent a shorter lifetime and blue to represent a longer lifetime.

8) Locked the fitting process and set it to “global fitting mode” in order to speed up the lifetime measurements.

2.6. Multi-colour chromosomes detection after In Situ hybridisation

To identify the chromosomes from the FLIM measurement, the standard 24XCyte Multiplex–Fluorescence *In Situ* Hybridisation (M-FISH, MetaSystems, Germany) probe kit and software on the Zeiss microscope (Yusuf *et al.*, 2011) were used. The kit identifies 24 colour combinations specific to the 24 human chromosomes. Each probe was labelled with up to 5 different fluorophores in a combination manner. The five fluorophores are FITC, Orange, TexasRed®, Aqua and Cy^{TM}5 and used DAPI as a counterstain. The probe kit is sensitive to light and should be stored in the dark at -20 °C. The M-FISH labelled chromosomes were visualised using a fluorescence microscope (Zeiss Z2Axioimager) combined with ISIS software for capturing and analysis.

2.6.1. Buffers prepared for M-FISH hybridisation

Several buffers were prepared prior to the start of the experiment. Some are pre-hybridisation, and some are post-hybridisation buffers, for example, 0.1 x and 2 x Saline-sodium citrate buffer (SSC), series of ethanol (100%, 95% and 70%), 0.07 mol/L as DNA denaturing buffer on the day, prior to the start of the experiment. 0.4 x SSC and SSCT (SSC with 20 % Tween) are washing buffers after hybridisation. Listed buffers are given below: -

1) 0.1 x SSC stock: Added 1 ml of 20 x SSC (Sigma-Aldrich) in a 200 ml milliQ water, pH 7.25. Transferred 50 ml of solution in two coplin jars, keeping one jar at room temperature and the other in a fridge at 4 °C.

2) Repeated the above procedure to prepare 2 x SSC stock, adding 20 ml of 20 x SSC in a 200 ml milliQ water, pH 7.45. Poured 50 ml of the solution into two coplin jars, keeping one jar at 70 °C (+/- 1°C) in a hot water bath and another in a fridge at 4 °C.

3) Prepared 0.07 mol/L by adding 1 ml of 7 M stock solution in a 100 ml of milliQ water and transferred 50 ml of solution in a coplin jar and stored at room temperature.

4) 100 %, 95% and 70% of ethanol series were prepared in a milliQ water and kept at room temperature.

5) Prepared 0.4 x SSC by mixing 1 ml of 20 x SSC in 50 ml of milliQ water, pH 7.2. Kept at 72 °C (+/- 1°C).

6) Prepared 2 x SSCT by dissolving 0.05 % Tween-20 (Polyoxyethylenesorbitan-monolaurate syrup, sigma P-1379) in a 50 ml of a 2 x SSC, pH 7.45 and kept at room temperature.

2.6.2. Protocol for multi-colour FISH

1) Prepared 0.1 x SSC and 0.2 x SSC, poured into coplin jars and placed into the refrigerator at 4 °C.
2) Prepared 2 x SSC, poured into a coplin jar and placed into a water bath at 70 °C (+/- 1°C).
3) Carefully removed coverslip from the glass slide used for the FLIM data acquisition.
4) Placed the required slides in a series of ethanol washes: 70%, 95%, 100% for 30 secs in each solution and left to dry in air.
5) Incubated the slides for 30 mins in the pre-warmed 2 x SSC at 70 °C (+/- 1°C) coplin jar.
6) Removed the coplin jar from the water bath and let it cool for 20 mins at room temperature.
7) Meanwhile, prepared the M-FISH probe cocktail according to the intended area for hybridisation e.g., 9 µl for an 18 x 18 mm^2 cover slip, 12 µl for a 22 x 22 mm^2 cover slip.
8) Denatured the probe by incubating at 75 °C (+/- 1°C) for 5 mins on the pre-warmed hot plate
9) Placed the probe on ice for 15 sec.
10) Incubated the probe at 37 °C (+/- 1°C) for 30 mins on the pre-warmed hot plate.
11) Once the slides are cooled to room temperature, placed the slides in the coplin jar containing 0.1 x SSC at room temperature for 1 min.
12) Denatured slides in 0.07 N NaOH at room temperature for 1 min.
13) Placed the slides into 0.1 x SSC 4 °C for 1 min.
14) Placed the slides into 2 x SSC 4 °C for 1 min.
15) Transferred to a coplin jar with 70 % ethanol for 1 min.
16) Transferred to a coplin jar with 95 % and 100 % ethanol and incubated for 1 min, then allowed the slides to air dry.
17) Pipette the denatured probe cocktail onto the denatured chromosome preparation and cover it with the required sized coverslip prior to fluorescence imaging.

18) Sealed the coverslip to the slide using rubber cement.
19) Incubated the slides for 1-2 days in a humidified chamber at 37 °C (+/- 1°C).
20) Following incubation, carefully removed the rubber cement and the cover slips.
21) Placed the slides into the coplin jar containing pre-warmed (72 °C (+/- 1°C) 0.4 x SSC for 2 mins.
22) Incubated the slides in the coplin jar containing 2 x SSCT for 30 secs.
23) Washed the slides briefly with milliQ water to avoid crystal formation and left them to dry in air at room temperature.
24) Applied 20 µl of the DAPI/ antifade compound, and overlaid the sample with a 24 x 60 mm^2 cover slip, and incubated for 10 mins.
25) Proceed with imaging and analysis. The samples can be stored at -20 °C for up to 2 weeks.

2.7. Coherence X-ray imaging

2.7.1. Sample preparation on silicon nitride windows

Two different sized silicon nitride membrane X-ray windows (Silson Ltd.), also called transmission electron microscopy (TEM) grids, were used. These were categorized as; 0.25 mm x 0.25 mm window opening, membrane thickness 30 nm and 100 nm or 0.50 mm x 0.50 mm window opening, membrane thickness 30 nm and 100 nm. In each case, the silicon nitride membrane was located at the centre of a 3 mm octagonal silicon frame of thickness 200 µm (Figure 2.3).

With the flat side of the membrane facing upward, the membrane windows were mounted on a parafilm-wrapped glass slide and placed inside the air chamber of an automated GloQube glow discharge system (Quorum Technologies Ltd., Sussex, England) designed for negative hydrophilization of TEM grids. The treatment was carried out for 30 secs at 30 mA current. This treatment causes chromosomes in suspension to adhere evenly to the surface of the silicon nitride windows.

Once the grids were made hydrophilic, 5 µl of MAA fixed chromosomes were dropped immediately from a height of 10 cm (to get well-scattered metaphase chromosome spreads) and left to air dry to produce chromosome spreads. Grids were validated using an Olympus LEXT laser scanning confocal microscope combined with custom analysis software, LEXT. A 10x objective was used for localisation of spreads, and 20x or 50x were used to confirm the presence of chromosomes, to be used for alignment and localisation of spreads during the X-ray imaging.

150 nm gold nanoparticles (Sigma-Aldrich) were used as a test pattern (fiducial markers) for X-ray imaging. 2 µl of gold nanoparticles were dissolved in 8 µl of milliQ water and then dropped (3 µl) on the silicon window (0.50 mm x 0.50 mm, membrane thickness 30 nm) and left to dry before imaging at room temperature.

2.7.2. Heavy metal stains

Two types of heavy metal stains were used for staining the chromosomes; once placed on the silicon nitride windows, they were used only for preliminary experiments:

a) Platinum blue, synthesised in our laboratory (Yusuf *et al.*, 2014) at Research Complex at Harwell (RCaH), Oxford, UK, at 5 mM concentration: 0.015 g of platinum blue powder dissolved in 5 ml of milliQ water and stored in a fridge at 4 ℃.

b) Uranyl acetate (UA), which is a negative stain, was prepared at 1% from a stock solution of 2% UA (Taab Laboratories Equipment Ltd.), in equal proportion of milliQ water and stored in the fridge at 4 ℃.

2.7.2.1. Procedure for staining

Chromosomes samples were mounted on the silicon nitride windows (see section 2.7.1.) and, once dry, they were stained either with 5 mM platinum blue or 1% uranyl acetate. To stain with platinum blue, 2 µl to 3 µl of 5 mM platinum

blue solution was dropped on the silicon windows containing chromosome spreads at room temperature. Excess dye was blotted off using Whatman filter paper and left to air dry. The dried grids were stored in a grid box and used during X-ray imaging.

To stain with 1% UA solution, the grids containing chromosome spreads were first washed twice, for 30 secs each wash, in milliQ water and then stained twice, for 30 sec, each stain, with 1% UA solution. After every wash and staining, the grids were blotted using Whatman filter paper. After the last stain cycle, the sample was blotted for a longer time, 1 min, to get rid of excess UA. This staining was performed in a radioactive laboratory with full safety and training. The stained chromosome samples were stored in the radioactive laboratory for 24 hrs to 48 hrs before taking them for X-ray imaging. Afterwards, the grids were observed under the confocal microscope to locate chromosome spreads. Grids with chromosome spreads were further taken for X-ray imaging.

2.7.3. Sample loading in the holders

The chromosomes mounted on silicon nitride windows were loaded into the sample holders, either in a single grid holder (prepared on SEM stubs in our laboratory) (Figure 2.3a) or on a 4 x 4 array 3D printed holder from I-13 beamline, DLS) depending on the number of samples to be imaged at a time. The recessed holes in the 4 x 4 array holder fit the 3 mm grids (Figure 2.3b), which are captured by the protruding ring on the mating part (Figure 2.3c). The lid of the holder was screwed carefully to avoid cracking the grids.

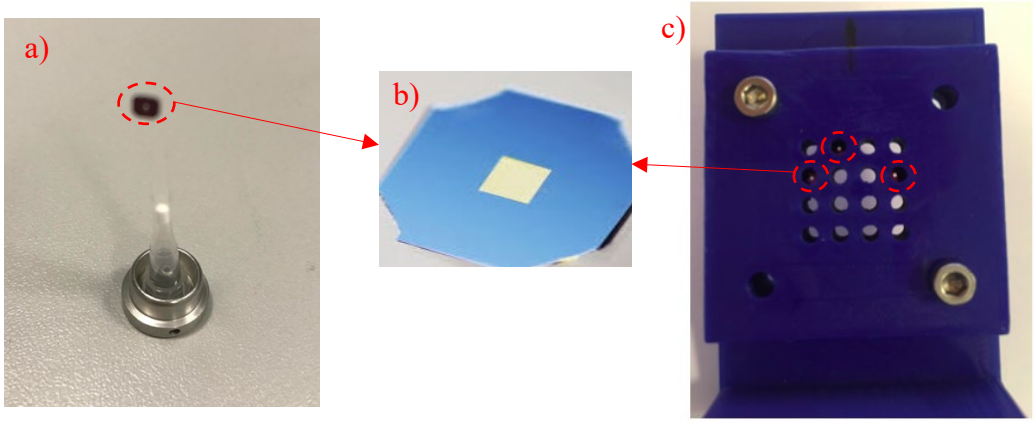

Figure 2.3: Silicon nitride window holders for X-ray imaging. a) A single grid holder, prepared on a SEM stub, b) Square shaped silicon nitride membrane at the centre of a 3 mm octagonal silicon frame and c) 3D printed 4 x 4 array of grid holder which contains 3 silicon nitride windows (red dashed circle).

2.7.4. Experimental setup for ptychography

The collimated X-ray beam from DLS entered the experimental hutch (I-13-1) through entrance slits, 2 x 3 mm upstream of the double-crystal Si (111) monochromator. The beam was focused using a Fresnel zone plate (FZP) of diameter 400 µm and a zone-width of 150 nm. A 50 µm order sorting aperture (OSA) further downstream was centred to allow only the first order diffraction from the FZP to pass through. A central stop (CS), made of 60 µm diameter of gold to occlude the OSA, was used to eliminate the un-diffracted zero order beam. The beam was slightly defocused to ~10 µm at the sample plane, which lies slightly beyond the focal plane of FZP, as shown in Figure 2.4. The measured beam size on the sample was later found to be ~7 µm as planned. The sample was mounted on a high-precision piezo stage and scanned in a raster fashion. A helium gas pipe was placed between the sample and detector to minimise the air scattering so that the sample scattering signal could be maximised. The X-ray photon-counting Excalibur detector (Marchal *et al.*, 2013)x (Medipix3 chip, 1806 x 1548 pixels and Pixel size: 55 µm x 55 µm), used for recording the X-ray diffraction pattern, was placed at 8 m beyond the sample.

Rapid initial scans were taken to align the sample with following parameters: i) select the region of interest (chromosome spreads) using a PCO camera; in our case, the most common values were, 64 µm x 64 µm/ 32 µm x 32 µm, depending upon the size of the spreads. ii) choose the position (1µm X 1µm) of the scan and iii) select the exposure time of the scan. The following variables were set to be the best scan parameters.

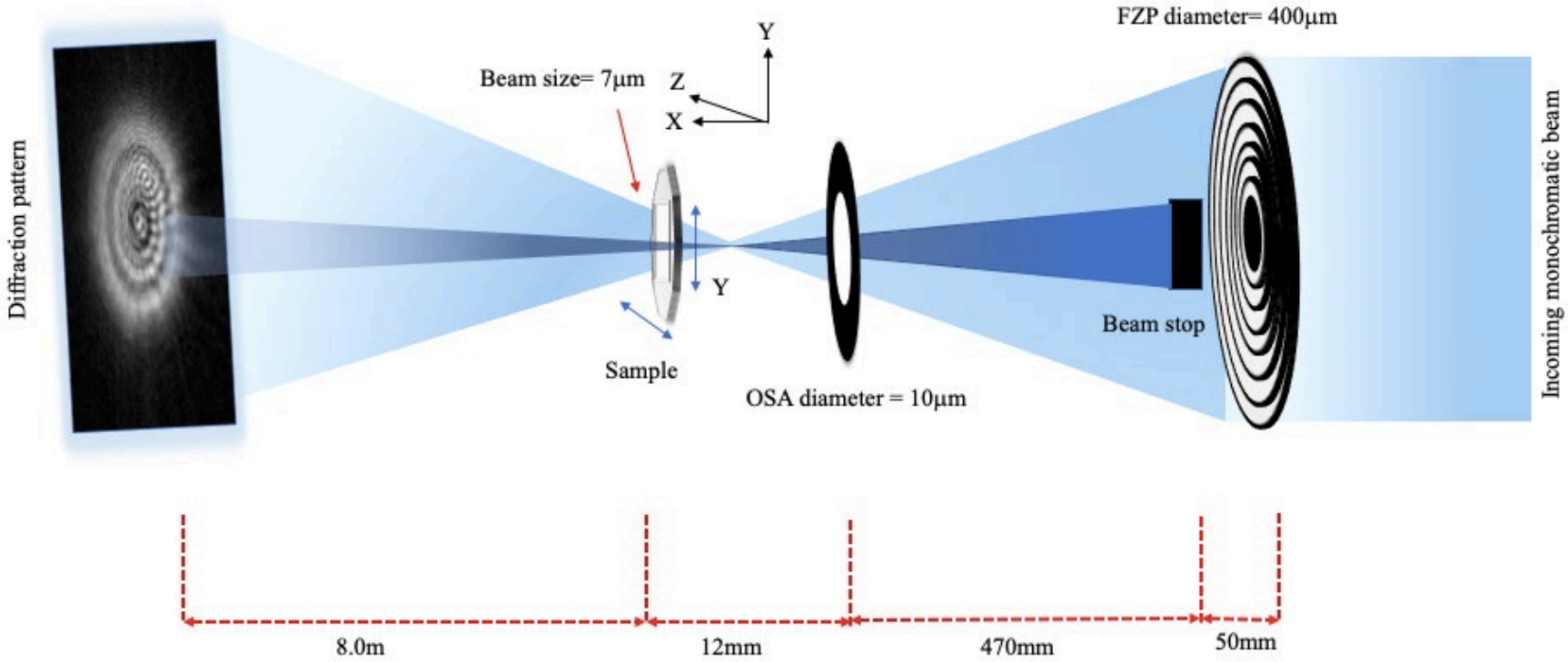

Figure 2.4: Schematic diagram of the beamline setup at I-13-1 Diamond light source for X-ray ptychography imaging.

Chapter 3

3. X-ray induced chromosomes assessed with the use of fluorescence lifetime imaging microscopy

Fluorescence lifetime imaging (FLIM) is a highly sensitive method for detecting environmental changes in fluorescence molecules. In this chapter, FLIM has been used to investigate the changes in the X-ray induced chromosomes. The effect of low X-ray irradiation dose in heteromorphic chromosomes was examined to determine if they maintain their structural characteristics, particularly near the pericentric region. The effect of irradiation was also examined in euchromatin regions (referred to as “non-heterochromatin regions” in this chapter) and in the pericentromeric region of all 46 human chromosomes. In addition, the effect of X-ray radiation was also investigated at three different time points of the passage.

3.1. Identification of lifetime components in a FLIM image

FLIM probes the fluorescence lifetime of a fluorophore; as the lifetime of the fluorophore depends on its local microenvironment, this technique produces colour-coded maps, which help to identify the sub-structures (heterochromatin and non-heterochromatin) of chromosomes. In this work, chromosomes extracted from human T-cells were stained with DAPI. The mean lifetime ± standard deviation (SD) measured for chromosomes 1, 9, 15 and 16 in Figure 3.1a showed a shorter lifetime (red: 2.71 ± 0.06 ns) at the proximity of the centromere- the region known as the pericentromeric heterochromatin. In contrast, the axial regions of heteromorphic chromosomes showed a longer lifetime (blue: 2.92 ± 0.03 ns). As shown in Figure 3.1, there is a significant difference between the regions with pseudo red colour that decay faster than the blue colour in the FLIM image (ANOVA: $P < 0.05$). One-way (statistical

analysis that involves one factor between two or multiple groups) ANOVA test demonstrated a significant difference exists between the red and the blue regions of the chromosomes. For example, the lifetime distribution along the "chromosome 9" length has been shown in (Figure 3.1c). The selected "chromosome 9" was obtained from the FLIM image (Figure 3.1b).

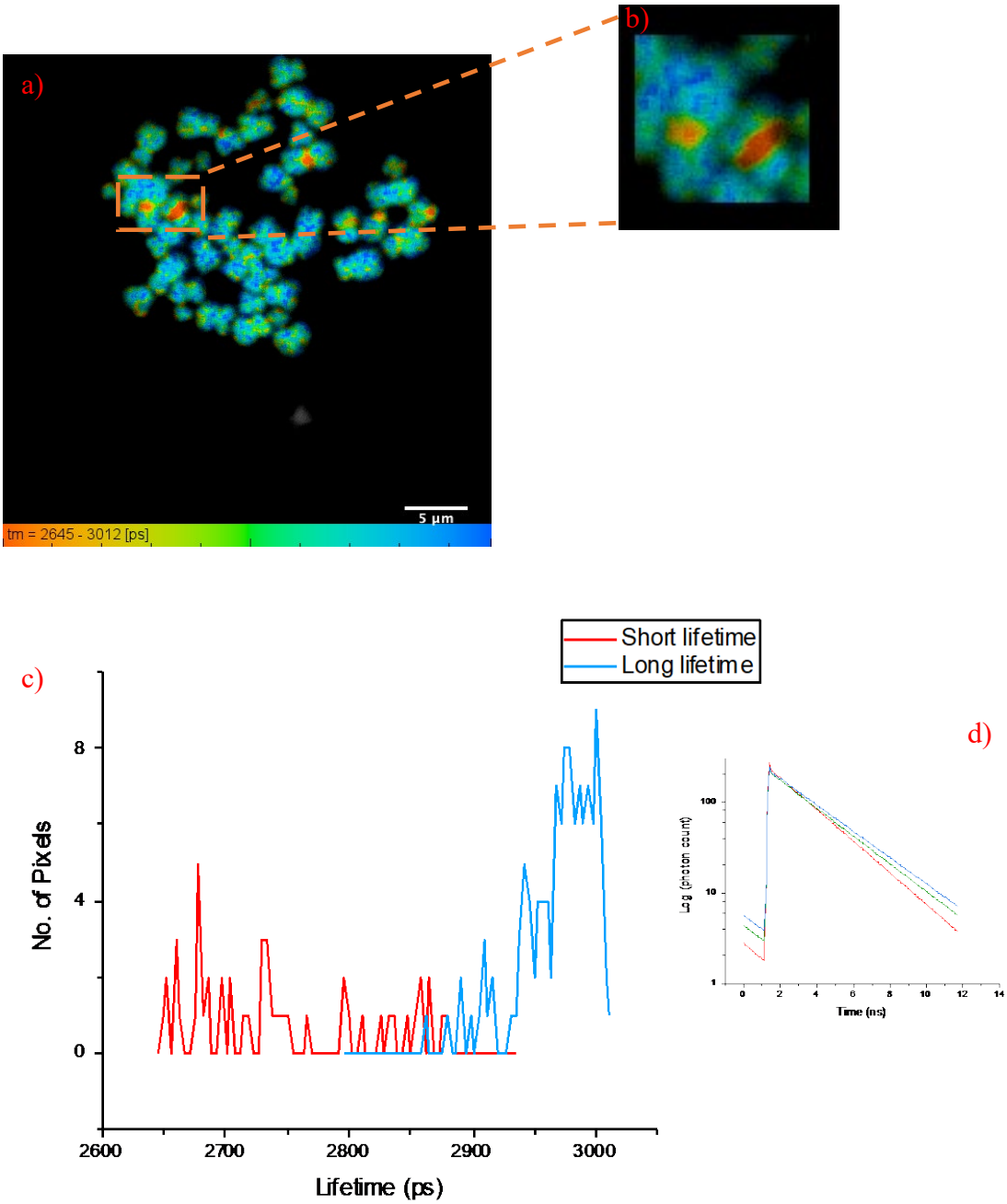

Figure 3.1: FLIM measurements of 4 µM DAPI stained, fixed metaphase chromosomes obtained from human T-cells: a) Shows lifetime change along the length of an individual chromosome. The lifetime values of heteromorphic chromosomes ranged from 2.71 ± 0.06 ns to 2.92 ± 0.02 ns (ANOVA: $P < 0.05$), within a field of view of 35 µm and scale bar of 5 µm. b) Zoomed image of chromosome 1 and 9 from Figure 3.1a. c) The lifetime distribution of chromosome 9 measured from Figure 3.1b, showed short lifetime at the pericentromeric (red: 2.67 ns) and longer lifetime at the axil region (blue: 2.90 ns). d) Fluorescence decay curve obtained from selected pixel of red, green, and blue region of chromosome 9 from Figure 3.1b.

3.2. DAPI lifetime of chromosome obtained from T-lymphocytes

The ability to identify the DAPI lifetime components in the FLIM image is stated above. The chromosomes were prepared as described in Chapter 2 (Materials and Methods). Here, a single spread of non-irradiated metaphase chromosomes was imaged using FLIM to identify the heteromorphic chromosomes (Figure 3.2a). The same chromosome spread was labelled with M-FISH probes (Figure 3.2b) and karyotyped (Figure 3.2c) to locate each chromosome in the spread. The overall lifetime distribution ranged from 2.4 ns to 3.2 ns, shown in Figure 3.2a. The lifetime distribution range was kept constant in the analysis throughout this chapter for comparison.

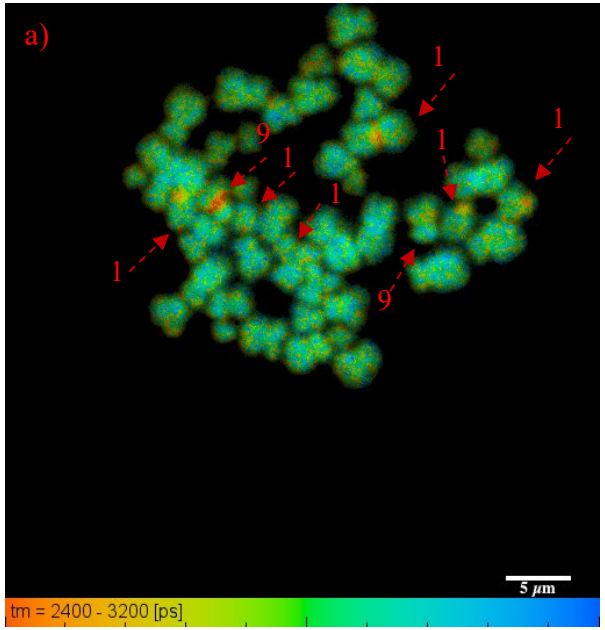

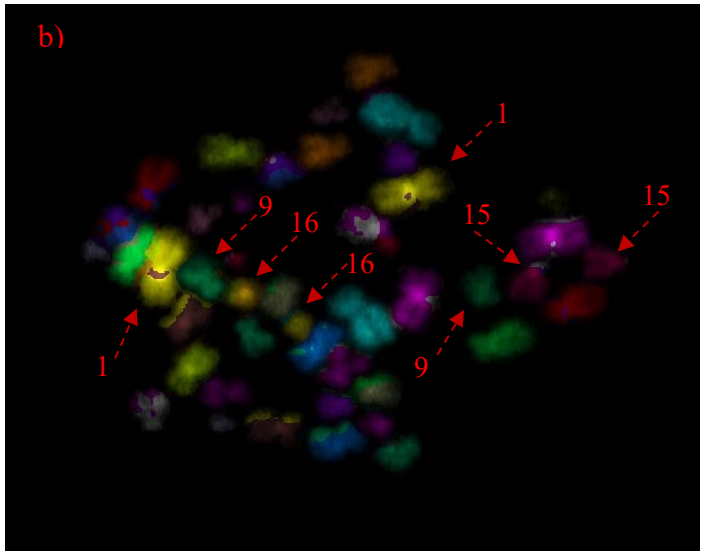

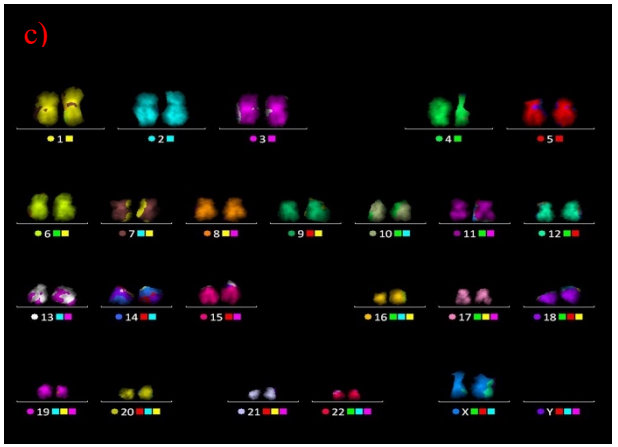

d)

Chromosomes	Mean lifetime (τ_m)
Chr 1	2.74
Chr 9	2.70
Chr 15	2.72
Chr 16	2.83

Figure 3.2: A single metaphase chromosome spread obtained from non-irradiated T-lymphocytes. a) FLIM image shows DAPI the lifetime of all 46 (X, X) chromosomes in a spread, scale bar = 5 µm. 60x water objective was used with an image pixel size of 512 x 512 b) M-FISH image of the same spread as a, c) Karyotype of image b, 63x oil objective used and d) Representation of mean lifetime of two homologous chromosomes (shown with red dashed arrows in a spread, figure 3.2 and 3.2b) in a spread with shorter lifetime at their pericentric region.

Figure 3.2a shows the DAPI lifetime of methanol: acetic acid (3:1) fixed human metaphase chromosomes obtained from T-lymphocytes. Chromosomes 1, 9, 15 and 16 show a lifetime variation along the chromosome length. Each of these individual chromosomes showed a reduced DAPI fluorescence lifetime at the proximity of the centromere (heterochromatin regions) and a longer lifetime at the distal (away from the centromere) regions of the chromosomes. These chromosomes are known as heteromorphic chromosomes because of the presence of many variants of DNA sequence repeats from one species to another (Tagarro, Fernández-Peralta and González-Aguilera, 1994). The size of constitutive heterochromatin blocks of heteromorphic chromosomes varies from one chromosome to another in different species (Staessen, Kirsch-Volders and Susanne, 1982) (Kosyakova *et al.*, 2013) (Madon, Athalye and Parikh, 2005).

Figure 3.2d shows a table of heteromorphic chromosomes and their DAPI lifetime values. As the chromosomes in a homologous pair have similar DAPI lifetimes at the heterochromatin region, the lifetime values reported in the table correspond to the average mean lifetime of two homologous chromosomes present in a single cell. The results show no significant difference (ANOVA: $P > 0.05$) in their lifetime values in the pericentromeric regions of heteromorphic chromosomes present in the single spread (Figure 3.2a).

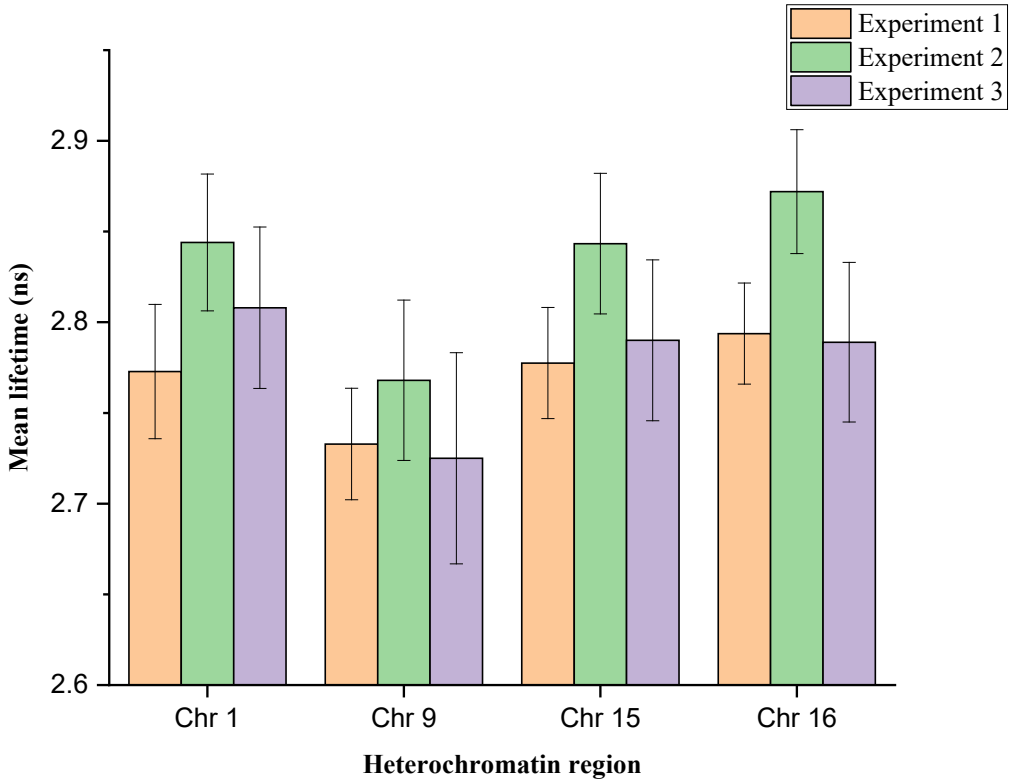

Figure 3.3: Representation of DAPI lifetime of heterochromatin regions of chromosomes 1, 9, 15 and 16, obtained from three independent repeated experiments performed on non-irradiated T-cells, number of spreads (n = 5). The error bar represents the SEM (standard error of the mean) values and ANOVA: *p > 0.05*. Each colour of the bar represents the repeated independent experiments (n=3).

Figure 3.3, shows the mean lifetime of DAPI-bound chromosomes obtained from non-irradiated T-lymphocytes. As shown in Figure 3.3, three independent repeats (passage numbers 3, 4 and 5, respectively) were performed to ensure the change in the lifetime values at the pericentromeric region of the heteromorphic chromosomes. The one-factor ANOVA test showed no significant difference in the lifetime values of three different repeats (ANOVA: *p > 0.05)*.

Each experiment's lifetime values of DAPI-bound heteromorphic chromosomes features an averaged lifetime from five individual chromosome spreads. The lifetime values for each heteromorphic chromosome are displayed in this manner (X- represents the averaged lifetime ± SEM). The averaged lifetime values from three independent experiments are 2.81 ± 0.04 ns for

chromosome 1, 2.74 ± 0.04 ns for chromosome 9, 2.80 ± 0.04 ns for chromosome 15, and 2.82 ± 0.04 ns for chromosome 16 (Figure 3.3).

3.2.1. DAPI lifetime of irradiated chromosomes obtained from T-lymphocytes

The FLIM technique was also applied to study the effect of X-ray irradiated chromosomes. The work aimed to investigate the X-ray induced metaphase chromosomal aberrations at three different consequent passages of the cell culture. Chromosomal aberrations such as translocations and breaks were also evaluated. The focus was to measure the lifetime change at the heterochromatin and the non-heterochromatin regions of aberrated and non-aberrated chromosomes.

First, the T-cells were cultured from passages 3 and 4, followed by irradiation with X-rays at different doses (i.e., 0.1 Gy, 0.5 Gy and 1 Gy) at a 0.5 Gy/min dose rate. After irradiation, the X-ray induced chromosomes were prepared (see Chapter 2, Materials and Methods), followed by FLIM imaging.

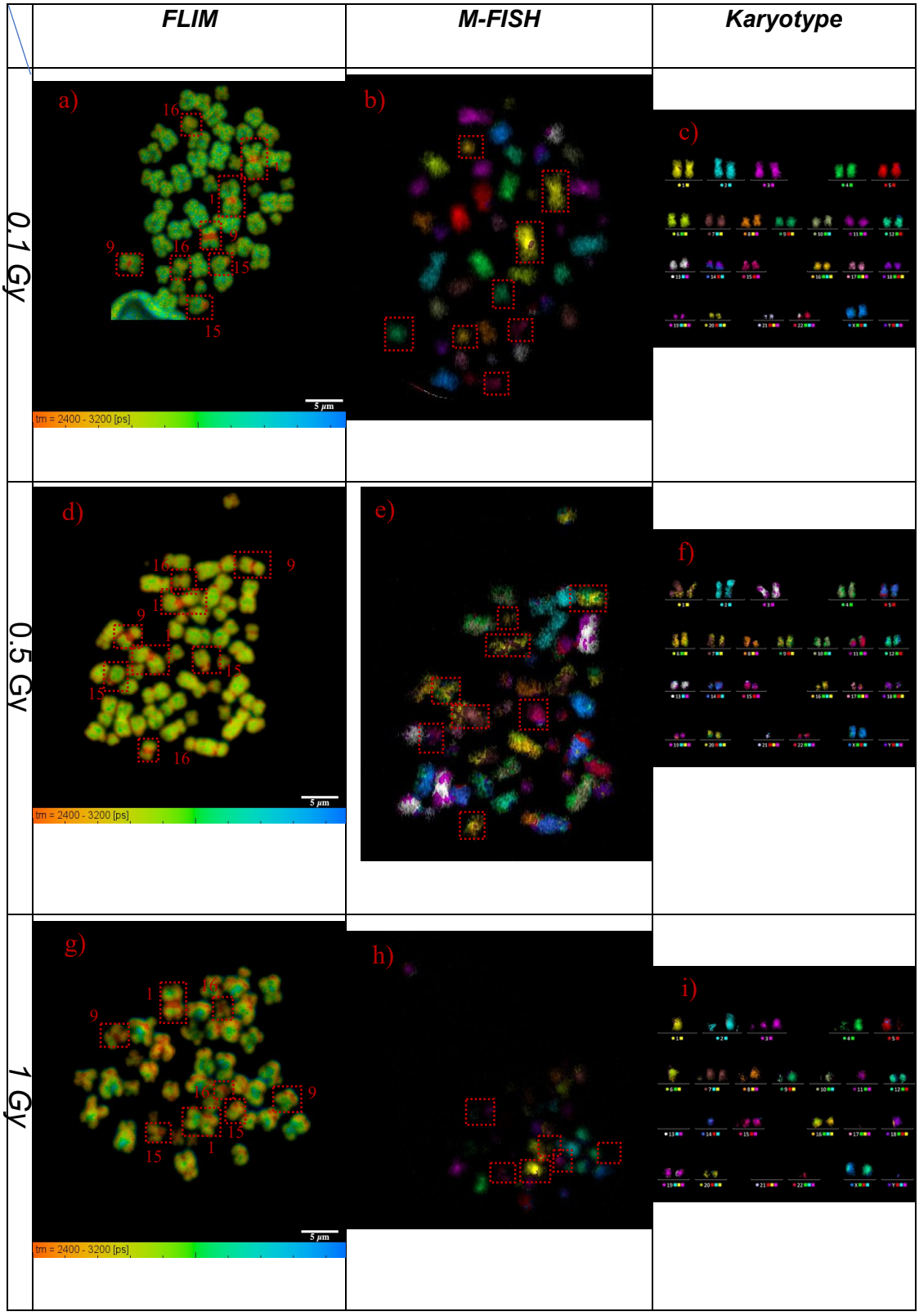
FLIM
M-FISH
Karyotype
0.1 Gy
0.5 Gy
1 Gy
a)
b)
c)
d)
e)
f)
g)
h)
i)
tm = 2400 - 3200 [ps]
5 µm

Figure 3.4: X-ray irradiated chromosome spreads from three different radiation doses, and the spreads shown are imaged using FLIM and M-FISH, followed by karyotypes. The rows define the three X-ray radiation doses, and the columns define the imaging techniques and the karyotype. Figure a), d), and g) are the FLIM images, b), e) and h) are the M-FISH images of the same spread, respectively, and c), f) and i) are the karyotypes of the same spread obtained from the respective M-FISH spread. Red boxes denote homologous heteromorphic chromosomes with a short lifetime at their heterochromatin region in all three independent spreads. A map of DAPI lifetime ranged between 2.4 ns to 3.2 ns, and scale bar= 5 µm. Objectives used for FLIM imaging are 60x water and for M-FISH is 63x immersion oil.

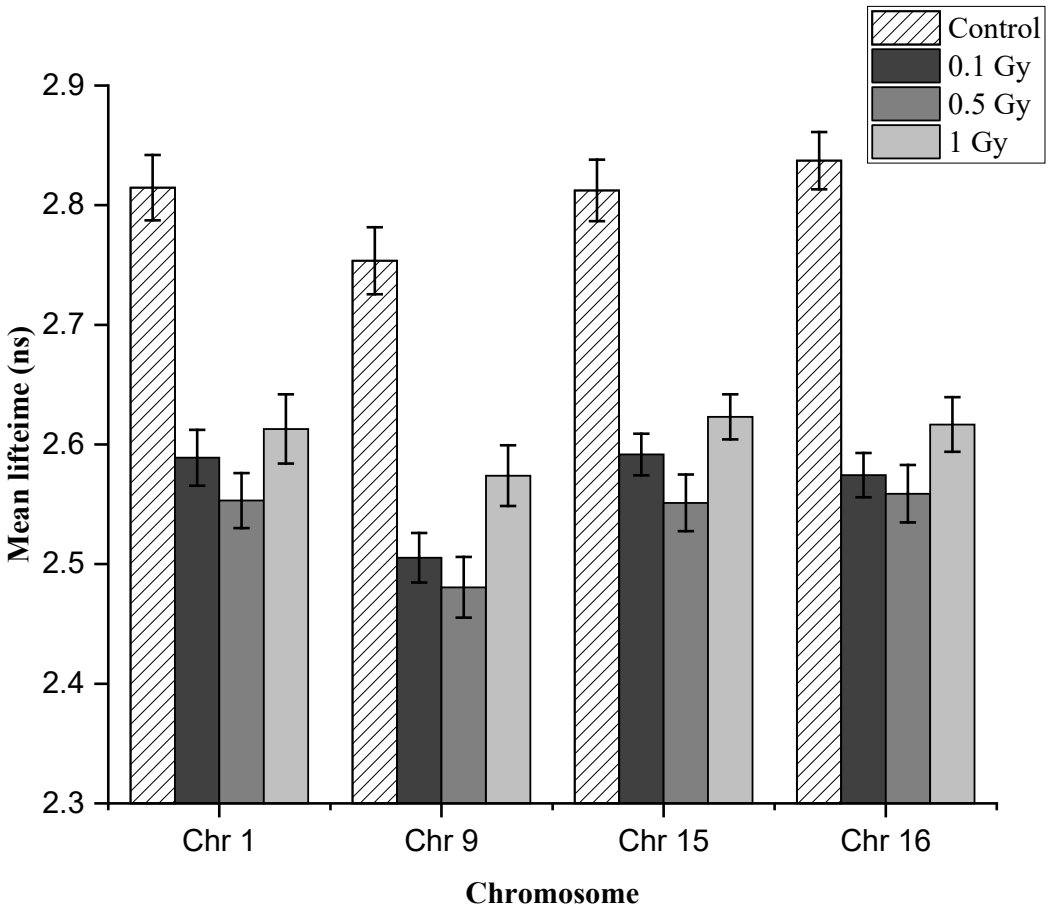

Figure 3.5: Representation of a different homologous pair of heteromorphic chromosomes with a short lifetime at their heterochromatin region at different radiation doses, number of spreads (n = 9). Error bar represents SEM, ANOVA: $p < 0.05$.

Figure 3.4 shows the FLIM and the respective M-FISH images of chromosome spreads obtained from X-ray induced T-cells at radiation doses of 0.1 Gy, 0.5 Gy and 1 Gy. Note that while FLIM measurements were performed for all 46 chromosomes, a complete M-FISH analysis was not possible; thus, the M-FISH images in Figure 3.4 do not show all chromosomes with 0.5 Gy and 1 Gy irradiation. This was due to the technical difficulty of rescuing all 46 chromosomes while performing M-FISH hybridisation on the same spread on which FLIM was already done.

To evaluate the DAPI lifetimes of X-ray irradiated chromosomes, Figure 3.5 shows the averaged mean lifetime values from nine independent chromosome spreads for each heteromorphic chromosome. The nine independent chromosome spreads were pooled from two independent experiments, and the obtained lifetimes are displayed as X- representing the averaged lifetime ± SEM for each heteromorphic chromosome. Figure 3.5 also shows the results of non-irradiated chromosomes to serve as the 'control' sample. Figure 3.5 reveals that the DAPI lifetime values decrease in X-ray induced heteromorphic chromosomes in comparison to the control sample. Thus, the average DAPI lifetime for non-irradiated chromosomes is 2.8 ± 0.03 ns while lower values of 2.57 ± 0.02 ns and 2.54 ± 0.02 ns are observed for 0.1 Gy and 0.5 Gy irradiated samples respectively. Interestingly, the average lifetime of 1 Gy appears to rise to 2.61 ± 0.02 ns in comparison to other radiation doses. Hence, the averaged mean lifetime exhibits the following sequence: control>1 Gy>0.1 Gy>0.5 Gy. The ANOVA test ($p < 0.05$) showed that the change in the lifetime values from the control to the irradiated samples is significant. Nonetheless, multiple comparisons using the Tukey test showed no significant difference among different radiation doses. Therefore, the significant difference in the DAPI lifetime occurs after irradiation but not within different radiation doses.

Surprisingly, the average DAPI lifetime in Figure 3.5 indicates a difference of ~0.23 ns between non-irradiated and irradiated chromosomes. Besides this, chromosome 9 has the shortest DAPI lifetime relative to other heteromorphic chromosomes in both the cases of irradiated and non-irradiated chromosomes.

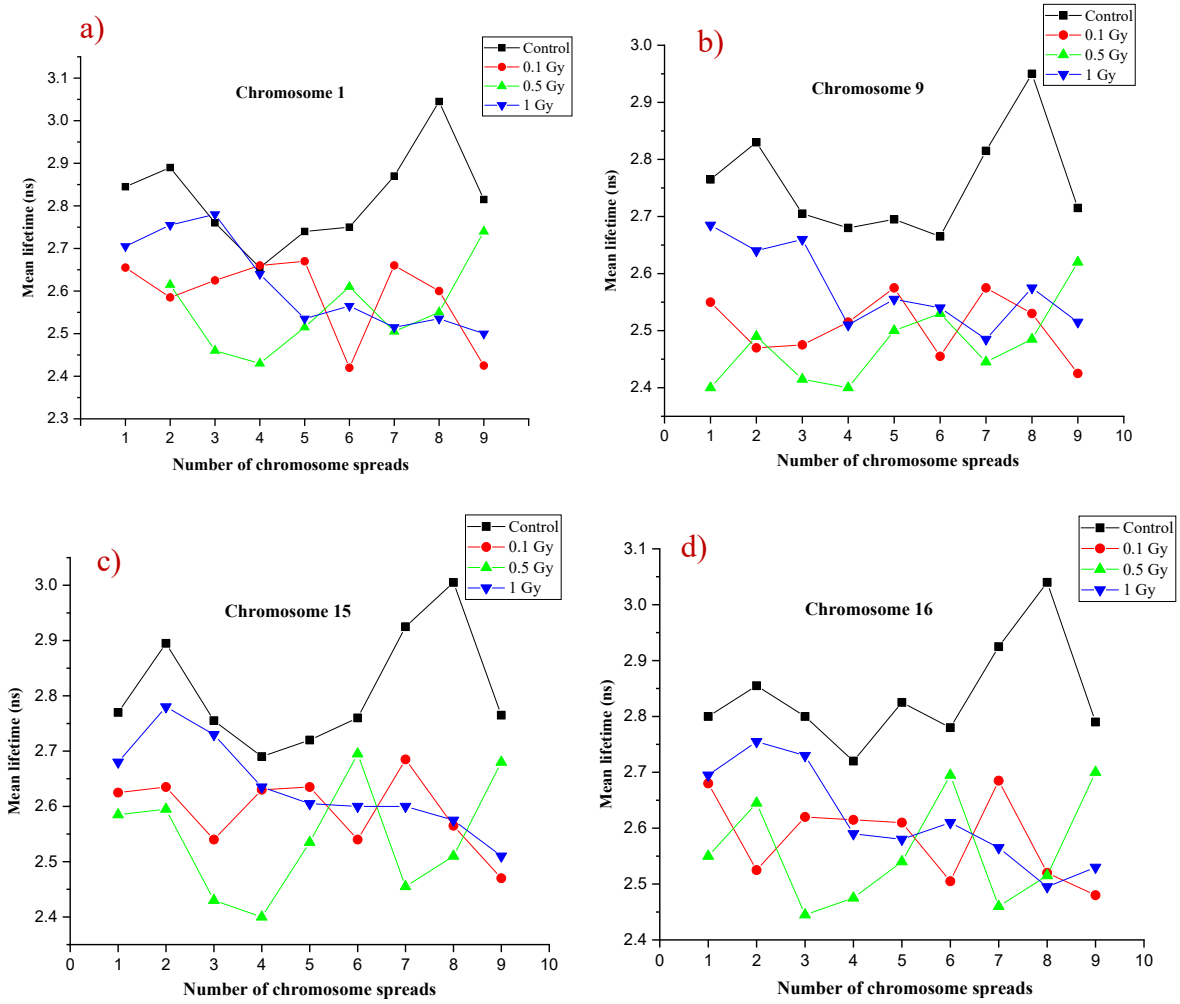

Figure 3.6: Represents DAPI lifetime change at the heterochromatin regions of each heteromorphic chromosome 1 (a), 9 (b), 15 (c) and 16 (d), obtained from both non-irradiated and irradiated chromosomes. Data points are the averaged lifetime of two homologous pairs of chromosomes present in a single chromosome spread. This is pooled data from nine independent chromosome spreads (n = 9).

In Figure 3.6, each data point represents the averaged lifetime of two pairs of homologous chromosomes obtained from T-lymphocytes. For each heteromorphic chromosome (1, 9, 15 and 16), it is observed in Figure 3.6 that the lifetime values are longer for non-irradiated, 'control' chromosomes relative to the irradiated ones. Furthermore, it also indicates that X-ray induced chromosomes affect the lifetime of DAPI-bound chromosomes after irradiation (Figure 3.5 and Figure 3.6). A significant change in the lifetime values can be observed after radiation but not across different low-level radiation doses,

ANOVA ($p < 0.05$). A multiple comparison Tukey test was performed to see the significant difference in lifetime after irradiation and within radiation doses.

3.2.2. DAPI lifetime of non-heterochromatin regions of chromosomes

DAPI lifetime variations probe the molecular environment of the chromosomes. In this section, DAPI lifetime variations are investigated for the most condensed (heterochromatin) and the least condensed (non-heterochromatin/euchromatin) sub-structures of the human chromosomes. The investigation is done in non-irradiated (control) and irradiated chromosomes. The heteromorphic chromosomes (1, 9, 15 and 16) showed a shorter DAPI lifetime at the pericentromeric region (Figure 3.4). On the other hand, the non-heteromorphic chromosomes showed a longer DAPI lifetime at the pericentromeric region compared to the heteromorphic regions (Figure 3.4).

T-lymphocytes were irradiated with low-level doses of X-ray (i.e., 0.1 Gy, 0.5 Gy and 1 Gy) at a 0.5 Gy/min dose rate to investigate the decay of DAPI-bound chromosomes. The DAPI lifetime of non- heterochromatin/euchromatin regions was also measured along the length of the heteromorphic chromosomes. The DAPI lifetime of non-heterochromatin regions was measured (Figure 3.7) from the same chromosome spreads from which the lifetime of heterochromatin regions was measured (Figure 3.5).

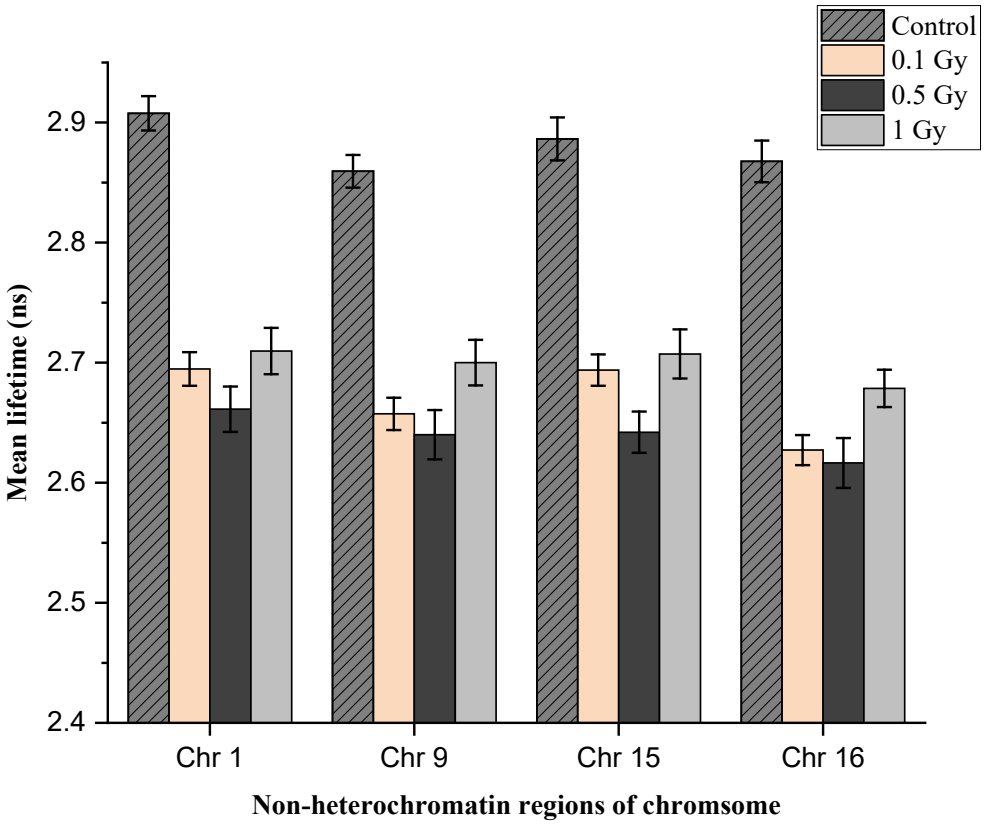

Figure 3.7: Represents the mean lifetime of non-heterochromatin regions of DAPI-bound chromosomes obtained from T-cells. The chromosomes are from both non-irradiated and irradiated T-cells, and the number of chromosomes spreads (n = 9). Error bar represents SEM, ANOVA: $p < 0.05$.

The mean lifetime of non-heterochromatin/euchromatin regions of heteromorphic chromosomes 1, 9, 15 and 16 were obtained from nine independent chromosome spreads (Figure 3.7). The results showed that the mean lifetime followed a similar pattern to the lifetime measurement of heterochromatin regions of heteromorphic chromosomes (Figure 3.5). The average lifetime of non-irradiated chromosomes calculated is 2.88 ± 0.02 ns, which is higher than the irradiated chromosomes (Figure 3.7). Furthermore, the average lifetime for the 0.1 Gy irradiated sample is 2.67 ± 0.01 ns, followed by 2.64 ± 0.02 ns for the 0.5 Gy sample. Interestingly, there is a significant increase in the averaged lifetime of 1 Gy at 2.70 ± 0.02 ns. The ANOVA test showed a significant difference in the DAPI lifetime after irradiation compared to the 'control' sample. Nevertheless, there is no significant difference in the lifetime of DAPI-bound chromosomes between different chosen radiation doses.

Interestingly, in the non-heterochromatin region, there is a significant difference between 0.5 Gy and 1 Gy irradiation doses (Figure 3.7) compared to the heterochromatic regions (Figure 3.5).

Among all the X-ray induced chromosomes, the 0.5 Gy sample has the lowest averaged mean lifetime, and the 1 Gy sample has the longest lifetime. Although, the averaged mean lifetime of non-heterochromatin regions of all heteromorphic chromosomes (Figure 3.7) showed a significantly higher mean lifetime compared to the heterochromatin regions. The averaged mean lifetime follows a sequence of; control>1 Gy>0.1 Gy>0.5 Gy.

3.2.3. FLIM measurement of heterochromatin and non-heterochromatin regions of all 46 chromosomes

FLIM was used to measure the DAPI lifetime of X-ray induced chromosomes at the heterochromatin and non-heterochromatin regions of human chromosomes. The X-ray induced chromosomes showed a shorter DAPI lifetime compared to the non-irradiated, 'control' chromosomes. In previous sections, the studies were performed only in the heteromorphic chromosomes 1, 9, 15 and 16 (Figure 3.5, Figure 3.6 and Figure 3.7) obtained from T-cells. This section includes FLIM imaging of all 46 DAPI-bound chromosomes combined with M-FISH hybridisation (Figure 3.8). This combined imaging aimed to measure the DAPI lifetime change that occurred due to intra or inter-chromosomal aberrations upon irradiation.

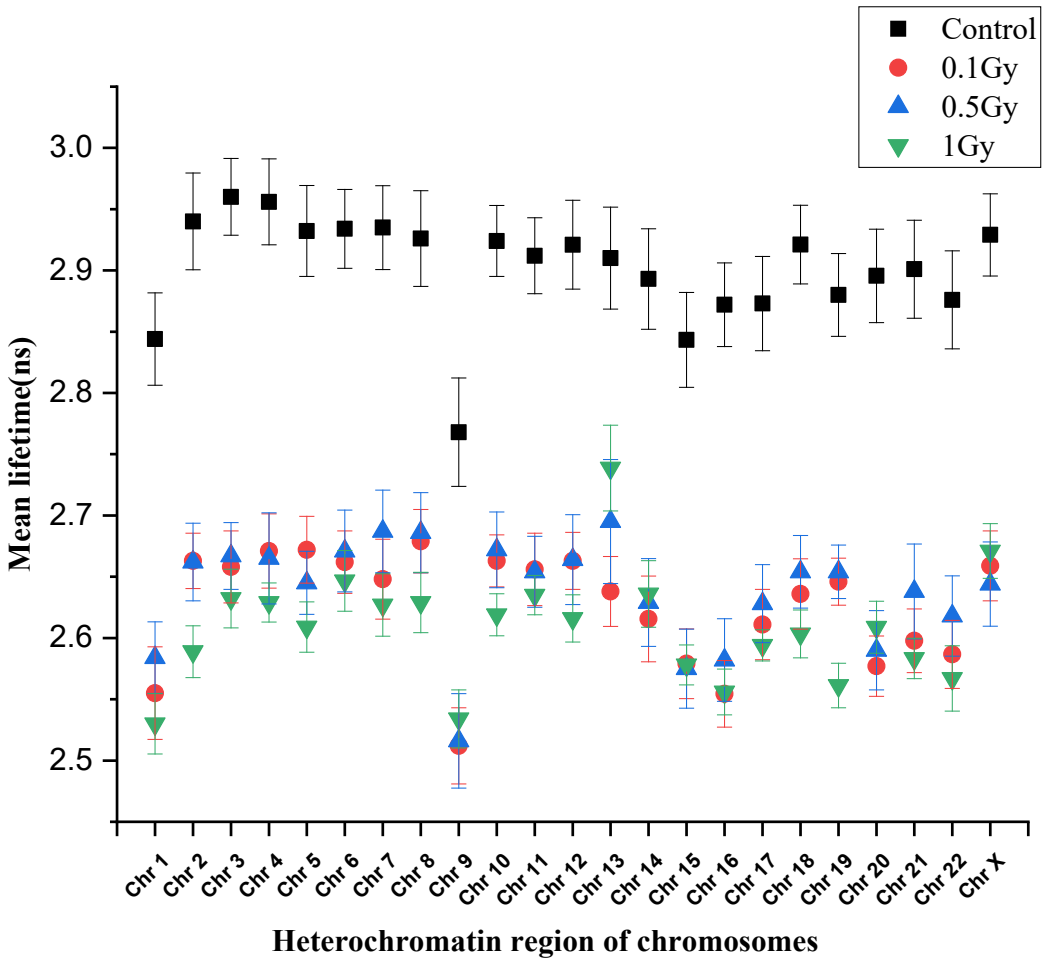

Figure 3.8: Measured mean lifetime of heterochromatin region of all 46 chromosomes obtained from T-lymphocytes, number of chromosome spreads (n = 5). Error bar represents SEM, ANOVA: $p < 0.05$.

Data represented in Figure 3.8 corresponds to averaged mean lifetime of five individual chromosome spreads obtained from T-lymphocytes, passage 4. It shows the averaged mean lifetime of heterochromatin regions of all 46 DAPI-bound chromosomes. The results show that the averaged mean lifetime of non-irradiated chromosomes (~ 3.0 ns) is longer than that of the X-ray induced chromosomes (~ 2.65 ns). In addition, the averaged mean lifetime of heteromorphic chromosomes 1, 9, 15 and 16 are exceptionally short in both non-irradiated and irradiated chromosomes, determined in Figure 3.8.

The mean lifetime of heterochromatic regions in all 46 DAPI-bound chromosomes (Figure 3.8) is 2.90 ± 0.04 ns for the control sample. The value decreases to 2.64 ± 0.03 ns for the 0.5 Gy irradiated sample, followed by 2.63

± 0.03 ns for 0.1 Gy irradiation, and then 2.61 ± 0.02 ns for 1 Gy irradiation. Hence, the averaged mean lifetime follows a sequence of; control>0.5 Gy>0.1 Gy>1 Gy (Figure 3.8). The ANOVA ($p < 0.05$) test confirmed a significant difference in the DAPI lifetime after irradiation. Nevertheless, there is no significant difference in the lifetime of DAPI-bound chromosomes between different chosen radiation doses. From these results, it can be assumed that the low-level X-ray irradiation doses cause possible chemical or structural changes that perturb in the chromosomes.

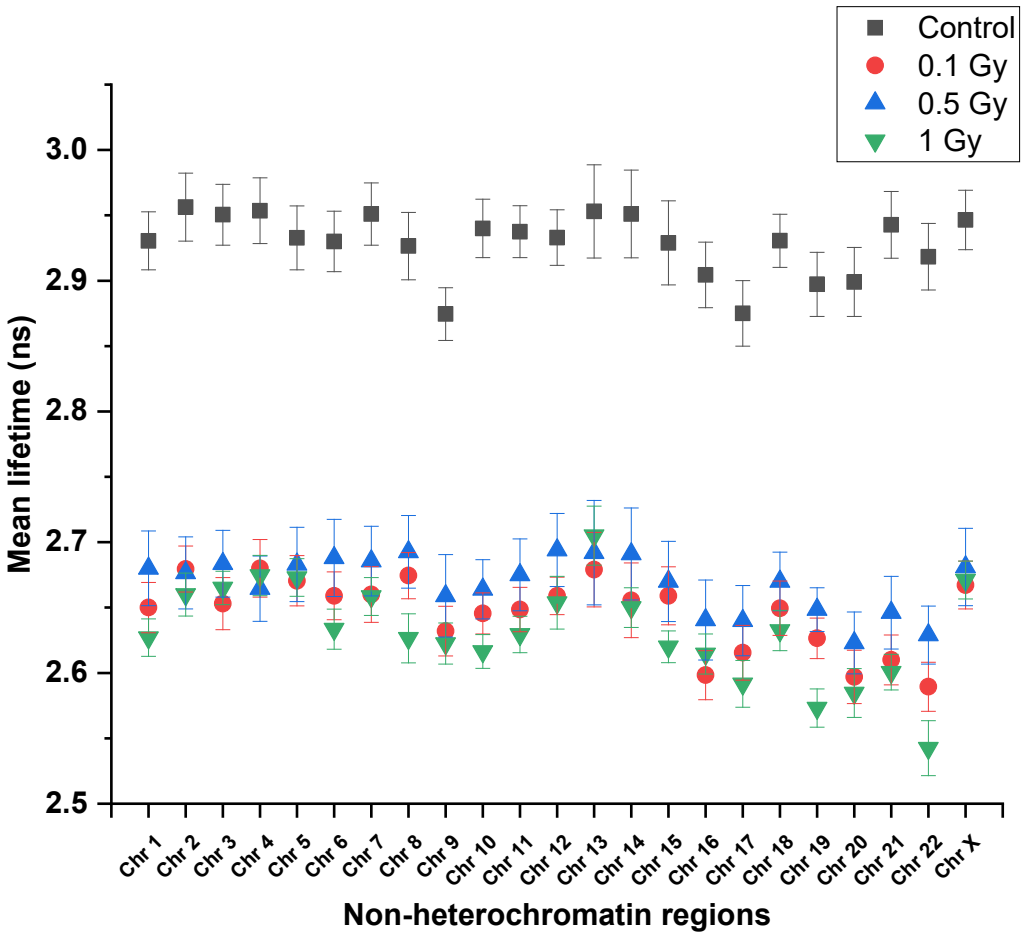

Figure 3.9: Measured mean lifetime of DAPI-bound, non-heterochromatin regions of all 46 chromosomes obtained from T-lymphocytes, number of chromosome spreads (n = 5). Error bar represents SEM, ANOVA: $p < 0.05$.

The fluorescence decay of all 46 DAPI-bound chromosomes was used to extract the mean lifetime of non-heterochromatin regions of chromosomes (Figure 3.9), using the same five individual chromosome spreads from which the DAPI lifetime of heterochromatin regions was elucidated (Figure 3.8).

Figure 3.9 shows the averaged mean lifetime of non-heterochromatin regions of all 46 chromosomes. A significant lifetime variation was not observed between heterochromatin (Figure 3.8) and the non-heterochromatin (Figure 3.9) regions of all 46 chromosomes. Note, however, that in Figure 3.9, a difference in averaged mean lifetime can be observed between non-irradiated and irradiated chromosomes similar to the heterochromatic regions (Figure 3.8). In the control sample, the averaged mean lifetime of heteromorphic chromosomes 1, 9, 15 and 16 significantly varied compared to the lifetime values of non-heteromorphic chromosomes (Figure 3.9). However, the averaged mean lifetime of heteromorphic chromosomes in the case of X-ray induced chromosomes is not significantly different from the non-heteromorphic chromosomes (Figure 3.9).

The averaged mean lifetime value for the non-irradiated (control) sample is 2.93 ± 0.02 ns; the values decrease to 2.67 ± 0.03 ns for 0.5 Gy irradiation, to 2.65 ± 0.02 ns after 0.1 Gy irradiation and to 2.63 ± 0.02 ns after 1 Gy irradiation. Therefore, the averaged mean lifetime follows a sequence of, control > 0.5 Gy > 0.1 Gy > 1 Gy (Figure 3.9). The ANOVA ($p < 0.05$) test showed a significant difference in the DAPI lifetime after irradiation. Nevertheless, there is no significant difference in the lifetime of DAPI-bound chromosomes between different chosen radiation doses. Interestingly, in the non-heterochromatin region, there is a significant difference between 0.5 Gy and 1 Gy irradiation doses (Figure 3.9) compared to the heterochromatic regions (Figure 3.8).

3.3. FLIM analysis of different time points of X-ray irradiation on the T-cells

Variation in the fluorescence lifetime components was observed between the control (non-irradiated) sample and the X-ray induced chromosomes. The difference in the lifetime values was observed in all 46 DAPI stained metaphase chromosomes (Figure 3.8 and Figure 3.9). The difference in the lifetime components in the metaphase chromosomes was observed after 16 hours of colcemid treatment. To get a maximum number of metaphase chromosomes, choose a 16 hrs colcemid treatment. The treatment was carried out immediately after radiation doses on passage number '4' of the cell cycle.

After obtaining lifetime values of metaphase chromosomes (passage 4) with 16 hrs of X-ray irradiation, T-cells were cultured for another '40 hrs' (passage 5), '64 hrs' (passage 6) and '88 hrs' (passage 6) after X-ray irradiation with low-level doses described below. The time points include the 16 hours of colcemid treatment to obtain irradiated metaphase chromosomes (see Chapter 2, Materials and Methods). The T-cells were X-ray irradiated at a rate of 0.5 Gy/min. The purpose of obtaining irradiated metaphase chromosomes at different time points of X-ray irradiation is to analyse the damage at each time points in the genetic material by measuring the lifetime components of metaphase chromosomes. The change in the lifetime values was observed in 4 μM DAPI stained metaphase chromosomes.

Note that the chromosomes extracted after 88 hrs following X-ray irradiation did not show enough metaphase spreads on the glass slides to perform FLIM and M-FISH. Therefore, the chromosomes obtained. After 88 hrs, of X-ray irradiation were not available for further analysis. It appears after 88 hrs the cells died due to prolonged culture after exposure to ionising radiation and did not reach the metaphase stage of the cell cycle.

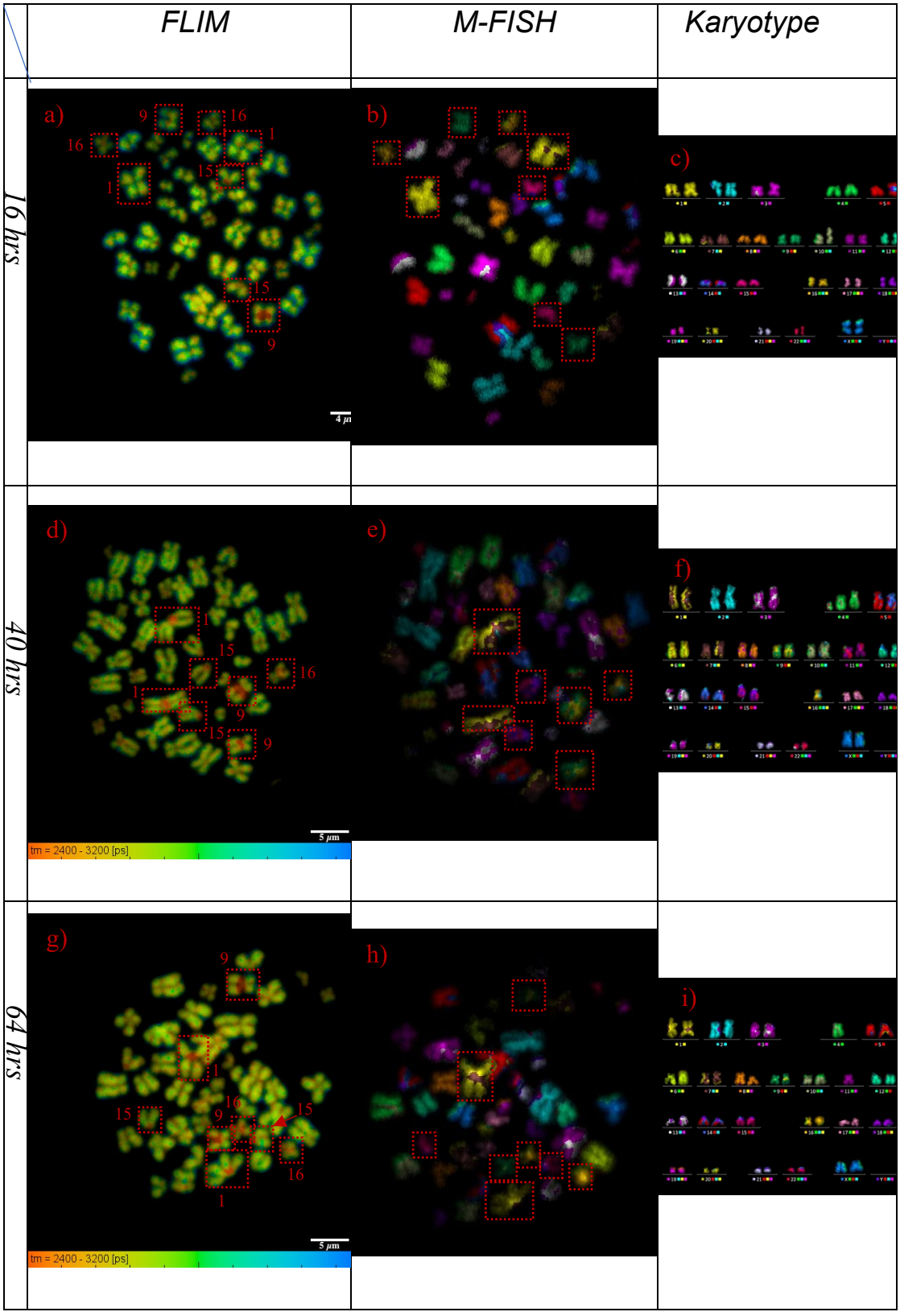

Figure 3.10: X-ray irradiated chromosome spreads from three different passages of the cell culture, irradiated at the rate of 0.5 Gy/min. It represents the DAPI lifetime maps of each spread imaged using FLIM and with their corresponding M-FISH images and karyotypes. The row defines the three different times of point of passage after irradiation, and the column defines the imaging techniques and the karyotype. Figure

a), d), and g) are the FLIM images; b), e) and h) are the M-FISH image of the same spread, respectively, and c), f), and i) are the karyotypes of the same spread obtained from M-FISH spreads. Red boxes denote homologous pairs of chromosomes with a short lifetime at their heterochromatin regions in all three spreads. Maps of DAPI lifetime ranged between 2.4 ns to 3.2 ns. Scale bar for FLIM images is as follow: 4 μm (figure a) and 5 μm (figure d and g), and the image are of size 512 x 512 pixels. Objectives used for FLIM imaging are 60x water and for M-FISH is 63x immersion oil. Though, chromosome 16, one out of two, is wrongly placed on position 4 in the M-FISH karyotype in a 40 hrs- passage row.

FLIM imaging was accomplished on several time points (16 hrs, 40 hrs and 64 hrs) of the cell cycle after irradiation; M-FISH and karyotyping followed this to identify each chromosome. The change in the lifetime components was observed in DAPI-bound chromosomes upon X-ray irradiation at different passages (Figure 3.10). The short lifetime component at the heterochromatin regions and the long lifetime component at the non-heterochromatin of heteromorphic chromosomes were observed (Figure 3.11). Moreover, the varied lifetime components can also be seen in non-heteromorphic chromosomes (Figure 3.10).

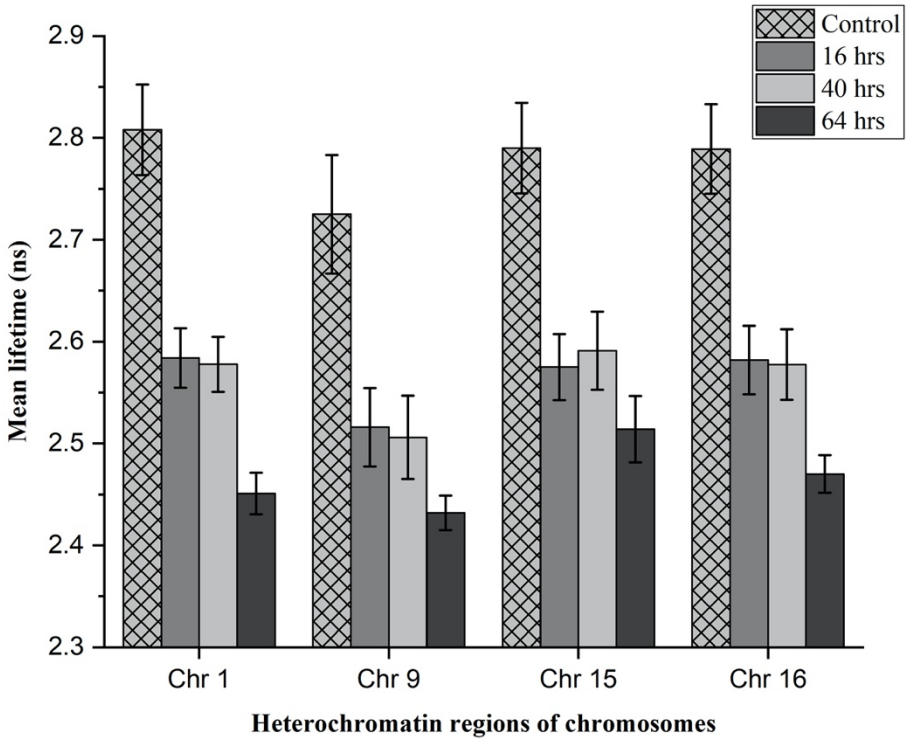

Figure 3.11: Measured mean lifetime of heterochromatin regions of DAPI stained heteromorphic chromosomes (1, 9, 15 and 16) obtained from irradiated T-cells. The cells were X-ray irradiated at a rate of 0.5 Gy/min. The different passages are as follow: 16 hrs, 40 hrs and 64 hrs along with the control sample, number of chromosome spreads (n = 5). Error bar represents the SEM, ANOVA: $p < 0.05$.

In Figure 3.11, the DAPI lifetime decreases in the X-ray induced chromosomes relative to non-irradiated chromosomes. In addition, the DAPI lifetime of heteromorphic chromosomes decreases with the increasing passage number after ionising radiation (Figure 3.11). However, with chromosome 15, there is a slight increase in the lifetime value with 40 hrs of passage compared to the 16 hrs of passage. Figure 3.11 represents the integrated data from five independent chromosome spreads (pooled from two independent experiments).

The averaged mean lifetime for the ‘control sample’ (non-irradiated) is determined to be 2.78 ± 0.05 ns, and then it drops to 2.56 ± 0.03 ns, 2.56 ± 0.04 ns, and 2.47 ± 0.02 ns for 16 hrs, 40 hrs and 64 hrs respectively (Figure 3.11). The ANOVA ($p < 0.05$) test showed a significant difference in the DAPI lifetime

after irradiation in all three-time points of the cell culture. Also, there is a significant difference between time points of 16 hrs to 64 hrs and 40 hrs, to 64 hrs, but there is no significant difference between 16 hrs and 40 hrs. The DAPI lifetime for 16 hrs and 40 hrs was similar but with different SEM values. However, a decrease in the DAPI-lifetime of chromosomes was observed in 64 hrs of passage, but with chromosome 15, there is a slight increase in the lifetime at 48 hrs of passage relative to heteromorphic chromosomes 1, 9, and 16 (Figure 3.11).

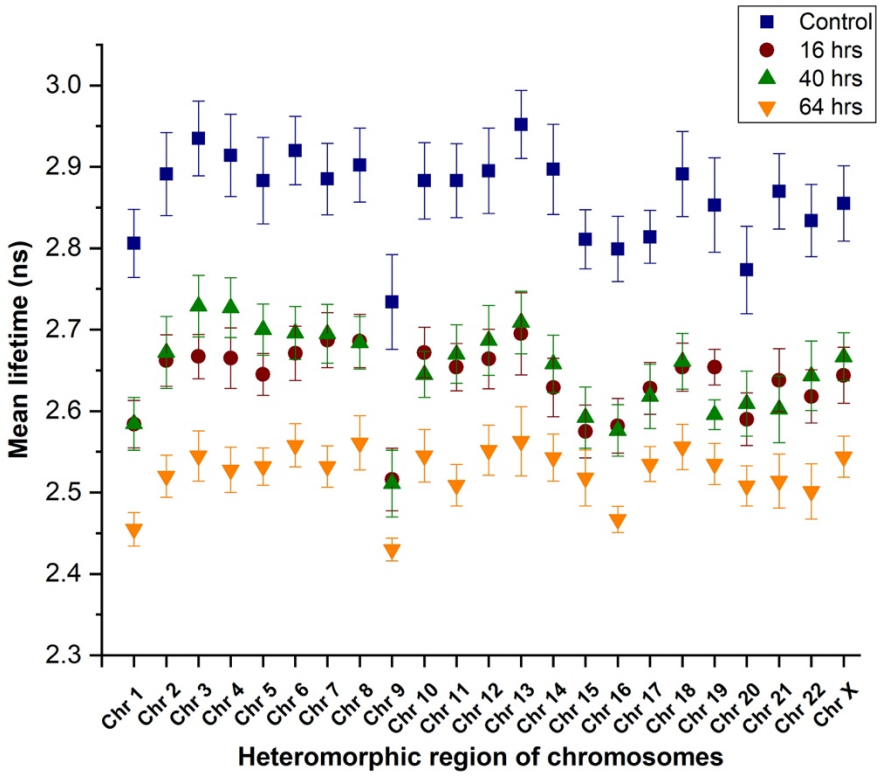

Figure 3.12: Measured mean lifetime of DAPI-bound, heterochromatin regions of all 46 chromosomes obtained from T-lymphocytes at different passages of the cell culture. The number of chromosome spreads (n = 5). Error bar represents SEM, ANOVA: $p < 0.05$.

The DAPI-lifetime of all 46 chromosomes was also measured by focusing only on heterochromatin regions from X-ray induced chromosomes (Figure 3.12); this was done for each passage (i.e., 16 hrs, 40 hrs and 64 hrs) along with the control sample. The data is the average of five different chromosome spreads, pooled from two independent experiments. The DAPI-lifetime of heteromorphic chromosomes diverges significantly and shows a reduced

lifetime compared to non- heteromorphic chromosomes present in the spreads (Figure 3.12). The ANOVA ($p < 0.05$) test showed a significant difference in the DAPI lifetime after irradiation in all three-time points of the cell culture. A significant difference was also obtained between time points of 16 hrs to 64 hrs and 40 hrs to 64 hrs; nonetheless, there is no significant difference between 16 hrs and 40 hrs.

Similarly, the DAPI lifetime of non-heterochromatin regions of the heteromorphic chromosome was also measured (Figure 3.13). The data shown is the average of the same five independent chromosome spreads (pooled from two independent experiments) from which the heterochromatin regions were measured for heteromorphic chromosomes (Figure 3.11) as well as for the DAPI lifetime of all 46 chromosomes (Figure 3.12).

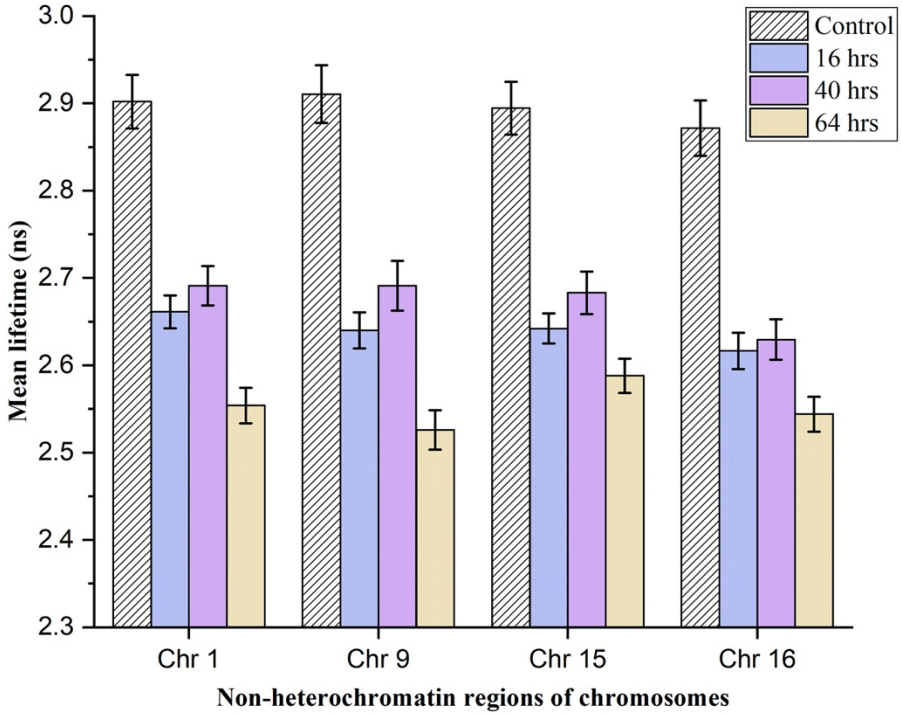

Figure 3.13: Mean lifetime of DAPI-bound DNA in heteromorphic chromosomes. The mean lifetime measurements are from the non-heterochromatin regions of chromosomes (obtained from T-lymphocytes). The cells were irradiated at a rate of 0.5 Gy/min of X-ray. The different passages are 16 hrs, 40 hrs and 64 hrs along with the control sample, number of chromosome spreads (n = 5). Error bar represents the SEM, ANOVA: $p < 0.05$.

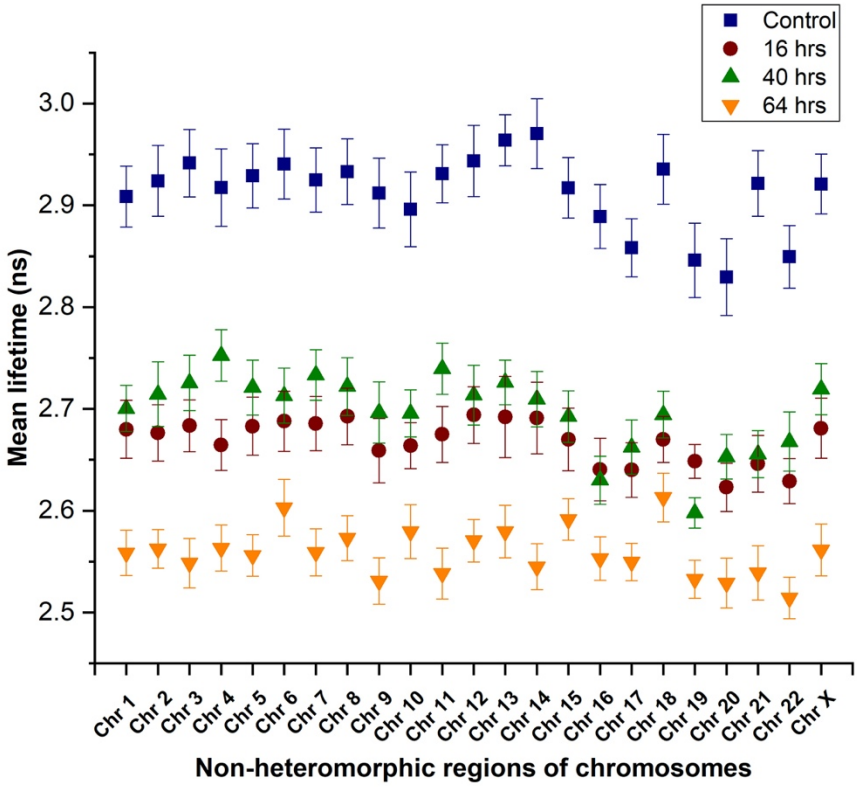

Figure 3.14: Measured mean lifetime of DAPI-bound, non-heterochromatin regions of all 46 chromosomes obtained from T-lymphocytes at three consecutive passages of the cell culture, number of chromosome spreads (n = 5). Error bar represents SEM, ANOVA: $p < 0.05$.

A reduced DAPI lifetime can be seen in X-ray induced heteromorphic chromosomes in both heterochromatin and non-heterochromatin regions (Figure 3.11 and Figure 3.13). The average mean lifetime for the non-heterochromatin region of heteromorphic chromosomes is as follow: 2.89 ± 0.03 ns for the control sample, followed by the 40 hrs passage (2.67 ± 0.02 ns), 16 hrs passage (2.64 ± 0.02 ns) and 64 hrs passage (2.55 ± 0.02 ns) (Figure 3.13).

It was observed that the mean lifetime for non-heterochromatin regions is slightly higher than the heterochromatin regions of heteromorphic chromosomes. The same five independent chromosome spreads have been used to determine the mean DAPI lifetime of non-heterochromatin regions of all 46 metaphase chromosomes (Figure 3.14). The same spreads were used to measure the DAPI lifetime of heterochromatin (Figure 3.11) and non-heterochromatin (Figure 3.13) regions of heteromorphic chromosomes and the

heterochromatin regions of all 46 metaphase chromosomes (Figure 3.12). Therefore, the difference in the DAPI lifetime between two sub-regions can be observed in all 46 metaphase chromosomes. In Figure 3.14, reduced DAPI lifetime can be observed with increasing passages after the irradiation. The chromosomes from the 64 hrs of passage have the lowest lifetime values compared to the chromosomes with 16 hrs and 40 hrs that have similar lifetime values for all 46 chromosomes. Overall, the ANOVA ($p < 0.05$) test showed a significant difference in the DAPI lifetime after irradiation in all three-time points of the cell culture. Also, there is a significant difference between time points of 16 hrs to 64 hrs and 40 hrs to 64 hrs, but there is no significant difference between 16 hrs and 40 hrs irrespective of different sub-regions of the human chromosomes.

3.4. Statistical Analysis

The one-way ANOVA and Tukey test were done using the GraphPad tool to show the significant differences between the DAPI lifetime of chromosomes induced with the different X-ray irradiation doses.

3.5. DAPI lifetime of metaphase chromosomes containing structural aberration

FLIM measurements were also performed on chromosomes containing structural aberrations. Chromosomes with aberrations were isolated from the five independent chromosome spreads (pooled from two independent experiments). Structural chromosomal aberrations were observed in the human metaphase chromosomes (fixed with methanol: acetic acid, 3:1). The chromosomal aberrations occurred due to exposure of T-cells to ionising radiation. The various chromosomal aberrations with different radiation doses are shown in Figure 3.15.

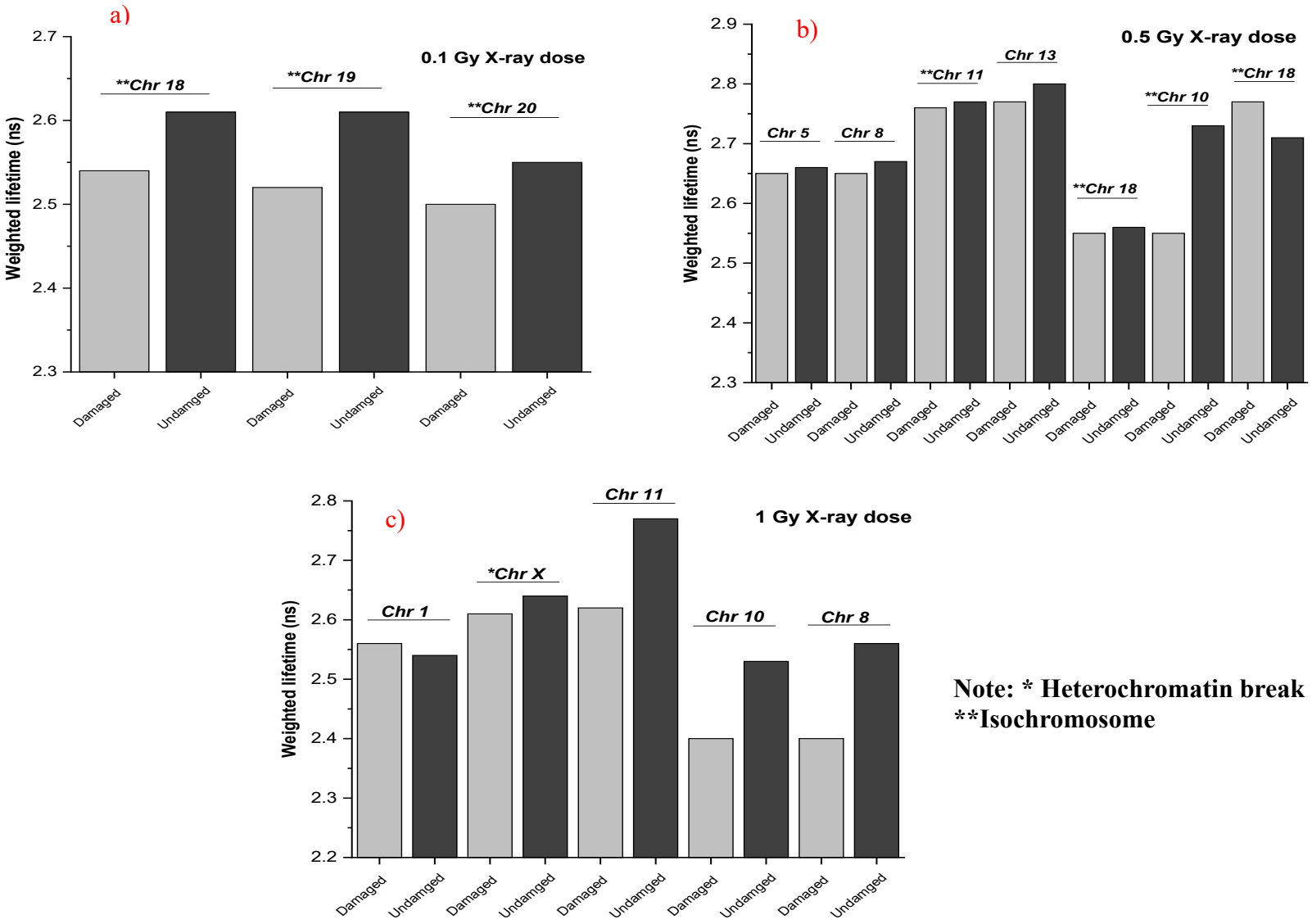

Figure 3.15: Representation of DAPI-lifetime of irradiated fixed human metaphase chromosomes containing structural aberrations upon X-ray irradiation. The bar chart represents the damaged and undamaged chromosomes from the same spread. Aberrations with different radiation doses are 0.1 Gy (a), 0.5 Gy (b) and 1 Gy (c).

Individual chromosomes were analysed from different chromosome spreads induced by different radiation doses (i.e., 0.1 Gy, 0.5 Gy and 1 Gy). The lifetime values show that the damaged chromosomes have a lower lifetime in comparison to the undamaged chromosomes, present in the same or different spread (Figure 3.15). The damaged chromosomes are the chromosomes that contain structural aberration and vice-versa. Fewer aberrations were observed in 0.1 Gy irradiation, and the number of aberrations increases with a higher dose. Interestingly, in this study, 0.5 Gy irradiation showed more structural aberrations than the 1 Gy irradiation (Figure 3.15).

Figure 3.16 suggests that chromosomes 18, 19 and 20 are ‘isochromosomes’ obtained from a single chromosome spread. The following individual chromosomes appeared as structurally detached, separating the p-arm and the q-arm when examined using FLIM and M-FISH techniques (Figure 3.16). The lifetime values represent the averaged mean lifetime of both heterochromatin and non-heterochromatin regions of the damaged and the undamaged parts of a chromosome (Figure 3.15a, 0.1 Gy X-ray dose). For example, the DAPI lifetime of undamaged chromosomes 18 and 19 was determined to be ~2.6 ns, and the damaged chromosomes are ~2.52 ns. However, there was not much difference observed in the DAPI-lifetime for damaged and undamaged chromosome 20 are, ~2.5 ns and ~2.54 ns (Figure 3.15a, 0.1 Gy X-ray dose), respectively.

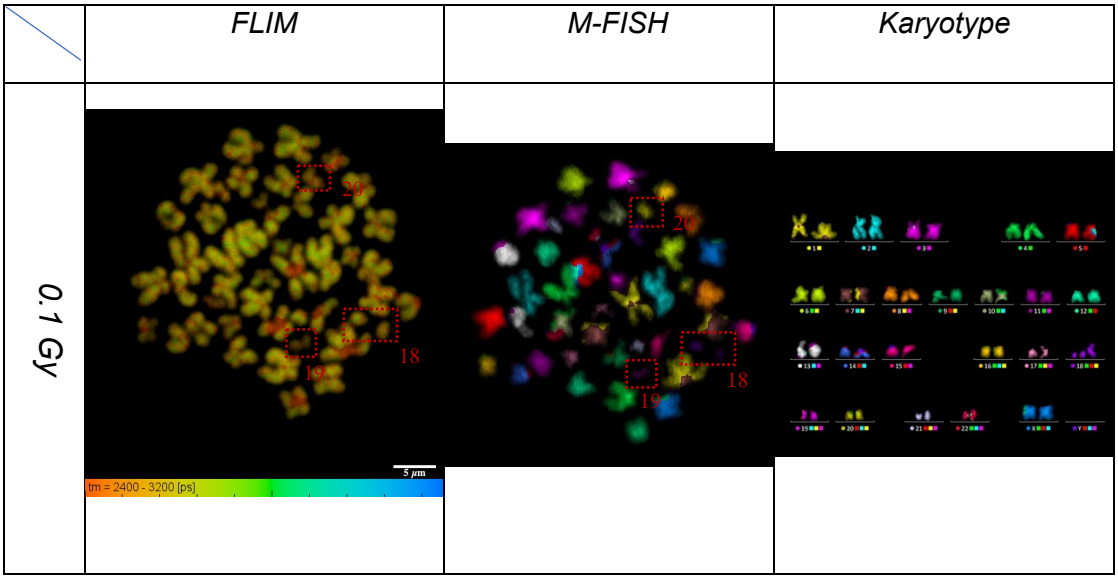

Figure 3.16: Representation of isochromosome aberrations originated from the T-cells exposed to 0.1 Gy X-ray exposure. Red dotted squares show chromosome underwent isochromosome aberrations. Scale bar= 5 µm.

Figure 3.17 shows the DAPI lifetime of structurally damaged chromosomes. The translocation upon aberration was observed between chromosomes 8 and 5 using M-FISH. It appears that the q-arm of chromosome 8 translocated onto the q-arm of chromosome 5 (Figure 3.17). The translocation cannot be seen in the karyotype because it was 'chopped off unknowingly during karyotyping' and placed on position 5 and position 19 in the karyotype (Figure 3.17). The lifetime of translocated q-arm of chromosome 8 and the truncated q-arm of chromosome 5 is 2.65 ns. Similarly, chromosome 13 has undergone a non-heterochromatin break (Figure 3.15b, 0.5 Gy X-ray dose) and the lifetime obtained is 2.8 ns, both for damaged and undamaged chromosomes present in the same spread.

Chromosomes 18, 10 and 18 have undergone isochromosome aberration (all three chromosomes are from three different spreads) (Figure 3.15b, 0.5 Gy X-ray dose). The DAPI lifetime of both the damaged and undamaged chromosomes is shown in Figure 3.15b (0.5 Gy X-ray dose). Unfortunately, a few chromosomes are missing in the M-FISH and the karyotype (Figure 3.17) due to difficulties in rescuing them during the M-FISH hybridisation. However,

FLIM measurements for all 46 chromosomes were obtained before the M-FISH hybridisation.

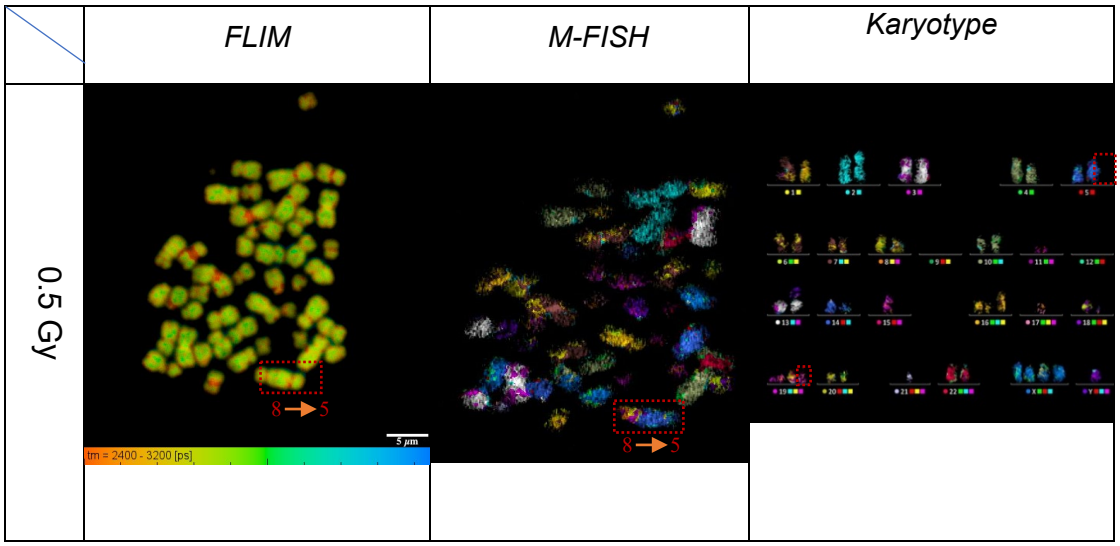

Figure 3.17: Representation of translocation of q-arm of chromosome 8 into the q-arm of chromosome 5 (shown with the red dotted rectangle), observed in both FLIM and M-FISH images. The aberration originated in the T-cells exposed to 0.5 Gy X-ray exposure. Scale bar= 5 µm.

Similarly, certain heterochromatin (chromosome X) and non-heterochromatin breaks, such as chromosome 1 (Figure 3.18) and chromosome 11 (Figure 3.15c), have been found after exposure to 1 Gy irradiation. These three aberrations were found in three different spreads. Also, chromosomes 10 and 8 have been found to be truncated with lost arms, observed in a single spread. A minor difference in the DAPI lifetime can be observed between damaged and undamaged chromosomes in Figure 3.15c (1 Gy X-ray dose).

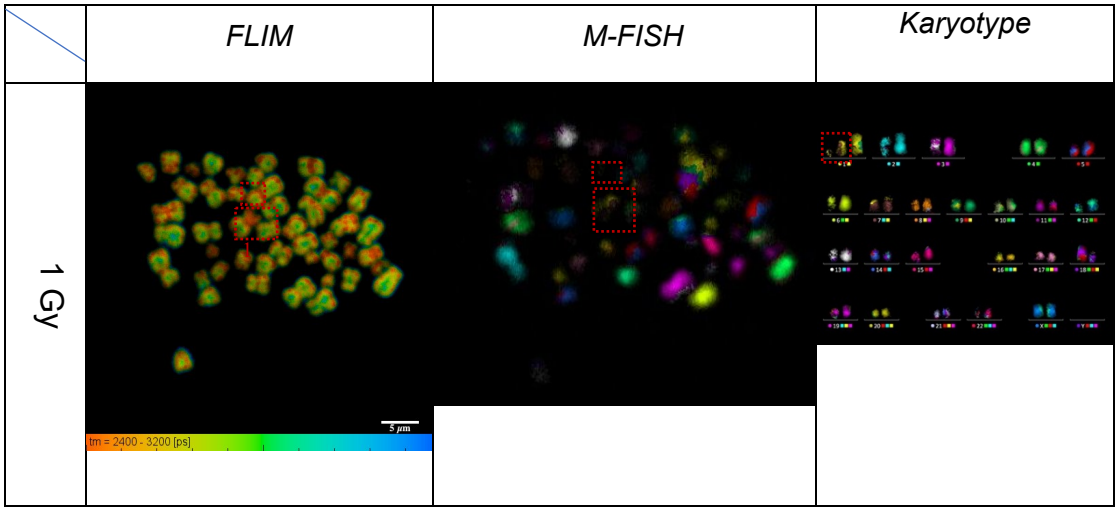

Figure 3.18: Represents the non-heterochromatin break of chromosome 1 and its fragment, shown in FLIM, M-FISH and the karyotype images (with the red dotted rectangles). The aberration originated in the T-cells exposed to 1 Gy X-ray exposure. Scale bar= 5 µm.

Chromosome 18 upon 0.5 Gy exposure and chromosome 1 upon 1 Gy X-ray exposure have shown opposite behaviour compared to the lifetime values of other structurally aberrated chromosomes (Figure 3.15b, c). The DAPI lifetime of damaged chromosomes 18 and 1 has increased compared to the undamaged ones regardless of sub-regions of chromosomes (Figure 3.15b, c). All the DAPI lifetime measurements were done in the methanol: acetic acid (3:1) fixed metaphase chromosome. In addition, the lifetime values are independent of morphology and the category of aberrations that occurred in the chromosomes.

3.6. FLIM on DAPI-bound chromosomes from B-lymphocytes

FLIM analysis was also performed on the B-lymphocytes cells but with a higher passage number, 15. The lifetime measurement was performed to observe the change in lifetime components in the heteromorphic chromosomes obtained from B-lymphocytes at the higher passage number. The FLIM analysis was performed only on the non-irradiated chromosomes stained with 4 µM freshly prepared DAPI. According to Estandarte *et al*. (2016), the short DAPI lifetime component was observed in the heteromorphic chromosomes due to the highly

dense heterochromatin packaging at the pericentric region (Estandarte *et al.*, 2016).

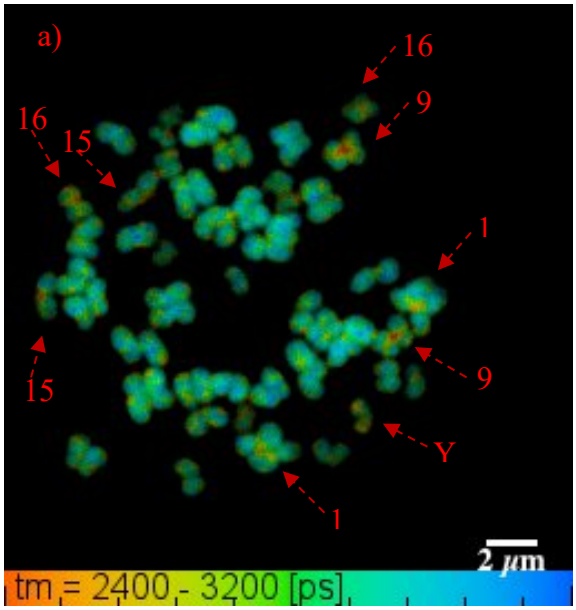

b)

Chromosomes	Mean lifetime (τ_m)
Chr 1	2.81
Chr 9	2.65
Chr 15	2.66
Chr 16	2.73
Chr Y	2.76

Figure 3.19: FLIM imaging performed on the spread obtained from non-irradiated B-lymphocytes. a) Shows the lifetime components of heteromorphic chromosomes, indicated with the red arrows. The lifetime distribution ranged between 2.4 ns to 3.2 ns (mentioned below the FLIM image), scale bar = 2 µm, image size is 256 x 256 pixels and the objective used is 60x water. b) The table shows heteromorphic chromosomes with short DAPI lifetime at the heterochromatin regions along with their SEM values.

In Figure 3.19a, the colour-coded map of the FLIM image shows that each heteromorphic chromosome has a short DAPI lifetime at the heterochromatic regions of the chromosomes. The mean lifetime value displayed in the table (Figure 3.19b) is the averaged mean lifetime of a homologous pair of chromosomes presents in a single spread.

The DAPI lifetime of non-heterochromatin regions was also measured of heteromorphic chromosomes along with the heterochromatin regions to observe the variation in their lifetimes (Figure 3.20). The purpose was to understand the genomic arrangement between two regions by measuring the lifetimes at the pixel level obtained from the colour coded FLIM image of the metaphase chromosome spreads.

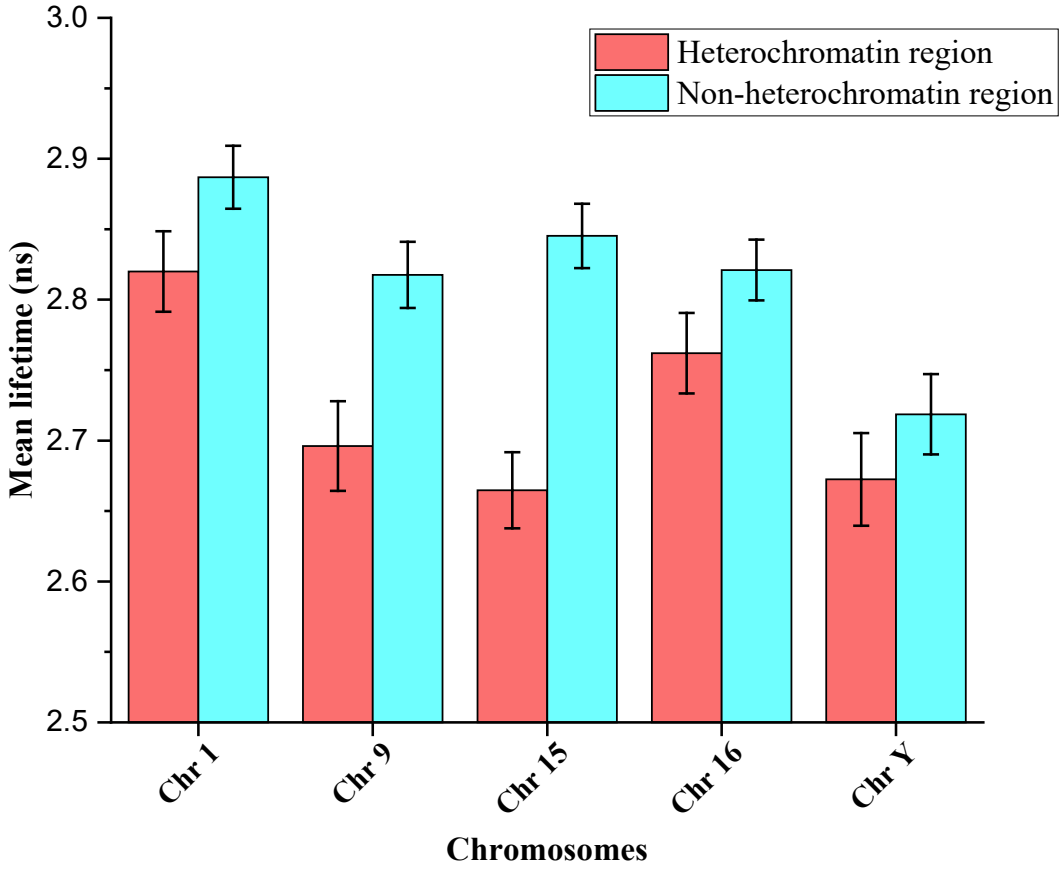

Figure 3.20: Represents the mean lifetime of both heterochromatin and non-heterochromatin regions of chromosomes 1, 9, 15, 16 and Y obtained from non-irradiated B-lymphocytes cells. Number of spreads (n) = 13. The bars represent the SEM values and $p < 0.05$.

Figure 3.20 shows the mean lifetime of heterochromatin and non-heterochromatin regions of chromosomes obtained from B-lymphocytes. The lifetime values are pooled from 13 independent chromosome spreads. It can be observed from Figure 3.20 that the heterochromatin regions of heteromorphic chromosomes have a shorter lifetime relative to the non-heterochromatin regions of chromosomes. The averaged lifetime of the heterochromatin region is determined to be 2.72 ± 0.03 ns, and the non-heterochromatin region is 2.82 ± 0.02 ns. It was observed that the averaged DAPI lifetime for both the heterochromatic and non-heterochromatic regions of the chromosomes, in the case of B-cells, has a slightly reduced lifetime compared to the T-cells.

On the other hand, the averaged (lifetime values pooled from 5 independent chromosome spreads) mean lifetime of the heterochromatin regions of heteromorphic chromosomes obtained from T-lymphocytes is determined to be 2.8 ± 0.03 ns (Figure 3.5) and for the non-heterochromatin region is 2.88 ± 0.02 ns (Figure 3.7).

3.7. DAPI lifetime of DNA oligomers

Previous sections focused on FLIM studies on the high order structure of irradiated and non-irradiated mitotic chromosomes obtained from T-lymphocytes. In this section, the DAPI lifetime of naked DNA is evaluated to observe the variation of DAPI lifetime caused by the varying DNA base sequences. Seven different oligomers of 20 mM concentration (stock) in solution (each containing 10 bases of DNA) were studied. Each oligomer in the solution were stained with 4 μM freshly prepared DAPI for lifetime analysis.

The mean lifetime values were obtained for each oligomer (Figure 3.21a). Each mean lifetime value is an average of six different lifetime values taken on the same glass slide but with different laser power. The lifetime value for 100% AT-rich oligomers has a longer single lifetime component. Therefore, for TTA-AAT-TTT-T is 3.99 ns and for AAA-TAT-ATA-A is 3.74 ns, compared to 100% GC-rich oligomers. The oligomers CGG-CGG-CGG-C and GCC-GCC-GCC-G has a mean lifetime value that contains two lifetime components, for example t1 = 0.89 ns, t2 = 5.37 ns and t1 = 0.96 ns, t2 = 3.68 ns respectively (Figure 3.21a). In addition, both the 100% GC-rich oligomers contain two amplitude components that are distributed as a1 = 76% and a2 = 24% (Figure 3.21b). Though 40% GC content produced a single lifetime component (t1 = 3.49 ns) and has a single amplitude component (a1 = 100%). However, 60% GC (AAC-CCG-GGT-A) content gave two lifetime components (t1 = 0.41 ns, t2 = 3.89) (Figure 3.21a) along with two amplitude components that are distributed as a1= 97% and a2= 3% (Figure 3.21b).

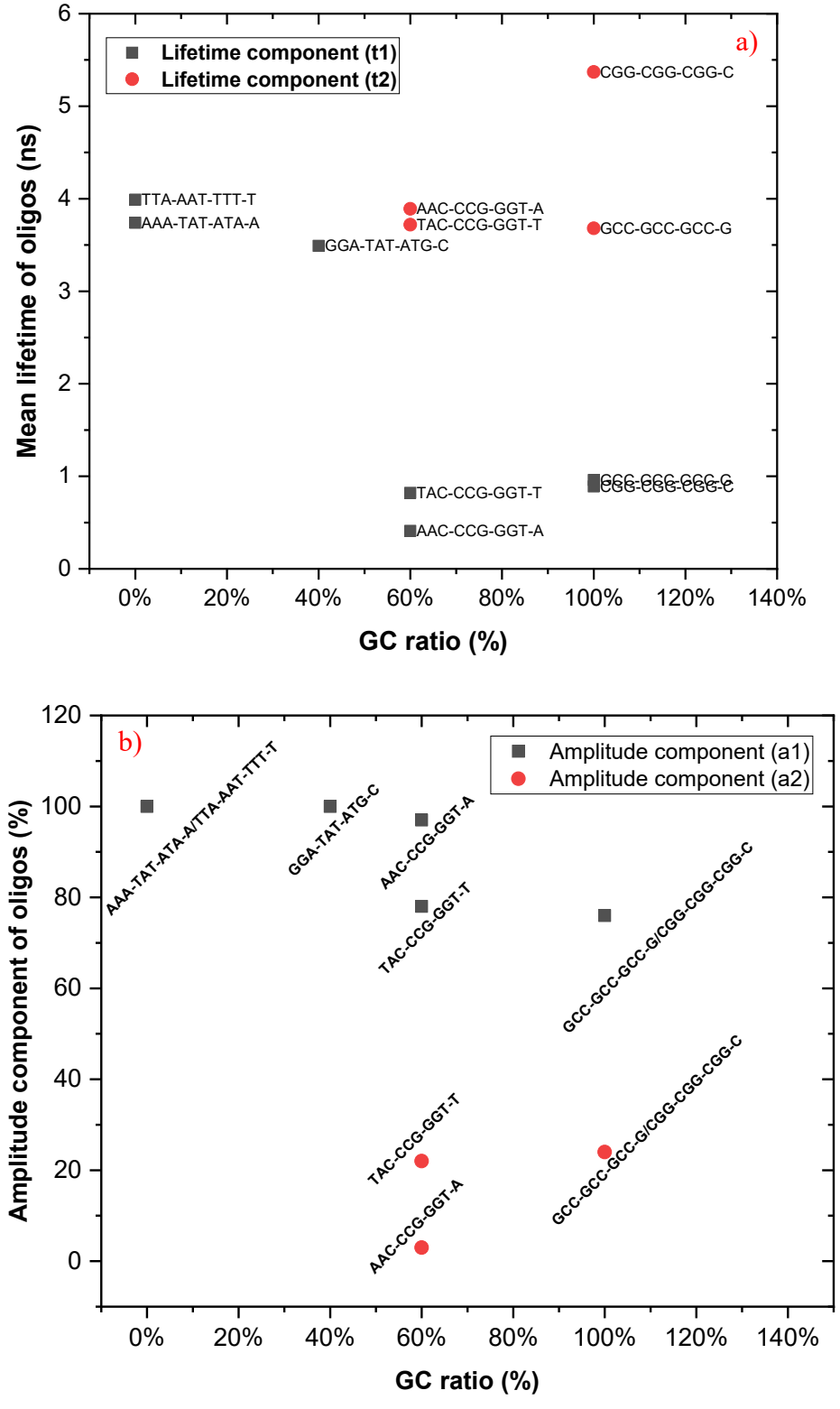

Figure 3.21: FLIM measurement of 4 µM DAPI labelled DNA oligomers, a) Representing the mean lifetime values *versus* % of GC ratio present in the oligomers. With 0% to 40% content of GC, the oligomers show single lifetime component (black squares) and above 60% of GC shows two lifetime components (1st-black boxes and 2nd-red circles). b) Amplitude component was also measured of those seven oligomers.

3.8. Discussion

Chromatin compaction is an essential entity for genomic stability as the chromatin architecture protects the DNA from both endogenous and exogenous events such as radiation damage. This chapter aims to understand the change in the DAPI lifetime after X-ray irradiation using the nanosecond excited-state lifetime imaging methods. This technique was applied along the length of the chromosomes obtained from T- and B-cells. The effect of ionising radiation was studied on both the heterochromatin and non-heterochromatin regions of the chromosomes as described above (Chapter 3). Moreover, the DAPI lifetime changes were also measured to evaluate the chromosomal aberrations occurring at different cell culture passages following ionising radiation. These studies were carried out using the FLIM technique followed by M-FISH to identify each chromosome in the spread.

The combined techniques of laser scanning confocal microscopy and multiphoton microscopy have been previously used to study the compaction (Estandarte *et al.*, 2016) and the condensation state of chromatin during mitotic cell division (Phengchat *et al.*, 2016). Our initial results reveal the DAPI lifetime variation at the heterochromatin regions of heteromorphic chromosomes from T and B-cells (Figure 3.2 and Figure 3.19). Following these observations from the heteromorphic chromosomes, FLIM and M-FISH techniques were combined to study the variation in the DAPI lifetime along the length of all 46 chromosomes obtained from B and T-cells upon ionising radiation. Short and long lifetime components along the length of the chromosomes appear similar to the G/R chromosome banding based on the base pair composition of GC (light/dark) and AT (dark/light) (Hozier, Furcht and Wendelshafer-grabb, 1981) (Shaw, 1973). Lifetime measurement along the length of the chromosomes contributes to the short (GC-rich) and long (AT-rich) lifetime components (Figure 3.21).

The heteromorphic chromosomes 1, 9, 15 and 16 consist of a large block of constitutive heterochromatin at the pericentromeric region of the chromosomes compared to the other non-heteromorphic chromosomes,

present in the human genome. The pericentromeric heterochromatin regions show reduced DAPI lifetime compared to non-heteromorphic chromosomes, possibly due to protonated DAPI (Barcellona and Gratton, 1989). The compact nature of the constitutive heterochromatin (Arrighi and Hsu, 1971) (Sahin *et al.*, 2008) may lead to a decrease in the degree of interaction between the indole group of the DAPI and the minor grooves of the DNA (Barcellona and Gratton, 1990). Consequently, the DAPI fluorophores are exposed to solvent leading to proton transfer (Barcellona, Cardiel and Gratton, 1990) (Mazzini *et al.*, 1992). Eventually, proton transfer leads to a short DAPI lifetime. On the other hand, unprotonated DAPI that interacts with the least compact regions of chromosomes leads to a long DAPI lifetime (Barcellona, Cardiel and Gratton, 1990). Therefore, a short DAPI lifetime at the pericentromeric heterochromatin of heteromorphic chromosomes may be due to the protonated DAPI and a long lifetime probably due to the unprotonated DAPI (Barcellona and Gratton, 1989) (Barcellona and Gratton, 1990) observed along the length of the chromosomes.

It has been shown that the compact pericentromeric heterochromatin region of heteromorphic chromosomes shows a shorter DAPI lifetime compared to non-heteromorphic chromosomes. Also, it has been shown that the least compact, non-heterochromatin region of chromosomes shows a long DAPI lifetime, irrespective of the cell type. We can hypothesise that the heteromorphic chromosomes have conserved pericentromeric heterochromatin regions in different cell types but may differ in heteromorphic variants present in each chromosome (Tagarro, Fernández-Peralta and González-Aguilera, 1994) (Estandarte *et al.*, 2016). Moreover, each heteromorphic chromosome has conserved heterochromatin regions, even in the cancerous cells such as HeLa cells that show a short DAPI lifetime (Estandarte *et al.*, 2016).

According to Pita et al., the pericentromeric region of human chromosome 9 incorporates a repeated sequence of satellite III DNA, which is considered to be an evolutionary fragment derived from the gorilla genome whose functional role remains unclear (Pita et al., 2010). In our finding, it is observed that chromosome 9 has the lowest DAPI lifetime compared to other heteromorphic chromosomes along the length of the chromosomes (Figure 3.5), and it could

be because of its highly polymorphic variants at the pericentromeric heterochromatin regions (Humphray et al., 2004) (Madon, Athalye and Parikh, 2005). Various speculative studies reported data on damaged heteromorphic chromosome 9 that can lead to infertility and miscarriages (Madon, Athalye and Parikh, 2005) (Sahin et al., 2008). The human sex chromosome Y is thought to have evolved from the primates like chimpanzees (Charlesworth, 2003). It is a hypothesis that the existence of the Y chromosome is disappearing due to the decay of the euchromatin genes into heterochromatin genes with the passing years (Charlesworth and Charlesworth, 2000). The heterochromatin block of the Y chromosome is almost 40 Mb long (Bachtrog, 2014). In addition, a report suggests that the variants of chromosome 16 lead to body dysmorphic features observed in a four-year-old child (Tadao ARINAM, 1988).

Heteromorphic chromosomes 9, 15 and a portion of chromosome 1 consist of DNA satellite III, showing reduced DAPI lifetime compared to chromosome 16, which consists of DNA satellite II (Figure 3.3) (Tagarro, Fernández-Peralta and González-Aguilera, 1994). It is assumed that the reduced lifetime of DNA satellite III maybe because of the arrangement of base-pairs GGAAT tandem repeats sequence and the photophysics of satellite III and unprotected interaction of DAPI. Constitutive heterochromatin of heteromorphic chromosomes is inheritable and preserved (Allshire and Madhani, 2018). However, the molecular mechanism behind the lifetime variation at the pericentromeric region of heteromorphic chromosomes is certainly unclear.

There are few examples in the literature which report short lifetimes for the compact architecture of chromatin and long lifetimes for least compact regions. Global compaction and decompaction in Hoechst 34580 stained chromatin were observed due to hyperosmolarity and histone deacetylase, respectively (Abdollahi, Taucher-Scholz and Jakob, 2018). Also, reduced lifetime was observed in differentiating cells due to compaction though some decompaction regions were also observed, which probably represents transcription repositories in a fixed cell; on the other hand, increased lifetime was observed in stem cells due to decompaction and the cells were stained with SiR-DNA stain (Hockings *et al.*, 2020). It can be determined that the DNA stains show

variation in lifetimes due to labelled chromosomes conformation. The measuring fluorescence lifetime of DAPI stained chromosomes represents a method for understanding chromatin compaction state along the length of fixed metaphase chromosomes. In further investigation, we hope to investigate whether pericentromeric heterochromatin of heteromorphic chromosomes are conserved following DNA damage by low-level ionising radiation also whether chromosomal aberrations are picked up during FLIM imaging.

3.8.1. Effects of post-irradiation on chromosomal substructures

The difference in the DAPI lifetime of heterochromatin and non-heterochromatin regions along the length of the chromosomes has been measured in non-irradiated samples, as described in the previous section of this chapter. After exposure to ionising radiation at low-level radiation doses, the DAPI lifetime variation of the pericentromeric heterochromatin of heteromorphic chromosomes was also explored.

DAPI-lifetime variations were measured along the length of all 46 chromosomes, including heteromorphic chromosomes, after exposure to X-ray irradiation (Figure 3.5, Figure 3.7, Figure 3.8, and Figure 3.9). The DAPI lifetime measurements were performed after 16 hrs of irradiation on fixed metaphase chromosomes. The lifetime values were pooled from five independent chromosome spreads of the same preparation. The differences in the DAPI lifetime measured between non-irradiated and irradiated chromosomes are as follows: ~270 picoseconds (ps) for 0.1 Gy dose, ~260 ps for 0.5 Gy dose and ~290 ps for 1 Gy irradiation. The trend suggests that the chromosomes induced with a 0.5 Gy dose have a slightly shorter DAPI-lifetime along the length of the chromosomes. The reduced lifetime values observed with low-level doses below ~1 Gy determined show that the chromosomes have perturbed after irradiation. Nevertheless, the pericentromeric heterochromatin of heteromorphic chromosomes remains conserved upon exposure to low-level irradiation in all three doses. The perturbed chromosomes are thought to

undergo structural conformation to become more compact along the length of the chromosomes and protect the genetic material from aberrations.

FLIM was used to explore the molecular environment change in the X-ray induced chromosomes. The information on the environmental change of DAPI fluorescence on a nanosecond time scale can be acquired by the fluorescence lifetime decay map (Suhling *et al.*, 2015). Chromosomes 1q, 9q, 15q and 17q irradiated using ^{60}Co radiation showed more number of translocations at 0.5 Gy than at 1 Gy (Lin, Wu and Lee, 2019). The non-heterochromatin regions of the following chromosomes in the human genome are more sensitive to ionising radiation, which leads to translocation. Therefore, this work aims to study the lifetime variation of the chromosomes that sustain inter or intra chromosomal aberrations upon low-level radiation doses.

This study showed the averaged DAPI lifetimes for non-heterochromatin regions of all 46 X-ray induced chromosomes (pooled from five independent chromosome spreads). The non-heterochromatin of chromosome 17 along with chromosomes 1, 9, 15, and 16 (Figure 3.9) showed a reduced lifetime, but the lifetime change was not observed at the heterochromatic region of chromosome 17. This could be because the chromosome 17 does not have a large block of pericentromeric heterochromatin and might be deficient in tandem repeats of GGAAT oligonucleotide like heteromorphic chromosomes. The averaged mean lifetime differences between non-irradiated and irradiated chromosomes are as follow ~280 ps for 0.1 Gy, ~260 ps for 0.5 Gy and ~300 ps for 1Gy in the case of non-heterochromatin regions. The following lifetime difference suggests that the chromosomes induced with a 1 Gy dose have the shortest DAPI-lifetime along the length of the chromosomes. Therefore, the ionising radiation treatment has an almost similar effect all over the length of chromosomes, irrespective of different regions of chromosomes.

The one-way ANOVA test showed a significant difference after irradiation but there is no significant difference between different chosen radiation doses. Nevertheless, a significant difference between 0.5 Gy and 1 Gy can be observed in the non-heterochromatin regions (Figure 3.7 and Figure 3.9) but

not in the heterochromatin regions of all 46 chromosomes (Figure 3.5 and Figure 3.8). This suggests that the non-heterochromatin regions are more vulnerable to ionising radiation than the heterochromatin regions of the chromosomes (Lin, Wu and Lee, 2019). In the case of heteromorphic chromosomes, the lifetime values of X-ray induced chromosomes obtained follow a sequence of; control>1 Gy>0.1 Gy>0.5 Gy. On the other hand, in case of all 46 chromosomes follow a sequence of: control > 0.5 Gy > 0.1 Gy > 1 Gy. This suggests that the different chromosomes may have different sensitivity to the ionising irradiation at 0.5 Gy (Lin, Wu and Lee, 2019).

Moreover, chromosomes 1, 9, 15, and 17 are possibly more sensitive to translocations at 0.5 Gy irradiation (Lin, Wu and Lee, 2019). The heteromorphic chromosomes (Figure 3.5 and Figure 3.7) show the shortest DAPI lifetime, although this was not the case for chromosome 17. However, when considering all 46 chromosomes, the 1 Gy dose shows the shortest DAPI lifetime (Figure 3.8 and Figure 3.9). This could be because the non-heteromorphic chromosomes like 2, 11, 16, 17 and 19 are more sensitive to 1 Gy dose (Lee *et al.*, 2014).

Some studies suggest DNA content and the size of each chromosome in the genome may be dose-dependent upon irradiation (Cigarrán *et al.*, 1998) (Cho *et al.*, 2015) (Lin, Wu and Lee, 2019). Therefore, the DAPI lifetime values variation at different doses may be indicative of this. So, in the case of heteromorphic chromosomes, X-ray induced at 0.5 Gy showed the shortest lifetime values. On the other hand, in the case of all 46 chromosomes, it was observed that the 1 Gy X-ray induced chromosomes showed the shortest DAPI lifetime values among other chosen doses.

According to the literature, DNA is damaged even at low-level radiation doses, ranges from 1 mGy to 0.5 Gy (Shimura and Kojima, 2018). A chromosomal aberration at 0.5 Gy irradiation can cause 8.0 ± 5.4 DSB, and with 1 Gy irradiation causes 38 ± 2.2 DSB (Schröder *et al.*, 2019) (S. W. Botchway *et al.*, 1997). With continuous exposure to γ-irradiation at the rate of 6-20 mGy/h for 7 days, instigated DNA damage and loss of histone proteins up to 40 % were

noticed (Lowe *et al.*, 2020). Core histone proteins such as H2A, H2A.Z, H2B, H3, H4 and linker histone H1 were reduced on chronic irradiation at 20 mGy/h whilst a reduced number of H2AX histone were also observed (Lowe *et al.*, 2020). This suggests that the reduced lifetime values of DAPI-bound chromosomes obtained after low-level irradiation may be due in part to altered associated chromosomal proteins.

The DAPI lifetime reduces in the X-ray induced chromosomes by around 26% to 30%. This suggests that both heterochromatin and non-heterochromatin regions of the chromosomes probably undergo chemical perturbation upon low-level ionising radiation. However, it is assumed that the regions involved probably become more compact to protect genetic material upon irradiation, as evidenced up by the FLIM technique. It was also observed that the effect of ionising radiation is directly proportional to the amount of radiation doses adsorbed about above 0.1 Gy (Pollycove and Feinendegen, 2001) (Feinendegen, Pollycove and Neumann, 2007). Although, there is a possibility of radiation hormesis after exposure to low-level doses, especially with 0.1 Gy (Feinendegen and Neumann, 2005) (Bolus, 2017). Hormesis is an “adaptive process” that occurs at low-level stress to protect the cells/genetic material from upcoming severe stress (Arumugam *et al.*, 2006). The reduced lifetime of DAPI-bound chromosomes observed at different doses probably undergoes hormesis. Hormesis usually changes gene expression and includes processes like DNA damage prevention, DNA repair, apoptosis and immune response (Feinendegen and Neumann, 2005) (Lin, Wu and Lee, 2019). The 1 Gy dose alters some of the gene expressions (Lin, Wu and Lee, 2019). However, with a 0.5 Gy dose, the change in the gene expression is very low compared to 1 Gy (Lee *et al.*, 2014).

Irradiation is known to cause several significant structural (Anderson *et al.*, 2006) and numerical (Cho *et al.*, 2015) chromosomal aberrations depending on the dose (Lin, Wu and Lee, 2019) and the dose rate (Nair *et al.*, 2019) in the live cells. DNA double-strand breakage, gene sequence rearrangements and recombination are the major aberrations at the initial stage (Pfeiffer, Goedecke and Obe, 2000), which continue to chromosomal aberrations in future cell

generations (Aparicio, Baer and Gautier, 2015). The aberrations range from point mutations to a missing set of homologous chromosomes, leading to lethal and non-lethal diseases, including cancer (Gospodinov and Herceg, 2013) (Durante and Formenti, 2018). Upon low-level irradiation doses, mild stresses that occur in nucleic acid/cells/organisms are oxidative, thermal, and metabolic stress (Arumugam *et al.*, 2006). 0.5 Gy dose of ^{60}Co irradiation mostly affects the nucleotide metabolism, whereas the 1 Gy dose of ^{60}Co irradiation mainly affects the immune system and the programmed cell death pathway (Lee *et al.*, 2014)

Our results show that the low dose ionising radiation about below 1 Gy induced chromosomes abnormalities in line with other studies. With perturbation characteristics after exposure between 0.1 Gy to 1 Gy are: nucleoplasmic bridges (NPBs), protein cross-links, and damaged protein-protein interactions also affects the protein expressions (Schröder *et al.*, 2019) (Shimura and Kojima, 2018). Although, according to (Schröder *et al.*, 2019), neither cytotoxic nor genotoxic effects were observed below 0.1 Gy radiation doses. Instead, it enhances the proliferation rate of the “Adipose-Derived Stem Cells” (ADSCs) (Schröder *et al.*, 2019). Cell proliferation characteristic below 0.1 Gy has an implication in the improvement of the radiotherapy (Liang *et al.*, 2016). Hence it is assumed that low dose irradiation leads to complex effects in cells and particularly the DNA.

3.8.2. Cell arrest upon irradiation-induced chromatin conformation changes

Exposure to X-rays affects the DNA and the chromosomes and causes aberrations: from point mutation to loss of the chromosomes, and influences the karyotypic instability (Shimura and Kojima, 2018). The effect of ionising radiation after 16 hrs of irradiation has been shown (Figure 3.5, Figure 3.7, Figure 3.8 and Figure 3.9). Following this, the effect of radiation on the metaphase chromosomes whose cells were cultured for 40 hrs, 64 hrs, and 88 hrs of time points was elucidated after the irradiation dose (Figure 3.11, Figure

3.12, Figure 3.13 and Figure 3.14). The fluorescence lifetime distribution of DAPI-bound chromosomes was measured for 40 and 64 hrs but not for the metaphase chromosomes obtained after 88 hrs of passage time point. With 88 hrs of time point, insufficient chromosome numbers were found in the spreads, and a maximum number of dead cells were observed in the preparation. It was noticed that the DAPI lifetime at 64 hrs is significantly decreased. Indicating the presence of irradiation effects even after 64 hrs of the cell culture. Therefore, our results indicate that the low dose ionising radiation may perturb the DNA, possibly through free reactive radicals, (Park *et al.*, 2013). However, direct radiation damage to the bases is not ruled out.

Moreover, according to Schröder et al., ADSCs cells proliferate after 24 and 48 hrs of irradiation at low ionising radiation (Schröder et al., 2019). In this work, no structural aberrations have been observed at 40 and 64 hrs of the time point. Despite this, a major DAPI lifetime change along the length of the chromosomes was observed at 64 hrs of time point (Figure 3.11 and Figure 3.13). According to Zhang et al., (2015), between 30 min - 6 hrs of post-irradiation, the heterochromatic regions decondenses to repair the damaged DNA and after 24 hrs of post-irradiation, the heterochromatin region again recondenses (Zhang et al., 2015). The obtained recondensation level was close to the non-irradiated heterochromatic regions. On the other hand, the euchromatin regions condense initially after irradiation, and after 24 hrs, euchromatin decondensed that is close to the non-irradiated euchromatic regions (Zhang et al., 2015). Our hypothesis is that the metaphase chromosomes analysed at 40 hrs and 64 hrs of post-irradiation have become more compact, leading to the reduced DAPI lifetime.

More chromosomal aberrations occurred in the case of the 16 hrs of passage time point after exposure compared to 40 and 64 hrs of the time point when considering structural aberration (Figure 3.15, 0.5 Gy X-ray dose). Consequently, the effect of chemical or structural disruptions in DNA/chromosomes can be assumed from the obtained DAPI lifetime at the 64 hrs of the time point upon exposure to low dose ionising radiation. As stated above, FLIM is highly sensitive to the changes that occur in the molecular

environment leading to the fluorescence decay maps (Suhling *et al.*, 2015) (Estandarte *et al.*, 2016).

Chemical disruptions such as the breakage of covalent bonds occur when chromosomes are struck by a high energy wave or particles (Cannan and Pederson, 2016). It may break into DNA fragments (Newman *et al.*, 1997) and can lead to the deleterious event (Reisz *et al.*, 2014). Even if the chromosome manages to remain intact, an individual gene along its length may be badly damaged, and a mutation may be produced in the local chromatin (Reisz *et al.*, 2014) (Sanders *et al.*, 2019) (Lin, Wu and Lee, 2019). In this work, a minimal number of chromosomal aberrations were observed at a selected low dose of radiation. Also, observed intact metaphase chromosomes but with a reduced DAPI lifetime upon X-ray exposure. This may mean that the chromosomes exposed to low dose radiation may have undergone mutation in the local regions of chromatin.

With higher doses, such as 4 Gy of γ-rays radiation, chromosomal aberrations like dicentric, acrocentric and telomeric deletions are produced (Kaddour *et al.*, 2017). The dicentrics decrease with every successive cell division, whereas, telomeric deletions increase with progressive cell division (Kaddour *et al.*, 2017). According to Truong *et al.*, in fibroblast cells, at low X-ray radiation (0.5 mGy) doses, the damaged DNA goes to a halt state immediately after radiation exposure, possibly to repair the damaged DNA and reduce the prolonged effects of radiation in further cell growth (Truong *et al.*, 2018).

In this chapter, it has been described how both the sub-structures (heterochromatin and non-heterochromatin regions) of the chromosome after 64 hrs of post-irradiation lead to a reduction in the fluorescence decay of DAPI-bound chromosomes relative to the non-irradiated chromosome (Figure 3.11, Figure 3.12, Figure 3.13 and Figure 3.14). The difference in DAPI lifetime is determined to be ~310 ps and ~340 ps for heterochromatin and non-heterochromatin, respectively. Though the structural aberration was not observed in the different passages of the cell culture, possibly some

chemical/structural changes might persist in the X-ray induced chromosome, which gives a reduced DAPI lifetime. Moreover, it has been observed in the human lymphocytes that radiation using either a high dose rate (HDR) or low-dose rate (LDR) the repair mechanism starts within 30 mins of post-irradiation to repair the damaged DNA (Nair *et al.*, 2019). The mechanism repairs DSBs up to 40 % within 24 hrs of post-irradiation, which is observed with reduced *γ*-H2AX foci as a marker (Nair *et al.*, 2019). As a result, the chromosomes extracted at 64 hrs of post-irradiation were repaired using DNA repair machinery but underwent a more compact conformational change. Consequently, DAPI-bound chromosomes showed a shorter lifetime compared to 16 and 40 hrs of post-irradiation.

3.8.3. FLIM measurement of chromosomal structural abnormalities of T-lymphocytes

FLIM has been used to characterise further the DAPI-bound chromosomes containing structural abnormalities such as translocation, isochromosomes, and heterochromatin and non-heterochromatin breaks (Figure 3.15). It is known that the chromosomes irradiation with low doses of X-ray (0.5 Gy) is liable to suffer from random molecular and structural aberrations such as DSBs, SSBs, base lesions, deletions, translocations and many more (Shimura and Kojima, 2018). The following aberrations lead to diseases and cell deaths (Lomax, Folkes and Neill, 2013). The number of DSBs increases in DNA with the increasing doses in both the case of HDR and LDR (Nair *et al.*, 2019). At 0.1 Gy, chromosomes protect themselves from further higher radiation doses by gene expression modification, introducing Reactive Oxygen Species (ROS) scavengers, DNA repair mechanism and immune response (Feinendegen, Pollycove and Neumann, 2007). On the other hand, apoptosis increases after a >0.5 Gy irradiation dose (Feinendegen and Neumann, 2005) (Feinendegen, Pollycove and Neumann, 2007). This agrees with our observation of greater number of structural chromosomal aberrations with above >0.5 Gy. Also, a slightly reduced DAPI lifetime in aberrated chromosomes was observed compared to the non-

irradiated chromosome (Figure 3.15). Perhaps, some chemical/structural conformational events might have occurred after damage.

Inter and intra-chromosomal aberrations were observed in X-ray induced chromosomes at low radiation doses (i.e., 0.1 Gy, 0.5 Gy and 1 Gy) using the FLIM technique. The aberrations were observed in all 46 fixed human metaphase chromosomes obtained from a single chromosome spread. The purpose of this study was to measure the variation in the DAPI lifetime of structurally aberrated chromosomes that occurred randomly upon excitation with low ionising radiation. In this work, upon low-level irradiation, a large amount of structural chromosomal aberrations was observed in metaphase chromosomes extracted, 16 hrs of post-irradiation (Figure 3.15). Comparatively, in the metaphase chromosomes with the passage time point of 40 and 64 hrs of post-irradiation. This could be because the stress-response mechanism is activated (El-Saghire *et al.*, 2013) and repairs the damaged cells within 24 to 48 hrs of post-irradiation (Schröder *et al.*, 2019).

Nevertheless, a reduced DAPI lifetime was observed with an increasing passage time point upon irradiation (Figure 3.11, Figure 3.12, Figure 3.13 and Figure 3.14). This could be because prolonged cultured, irradiated cell repairs the damaged DNA. Most likely, the repaired chromosomes become more compact to protect the genetic material from further damage. Consequently, the compacted chromosomes show a reduced DAPI lifetime.

Typically, chromosomal aberrations are randomly produced upon exposure to ionising radiation (Reisz et al., 2014) (Shimura and Kojima, 2018). For example, in this work, structural aberrations upon low-dose irradiation were isochromosomes in chromosomes 18, 19 and 20 from the single chromosome spread (Figure 3.15, 0.1 Gy X-ray dose) and translocation was observed between chromosomes 8 and 5 at 0.5 Gy (Figure 3.17). Similarly, with exposure to 1 Gy irradiation, some heterochromatin (chromosome X) and non-heterochromatin breaks, were observed, such as on chromosome 1 (Figure 3.18) and chromosome 11 (Figure 3.15).

It was noticed that the FLIM measurements are independent of structural chromosomal aberrations at different doses but dependent on the region of a chromosome damaged, as described in the chapter (Figure 3.15, section 3.4.). The condensed and decondensed nature of a chromosome and the perturbation in the DNA upon exposure to low-level X-ray doses were measured using FLIM. At 1 Gy, chromosome 11 has non-heterochromatin breaks and a longer lifetime compared to chromosome X, which has a reduced lifetime because of heterochromatin breaks (Figure 3.15). It has been shown that heterochromatin undergoes relaxation, and the euchromatin shows complementary behaviour soon after irradiation (less than 5 min) (Zhang *et al.*, 2015). However, with the time point, ≥ 6 hrs, the relaxation of heterochromatic and condensation of euchromatic regions revert to a non-irradiated chromosome state. Therefore, it is said that the two major sub-regions of the chromosomes behave in the opposite way after radiation damage (Zhang *et al.*, 2015). Chromosomal aberrations are likely random, and accordingly, the repair mechanism follows. Similarly, some random structural chromosomal aberrations were observed upon low-dose radiation throughout the length of the chromosomes that were measured by the FLIM (Figure 3.15).

In further investigation, the lifetime of naked DNA labelled with DAPI in solution was measured. Naked DNA has a longer lifetime value, >3.5 ns (Figure 3.21). However, when polynucleotide is wrapped around histone proteins, that leads to a more compact structure with a lifetime value of < 2.88 ns. DAPI binding to AT-rich regions is unprotonated, therefore, it gives a longer DAPI lifetime (Figure 1.8). However, with DAPI intercalating in GC-rich regions, the protonation state gives a short DAPI lifetime (Figure 3.21). A protonated chemical reaction occurs when the indole group of DAPI binds to the AT-rich regions. An unprotonated chemical reaction occurs when the indole group of DAPI are loosely interacts with GC-rich regions (Barcellona and Gratton, 1989) (Barcellona and Gratton, 1990). It is observed that DAPI binds to AT-rich regions of DNA and gives a single exponential lifetime component. DAPI intercalating with GC-rich regions provides two exponential excited state lifetime components.

The DAPI lifetime of seven oligomers with varying the percentage of AT and GC-rich contents present in the oligomers were studied. 100 % AT-rich oligomers showed single and longer lifetime components. Whereas 60 - 100 % of GC-rich oligomers showed two lifetime components. For example, with 100 % GC-rich content gives one very short lifetime t1 = 0.89 ns and another long lifetime t2 = 5.37 ns (Figure 3.21). This result is indicative that DAPI intercalating with GC is not shielded from the solvent, in contrast to the interaction of AT with DAPI (Barcellona and Gratton, 1990) (Mazzini *et al.*, 1992).

The large constitutive heterochromatin blocks of heteromorphic chromosomes are made up of classical satellites II and III. The following satellites consist of tandem repeats of 5 bp nucleotides of GGAAT- sense strand and ATTCC- antisense strands of DNA. Therefore, it can be assumed that the obtained mean excited-state lifetime of oligomer GGA-TAT-ATG-C is one of the closest oligomers, that relates to the classical pentanucleotide, GGAAT (Figure 3.21). The anticipation is that the DNA sequence present at the heterochromatic regions of the heteromorphic chromosomes 1, 9, 15, 16 and Y might consist of 40 % GC content. The following purine-rich pentanucleotide DNA sequence possesses unusual hydrogen bonding and thermal stability, moreover, it is also considered a highly conserved regions at the proximal of the human centromere (Grady *et al.*, 1992). The same sequence has been found in the central region of the yeast (Grady *et al.*, 1992). Moreover, the guanosine base has a high damage rate upon excitation, even with a low-level of ionising radiation, because of its oxidising characteristic and high ionising potential (Melvin *et al.*, 1998).

3.9. Summary

FLIM imaging has been used to investigate the two main chromatin regions: heterochromatin (most compact), and euchromatin/non-heterochromatin (less compact). This was performed on fixed (using fixative methanol: acetic acid at a ratio of 3:1) human metaphase chromosomes using DNA specific-DAPI fluorophore following exposure to low-dose ionising radiation. The three main investigations comprised of the measurement: 1) DAPI lifetime variation along the length of all 46 chromosomes obtained from T-lymphocytes, 2) DAPI lifetime

of heterochromatic and the non-heterochromatic regions of heteromorphic chromosomes upon X-ray irradiation, and 3) DAPI lifetime at 16 hrs, 40 hrs and 64 hrs of post-irradiation. The low-dose X-ray radiations used were 0.1 Gy, 0.5 Gy and 1 Gy. The DAPI lifetime of naked DNA in solution was also investigated to determine the DNA sequence relationships that might be present in the heterochromatic regions of heteromorphic chromosomes that showed a short DAPI lifetimes.

The change in the DAPI excited state lifetime was observed in all 46 chromosomes, including heteromorphic chromosomes (chromosomes 1, 9, 15 and 16) obtained from T-lymphocytes and in Y-chromosome, obtained from B-lymphocytes. A reduced DAPI excited state lifetime was observed at the heterochromatic regions, and a long lifetime component at the non-heterochromatic regions of the chromosomes was observed. The change in the DAPI lifetime observed between the two different chromatin regions (heterochromatin (2.90 ± 0.04 ns) and euchromatin/non-heterochromatin (2.93 ± 0.02 ns)) of all 46 chromosomes were not found to be significant. Although, a significant change in the DAPI lifetime was observed in both chromatin regions of all 46 chromosomes upon X-ray irradiation. However, there was no significant variation in the DAPI lifetime between different radiation doses (0.1 Gy, 0.5 Gy and 1 Gy). It can be assumed that the reduced DAPI lifetime values that were observed may be due to protonated DAPI bound to the metaphase chromosomes at the compact regions of heterochromatin (Barcellona and Gratton, 1990). In contrast, long DAPI lifetime values were observed due to unprotonated DAPI bound to the metaphase chromosomes at the less compact regions of euchromatin/non-heterochromatin (Barcellona and Gratton, 1989) (Barcellona and Gratton, 1990).

Naked DNA was also investigated, with a longer DAPI lifetime component (~4.0 ± 0.39 ns) compared to the heteromorphic mitotic chromosomes (~2.8 ± 0.03 ns); this was attributed to unshielded DAPI from the solvent. Additionally, the specific DNA base sequences at the heterochromatic regions could also contribute to the reduced lifetime of DAPI. The heteromorphic chromosome shows a significantly lower DAPI lifetime at the heterochromatic region in

comparison to the rest of the chromosomes present in the spread. This could be explained by the presence of a large block of compact heterochromatin at the pericentromeric region of the heteromorphic chromosomes.

In addition, the heteromorphic chromosomes contain tandem repeats of DNA pentanucleotide (GGAAT) sequences. This is a type of DNA satellite present at the pericentromeric region of the chromosomes 1, 9, 15, 16 and the distal region of the Y-chromosome. The presence of guanosine nucleotides in the repeats of DNA pentanucleotide sequences led to a short lifetime component. A short lifetime component was observed in both non-irradiated (control) and irradiated heteromorphic chromosomes. However, the lifetime values even reduce further in the X-ray induced heteromorphic chromosomes.

The DAPI lifetime reduces further with increasing passage time point after X-ray irradiation, especially with the passage time point of 64 hrs. This suggests that the X-ray induced chromosomes condense after immediate DNA damage and the subsequent repair process, which results in a reduced DAPI lifetime. Interestingly, increased radiation dose and post-irradiation passage time point result in decondensed metaphase chromosomes (with increased DAPI lifetime component), a phenomenon that requires future investigation.

Chapter 4

4. Mass measurement of chromosomes from the phase-contrast imaging

The study of the structural and functional role of chromosomes in cytogenetics has spanned more than 10 decades, but still, the details of chromosomes structure is poorly understood. In this chapter, the aim was to extract the individual masses of all 46 chromosomes of both stained and unstained chromosome spreads obtained from B and T-cells. The method of hard X-ray ptychography was used to measure the mass of individual chromosomes to produce “X-ray karyotypes”. The obtained measured mass will aid in determining the gain or loss of genetic material upon low dose X-ray irradiation and any mass loss that might occur due to radiation damage while scanning the spreads.

All the experiments were performed at the I-13 beamline, Diamond Light Source, Oxford, UK, using the ptychography reconstruction algorithms of Dr Darren Batey (Batey, 2014).

The ptychography setup was configured according to Figure 2.4. A 9.7 kiloelectron volt (keV) energy was used on a “Siemens star” test sample with 500 nm, 200 nm and 100 nm radially separated spokes (Batey et al., 2019), This was done to check the accuracy of the setup to obtain an accurate image of the complex probe on the sample. The sharp contrast of the spokes in the Siemens star helps the characterisation of the coherent beam and allows measurement of the spatial resolution of the imaging system.

The probe was reconstructed from the Siemens star using the PtyREX ptychographic reconstruction package (Batey, 2014) using e-PIE reconstruction

algorithms (Maiden and Rodenburg, 2009) (Rodenburg *et al.*, 2007). The reconstructed probe (Figure 4.1a) was optimised and later used to assist the reconstruction of chromosomes samples as an initial starting probe. As a further calibration, 150 nm gold nanoparticles were first scanned and then reconstructed to optimise the phase contrast (Figure 4.1c). The diffraction patterns obtained from the weak scattering chromosome samples were reconstructed using ptychography algorithms (Batey, 2014).

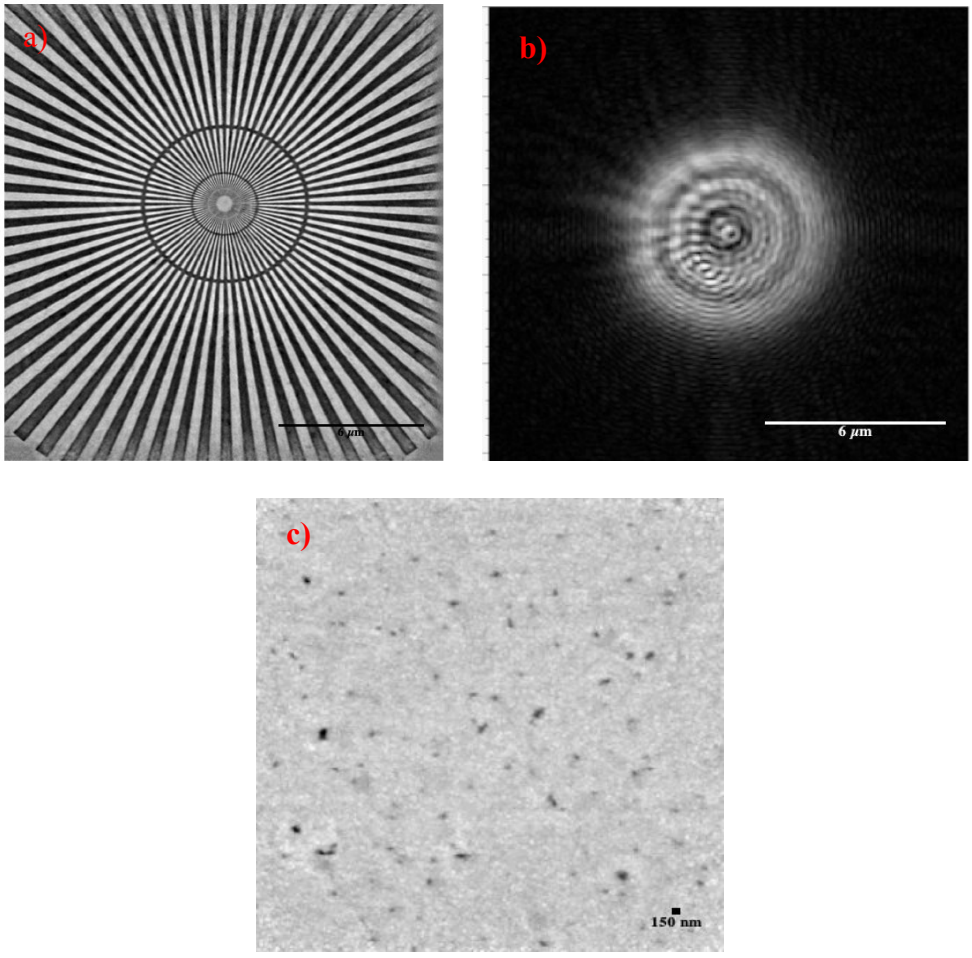

Figure 4.1: Test sample images used for calibration of the X-ray ptychography a) Reconstructed image of a 'Siemens star' standard for measurement of spatial resolution. Field of view (FoV): 64 µm x 64 µm, X-ray exposure time: 0.01 sec, scale bar = 6 µm and b) Amplitude of the X-ray beam illumination function ('probe') which is the modulus of the complex wave function, scale bar = 6 µm. c) Reconstructed phase image of 150 nm gold nanoparticles for characterisation of the effectiveness of the phase contrast capability of ptychography. FoV is 32 µm x 32 µm and exposure time is 0.1 sec per frame.

Due to the very low absorption coefficient of chromosomes at 9.7 keV energy, only the phase component of the reconstruction was extracted and analysed further. Ptychographic reconstruction images are quantitative; therefore, the phase values extracted from the images can be converted into the absolute number of electrons in the sample, giving an absolute measure of its mass. The phase component of the reconstruction was analysed using ImageJ software, where the mass of the chromosomes was determined.

4.1. Analysis of the phase value obtained from the chromosome reconstructions

From the ptychography experimental results, the mass of the individual chromosomes was calculated from the phase value of the reconstructed chromosomes scanned at 9.7 keV. The reconstructed phase image of the chromosome spread was processed in ImageJ software using a Gaussian filter (helps to reduce noise and, by doing so, to segment the edges of the chromosomes) and an optimum threshold. Several other parameters were needed to calculate the electron count of the objects. The summation of the phase shift pixel values ($\sum_j \emptyset_j$) across the chromosome area (Shemilt *et al.*, 2015) was calculated using the freehand tool in ImageJ software; the wavelength of the X-ray beam, λ = 0.13 nm; the real space pixel size of 2 dimensional (2D) chromosome images, $P_x P_y$ = 32 nm x 32 nm or 35 nm x 35 nm (depending upon the experiment) and the constant classical radius of the electron, $r_0 = 2.82 \times 10^{-6}$ nm.

The number of electrons, M, within an individual chromosome is obtained by summing up the phase shift values inside each image pixel, counted by j, using **Equation** (4.1**)** (Als-Nielsen and McMorrow, 2011):

$$\boldsymbol{M = \sum_j \frac{\emptyset_j}{\lambda r_0} P_x P_y} \qquad (4.1)$$

The diploid (2-copy) human genome consists of slightly more than 6.4 billion base pairs (bp) (Goldfeder *et al.*, 2017) located within 22 pairs of autosome chromosomes and one pair of sex chromosomes (Brown., 2002). The chromosomes are numbered according to their size determined by flow cytometry (Harris *et al.*, 1986). Chromosome 1 is the largest and has 248,956,422 base pairs (per copy), and the smallest chromosome 21, comprises 46,709,983 base pairs. In the whole human genome, only 30,000-40,000 genes (information carrying fragments of DNA) are protein-coding genes (Lander *et al.,* 2001).

The average molecular weight of a DNA base pair is 660 g/mol (Dalton) (Bench *et al.*, 1996), and so a single base is 330 g/mol. The DNA base pairs are measured in picograms (pg), megabase pairs (Mbp) or Dalton (Da) (Doležel *et al.*, 2003).

Where in (Doležel *et al.*, 2003):

$$1\ Da = 1.67 \times 10^{-12}\ pg \text{ and } 1\ Mbp = 10^{6}\ base\ pairs$$

$$DNA\ content\ (pg) = genome\ size\ (Mbp) \times 660\ Da$$

With this understanding (the average MW of base pair is 660 Da), calculated the masses of the known base pairs of each human chromosome. Since only light atoms are present in DNA, which all contain the same number of protons, neutrons, and electrons. The number of electrons measured by ptychography is precisely half the number of Daltons of mass. For example, the longest chromosome, 1, has a mass of DNA of 0.27 pg containing 8.2×10^{10} electrons. The smallest chromosome, 21, has a mass of 0.05 pg. In this fashion, calculated the mass of all 46 chromosomes from known human genomic size. Henceforth, masses calculated from the known base pairs are used as a reference to karyotype the measured masses of chromosomes obtained from the summation of phase shift across each pixel of the chromosome images (Als-Nielsen and McMorrow, 2011).

4.2. Karyotype of human chromosomes with a M-FISH technique

For identification of any chromosomal aberrations, the karyotype was first performed on non-irradiated chromosomes obtained from both the T and B-cells with the help of a chromosome identification technique known as M-FISH. The chromosomes were stained with a 24XCyte probe kit (see chapter-2, Materials and Methods) which labels all 24 chromosomes with 5 different fluorochromes arranged in a combinatorial manner. This helps to visualise the structural rearrangements (e.g. translocation) of chromosomes and numerical aberrations (Anderson, Stevens and Goodhead, 2002) (Balajee *et al.*, 2014).

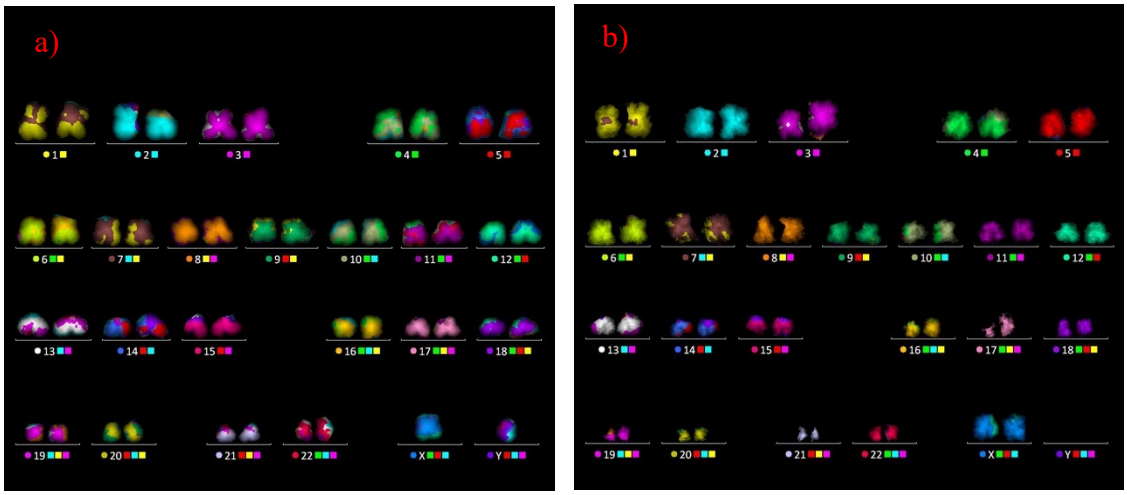

Figure 4.2: M-FISH karyotype performed on non-irradiated chromosomes obtained from a) B-lymphocytes, a male cell line (1-22, XY chromosomes) and b) Primary T-lymphocytes from a female donor (1-22, XX chromosomes).

The M-FISH karyotype in Figure 4.2 shows a set of 22 pairs of autosome chromosomes and one pair of sex chromosomes in each, depending upon the gender. The chromosome numbers are allocated the same colour as coded by the computerised-colour-code scheme of MetaSystem and placed above the number assigned to each colour (Speicher, Ballard and Ward, 1996) (Anderson, 2010). The karyotype helps to identify the stability and the quality of the

chromosomes obtained from B and T-lymphocytes. After validation, the same preparation of chromosomes (see chapter-2, Materials and Methods) was used for X-ray ptychography imaging to generate masses of each chromosome from the phase shift reconstructions.

4.3. Hard X-ray imaging of stained chromosomes

Investigation of biological samples with electron microscopy and hard X-ray imaging is very challenging because of the weak scattering of its light atoms. Therefore, investigated staining the chromosomes with 1% uranyl acetate (Figure 4.3a) and 6 mM platinum blue (Figure 4.3b) to add additional mass to increase the sensitivity of the phase contrast (see chapter-2 Materials and Methods). Staining deposits, a thin layer of additional electron density on the top of the chromosome samples to increase the scattering intensity of the beam. Chromosome-specific staining could also help to visualise and segment each chromosome from nuclei and other debris. ImageJ software used to calculate the mass of the metaphase chromosomes.

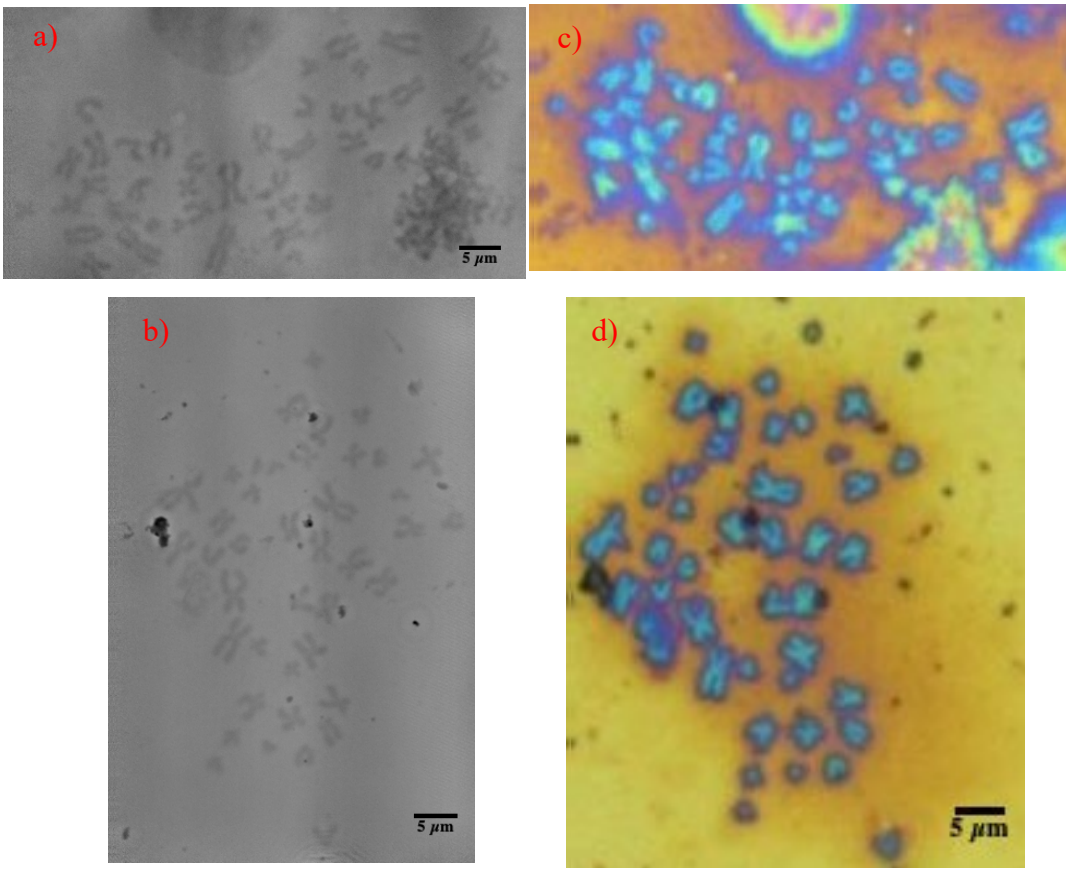

Figure 4.3: Ptychographic reconstructed phase-retrieval images of chromosome spreads measured in the air, FoV: 64 μm × 64 μm a) 1% UA -stained chromosomes with 1.0 sec exposure of X-rays, b) 6 mM Pt-blue stained chromosomes with 1.0 sec exposure. It also contains residues of Pt-blue aggregates (black spots in the image). The chromosomes appeared with a high intensity of grey level separated from the even background. Image c and d are the optical images of respective spreads with the stains. The blue objects are the stained chromosomes. Scale bar = 5 μm.

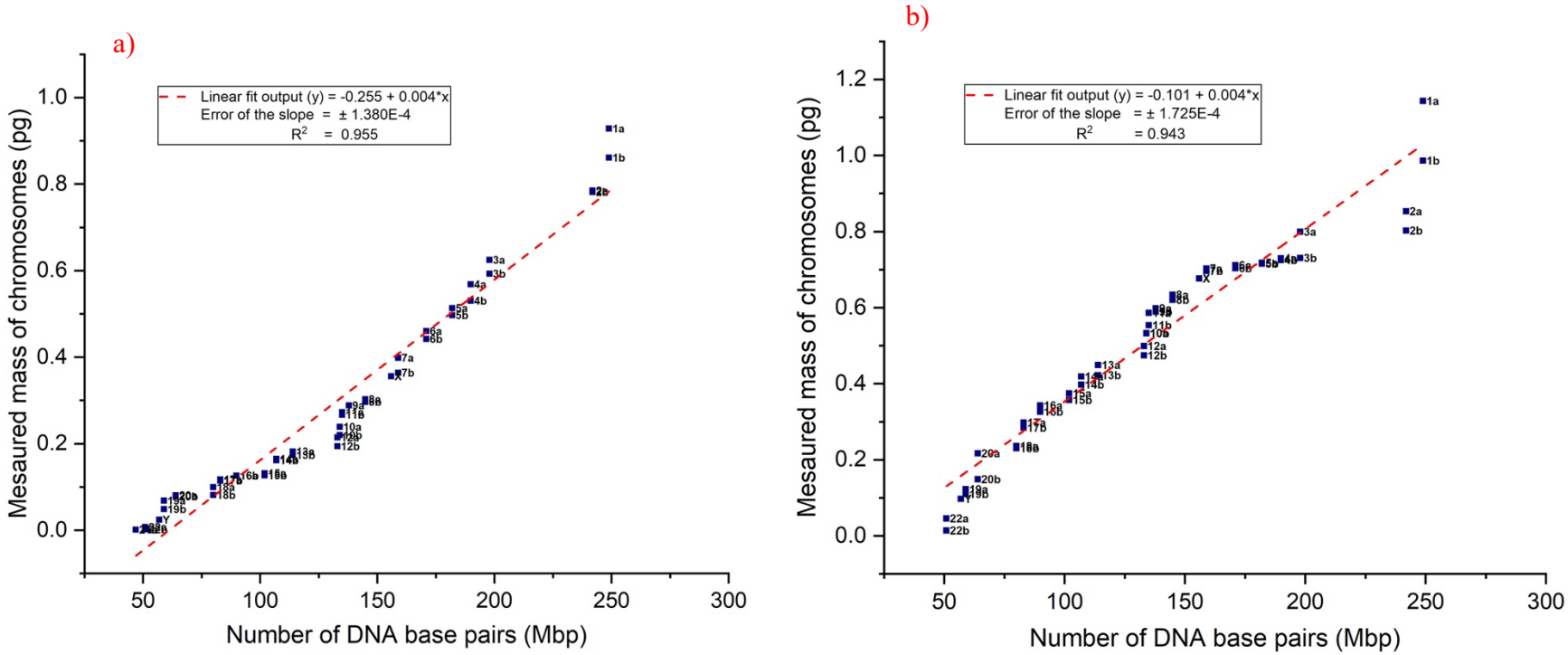

Figure 4.4: X-ray karyotypes produced from the phase image of chromosome spreads obtained from B-cell, accompanied with a best-linear-fit. a) The X-ray karyotype of measured mass of 45 out of 46 human chromosomes, stained with 1% UA, against the known base pair length of each chromosome. b) The X-ray karyotype of measured mass of 44 out of 46 human chromosomes, stained with 6 mM Pt-blue, against the known base pair length of each chromosome. The “a” and “b” labels in the karyotypes states the homologous chromosomes in each pair. Mass of the chromosomes falls within a range of picograms for both karyotypes.

X-ray phase contrast is a quantitative way to measure the masses of heavily stained chromosome samples. Each reconstruction has been run through 50 iterations of the ptychographic algorithms to get a well-converged image. Subsequently, the reconstructed images were segmented with a free hand tool in ImageJ to obtain the raw integer density (RawIntDen) value. The background pixel values were subtracted to obtain the pixel values within an isolated chromosome. The following obtained values were fitted into the derived equation (4.1). Henceforth, the number of electrons present in each chromosome was measured and later multiplied with the mass of the two nucleons (2 Da = 3.35×10^{-27} kg) present in an atom to generate the observed masses of each chromosome. The graphs in Figure 4.4 were plotted *versus* the known number of DNA base pairs of each chromosome to produce an X-ray karyotype from each stained spread. As with other karyotype methodologies, it is assumed that the sequence of observed masses follows the same numbering of the chromosomes.

It is observed that the measured masses are 3-4 times higher than the DNA alone. A factor of 2 is due to the two genome copies present in the chromosomes at the metaphase, and the rest is attributed to the protein complement and the stain. It is noted that the mass measurements slightly underestimate the mass of the stain because the heavy elements (Uranium and Platinum) contain additional neutrons to the simple 1:1, proton: neutron ratio of light elements. The potential benefit of heavy metal stain is to improve the contrast of the weak scattering biological sample, and it has been observed for both the stains used. It appears that one chromosome in UA stained and two chromosomes in platinum blue stained have been missed (Figure 4.3 and Figure 4.4). The sum of the measured masses of 45 out of 46 chromosomes is 13.18 pg for UA stain and 22.18 pg for platinum stain with 44 out of 46 chromosomes. Both the chromosome spreads were obtained from the B-lymphocyte cell line.

4.4. X-ray ptychography of unstained human chromosomes

After obtaining successful results of ptychographic reconstructions from stained chromosomes, furthermore, unstained metaphase chromosomes were investigated, closer to their native state using X-ray ptychography. The same procedure was applied to prepare chromosome spreads on the Si_3N_4 membrane (see Chapter 2, Materials and Methods) and imaged them at room temperature. This powerful technique provides quantitative information, and from these data, the masses of the chromosomes were extracted that obtained from both the male and female cell lines without any staining.

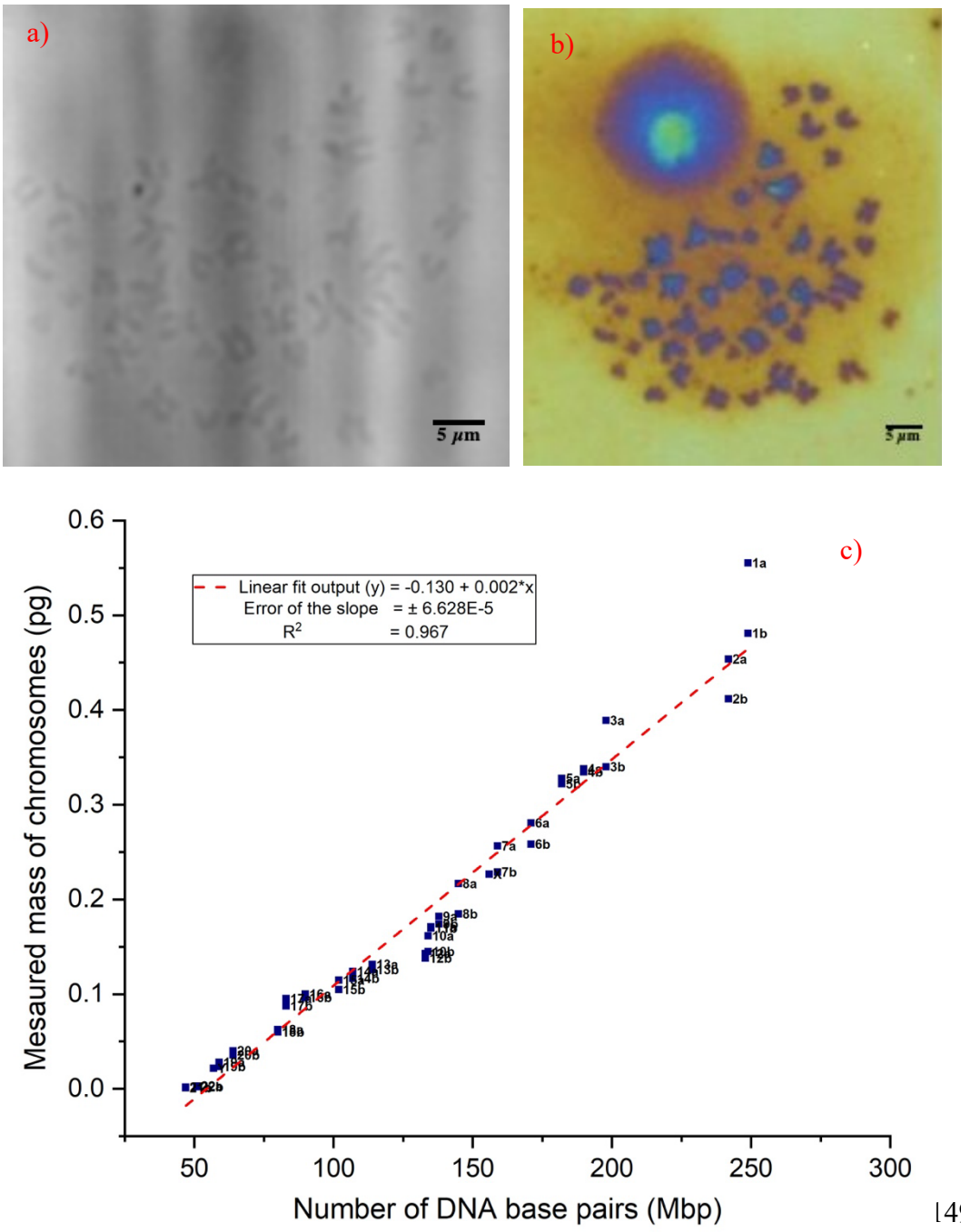

Figure 4.5: Ptychographic reconstructed unstained chromosome spread obtained from B-lymphocytes; a) phase image of B-lymphocytes (male cell line), FoV: 64 µm × 64 µm, with a 1.0 sec of exposure, b) optical microscope image of the same chromosome spread, including a big blob of nuclei, scale bar = 5 µm, cropped from a bigger FoV image. c) X-ray karyotype of the same spread, the “a” and “b” labels in the karyotype states the homologous chromosomes in each pair.

The graph plotted between measured masses and the known number of DNA base pairs of the individual unstained chromosome from a single spread (Figure 4.5c). The order of the chromosomes is aligned in the following sequence:
1>2>3>4>5>6>7>X>8>9>11>10>12>13>14>15>16>17>18>20>19>Y>22>21.
The position of sex chromosomes is as follows: chr Y falls in between chr 19 and 22, and chr X falls between chr 7 and 8. In addition, chr 11 falls before chr 10; similarly, chr 20 falls before chr 19 and chr 22 before chr 21. Chromosome 1 has the highest mass, and chr 21 has the lowest mass.

In the first experiment, B-cells showed a decrease in the measured masses of the unstained chromosomes compared to stained chromosomes. This indicates that the stains significantly add extra mass to the chromosomes, and this work presents the first quantitative evaluation of how much stain is apparently bound. The sum of the mass for the unstained B-lymphocytes is 8.26 pg of all 46 chromosomes. From the human genome sequence, it is known that the amount of DNA content in a male human genome is 6.54 pg per cell (Doležel *et al.*, 2003) (Piovesan *et al.*, 2019).

4.5. Phase-retrieval reconstructions of irradiated unstained human chromosome spreads

With the successful experiment to image unstained human chromosomes from B-cells at a high resolution. Thereafter, in the second experiment, X-ray ptychography was performed to image unstained chromosomes obtained from primary T-lymphocytes at the I-13-1 beamline, Diamond Light Source, Didcot, UK. Metaphase human chromosomes were prepared on silicon nitride membrane (see chapter 2, Materials and Methods) and imaged at room temperature. The obtained diffraction patterns were reconstructed using

ptychographic algorithms, and an X-ray karyotype was generated from the obtained quantitative values, as described above.

In addition, X-ray ptychography was also performed on X-ray induced chromosomes during the experiment. The aim was to observe any potential structural or numerical aberrations that occurred due to the irradiation of the chromosomes. To accomplish this experiment, based on previous experience, chosen three X-ray radiation doses, 0.1 Gy, 0.5 Gy and 1 Gy, to induce live cultured cells. In order to understand the structural rearrangement and change in the individual masses of the chromosomes. After imaging, each reconstruction ran for 500 iterations of the ptychographic algorithm, as described above.

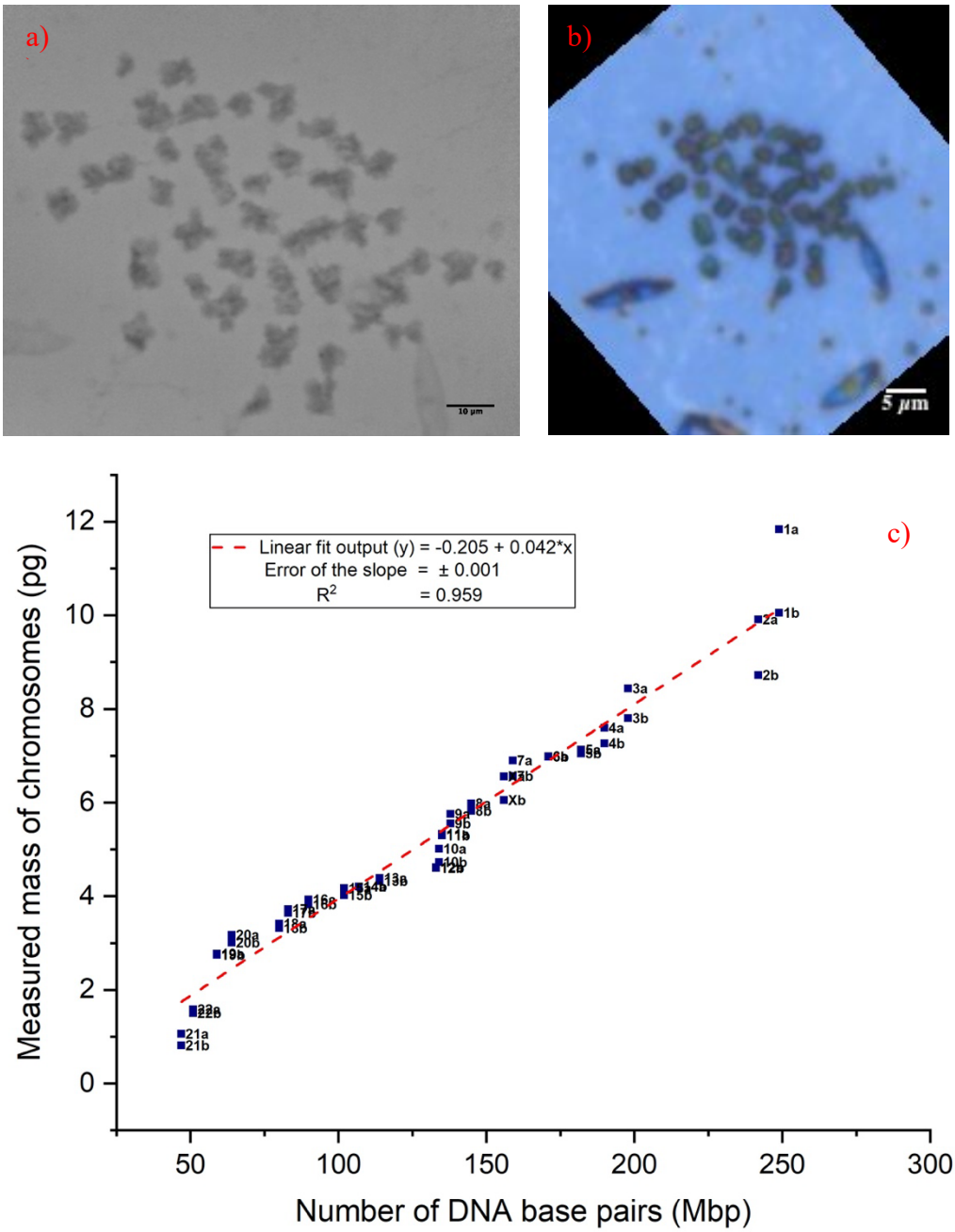

Figure 4.6: Ptychographic reconstructed unstained chromosome spread obtained from non-irradiated T-lymphocytes, as a control; a) phase image of the T-lymphocytes (female cell), FoV: 32 µm × 32 µm, with 0.3 sec of exposure, scale bar = 10 µm. The fibrous structure of the chromosomes can be seen. b) optical microscope image of the same chromosome spread, with some debris on the membrane, scale bar = 5 µm, cropped from a bigger (100 µm) FoV image, c) X-ray karyotype of the same spread, with a best-linear-fit. The “a” and “b” labels in the karyotype states the homologous chromosomes in each pair.

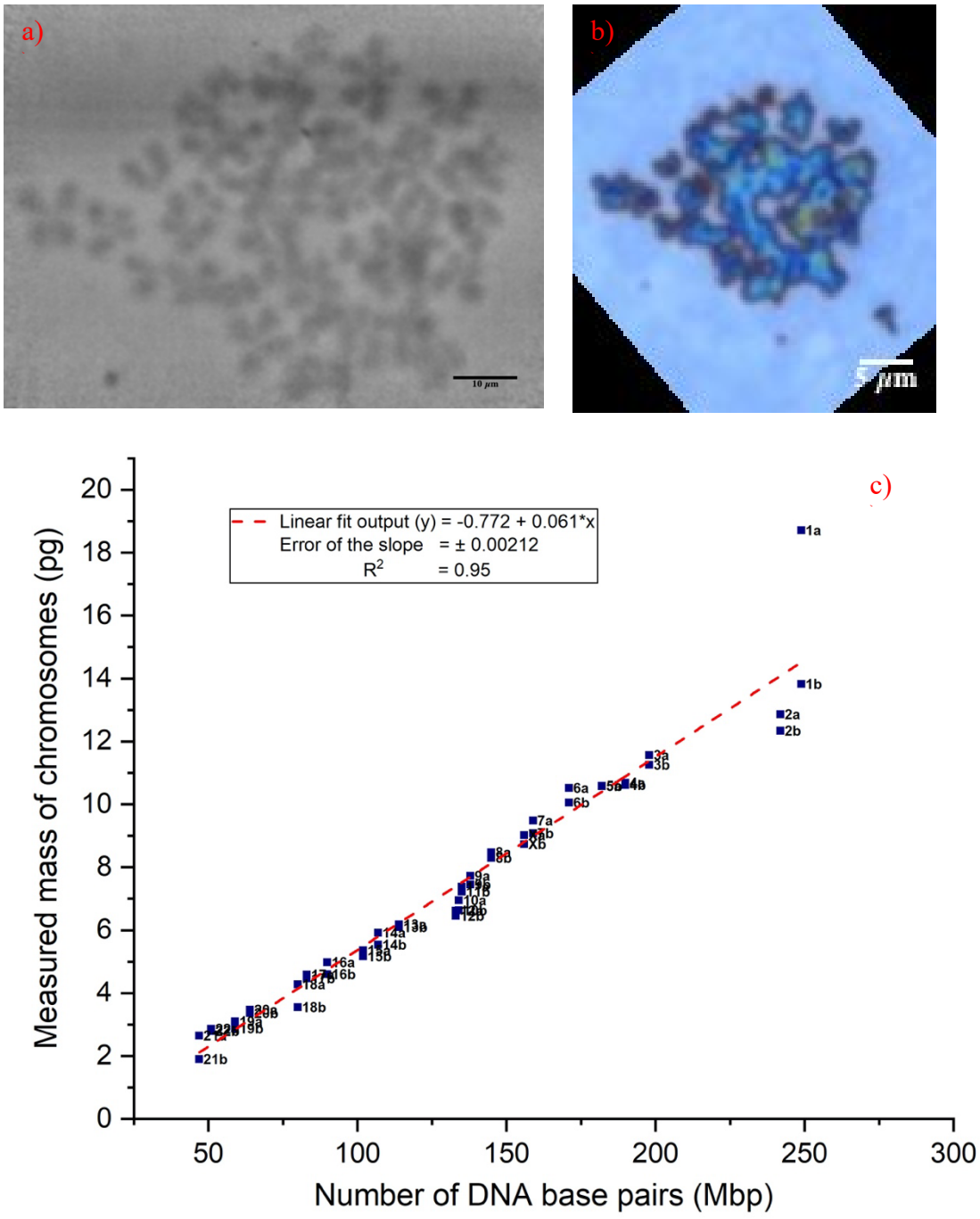

Figure 4.7: Ptychographic reconstruction of unstained chromosome spread obtained from X-ray induced T-lymphocytes cells at 0.1 Gy; a) phase image of the T-lymphocytes (female cell), FoV: 32 µm × 32 µm, with a 0.3 sec of exposure. Scale bar = 10 µm, b) optical microscope image of the same chromosome spread. Blue clustered features are chromosomes, scale bar = 5 µm, cropped from a bigger (100 µm) FoV image, c) X-ray karyotype of the same spread, with a best-linear-fit. The “a” and “b” labels in the karyotype states the homologous chromosomes in each pair.

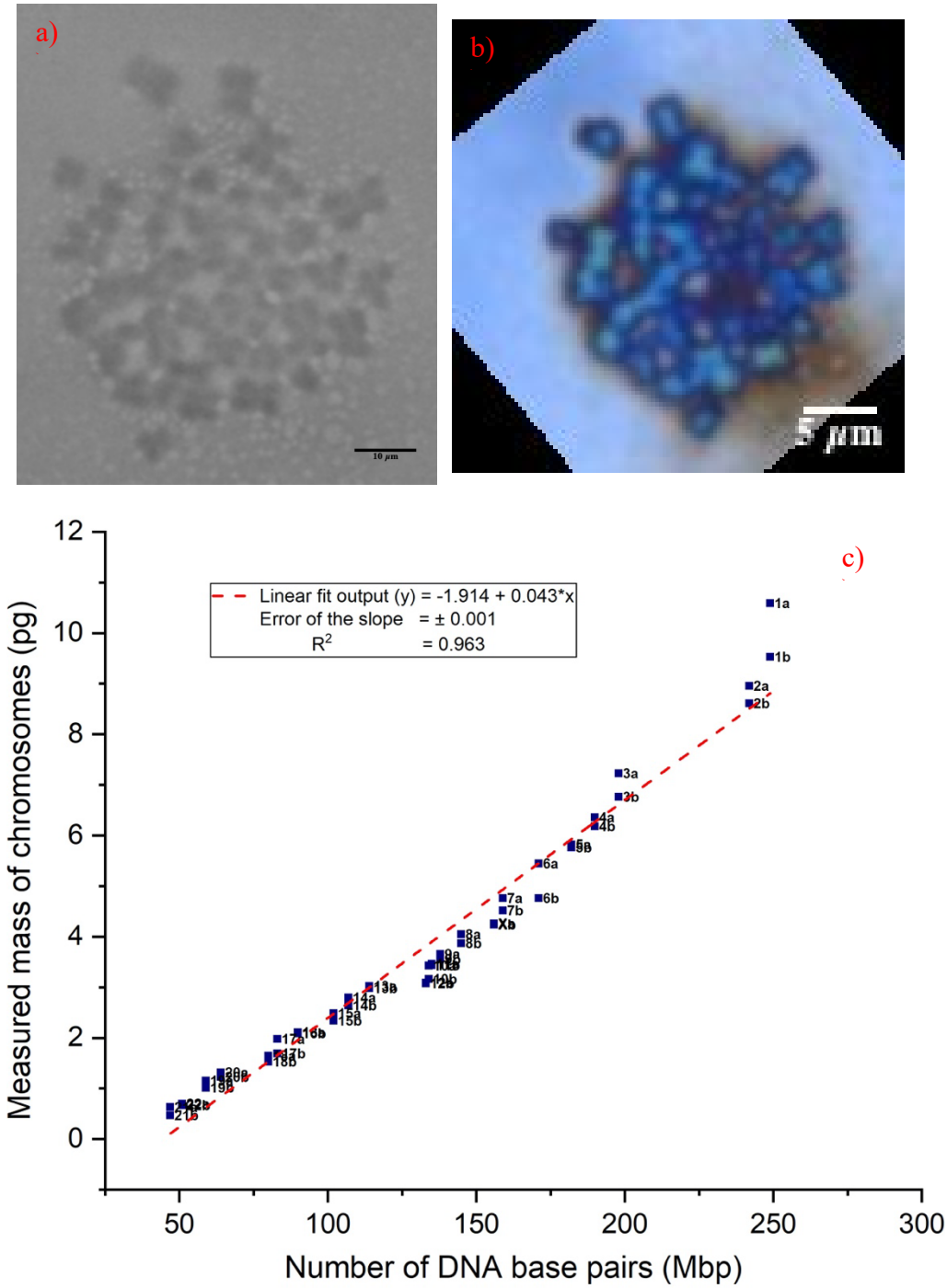

Figure 4.8: Ptychographic reconstruction of unstained chromosome spread obtained from X-ray induced T-lymphocytes cells at 0.5 Gy; a) phase image of the T-lymphocytes (female cell), FoV: 32 μm × 32 μm, with a 0.3 sec of exposure. Scale bar = 10 μm, b) optical microscope image of the same chromosome spread. Blue clustered features are chromosomes, scale bar = 5 μm, cropped from a bigger (100 μm) FoV image, c) X-ray karyotype of the same spread, with a best-linear-fit. The “a” and “b” labels in the karyotype states the homologous chromosomes in each pair

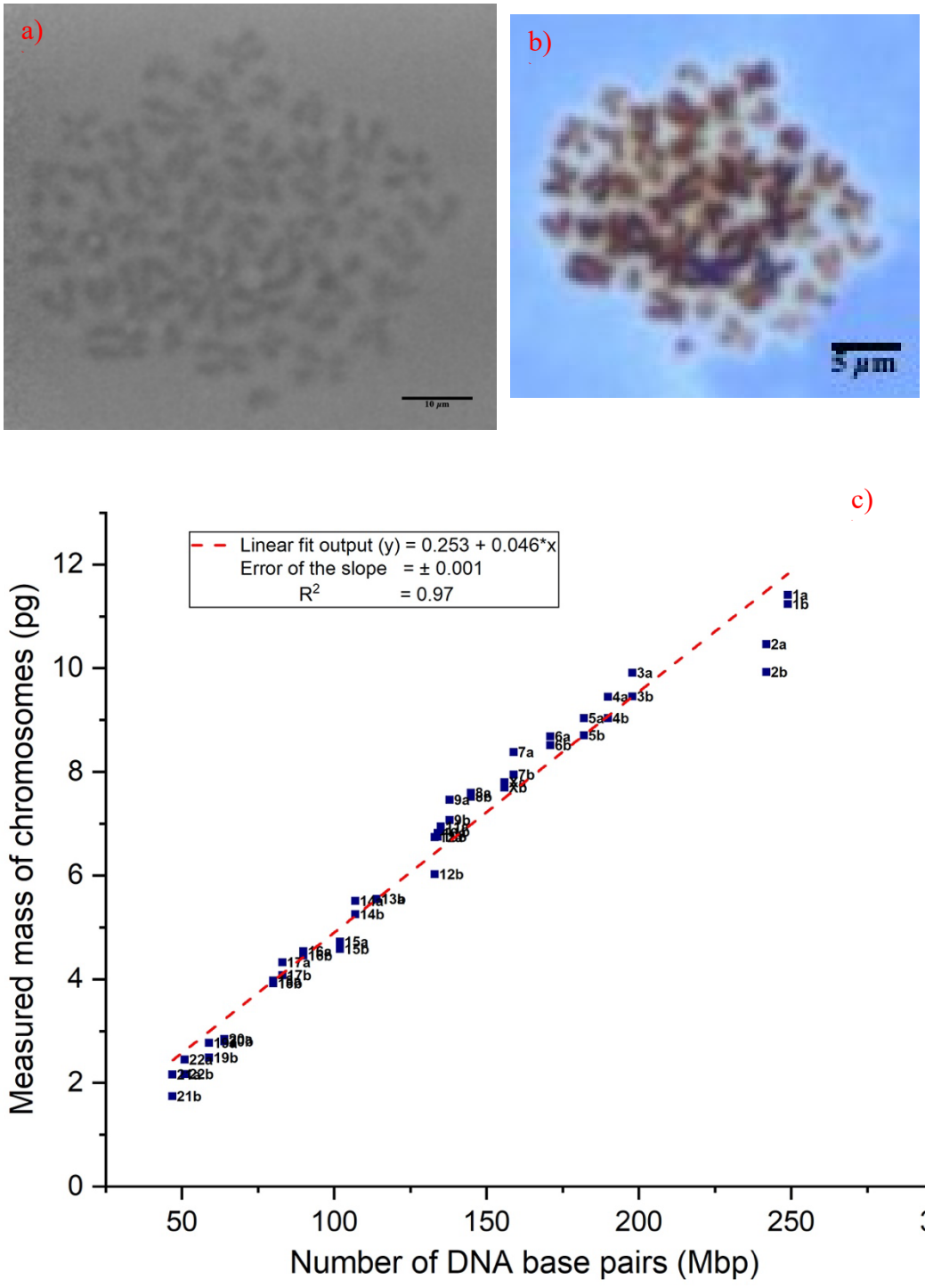

Figure 4.9: Ptychographic reconstruction of unstained chromosome spread obtained from X-ray induced T-lymphocytes cells at 1 Gy; a) phase image of the T-cells (female cell), FoV: 32 µm × 32 µm, with a 0.3 sec of exposure. Scale bar = 10 µm, b) optical microscope image of the same chromosome spread. Brown objects are chromosomes, scale bar = 5 µm, cropped from a bigger (100 µm) FoV image, c) X-ray karyotype of the same spread, with a best-linear-fit. The “a” and “b” labels in the karyotype states the homologous chromosomes in each pair.

From each X-ray ptychography image, measured the masses of the non-irradiated (control) and irradiated chromosomes obtained from T-lymphocytes to produce an X-ray karyotype of each. The outcome, shown in Figure 4.6, Figure 4.7, Figure 4.8 and Figure 4.9, is that the data points fall nicely on a straight line, as before, which means there is a positive relationship between the measured masses and the known DNA base pairs present in each chromosome. The total masses of all 46 chromosomes have been summed and they are as follows: 242 pg, 336 pg, 172 pg and 293 pg, for the control (Figure 4.6) and the radiation doses, 0.1 Gy (Figure 4.7), 0.5 Gy (Figure 4.8) and 1 Gy (Figure 4.9) respectively. Surprisingly, the total mass for 0.1 Gy is higher than the non-irradiated chromosomes (242 pg), then significantly decreases for 0.5 Gy before rising again for 1 Gy. Overall, it follows the trend: 0.5 Gy<control<0.1 Gy<1Gy, with regards to 'summed-masses'. Moreover, it has been noticed that for each X-ray karyotype plot, the average mass of the two chromosomes, 1s and 2s, is much higher than the expected extrapolation from the rest of the chromosomes in the spread, irrespective of radiation doses.

It is noteworthy that the mass numbers emerging from this second experiment are an order of magnitude higher than the first experiment, reported in sections 4.3 and 4.4. This discrepancy, which is noticed immediately in the apparent contrast of the raw ptychography images, is not fully explained. The experiments were separate runs at Diamond, about a year apart, and both the measurement and reconstruction methods improved considerably over that time. But this would be expected to improve the only efficiency and not the phase contrast values, which should be highly quantitative. The most likely explanation was the significant delay of 5-6 months between the sample preparation, with the samples stored in 3:1 methanol: acetic acid in the refrigerator, and the measurement for the first experimental run. Some of the chromosome mass may have been "lost" during storage during that time. Therefore, the quantitative numbers for the second batch, where the samples were freshly prepared, are therefore probably more reliable.

4.6. Protein composition determined in human metaphase chromosome

Chromosomes are composed of a DNA-protein complex. From the human genome literature, the amount of DNA present in each human chromosome (Lander *et al.*, 2001) (Piovesan *et al.*, 2019) is reckoned to be known. However, the protein composition of the metaphase chromosomes is still somewhat less clear. It is noted that the human genome only records the coding part of the DNA and that the sequencing methods are unable to adequately record repeated sequences. Consequently, the DNA masses based on the human genome sequence will be underestimated. This is most likely the case for chromosomes 1, 9, 15 and 16, which are heteromorphic and contain heterochromatin-rich regions.

From the phase-contrast reconstructions obtained using X-ray ptychography, an attempt made to determine the amount of protein (histone and non-histone) present in each metaphase chromosome from the obtained masses. Firstly, extracted the number and the amount of histones from the Protein Data Bank (PDB) (Table 4.1), that are known to be associated with around 166 bp of DNA, wrapped around the protein core to form each nucleosome – the fundamental structural subunit of the chromatin fibre, the DNA-protein complex. A single nucleosome contains eight histones, two each of H2A, H2B, H3 and H4 (~146 DNA base pairs) and one linker histone (20 base pairs), which connects two nucleosomes to form a chain of chromatin (Harshman *et al.*, 2013). Secondly, calculated the mass of the 166 bp of DNA to obtain the mass of the DNA component of the nucleosome by multiplying by the average molecular weight (660 Da) of a base pair (bp) (Bench *et al.*, 1996). Using 1Da = 1.66×10^{-27} kg, this gives the true physical mass of the nucleosome (Doležel *et al.*, 2003). From this, the mass of the nucleosome can be calculated and hence from the DNA content; the protein content can be determined for all 46 human chromosomes.

Protein	Amount (Da)
H2A histone	14, 135 x2
H2B histone	13,906 x2
H3 histone	15404 x2
H4 histone	11367 x2
H1 linker histone	32000 x1
Sum	141624 Da

Table 4.1: A list of histone proteins present in a single nucleosome (from the PDB)

Uchiyama *et al*. (2005) measured the breakdown of all proteins involved with the metaphase chromosomes. They found a total of 48 % histone protein and 12 % of linker histone (Uchiyama *et al.*, 2005). The total histones represent 60 % of the total, so the non-histone component can be estimated to be the fraction 40/60 (non-histones/histones) = 0.67 x 141624 Da per nucleosome. The histone proteins thus make up most of the mass of the chromosomes (Uchiyama *et al.*, 2005). Consequently, the estimated mass of one nucleosome can be calculated by considering three important components:

i) *DNA = 166 x 660= 109,560 Da per base pair*

ii) *Sum of the histone protein = 141,624 Da*

iii) *Non-histone protein = 0.67 x 141,624 Da*

So, total= 346,072.08 Da per nucleosome

Therefore, the total mass of a single nucleosome is 3.5×10^5 Da. Consequently, the mass of chromosome 1 can be estimated by calculating the number of nucleosomes as 248956422/166 = 1.50×10^6, giving a total mass of $1.50 \times 10^6 \times 3.5 \times 10^5$ Da $\times 1.66 \times 10^{-27}$ kg = 0.86 pg. The DNA alone would be 0.27 pg. with the remaining 0.59 pg. being protein. Therefore, the expected mass of chromosome 1 is 0.86 pg. and further multiplied by a factor of 2 to obtain the mass of 4 copies of DNA content and chromosomal proteins of metaphase chromosomes and with this manner, the expected mass of all 46

chromosomes has been illustrated in the below table for both the cell types (Table 4.2 and Table 4.3), along with the suspected mass loss (Table 4.2) due to long-term storage of the prepared chromosomes before imaging in methanol acetic acid (3:1) solution.

chromosome (number)	Known DNA base pairs/(M1) (pg)	Measured masses/(M2) (pg)	Expected histones/(M3) (pg)	Expected non-histones/(M4) (pg)	Expected mass/(M5) = (M1+M3+M4) (pg)	Mass loss/(M6) = (M5-M2) (pg)
1a	0.55	0.55	0.71	0.47	1.72	1.17
1b	0.55	0.48	0.71	0.47	1.72	1.24
2a	0.53	0.45	0.69	0.46	1.68	1.22
2b	0.53	0.41	0.69	0.46	1.68	1.27
3a	0.43	0.39	0.56	0.38	1.37	0.98
3b	0.43	0.34	0.56	0.38	1.37	1.03
4a	0.42	0.34	0.54	0.36	1.32	0.98
4b	0.42	0.33	0.54	0.36	1.32	0.98
5a	0.40	0.33	0.51	0.34	1.26	0.93
5b	0.40	0.32	0.51	0.34	1.26	0.94
6a	0.37	0.28	0.48	0.32	1.18	0.90
6b	0.37	0.26	0.48	0.32	1.18	0.92
7a	0.35	0.26	0.45	0.30	1.10	0.85
7b	0.35	0.23	0.45	0.30	1.10	0.87
X	0.34	0.23	0.44	0.30	1.08	0.85
8a	0.32	0.22	0.41	0.28	1.00	0.79
8b	0.32	0.18	0.41	0.28	1.00	0.82
9a	0.30	0.18	0.39	0.26	0.96	0.78
9b	0.30	0.17	0.39	0.26	0.96	0.78
11a	0.30	0.17	0.38	0.26	0.94	0.76
11b	0.30	0.17	0.38	0.26	0.94	0.77
10a	0.29	0.16	0.38	0.25	0.93	0.76
10b	0.29	0.14	0.38	0.25	0.93	0.78
12a	0.29	0.14	0.38	0.25	0.92	0.78
12b	0.29	0.14	0.38	0.25	0.92	0.78
13a	0.25	0.13	0.32	0.22	0.79	0.66
13b	0.25	0.13	0.32	0.22	0.79	0.67
14a	0.23	0.12	0.30	0.20	0.74	0.62
14b	0.23	0.12	0.30	0.20	0.74	0.62
15a	0.22	0.11	0.29	0.19	0.71	0.59
15b	0.22	0.10	0.29	0.19	0.71	0.60
16a	0.20	0.10	0.26	0.17	0.63	0.53
16b	0.20	0.10	0.26	0.17	0.63	0.53
17a	0.18	0.10	0.24	0.16	0.58	0.48
17b	0.18	0.09	0.24	0.16	0.58	0.49
18a	0.18	0.06	0.23	0.15	0.56	0.49

18b	0.18	0.06	0.23	0.15	0.56	0.50
20a	0.14	0.04	0.18	0.12	0.45	0.41
20b	0.14	0.04	0.18	0.12	0.45	0.41
19a	0.13	0.03	0.17	0.11	0.41	0.38
19b	0.13	0.02	0.17	0.11	0.41	0.38
Y	0.13	0.02	0.16	0.11	0.40	0.37
22a	0.11	0.00	0.14	0.10	0.35	0.35
22b	0.11	0.00	0.14	0.10	0.35	0.35
21a	0.10	0.00	0.13	0.09	0.32	0.32
21b	0.10	0.00	0.13	0.09	0.32	0.32

Table 4.2: Identification of all 46 chromosomes based on their measured and expected masses of each chromosome. The position of X and Y are highlighted in blue in the table. The table was generated from the phase image of chromosome spread obtained from unstained non-irradiated, chromosome spread shown in Figure 4.5. The “a” and “b” labels in the first column states the homologous chromosomes in each pair. The mass loss is a difference of calculated expected mass and the measured mass.

In Table 4.2, the expected mass of histones, non-histones, and an integrated mass of each chromosome has been calculated from the known DNA and the histone/non-histone content. However, the measured mass was obtained from an unstained chromosome spread extracted from the non-irradiated B-cells. It is noted that the spreads have been exposed to X-ray dose for roughly one second during ptychographic scanning.

In the first experiment, the calculated expected mass is 2.5 times higher than the measured mass for the chromosomes obtained from B-cells. Therefore, the mass loss can be determined by subtracting the measured mass from the expected mass for each chromosome (Table 4.2). Moreover, the expected mass is the sum of the calculated masses of histones, non-histone proteins and the known DNA mass calculated for each chromosome. It is noted that the DNA content for the complete set of male diploid human chromosomes is 6.54 pg (Lander *et al.*, 2001) (Doležel *et al.*, 2003) (Piovesan *et al.*, 2019).

chromosome (number)	Known DNA base pairs/(M1) (pg)	Measured masses/(M2) (pg)	Expected histones/(M3) (pg)	Expected non-histones/(M4) (pg)	Expected mass/(M5) = (M1+M3+M4) (pg)	Mass gain/(M6) = (M2-M5) (pg)
1a	0.55	11.83	0.71	0.47	1.72	10.11
1b	0.55	10.05	0.71	0.47	1.72	8.33
2a	0.53	9.91	0.69	0.46	1.68	8.23
2b	0.53	8.72	0.69	0.46	1.68	7.04
3a	0.43	8.43	0.56	0.38	1.37	7.06
3b	0.43	7.80	0.56	0.38	1.37	6.43
4a	0.42	7.60	0.54	0.36	1.32	6.28
4b	0.42	7.26	0.54	0.36	1.32	5.94
5a	0.40	7.12	0.51	0.34	1.26	5.87
5b	0.40	7.05	0.51	0.34	1.26	5.79
6a	0.37	6.99	0.48	0.32	1.18	5.80
6b	0.37	6.98	0.48	0.32	1.18	5.80
7a	0.35	6.90	0.45	0.30	1.10	5.79
7b	0.35	6.56	0.45	0.30	1.10	5.46
Xa	0.34	6.56	0.44	0.30	1.08	5.48
Xb	0.34	6.05	0.44	0.30	1.08	4.97
8a	0.32	5.98	0.41	0.28	1.00	4.97
8b	0.32	5.82	0.41	0.28	1.00	4.81
9a	0.30	5.76	0.39	0.26	0.96	4.80
9b	0.30	5.55	0.39	0.26	0.96	4.59
11a	0.30	5.32	0.38	0.26	0.94	4.39
11b	0.30	5.30	0.38	0.26	0.94	4.36
10a	0.29	5.01	0.38	0.25	0.93	4.08
10b	0.29	4.73	0.38	0.25	0.93	3.80
12a	0.29	4.62	0.38	0.25	0.92	3.69
12b	0.29	4.60	0.38	0.25	0.92	3.67
13a	0.25	4.38	0.32	0.22	0.79	3.59
13b	0.25	4.32	0.32	0.22	0.79	3.53
14a	0.23	4.20	0.30	0.20	0.74	3.46
14b	0.23	4.20	0.30	0.20	0.74	3.46
15a	0.22	4.17	0.29	0.19	0.71	3.46
15b	0.22	4.02	0.29	0.19	0.71	3.31
16a	0.20	3.93	0.26	0.17	0.63	3.30
16b	0.20	3.82	0.26	0.17	0.63	3.19
17a	0.18	3.72	0.24	0.16	0.58	3.14
17b	0.18	3.64	0.24	0.16	0.58	3.06
18a	0.18	3.41	0.23	0.15	0.56	2.85
18b	0.18	3.31	0.23	0.15	0.56	2.76
20a	0.14	3.17	0.18	0.12	0.45	2.72
20b	0.14	3.00	0.18	0.12	0.45	2.56
19a	0.13	2.77	0.17	0.11	0.41	2.36
19b	0.13	2.74	0.17	0.11	0.41	2.34
22a	0.11	1.58	0.14	0.10	0.35	1.23

22b	0.11	1.50	0.14	0.10	0.35	1.15
21a	0.10	1.05	0.13	0.09	0.32	0.73
21b	0.10	0.81	0.13	0.09	0.32	0.49

Table 4.3: Retrieved masses of all 46 chromosomes from a phase-contrast image of an unstained non-irradiated T-lymphocytes, exposed for 0.3 sec during X-ray imaging. It also shows the calculated expected masses, including the mass of DNA, histones, and non-histone proteins. The assumed position of XX are highlighted in blue. The mass gain is a difference of measured mass and the expected mass. The "a" and "b" labels in the first column states the homologous chromosomes in each pair.

	T-lymphocytes Masses (Picograms)	**B-lymphocytes Masses (Picograms)**
Base pairs	13.3	13.1
Histones	17.2	16.9
Non-histones	11.5	11.3
Expected mass	42	41.3
Measured mass	242	8.3
Mass gain	200	_
Mass loss	_	33

Table 4.4: Shows the mass of bp, proteins and the expected and measured masses of all 46 chromosomes in two different cells. The amount of mass gain (T-cells) and mass loss (B-cells).

Similarly, in the second experiment, calculated the measured and the expected mass of a spread obtained from a female primary T-cells. Here, a mass gain has been observed since the measured mass is higher than the expected mass. The mass gain has been calculated by subtracting the expected mass from the measured mass. Moreover, it can also be noted that the estimated expected mass of two homologous chromosomes in a spread has the same mass, but the measured mass differs between two homologous pairs (Table 4.3).

The mass of DNA content for the complete set of female diploid human chromosomes is 6.64 pg. (Doležel *et al.*, 2003) (Piovesan *et al.*, 2019). The chromosome spreads were exposed to an X-ray dose for 0.3 sec while scanning

the silicon nitride membrane containing the sample. Table 4.4 shows the difference in the masses of expected and measured mass of DNA and associated chromosomal proteins between two spreads of two different cells. The mass gain (Table 4.3) observed could be from the additional chromosomal proteins and trapped buffers on the surfaces of the silicon nitride membrane. There is also the important question of possible DNA components missing from the human genome sequence.

4.7. Discussion

In this chapter, the measurements of individual chromosome masses have been presented that were obtained from high-resolution phase-contrast reconstruction using hard X-ray ptychography. The use of “spreads”, in which all chromosomes from a given cell are measured together, allowed us to create “X-ray karyotypes” of fixed human metaphase chromosomes. The chosen biological sample is a human chromosome obtained from B and T-cells, and the karyotype has been performed on both stained and unstained chromosome spreads. In addition, the X-ray karyotypes have also been implemented on the X-ray radiation-induced chromosomes at relevant doses of 0.1 Gy, 0.5 Gy and 1 Gy to investigate the gain or loss of DNA-protein complex. Moreover, the karyotype was also done on chromosome spreads with different exposure time intervals during scanning, 0.3 sec, 0.6 sec and 0.9 sec, one after the other.

In the literature, the chromosomes are karyotyped based on morphology, volume and the DNA content using techniques such as M-FISH (Yusuf et al., 2011) (Anderson, Stevens and Goodhead, 2002), SBFSEM (Chen et al., 2017) and flow cytometry (Harris et al., 1986), respectively. Following this, it was decided to introduce the X-ray karyotype method based on the ranking of chromosome masses for both radiation-induced and non-irradiated chromosomes. The plotted mass karyotype graphs show a linear relationship between measured mass and the known DNA content present in each chromosome. The X-ray phase contrast imaging is a direct measure of the electron density of the chromosomal material at that location. Once segmented

in the image, the 2D integral of the phase shift over the isolated object directly measures the amount of matter present.

4.7.1. Mass quantification of stained and unstained metaphase chromosomes

Our first approach was to karyotype fixed human metaphase chromosomes stained with heavy atom elements to obtain better phase-contrast images. The 1 % Uranyl Acetate and the 6 mM platinum blue stain enhances the phase-contrast upon the presence of electron density map, which prevails scattering (Cao, Xu and Mao, 2011) (Carlo and Harris, 2012) (Yusuf, Millas, *et al.*, 2014). Although the UA is radioactive and toxic to the biological specimen, it disturbs the protein-protein/DNA-protein interactions and induces conformational changes (Lin, 2020). Moreover, it can form microcrystals once dried on the substrate (Carlo and Harris, 2012). Consequently, the less toxic platinum blue stain is a preferred substitute for Uranyl Acetate in TEM and SEM imaging (Inaga *et al.*, 2007), (Wanner and Formanek, 1995). One purpose of staining is to precipitate a thin layer deposit of electron density on the sample to enhance photon/electron scattering of the X-ray/electron beam (Wanner and Formanek, 1995).

The staining of a complete set of weak scattering chromosome spreads at high resolution served to calibrate the hard X-ray ptychography imaging technique at room temperature. Thereafter, applied the same technique to image unstained chromosome spreads and built a karyotype of a full chromosome spread ranked according to their component masses. The total mass for 1 % UA, 6 mM platinum stain and unstained chromosomes were 13.18 pg, 22.18 pg and 8.26 pg, respectively, obtained in the first experiment.

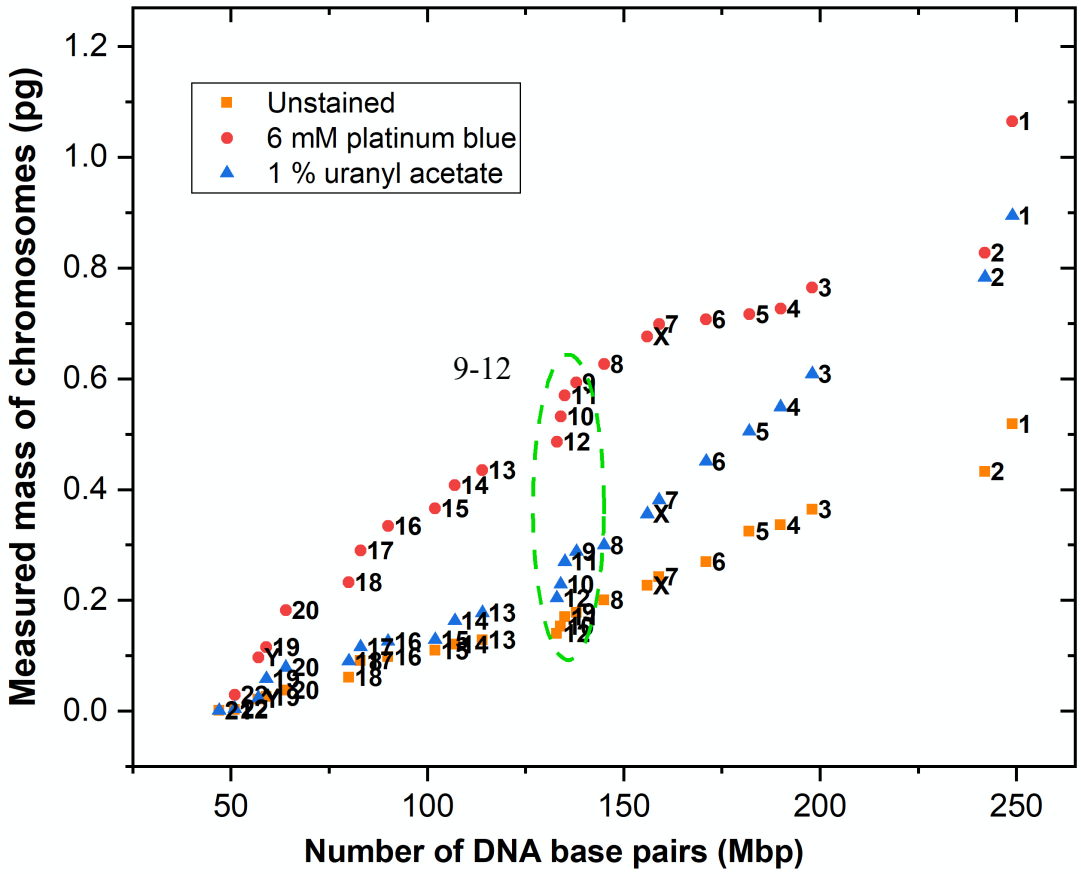

Figure 4.10: The X-ray karyotype comapares the measured masses of individual chromosomes, stained with heavy metals and unstained. The masses were retrived from the ptychography phase images of B-lymphocytes cells. The green dashed oval encircles the region of chromosomes 9-12, from each spread.

In the X-ray mass karyotypes from both stained and unstained chromosome spreads (Figure 4.10), it is observed that the larger chromosomes, 1-2 have the highest variability among their homologs, followed by chromosomes 3-6, perhaps due to their enormous base pair ratio and for smaller chromosomes the variability of base pair ratio decreases. Similar phenomena were observed in all 24-chromosomes, labelled with quinacrine and its brightness, observed by autoradiography (Korenberg and Engels, 1978). The brightness indicates the amount of AT base pairs present in each chromosome, and the Y-chromosome shows the highest base pair ratio than the other chromosomes (Korenberg and Engels, 1978). Moreover, the base ratios also differ between the segments of a chromosome and among a full set of chromosomes (Korenberg and Engels, 1978). The other quantitative karyotyping techniques, including bivariate flow cytometry approaches, do not

resolve chromosomes 9-12, perhaps because of their similar DNA content and the base pair compositions (Mendelsohn *et al.*, 1973) (Korenberg and Engels, 1978) (Langlois *et al.*, 1982) (Boschman *et al.*, 1991). Two-colour flow cytometry with different dyes allows separations of these chromosomes.

The phase contrast imaging technique is adequately sensitive to resolve the relative masses of chromosomes 9-12 in linear regression karyotypes (Figure 4.10). This method gives the total mass of DNA content and chromosomal proteins present. This could explain why the masses of chromosomes 9-12 differ significantly and can be easily distinguished in linear regression. The green oval (Figure 4.10) indicates the concentrated data points of chromosomes 9-12, where the measured masses are well-separated in contrast to their similar genome lengths.

In Figure 4.10, it is clearly seen that stained chromosomes are approximately 2–3 times heavier in their measured masses, relative to the unstained example, with some notable differences in the magnitude of the staining effect on different chromosomes. Heavy atom staining can add up to 100% more mass to stained chromosomes, according to the finding. There are differential staining effects visible between the UA and Pt-blue agents. The heaviest chromosomes are stained almost equally, while the intermediate masses, particularly the tightly bunched region of chromosomes 9–12 (green dashed oval in Fig. 4.10), show differences close to a factor of three. The lower mass chromosomes are almost unaffected by UA, while Pt-blue preferentially stains them. It is likely that differential staining may have affected the numerical identification of chromosomes based on the ranking of their masses, but it is noted that the clustering of chromosomes 9–12 is preserved by the staining in both cases. The potential benefit of heavy metal stains is improving the contrast of the weak scattering biological sample, which has been observed for both the stains used.

In the second round of the experiment, the following improvements of the reconstruction algorithms (Batey, 2014) and the use of more freshly prepared samples. The sufficient sensitivity enabled the need to drop the staining and

perform the whole radiation dose experiment with unstained chromosome spreads. The X-ray phase shifts recorded from the images of the second experiment range up to 0.06 radians, which is a direct measure of the electron density of the chromosomal material at that location. The values recorded in the first experiment were only 0.01 radians. It is noteworthy that the average phase values (and hence mass numbers discussed in the chapter) emerging from the second experiment were an order of magnitude higher than those from the first experiment. This discrepancy, which was noticed immediately in the apparent contrast of the raw ptychography images, is not fully explained. The experiments were separate runs at Diamond, about a year apart, and both the measurement and reconstruction methods improved considerably over that time. But this would be expected only to improve the efficiency and not the phase contrast values, which should be highly quantitative.

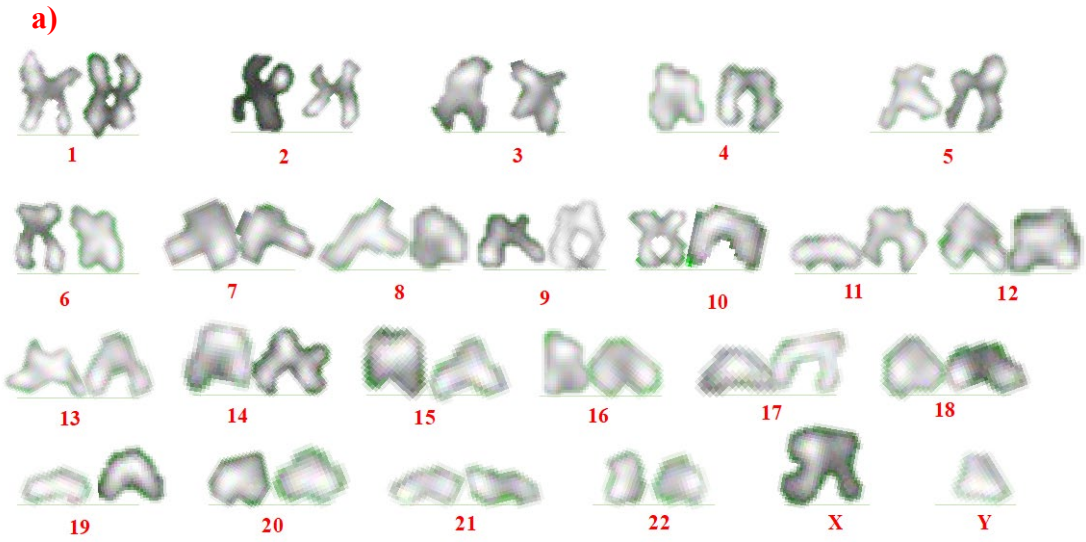

Figure 4.11: Segmented chromosomes from a single spread, imaged by X-ray ptychography and arranged based on their individual masses; the numbers shown below indicates the position of each homologous pair of chromosomes. The following chromosomes were extracted from unstained non-irradiated a) B-cells measured during the first experiment and b) T-cells measured during the second experiment.

The knowledge of the weights allows a fully quantitative X-ray karyotype to be generated since the number of DNA base pairs is known for each of the chromosomes in the human genome sequence. Furthermore, to test the accuracy of the method (hard X-ray ptychography imaging), the 2D integral of the phase shift over the isolated objects was segmented individually in the ImageJ software. And once the chromosomes were segmented in the image, then the following segmented images were processed in the software using the following tools: i) converted into a 16 bits image, ii) subtracted the background, iii) adjusted the threshold and iv) inverted the pixel values by using a tool called “invert LUT (Look-Up Table)”. Eventually, by arranging into a descending order according to the obtained measured masses, the X-ray karyotypes of both the B and T-lymphocytes cells as shown in Figure 4.11.

Afterwards, the chromosomes from groups A (chromosomes 1-3) and B (chromosomes 4 and 5) can be reliably karyotyped, similar to the conventional methods (Figure 1.6) of chromosome karyotyping. However, for the smaller chromosomes, we can observe some shuffling among them, by visualising morphologically (Figure 4.11). According to our hypothesis, the alteration in the karyotype differs from what is conventional seen by G-banding. This is probably due to the presence of a different concentration of chromosomal proteins in each chromosome and their homologs as the phase shift gives a direct measure of the amount of matter present (Shemilt et al., 2015), which has not been elucidated so far according to our knowledge.

Although, it is known that the amount of histones, non-histones, and other chromosomal proteins that are illustrated by Uchiyama *et al.* (2005), has been performed on the aggregates of metaphase human chromosomes (Uchiyama *et al.*, 2005). In future, correlative imaging can be achieved by accompanying immunolabelling and M-FISH technique on fixed human metaphase chromosomes (Shemilt *et al.*, 2015). Followed by coherent X-ray scanning on

the same spread to independently verify the X-ray karyotype of chromosomes, including larger to smaller chromosomes. Moreover, the minor segmentation changes were found in the assignment of chromosome numbers, mostly in the closely spaced 9-12 region. The reconstruction error was not found, but the phase shift values were different between two separate experiments (see statistical analysis and error estimation, section 4.8). This discrepancy, which was noticed immediately in the phase contrast of the raw ptychography images, is not fully explained.

A significant difference in the measured mass of non-irradiated unstained B and T-cells was found in this study. The masses are 8.3 pg for B-cells and 242 pg for T-cells. The following could be the reasons: firstly, the chromosomes obtained were from the stored B-lymphocytes cell line, whereas the chromosomes were freshly prepared from primary T-lymphocytes. Apparently, this could lead to a difference in epigenetics. In addition, the B-cells were from a long-term propagated subculture with passage 15.

On the other hand, T-cells were only short-term propagated from a subculture with passage 3. However, the former subculture is reported to undergo genomic instability and probably has an imbalance of the DNA content and histone modifications compared to the latter (Hiorns *et al.*, 2004). The chromosomes acquired from B-cells were stored in methanol acetic acid, with a ratio of 3:1 for 5-6 months in the fridge. According to Ronne *et al.* (1979), the methanol: acetic acid (3:1) fixation degrades histones and other relative chromosomal proteins and increases the length of the chromosomes. Prolonged fixation has a higher effect on epigenetics (Ronne, Andersen and Erlandsen, 1979). Most likely, the H1 histone protein is the most affected one in the methanol acetic acid fixation and apparently changes its conformation due to protonated phosphate groups of DNA (Duijn, Prooijen-Knegt and Ploeg, 1985).

Secondly, the chromosomes obtained from B-cells and T-cells are from two different experiments performed separately at different time intervals in the same beamline line (I-13-1, DLS, Oxford, UK) at room temperature. The mass

differences between the two separate experiments were observed. The masses obtained from T-cells are ~30x higher than the B-cells. It is noted that during the X-ray scanning, while collecting diffraction patterns for the quantitative analysis, the B-cells and the T-cells chromosome spreads were exposed for 1.00 sec and 0.3 sec, respectively. Lastly, the radiosensitivity of B-cells to the aberrations compared to T-cells with direct X-ray scanning while imaging (Heylmann *et al.*, 2014), even after the chemical fixation.

4.7.2. Ionising radiation affects the mass content of the metaphase chromosomes.

The X-ray ptychography technology gives us a powerful way to connect between known human genome sequence and the measured masses of the obtained chromosomes. Following the X-ray karyotype of fixed human metaphase chromosomes of heavy atom stained (Figure 4.4) and non-irradiated chromosomes (Figure 4.5 and Figure 4.6). The second series of experiments to X-ray karyotype the X-ray induced chromosomes was carried out at different radiation doses, 0.1 Gy (Figure 4.7), 0.5 Gy (Figure 4.8) and 1 Gy (Figure 4.9), irradiated at a dose rate of 0.5 Gy/min (see chapter 2, Materials and Methods). To distinguish the mass difference between non-irradiated and irradiated chromosomes and if the content of DNA and chromosomal proteins alters and can be picked up by the quantitative X-ray karyotype.

In a typical human cell cycle, before, a nucleus will consist of 46 chromatids before the DNA synthesis in S-phase. After that, it will replicate to 92 chromatids before separation at anaphase to form two daughter cells (Figure 1.5). On the other hand, the protein content differs at different stages of the cell cycle (Gookin *et al.*, 2017), such as protein from the minichromosome maintenance (MCM) family that binds to the replicating point of the DNA at the G1-phase and then it disappears once the replication starts (Forsburg, 2004). Similarly, condensin and topoisomerase II**α** proteins are involved in the condensation and decatenation of chromosomes which appears at the S-phase after DNA replication and disintegrate once the chromosomes are segregated

properly at anaphase (Charbin, Bouchoux and Uhlmann, 2014). Above all, the core histone proteins are always present, which forms a DNA-protein complex (Maeshima and Eltsov, 2008). Moreover, 209 interphase proteins and 107 metaphase proteins were identified in humans depending on their localisation and function, respectively (Uchiyama *et al.*, 2005).

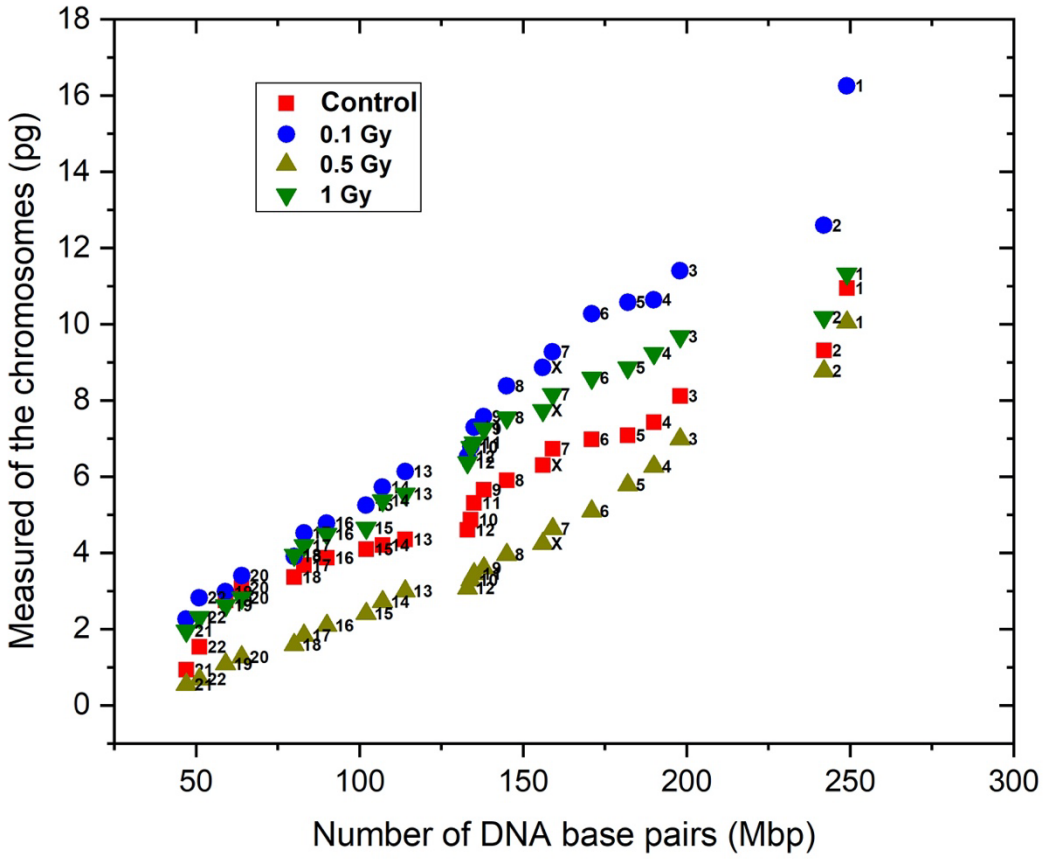

Figure 4.12: Average mass of each homologous pair of chromosomes segmented from the phase image of unstained chromosomes of irradiated chromosome compared to non-irradiated chromosomes. Chromosomes were obtained from T-lymphocytes, and the spreads shown were exposed for 0.3 sec during X-ray scanning.

Figure 4.12 indicates the effect of ionising radiation on the acquired measured masses of a full set of chromosomes. One hypothesis is that it should show a decreasing trend in mass with increased induced X-ray irradiation doses, potentially due to various DNA lesions (Borrego-Soto et al., 2015) and protein modifications upon X-ray doses (Reisz et al., 2014) (Lowe et al., 2020). With 0.1 Gy and 1 Gy, the total obtained quantitative masses are 336.53 pg and 293.12 pg, respectively; a noticeable increase in mass can be spotted relative

to non-irradiated chromosome spread, which is 242.21 pg, whereas, at 0.5 Gy dose, the measured mass decrease to 172.90 pg.

To understand these results, it is considered that, upon irradiation, various stress-responsive enzymes and proteins come into an action, including DNA-PKs, 53BP1, Ku70/Ku80 (Biau *et al.*, 2019) and the DNA damage response signalling pathway activates NHEJ and HRR mechanisms to repair the DNA lesions (Mahaney, Meek and Lees-Miller, 2009). Immediately after radiation exposure, the cell cycle checkpoints response with the inclusion of related proteins comes into play (Mahaney, Meek and Lees-Miller, 2009). It has been observed in the male germ cells, that with increased doses of ionising radiation, the DSB number increases; on the other hand, the repair mechanism activates and repairs the lesions within 4 to 16 hours (Singh *et al.*, 2018). Therefore, it can be postulated that the extra mass may be added to the irradiated chromosome spreads, which could be because of the proteins and enzymes coming into play to initiate the repair mechanism of the various DNA lesions that occurred immediately after the irradiation at a 0.1 Gy dose. However, this does not explain the lower masses found at the 0.5 Gy dose which, interestingly, has relatively low mass compared to non-irradiated chromosomes and other chosen X-ray doses.

The observation is that by using ptychography, the mass of the chromosomes is seen to increase upon irradiation at 0.1 Gy compared to 0.5 Gy and higher is unusual. However, it is speculated that, since the adaptive response to low dose irradiation (< 0.1 Gy) or low dose rate (0.06 mSv/h) has been reported to increase certain cell proliferation (von Sallmann, 1952), a similar process may apply to DNA induction, but this is yet untested or unknown. It is worth noting that in a separate technique using fluorescence lifetime imaging microscopy, a correlation has been shown between 0.1 Gy radiation–induced excited state lifetime decrease over 0.5 Gy and non-radiation of cell chromosomes (Chapter 3 of the thesis), thus indicating an effect on chromosomes following ionising radiation at 0.1 Gy. Low-dose irradiation is thought to induce an adaptive or hormetic response under certain conditions

(Luckey, 2006; van Wyngaarden & Pauwels, 1995). Further studies are needed to characterise these effects fully.

Furthermore, in the literature, the radiosensitivity of the immune cells has been studied from low-dose radiotherapy (LDRT) to high-dose radiotherapy (HDRT) and has shown that the viability of the cells decreases after 1 Gy exposure and the aberration increases. Consequently, apoptosis and cell death occur at doses above 10 Gy (Falcke *et al.*, 2018). Nevertheless, continuous exposure to ionising radiation leads to histone protein degradation up to 40 % after irradiating with the dose rate of 6 mGy/hr to 20 mGy/hr for 7 days (Lowe *et al.*, 2020).

4.7.3. Effect of radiation upon longer exposure

As a follow-up investigation, measured the quantitative masses at discrete intervals of exposure time used in the ptychography measurement. The same methanol: acetic acid (3:1) fixed human metaphase chromosome spread was scanned for three different image exposure times in sequence, 0.3 sec, 0.6 sec and 0.9 sec. Then collected the diffraction patterns from both irradiated (0.1 Gy, 0.5 Gy and 1 Gy) and non-irradiated (control) chromosomes. In Figure 4.13, 22 pairs of autosomes and one pair of sex chromosomes (XX) are listed. The mass of each chromosome is the averaged mass of two homologous chromosomes obtained from primary T-lymphocytes.

In Figure 4.13, the box plot depicts the following information; the big box shows the distribution of 50 % of the data points, and the upper and lower whiskers define the maxima and minima, respectively. The median line and the small box inside the big box are the median and the average distribution values, respectively. The data points are the acquired measured masses of fixed human metaphase chromosomes from T-lymphocytes.

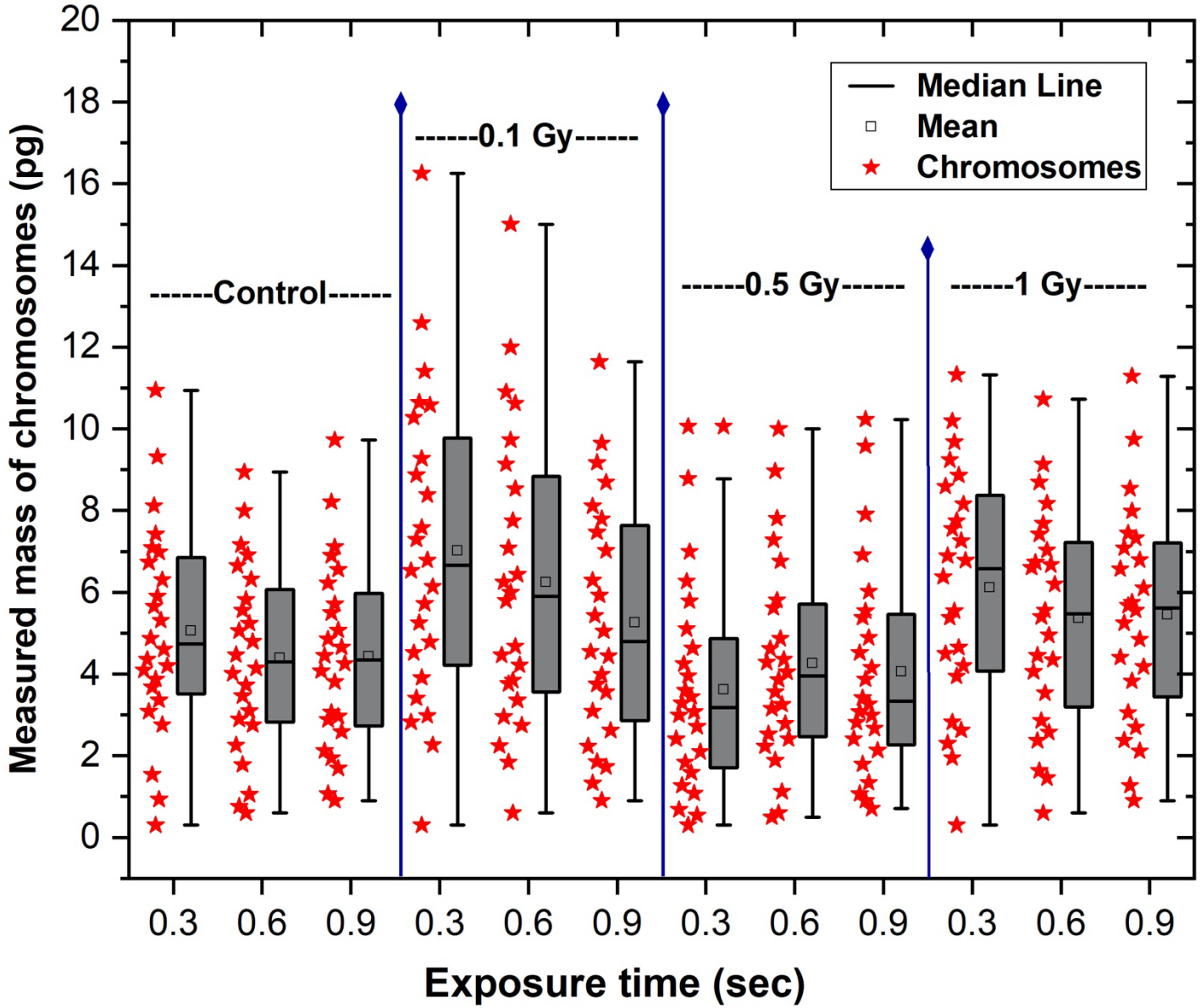

Figure 4.13: Measured mass of chromosomes from reconstructed phase images of non-irradiated and irradiated chromosomes spreads (n=1). The x-axis represents the exposure time to each sample during imaging. The red stars show the averaged masses of homologous pairs (22, XX) chromosomes from different spreads of different sample. The boxes alongside of red stars represents the maximum and minimum values of each spread. The mean and the median lines are also shown inside the boxes of a figure.

High-resolution X-ray ptychography images, <100 nm, of fixed human metaphase chromosomes were used to measure masses of each segmented chromosome to build an X-ray karyotype. Chromosome spreads laid on the silicon nitride membrane were scanned at room temperature and direct exposure to the X-ray radiation, leading to mass loss at every scan for both irradiated and non-irradiated (control) samples. For the control sample, the summed masses (of all 46 chromosomes at the metaphase stage) at different intervals are 242 pg, 210 pg and 211 pg for 0.3 sec, 0.6 sec and 0.9 sec, respectively. Thus, a ~1.2-fold decrease in mass has been observed for 0.6 sec and 0.9 sec. Longer exposure to ionising radiation leads to the destruction of the biological samples (Reisz *et al.*, 2014) (Lowe *et al.*, 2020) while scanning at room temperature without any cryoprotectant. Henceforth, cryo-imaging is the future of biological imaging (Yusuf *et al.*, 2017) (Yusuf *et al.*, 2019).

The increased measured masses were observed at 0.1 Gy and 1 Gy relatively to the non-irradiated sample and 0.5 Gy X-ray dose (Figure 4.12 and Figure 4.13). Moreover, a decrease with exposure sequence was observed in the measured masses, which was similarly observed for 0.1 Gy and 1 Gy irradiations. The summed masses for 0.1 Gy irradiation were 337 pg, 299 pg. and 251 pg. at 0.3 sec, 0.6 sec and 0.9 sec, while at 1 Gy, they were 293 pg, 257 pg and 260 pg, respectively. However, the summed masses at 0.5 Gy dose were 173 pg, 203 pg and 193 pg at 0.3 sec, 0.6 sec and 0.9 sec, respectively, suggesting an increasing trend. It may be that the results of Figure 4.13 mainly reflect the overall reproducibility of the mass determination experiment, at the level of about 10%, without any significant effect of exposure time over the range studied. However, the increase in measured masses observed at 0.1 Gy and 1 Gy relative to the non-irradiated control sample is statistically significant at all exposure times and supports our hypothesis of the immediate initiation of cell cycle checkpoint responses and the activation of DNA damage repair protein signalling pathway, which add mass to the irradiated chromosomes (Huang & Zhou, 2020). In the study of Neumaier *et al.*, (2012), it has been shown that “Radiation-induced foci” (RIF) were more at 0.1 Gy (64 RIF/Gy) dose compared to 1 Gy (23 RIF/Gy) dose, which means the number of DSBs is independent of irradiation doses in human

cells at low dose levels. Apparently, relative DNA repair proteins start the repair mechanism after IR exposure.

4.8. Statistical analysis and error estimations

Each spread took about 3 hrs to measure. This was mostly spent cross correlating the optical images to locate well-isolated spreads, then performing a series of quick scans to centre them in the available field of view (FoV) of the ptychographic scan before the final measurement. Since it is depended on capturing a complete set of 46 chromosomes in order to rank the masses into a karyotype safely, it was important that one or more chromosomes had not strayed far from the FoV that it might be accidentally associated with another spread. It was also found that the segmentation step was occasionally ambiguous, making it hard to divide two overlapping or touching chromosomes. For these reasons, more than half of the results had to be discarded, and we were sometimes left with just one good example of a well-measured ‘spread’ for given sample preparation.

Because the beamtime at Diamond Light Source was challenging to get and limited in duration to two experimental runs, there was not enough time to measure a large number of ‘spreads’ from each chromosome preparation and do a full statistical analysis of the variations of the masses. The focus was on looking at a single series of samples from the irradiation experiments. Better statistical and additional analysis is planned for the future.

Fortunately, managed to measure the reproducibility of all the major steps of the mass determination itself. The ptychography measurement was repeated three times with different exposures (Figure 4.14). The images were reconstructed independently and integrated separately to give independent mass karyotypes. When the segmentation was performed independently on each image, only minor changes were found in the assignment of chromosome numbers, mostly in the closely spaced 9-12 region. It was found that, within error, there was no significant mass loss due to X-ray exposure from one measurement to the next. The mass distributions were reproducible with an asymmetric tail on

the high mass side: the mean was higher than the median in all cases except the highest irradiation level, where it reversed. In that highest dose example, where the mass distribution had become changed to a more symmetric one, the observation was reproducible over the three exposure times.

The delay or phase observed is directly related to the material's electron density and is used to determine the mass of the chromosomes. Phase measurement of chromosome 1 from three images of the same chromosome spread (Figure 4.14) taken sequentially (with different exposure times) shows the reproducibility of the phase values. The average phase values from chromosome 1 were 33 ± 14, 33 ± 11, and 41 ± 17 at 0.3 sec, 0.6 sec and 0.9 sec, respectively. The obtained phase values were taken from 10 different positions in a single chromosome 1 from three images of the same chromosome spread taken sequentially (Figure 4.14). The background phase surrounding the chromosome has been subtracted. The error given by the standard deviation is overestimated because it includes sampling of the natural density variations within the chosen chromosome. Therefore, the ptychographic mass estimate is quite reliable.

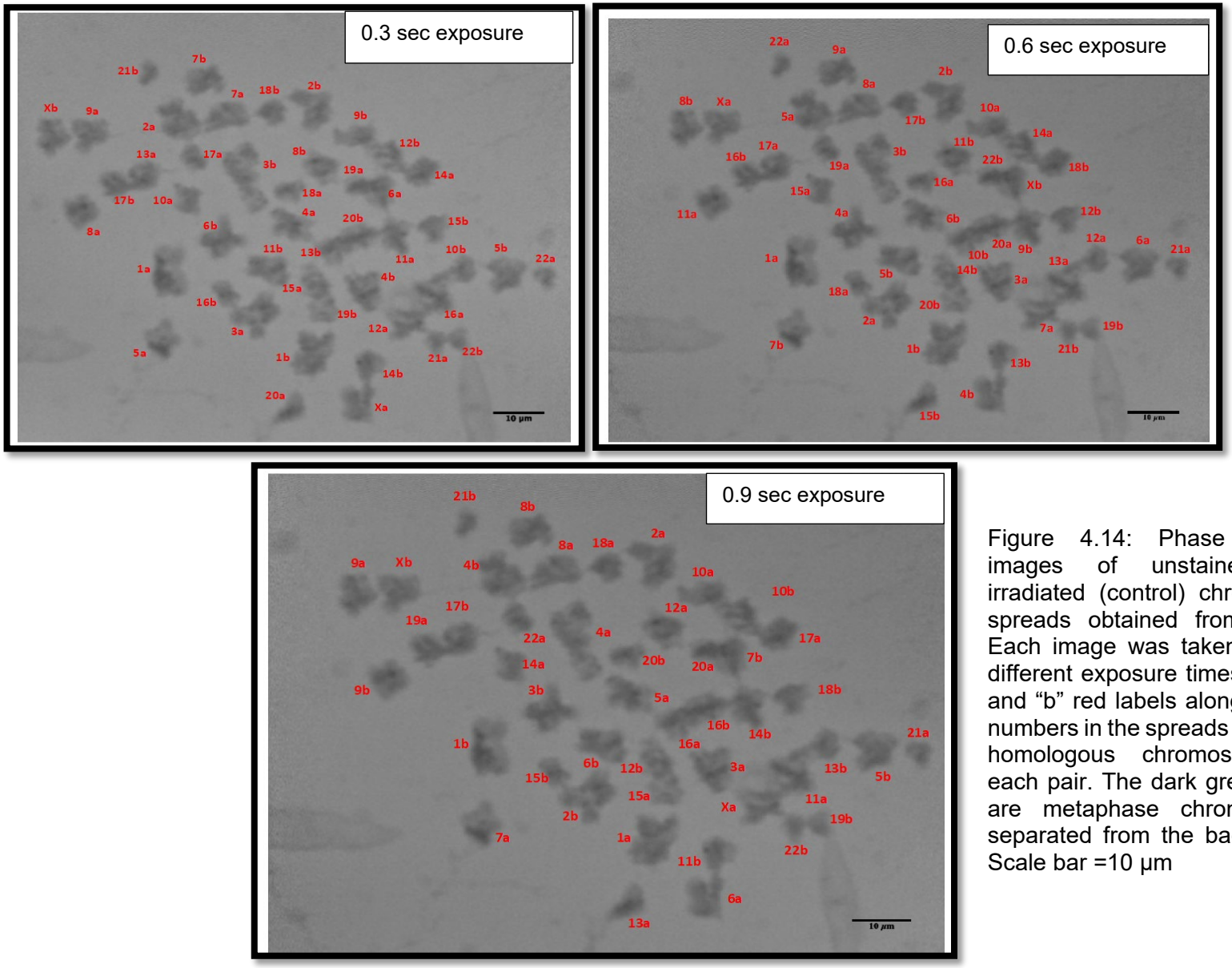

Figure 4.14: Phase retrieval images of unstained non-irradiated (control) chromosome spreads obtained from T-cells. Each image was taken at three different exposure times. The “a” and “b” red labels along with the numbers in the spreads states the homologous chromosomes in each pair. The dark grey objects are metaphase chromosomes, separated from the background. Scale bar =10 µm

	Error plot	Object_phase	Probe
Control	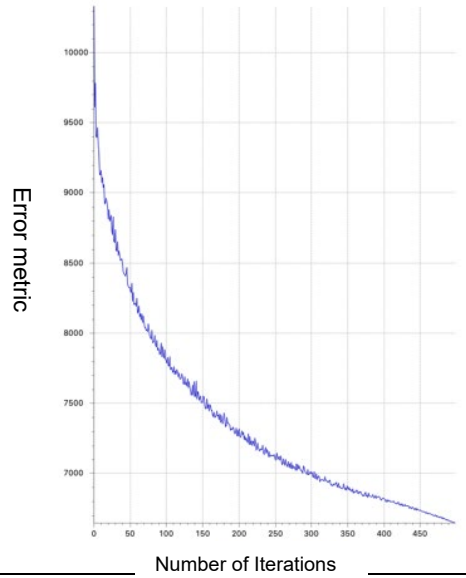	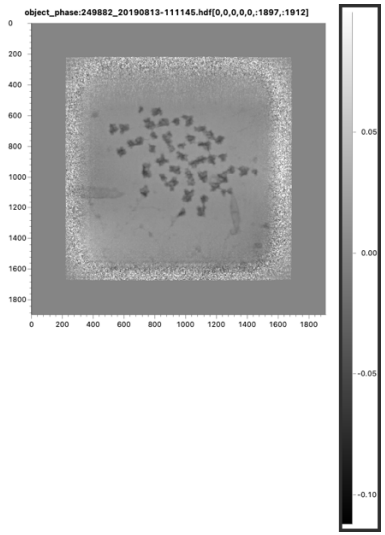	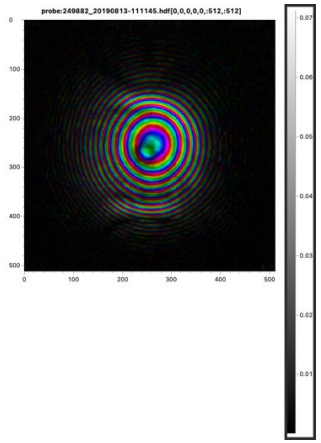

0.1 Gy	Error metric 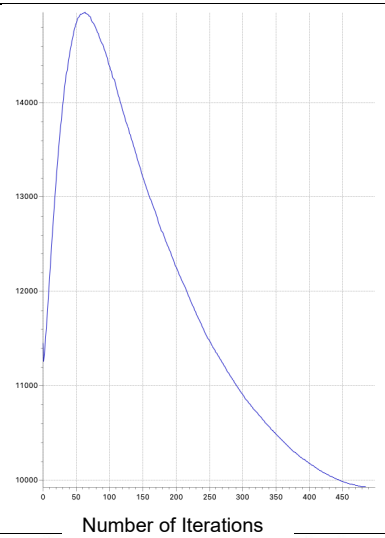 Number of Iterations	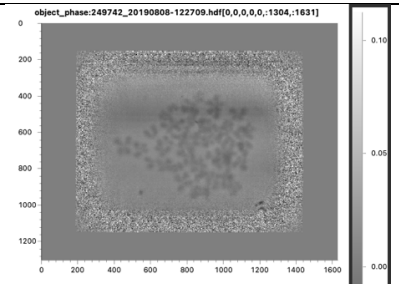 	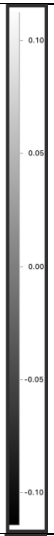	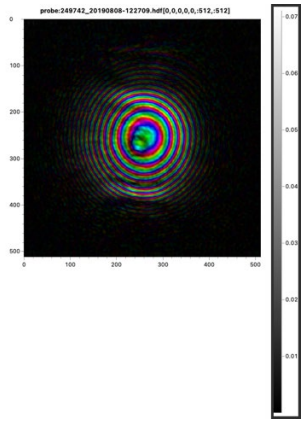
0.5 Gy	Error metric 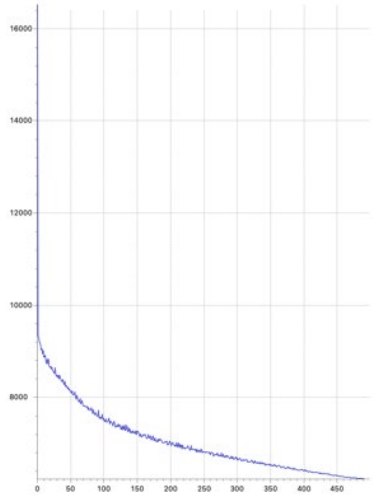 Number of Iterations	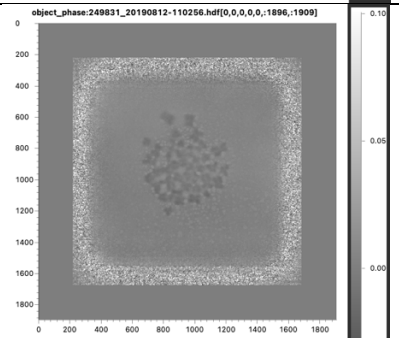 	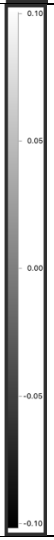	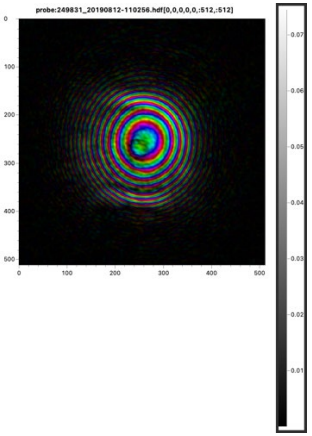

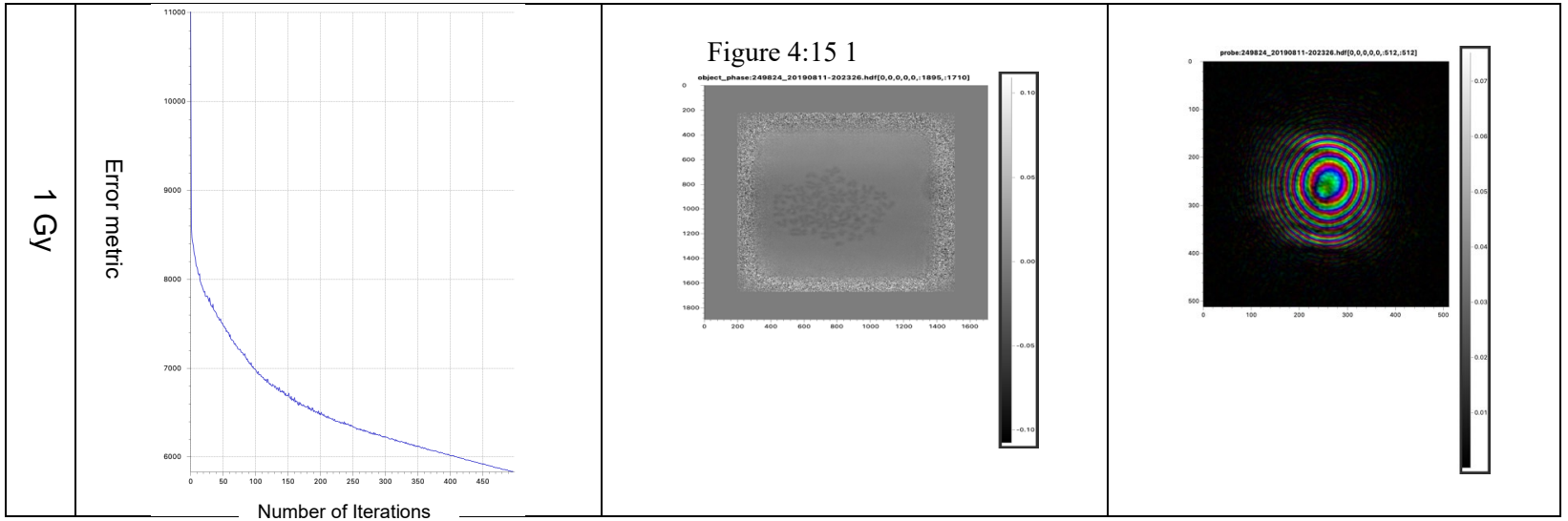

Figure 4.15: Error metrics over 500 iterations of chromosome spreads obtained from T-cells. The rows show the control sample and with different radiation doses, and the columns show the error plot, retrieval phase image and the probe of the respective samples.

The unstained chromosome spreads of each sample show good convergence over 500 iterations (Figure 4.15). The control sample and the 1 Gy show good convergence and a clear phase image. However, with the 0.1 Gy sample, the ePIE algorithms did not update the probe during the first 70 iterations and so did not converge well like others (Figure 4.15) or there might be a sample issue that makes phase image slightly blurred. There was also a beam top-up issue which may have led to dark stripes in the images, possibly from poor normalisation. Moreover, with the 0.5 Gy sample using the error reduction method, a good convergence was observed, but still, it gives a slightly blurred phase image, possibly due to the deposition of buffer on the TEM grid (white patches). Overall, it is noted that the background pixels were subtracted from each image to minimise the error in the mass calculation. Each chromosome was segmented to measure the pixels that were converted to masses. It is noted that the chosen 500 iterations to obtain good quality phase images is based on experience with the ptychography algorithm applied to other samples. This is the first attempt to measure the mass of the complete set of chromosomes using ptychography; more future experiments and additional analysis will be helpful to answer why some images are blurred and have dark stripes.

4.9. Summary

This work demonstrates the ability to extract the individual masses of complete metaphase human chromosome spreads using two-dimensional phase-contrast images and builds the X-ray Karyotype. The successful combination of scanning X-ray ptychography technologies allows us to measure the masses of stained and unstained metaphase human chromosomes at room temperature. It strongly correlates between the known genome sequence and the measured mass of the chromosomes obtained using X-ray ptychography.

X-ray ptychography is a useful technique to determine the total genome mass of a species, including DNA and the related chromosomal proteins present at the different stages of the cell cycle without invasive staining. Any improvements in chromosome imaging would be precious in medical research to diagnose cancer and other diseases.

The quantitative information obtained from X-ray ptychography images allowed us to measure the masses from Uranyl Acetate and platinum blue stained chromosome spreads obtained from the B-cells. Subsequently, an X-ray karyotype is built according to the mass ranking of the chromosomes in a spread and build an X-ray karyotype. The same procedure was applied to extract the masses from the unstained X-ray induced chromosome spreads obtained from T-cells. Moreover, the X-ray karyotype was also built from the chromosome spreads with the three different exposure times. The obtained images were reconstructed independently and integrated separately to give independent mass karyotypes.

The individual measured masses of isolated chromosomes provided information on their DNA content along with the relative chromosomal proteins that are divided into histones and non-histones. Henceforth, the measured and expected masses of each chromosome can be determined. Furthermore, with the X-ray ptychography, the difference in masses of all 46 human chromosomes can be visualised in a linear regression plot, including chromosomes 9-12, which

is impossible in two-colour flow cytometry because of their very similar DNA content.

Chapter 5

5. General discussions and conclusions

X-ray irradiation remains a vital component for shrinking/killing cancer cells by causing DNA breaks such as dsDNA. In addition, decreasing the efficiency of the DNA-damage repair mechanism that starts straight after radiation exposure (Borrego-Soto, Ortiz-López and Rojas-Martínez, 2015) (Falcke *et al.*, 2018) (Shimura and Kojima, 2018) (Singh *et al.*, 2018). X-ray irradiation is helpful in the diagnosis and treatment of diseases. For example, computed tomography (CT) scans use millisievert (mSv) doses for routine check-ups in hospitals to identify unusual characteristics in human cells (Linet *et al.*, 2012). Although, after a decade of investigation, the effect of low dose ionising radiation on the structure of chromosomes has been poorly understood. In the current thesis, the structure of human chromosomes has been examined using advanced and emerging microscopy methods, namely FLIM and X-ray ptychography.

In this thesis, both the imaging methods have been explained. For example, variation in DAPI lifetime along the length of the metaphase chromosomes has been shown using FLIM, combined with multiphoton microscopy. As well as measured the masses of the chromosome spreads using phase-contrast X-ray ptychography imaging technique. Studies on DNA oligonucleotides indicate that base sequence effects leading to a difference in lifetime seen by FLIM cannot be ruled out. It was important to have the full karyotype present in the X-ray ptychography experiment in order to identify the entire genome.

Furthermore, the effect of X-ray induced chromosomes in the genome was also examined. FLIM is a valuable method for providing information on the heteromorphic regions of the fixed human metaphase chromosomes showing lifetime differences with low-level X-ray irradiation. Also, the lifetime variation was observed at different passages of the cell culture in both heteromorphic as well

as in all 46 fixed human metaphase chromosomes. This indicates that the X-ray induced chromosomes at different passages may have undergone some chemical alterations which are observed by FLIM.

The lifetime variations and the mass measurement did not show a continuous trend which means the effect of irradiation is independent at low radiation doses. Although chromosomal breaks such as DSBs number increase with increasing irradiation doses. The effect of low-level irradiation doses observed in the fixed human metaphase chromosomes could be due to chemical perturbations that occurred in the chromosomes. The DAPI lifetime variation and the difference in the masses of all 46 chromosomes present in the chromosome spreads were also observed in the X-ray induced chromosomes. In addition, M-FISH aids in identifying each chromosome in a spread on which FLIM was already performed. The purpose of the correlative imaging was to detect any inter-chromosomal aberrations that occurred upon irradiation as well as to observe fluorescence decay maps along the length of all 46 chromosomes to investigate the structural abnormalities at the nanosecond time scale of fluorescence decay upon excitation.

Time-domain FLIM or FLIM-FRET are a very useful tool to investigate the molecular environment of the chromosomes under environmental stress; for example, lifetime variation was observed due to loss of histones (Sherrard *et al.*, 2018), calcium ion regulation in chromatin (Phengchat *et al.*, 2016), physical change in the chromatin (Estandarte *et al.*, 2016) and effect of irradiation at higher X-ray dose (Abdollahi, Taucher-Scholz and Jakob, 2018). In this work, in chapter 3, ionising radiation is applied to understand the nature of the high-order structure of mitotic chromosomes under oxidative stress conditions. The FLIM and the mass measurement were performed on the X-ray induced chromosomes at 0.1 Gy, 0.5 Gy and 1 Gy radiation doses. Typically, the number of chromosomal aberrations increases with increasing dose. This study, observed that the 0.5 Gy irradiated chromosomes showed the lowest lifetime values, but that 0.1 Gy showed increased lifetime values, followed by 1 Gy. Although there is no significant difference between the lifetime values of all three radiation doses,

however, there is a significant difference in the lifetime values compared to the non-irradiated samples.

The averaged lifetime of all 46 chromosomes from five independent chromosome spreads was measured, and the DAPI lifetime values from different radiation doses followed a sequence of; 0.5 Gy>0.1 Gy>1 Gy. It can be assumed that the chromosome under chemical or molecular stress behaves differently at different low-level irradiation doses. The same pattern of lifetime variation was observed with heterochromatin and non-heterochromatin regions of the chromosomes when all 46 chromosomes were considered.

Intense beams of ionising radiation disturb the chemistry of DNA and affect the sub-regions of the chromosomes that include the evolutionarily conserved regions of heteromorphic chromosomes. Therefore, it could be predicted that the disturbance in the chemistry of affected DNA leads to variation in DAPI lifetime and possibly a change in the mass measurement of the chromosomes upon the onset of the DNA repair mechanism after low-dose radiation exposure.

In chapter 3, the reduced lifetime was maintained in heteromorphic chromosomes. This agrees with the other cell lines and also in cancerous cells (Estandarte *et al.*, 2016). In addition, the reduced lifetime was also observed in X-ray induced chromosomes at low-level doses. The effect of ionising radiation was noticed, but no significant difference was observed in the DAPI lifetime values within the different chosen radiation doses. The pentanucleotide (GGAAT) is present in the heteromorphic chromosomes; among these pentanucleotides, the guanosine base has a high rate of damage upon excitation, even with a low level of ionising radiation, because of its oxidising characteristic and high ionising potential (Melvin *et al.*, 1998).

With the information that the heteromorphic chromosomes show variation in DAPI lifetime along the length of the chromosomes, depending upon the compactness of chromatins in the local regions of the chromosomes (Estandarte *et al.*, 2016). Also, chromatin decompaction was observed at a 10 Gy dose of X-ray irradiation when shown by FLIM (Abdollahi, Taucher-Scholz and Jakob,

2018). In the current work, X-ray induced chromosomes showed reduced DAPI lifetime, but within the range of radiation doses used, no significant difference was observed in DAPI lifetime values. After irradiation, the reduced lifetime values were observed along the length of all 46 metaphase chromosomes, including heteromorphic chromosomes. A difference in lifetime is ~290 ps observed between non-irradiated and irradiated chromosomes.

In chapter 4, X-ray ptychography has been used to measure the masses of chromosomes induced with X-ray doses (i:e. 0.1 Gy, 0.5 Gy and 1 Gy). It has been observed that the summed mass of all 46 chromosomes with a 0.5 Gy dose has the lowest mass and then the mass increase for the control sample was followed by 1 Gy and 0.1 Gy doses. This novel technique is useful as it gives accurate mass: including the number of chromosomal proteins and amount of DNA-content present in the entire genome of a species at the different stages of the cell cycle, without invasive staining. Measured in both non-irradiated and irradiated chromosomes and further built X-ray karyotypes. The chromosomes are ranked according to their respective masses *versus* known human genome DNA sequence length. However, it is worth noting that by using the FLIM technique, it has been shown that there is a correlation between a 0.1 Gy radiation-induced excited state lifetime decrease over 0.5 Gy and non-radiation of cell chromosomes (Chapter 3 of the thesis), thus indicating an effect on chromosomes following ionising radiation at 0.1 Gy. Low-dose irradiation is thought to induce an adaptive or hormetic response under certain conditions (Luckey, 2006; van Wyngaarden & Pauwels, 1995). Further studies are needed to characterise these effects fully.

According to our knowledge, the mass of the entire genome has not been measured yet; that includes the amount of chromosomal protein and expected DNA content present in each chromosome, available in a single chromosome spread. This helped to calculate the expected and the measured masses of the chromosomes, along with the expected histones and non-histones present. Furthermore, mass gain or mass loss that occurred due to irradiation can also be determined. For the first time, the mass of a complete set of chromosomes was accurately measured, including known and unknown chromosomal proteins and

DNA content (also the tightly packed DNA sequences which have not been discovered during the HGP) (Bhartiya *et al.*, 2021). In the future, this can be useful to identify the genome affected by diseases such as cancer by measuring the masses of each chromosome from a spread and ranking them according to their masses and comparing them with the control sample. A better understanding of chromosomes may have important implications for human health. The X-ray ptychography results are fascinating. The importance of this research lies in the development of new and improved techniques to image and weigh individual chromosomes that will benefit medicine to diagnose cancer from patient samples.

Also, measured the masses of stained and unstained fixed metaphase chromosomes and can assume that up to 100% of the masses were added to the stained chromosomes. Therefore, staining is discouraged and only imaged unstained metaphase chromosomes at room temperature. The X-ray karyotype ranked according to their masses, obtained from unstained B and T-cells, were further segmented and placed in their respective positions in the karyogram. In addition, the same fixed metaphase chromosome spreads are imaged at three different time intervals (i.e., 0.3 sec, 0.6 sec and 0.9 sec) to show the reproducibility and reliability of the measured masses. The obtained masses from the control sample, 0.1 Gy and 1 Gy, show decreased summed masses with the increasing amount of dose at every scan. Moreover, differences in decreased mass were observed with 0.1 Gy and 1 Gy. Nevertheless, with a 0.5 Gy irradiation dose, the masses increase with increasing dose at every interval.

Overall, this study is useful to explore further the chemical modification and the mechanism involved in the damage and the repair signalling that occurred upon low-level irradiation within the chromatin. More repeats are needed to obtain better results on the cytochemistry and the biochemical reaction occurring in the chromosomes upon low-level X-ray induction

Chapter 6

6. Future works

The study has demonstrated two promising imaging techniques for chromosomal structural studies after X-ray irradiation. Firstly, investigated molecular environmental changes that occurred in the aberrated/damaged chromosomes using combined FLIM and multiphoton microscopy. The effect of low-level X-ray irradiation can be observed in heteromorphic regions, and the rest of the chromosomes in the chromosome spreads. Irradiation effects were observed in both the heterochromatin and non-heterochromatin regions of the chromosomes. Moreover, the effect was also observed in a different passage of the cell culture.

Secondly, measured mass of a human genome using X-ray ptychography to build X-ray karyotype, ranked according to their masses. The advantage of this karyotyping method is that it considers the contribution from both the DNA and the chromosomal proteins present in the metaphase chromosomes and can be achieved without using invasive staining methods. Hard-X-rays phase-contrast imaging of heavy metal stained and unstained “spreads” (a full set of 46 chromosomes captured in one frame) was also achieved.

In the future, FLIM measurement can be performed on ultraviolet (UV) induced metaphase chromosomes. Immunofluorescence labelling of metaphase chromosomes (Terrenoire, Halsall and Turner, 2015) would be helpful to identify the chromosomal aberrations which occurred due to low-level ionising radiation. For example labelling *γ*-H2AX with antibodies to identify DSBs in the DNA (Dickey *et al.*, 2009) (Nair *et al.*, 2019) following FLIM imaging. It may be a helpful tool to diagnose genomic instability in healthy and diseased cells.

The condensation and de-condensation that occurred due to ionising radiation in chromosomes could be studied in polyamine prepared chromosomes in real-time as an alternative to the methanol-acetic acid preparations that have been used in the current study. The FLIM-FRET technique can be utilised to

unravel the intermediate 11 nm, while single-molecule and super-resolution imaging techniques may be useful to determine the structure around 150 nm of chromatin.

X-ray ptychography of unstained metaphase chromosomes at room temperature achieved at I-13-coherence branch, Diamond Light Source, UK, provides the basis for future 2D and 3D imaging of biological samples in a cryo-environment, for example, to elucidate the fine ultra-structure of chromatin. Observing the chromosome bands and internal details within the complete set of human chromosomes would be advantageous. However, there are several technical issues to overcome, as mentioned in (Yusuf *et al.*, 2017). The prime problem is to avoid ice formation throughout the cryo-imaging imaging procedure.

Another approach is to perform M-FISH on the retrieved silicon nitride membranes to correlate with X-ray karyotype (ranked according to individual masses *versus* known DNA sequences) with standard cytogenetic staining patterns (M-FISH hybridisation karyotype). This can be achieved with some optimised protocols. Possibly several repeats of FLIM and X-ray ptychography experiments in the future will give a more concrete conclusion to the research.

7. References

Abdollahi, E., Taucher-Scholz, G. and Jakob, B. (2018) ‘Application of fluorescence lifetime imaging microscopy of DNA binding dyes to assess radiation-induced chromatin compaction changes’, *International Journal of Molecular Sciences*, 19(2399), pp. 1–15. doi: 10.3390/ijms19082399.

AbdulSalam, S. F., Thowfeik, F. S. and Merino, E. J. (2017) ‘Excessive Reactive Oxygen Species and Exotic DNA Lesions as an Exploitable Liability’, *Biochemistry*, 55(38), pp. 5341–5352. doi: 10.1021/acs.biochem.6b00703.

Ahmed, A., Schoberer, J., Cooke, E. and Botchway, S. W. (2020) ‘Multicolor FRET-FLIM Microscopy to Analyze Multiprotein Interactions in Live Cells’, in Poterszman, A. (ed.) *Methods in Molecular Biology*. 2247th edn. New York: Humana Press, pp. 287–301. doi: 10.1007/978-1-0716-1126-5_16.

Akbas, E., Senli, H., Hallioglu, O., Batmaz, S. and Erdogan, N. E. (2010) ‘Association of pericentric inversion of chromosome 9 (inv[9][p11q13]) and genetic diseases: Case report’, *Laboratory Medicine*, 41(2), pp. 96–98. doi: 10.1309/LM9ESUC9O8QKZOYO.

Alberts, B., Johnson, A., Lewis, J., Raff, M., Roberts, K. and Walter, P. (2002) ‘An Overview of the Cell Cycle’, in *Molecular Biology of the Cell*. Fourth. New York: Garland Science. Available at: https://www.ncbi.nlm.nih.gov/books/NBK26869/.

Allshire, R. C. and Madhani, H. D. (2018) ‘Ten principles of heterochromatin formation and function’, *Nature Reviews Molecular Cell Biology*, 19(4), pp. 229–244. doi: 10.1038/nrm.2017.119.

Als-Nielsen, J. and McMorrow, D. (2011) *Elements of Modern X-ray Physics*. 2nd edn. West Sussex: John Wiley & Sons, Ltd. doi: 10.1002/9781119998365.

del Amo, A. and Gullón, A. (1972) ‘Familial translocation t(3q+;8q-) studied by banding with Giemsa staining’, *Human Genetics*, 15(1), pp. 14–19. doi: 10.1007/BF00273426.

Anderson, R. (2010) ‘Multiplex Fluorescence in situ Hybridization (M-FISH)’, in Bridger, J. M. and Volpi, E. V (eds) *Fluorescence in situ Hybridization (FISH)*

Protocols and Applications. Totowa NJ: Humana Press, pp. 83–97.

Anderson, R. M., Stevens, D. L. and Goodhead, D. T. (2002) 'M-FISH analysis shows that complex chromosome aberrations induced by alpha-particle tracks are cumulative products of localized rearrangements', *Proceedings of the National Academy of Sciences of the United States of America*, 99(19), pp. 12167–12172. doi: 10.1073/pnas.182426799.

Anderson, R. M., Sumption, N. D., Papworth, D. G. and Goodhead, D. T. (2006) 'Chromosome breakpoint distribution of damage induced in peripheral blood lymphocytes by densely ionizing radiation', *International Journal of Radiation Biology*, 82(1), pp. 49–58. doi: 10.1080/09553000600579231.

Anthony, N., Guo, P. and Berland, K. (2009) 'Principles of Fluorescence for Quantitative Fluorescence Microscopy', in Periasamy, A. and Clegg, R. M. (eds) *FLIM Microscopy in Biology and Medicine*. 1st edn. New York: Taylor & Francis Group, LLC, pp. 35–59. doi: https://doi.org/10.1201/9781420078916.

Aparicio, T., Baer, R. and Gautier, J. (2015) 'DNA double-strand break repair pathway choice and cancer', *DNA Repair (Amst)*, 19, pp. 169–175. doi: 10.1016/j.dnarep.2014.03.014.

Arrighi, F. E. and Hsu, T. C. (1971) 'Localization of heterochromatin in human chromosomes.', *Cytogenetics*, 10(2), pp. 81–86. doi: 10.1159/000130130.

Arumugam, T. V., Gleichmann, M., Tang, S. C. and Mattson, M. P. (2006) 'Hormesis/preconditioning mechanisms, the nervous system and aging', *Ageing Research Reviews*, 5(2), pp. 165–178. doi: 10.1016/j.arr.2006.03.003.

Atef, S. H., Hafez, S. S., Mahmoud, N. H. and Helmy, S. M. (2011) 'Prenatal diagnosis of fetal aneuploidies using QF-PCR: the egyptian study.', *Journal of prenatal medicine*, 5(4), pp. 83–9. Available at: http://www.ncbi.nlm.nih.gov/pubmed/22905299%0Ahttp://www.pubmedcentral.nih.gov/articlerender.fcgi?artid=PMC3399051.

Azzam, E. Jay-Gerin, J. Pain, D. (2012) 'Ionizing radiation-induced metabolic oxidative stress and prolonged cell injury', *Cancer Letters*, 327(1–2), pp. 48–60. doi: 10.1016/j.canlet.2011.12.012.

Bachtrog, D. (2014) 'Y chromosome evolution: emerging insights into processes

of Y chromosome degeneration', *Nature Reviews Genetics*, 14(2), pp. 113–124. doi: 10.1038/nrg3366.

Balajee, A. S., Bertucci, A., Taveras, M. and Brenner, D. J. (2014) 'Multicolour FISH analysis of ionising radiation induced micronucleus formation in human lymphocytes', *Mutagenesis*, 29(6), pp. 447–455. doi: 10.1093/mutage/geu041.

Bannister, A. J., Zegerman, P., Partridge, J. F., Miska, E. A., Thomas, J. O., Allshire, R. C. and Kouzarides, T. (2001) 'Selective recognition of methylated lysine 9 on histone H3 by the HP1 chromo domain', *Nature*, 410(6824), pp. 120–124. doi: 10.1038/35065138.

Barcellona, M. L., Cardiel, G. and Gratton, E. (1990) 'Time-resolved fluorescence of DAPI in solution and bound to polydeoxynucleotides', *Biochemical Biophysical Research Communications*, 170(1), pp. 270–280. doi: 10.1016/0006-291x(90)91270-3.

Barcellona, M. L. and Gratton, E. (1989) 'Fluorescence lifetime distributions of DNA-4′,6-diamidino-2-phenylindole complex', *BBA - General Subjects*, 993(2–3), pp. 174–178. doi: 10.1016/0304-4165(89)90160-8.

Barcellona, M. L. and Gratton, E. (1990) 'The fluorescence properties of a DNA probe - 4???-6-Diamidino-2-phenylindole (DAPI)', *European Biophysics Journal*, 17(6), pp. 315–323. doi: 10.1007/BF00258380.

Barke, I., Hartmann, H., Rupp, D., Flückiger, L., Sauppe, M., Adolph, M., Schorb, S., Bostedt, C., Treusch, R., Peltz, C., Bartling, S., Fennel, T., Meiwes-Broer, K. H. and Möller, T. (2015) 'The 3D-architecture of individual free silver nanoparticles captured by X-ray scattering', *Nature Communications*, 6, pp. 1–7. doi: 10.1038/ncomms7187.

Batey, D. J. (2014) *Ptychographic Imaging of Mixed States*. University of Sheffield. Available at: http://etheses.whiterose.ac.uk/8524/ (Accessed: 25 October 2020).

Batey, D. J., Cipiccia, S., Van Assche, F., Vanheule, S., Vanmechelen, J., Boone, M. N. and Rau, C. (2019) 'Spectroscopic imaging with single acquisition ptychography and a hyperspectral detector', *Scientific Reports*. Springer US, 9(1), pp. 1–7. doi: 10.1038/s41598-019-48642-y.

Becker, W. (2012) ‘Fluorescence lifetime imaging - techniques and applications’, *Journal of Microscopy*, 247(2), pp. 119–136. doi: 10.1111/j.1365-2818.2012.03618.x.

Beckers, M., Senkbeil, T., Gorniak, T., Reese, M., Giewekemeyer, K., Gleber, S. C., Salditt, T. and Rosenhahn, A. (2011) ‘Chemical contrast in soft X-ray ptychography’, *Physical Review Letters*, 107(20), pp. 1–4. doi: 10.1103/PhysRevLett.107.208101.

Bench, G. S., Friz, A. M., Corzett, M. H., Morse, D. H. and Balhorn, R. (1996) ‘DNA and Total Protamine Masses in Individual Sperm From Fertile Mammalian Subjects’, *Cytometry*, 23, pp. 263–271.

Berger, F. (2019) ‘Emil Heitz, a true epigenetics pioneer’, *Nature Reviews Molecular Cell Biology*, 20, p. 572. doi: 10.1038/s41580-019-0161-z.

Bhartiya, A., Batey, D., Cipiccia, S., Shi, X., Rau, C., Botchway, S., Yusuf, M. and Robinson, I. K. (2021) ‘X-ray Ptychography Imaging of Human Chromosomes After Low-dose Irradiation’, *Chromosome Research*. Chromosome Research, 29(1), pp. 107–126. doi: 10.1007/s10577-021-09660-7.

Bhatnagar, M. C. and Bansal, G. (2009) ‘The Chromosomes’, in *Cell Biology and Genetics*. 3rd edn. Meerut: Krishna Prakashan Media (P) Ltd., pp. 131–134.

Biau, J., Chautard, E., Verrelle, P. and Dutreix, M. (2019) ‘Altering DNA repair to improve radiation therapy: Specific and multiple pathway targeting’, *Frontiers in Oncology*, 9: 1009, pp. 1–10. doi: 10.3389/fonc.2019.01009.

Bishop, R. (2010) ‘Review Applications of fluorescence in situ hybridization (FISH) in detecting genetic aberrations of medical significance’, *Bioscience Horizons*, 3(1), pp. 85–95.

Blanpain, C., Mohrin, M., Sotiropoulou, P. A. and Passegue, E. (2011) ‘Review DNA-Damage Response in Tissue-Specific and Cancer Stem Cells’, *Cell Stem Cell*, 8, pp. 16–29. doi: 10.1016/j.stem.2010.12.012.

Bloomer, W. D. and Adelstein, S. J. (1982) ‘The Mammalian Radiation Survival Curve’, *Journal of Nuclear Medicine*, 23(3), pp. 259–265.

Bolus, N. E. (2017) ‘Basic review of radiation biology and terminology’, *Journal of Nuclear Medicine Technology*, 45(4), pp. 259–264. doi:

10.2967/jnmt.117.195230.

Borràs-fresneda, M., Barquinero, J., Gomolka, M. and Hornhardt, S. (2016) 'Differences in DNA Repair Capacity , Cell Death and Transcriptional Response after Irradiation between a Radiosensitive and a Radioresistant Cell Line', *Scientific reports*. Nature Publishing Group, 6:27043, pp. 1–11. doi: 10.1038/srep27043.

Borrego-Soto, G., Ortiz-López, R. and Rojas-Martínez, A. (2015) 'Ionizing radiation-induced DNA injury and damage detection in patients with breast cancer', *Genetics and Molecular Biology*, 38(4), pp. 420–432. doi: 10.1590/S1415-475738420150019.

Boschman, G. A., Rens, W., van Oven, C. H., Manders, E. M. M. and Aten, J. A. (1991) 'Bivariate flow karyotyping of human chromosomes: Evaluation of variation in Hoechst 33258 fluorescence, chromomycin A3 fluorescence, and relative chromosomal DNA content', *Cytometry*, 12(6), pp. 559–569. doi: 10.1002/cyto.990120613.

Botchway, A. S. W., Stevens, D. L., Hill, M. A., Jenner, T. J. and Neill, P. O. (1997) 'Induction and Rejoining of DNA Double-Strand Breaks in Chinese Hamster V79-4 Cells Irradiated with Characteristic Aluminum K and Copper L Ultrasoft X Rays', *Radiation Research*, 148(4), pp. 317–324.

Botchway, S. W., Farooq, S., Sajid, A., Robinson, I. K. and Yusuf, M. (2021) 'Contribution of advanced fluorescence nano microscopy towards revealing mitotic chromosome structure', *Chromosome Research*. Chromosome Research. doi: 10.1007/s10577-021-09654-5.

Botchway, S. W., Stevens, D. L., Hill, M. A., Jenner, T. J. and O'Neill, P. (1997) 'Induction and rejoining of DNA double-strand breaks in Chinese hamster V79-4 cells irradiated with characteristic aluminum K and copper L ultrasoft X rays', *Radiation Research*, 148(4), pp. 317–324. doi: 10.2307/3579516.

Brothman, Arthur R., Schneider, N. R., Saikevych, I., Cooley, L. D., Butler, M. G., Patil, S., Mascarello, J. T., Rao, K. W., Dewald, G. W., Park, J. P., Persons, D. L., Wolff, D. J. and Vance, G. H. (2006) 'Cytogenetic heteromorphisms: Survey results and reporting practices of Giemsa-band regions that we have pondered for years', *Archives of Pathology and Laboratory Medicine*, 130(7), pp. 947–949.

doi: 10.1043/1543-2165(2006)130[947:CHSRAR]2.0.CO;2.

Brothman, Arthur R, Schneider, N. R., Saikevych, I., Cooley, L. D., Park, J. P., Persons, D. L., Wolff, D. J. and Vance, G. H. (2006) 'Cytogenetic heteromorphisms: survey results and reporting practices of giemsa-band regions that we have pondered for years', *Arch Pathol Lab Med*, 130(Iscn), pp. 947–949.

Brown., T. A. (2002) *Genomes*. 2nd edn. Oxford: Wiley-Liss: Graland Science.

Buehring, G. C. and Williams, R. R. (1976) 'Growth Rates of Normal and Abnormal Human Mammary Epithelia in Cell Culture', *Cancer Research*, 36(10), pp. 3742–3747.

Cannan, W. J. and Pederson, D. S. (2016) 'Mechanisms and Consequences of Double-strand DNA Break Formation in Chromatin', *Journal of Cellular Physiology*, 231(1), pp. 3–14. doi: 0.1002/jcp.25048.

Cao, B., Xu, H. and Mao, C. (2011) 'Transmission electron microscopy as a tool to image bioinorganic nanohybrids: The case of phage-gold nanocomposites', *Microscopy Research and Technique*, 74(7), pp. 627–635. doi: 10.1002/jemt.21030.

Carlo, S. De and Harris, J. R. (2012) 'Negative staining and Cryo-negative Staining of Macromolecules and Viruses for TEM', *Micron*, 42(2), pp. 117–131. doi: 10.1385/1-59259-201-5.

Chapman, Henry N., Barty, A., Bogan, M. J., Boutet, S., Frank, M., Hau-Riege, S. P., Marchesini, S., Woods, B. W., Bajt, S., Benner, W. H., London, R. A., Plönjes, E., Kuhlmann, M., Treusch, R., Düsterer, S., Tschentscher, T., Schneider, J. R., Spiller, E., Möller, T., Bostedt, C., Hoener, M., Shapiro, D. A., Hodgson, K. O., van der Spoel, D., Burmeister, F., Bergh, M., Caleman, C., Huldt, G., Seibert, M. M., Maia, F. R. N. C., Lee, R. W., Szöke, A., Timneanu, N. and Hajdu, J. (2006) 'Femtosecond diffractive imaging with a soft-X-ray free-electron laser', *Nature Physics*, 2(12), pp. 839–843. doi: 10.1038/nphys461.

Chapman, Henry N, Barty, A., Marchesini, S., Noy, A., Cui, C., Howells, M., Rosen, R., He, H., Spence, J. C., Beetz, T., Jacobsen, C., Shapiro, D. and Hau-riege, S. P. (2006) 'High-resolution ab initio three-dimensional x-ray diffraction microscopy', *Journal of the Optical Society of America A.*, 23(5), p. 1179.

Chapman, H. N. and Nugent, K. A. (2010) ‘Coherent lensless X-ray imaging’, *Nature Photonics*, 4(12), pp. 833–839. doi: 10.1038/nphoton.2010.240.

Charbin, A., Bouchoux, C. and Uhlmann, F. (2014) ‘Condensin aids sister chromatid decatenation by topoisomerase II’, *Nucleic Acids Research*, 42(1), pp. 340–348. doi: 10.1093/nar/gkt882.

Charlesworth, B. (2003) ‘The organization and evolution of the human Y chromosome’, *Genome Biology*, 4(9), pp. 9–11. doi: 10.1186/gb-2003-4-9-226.

Charlesworth, B. and Charlesworth, D. (2000) ‘The degeneration of Y chromosomes’, *Philosophical Transactions of the Royal Society B: Biological Sciences*, 355(1403), pp. 1563–1572. doi: 10.1098/rstb.2000.0717.

Chen, B., Yusuf, M., Hashimoto, T., Estandarte, A. K., Thompson, G. and Robinson, I. (2017) ‘Three-dimensional positioning and structure of chromosomes in a human prophase nucleus’, *Science Advances*, 3(7), pp. 1–9. doi: 10.1126/sciadv.1602231.

Chen, T. R., Kao, M. L., Marks, J. and Chen, Y. Y. (1981) ‘Polymorphic variants in human chromosome 15’, *American Journal of Medical Genetics*, 9(1), pp. 61–66. doi: 10.1002/ajmg.1320090111.

Cho, Y., Kim, S., Woo, H., Kim, Y., Ha, S. and Chung, H. (2015) ‘Delayed Numerical Chromosome Aberrations in Human Fibroblasts by Low Dose of Radiation’, *International Journal of Environmental Research and Public Health*, 12(12), pp. 15162–15172. doi: 10.3390/ijerph121214979.

Choo, A. K. H. (1997) ‘Anomalies of the human centromere’, in *The Centromere*. Melbourne: Oxford University Press, pp. 255–265.

Cigarrán, S., Barrios, L., Barquinero, J. F., Cabalín, M. R., Ribas, M. and Egozcue, J. (1998) ‘Relationship between the DNA content of human chromosomes and their involvement in radiation-induced structural aberrations, analysed by painting’, *International Journal of Radiation Biology*, 74(4), pp. 449–455. doi: 10.1080/095530098141311.

Cooper, Geoffrey. M (2000) *The cell: A Molecular Approach.* 2nd edn. Sunderland (MA): Sinauer Associates.

Cooper, Geoffrey M. (2000) *The Cell: A Molecular Approach*. 2nd edn. ASM

Press.

Craig, J. M., Earle, E., Canham, P., Wong, L. H., Anderson, M. and Choo, K. H. A. (2003) 'Analysis of mammalian proteins involved in chromatin modification reveals new metaphase centromeric proteins and distinct chromosomal distribution patterns', *Human Molecular Genetics*, 12(23), pp. 3109–3121. doi: 10.1093/hmg/ddg330.

Cram, L. S., Bartholdi, M. F., Ray, F. A., Meyne, J., Moyzis, R. K., Schwarzacher-Robinson, T. and Kraemer, P. M. (1988) 'Overview of flow cytogenetics for clinical applications', *Cytometry*, 9(3 S), pp. 94–100. doi: 10.1002/cyto.990090819.

Cremer, T. and Cremer, M. (2010) 'Chromosome territories.', *Cold Spring Harbor perspectives in biology*, 2(3), pp. 1–22. doi: 10.1101/cshperspect.a003889.

Cuvier, O. and Hirano, T. (2003) 'A role of topoisomerase II in linking DNA replication to chromosome condensation', *Journal of Cell Biology*, 160(5), pp. 645–655. doi: 10.1083/jcb.200209023.

Dai, X., Yang, G., Liu, J. and Song, Y. (2006) 'Mouse karyotype obtained by combining DAPI staining with image analysis', *Wuhan University Journal of Natural Sciences*, 11(2), pp. 441–446. doi: 10.1007/BF02832140.

Dendy, P. and Heaton, B. (1999) *Physics for Diagnostic Radiology*. 2nd edn. Philadelphia, PA: Institute of Physics Publishing.

Deng, J., Chen, S., Jin, Q., Vacek, E., Jacobsen, C., Lai, B. and Vogt, S. (2019) 'Correlative X-ray Ptychographic and Fluorescence Imaging at the Advanced Photon Source', *Microscopy and Microanalysis*, 25(S2), pp. 1030–1031. doi: 10.1017/s1431927619005889.

Deng J., Vine D. J., Chen, S., Nashed, Y. S. G., Jin, Q., Peterka, T., Vogt, S. and Jacobsen, C. (2015) 'Advances and challenges in cryo ptychography at the Advanced Photon Source', *Proceedings of the National Academy of Sciences of the United States of America.*, 112, pp. 2314–9. doi: 10.1016/j.physbeh.2017.03.040.

Derksen, J. and Meekes, H. (1984) 'Selective staining of nucleic acid containing structures by uranyl acetate-lead citrate', *Micron and Microscopica Acta*, 15(1), pp. 55–58.

Desouky, O., Ding, N. and Zhou, G. (2015) 'ScienceDirect Targeted and non-targeted effects of ionizing radiation', *Journal of Radiation Research and Applied Sciences*, 8(2), pp. 247–254. doi: 10.1016/j.jrras.2015.03.003.

Dickey, J. S., Redon, C. E., Nakamura, A. J., Baird, B. J., Sedelnikova, O. A. and Bonner, W. M. (2009) 'H2AX: Functional roles and potential applications', *Chromosoma*, 118(6), pp. 683–692. doi: 10.1007/s00412-009-0234-4.

Dierolf, M., Menzel, A., Thibault, P., Schneider, P., Kewish, C. M., Wepf, R., Bunk, O. and Pfeiffer, F. (2010) 'Ptychographic X-ray computed tomography at the nanoscale', *Nature*, 467(7314), pp. 436–439. doi: 10.1038/nature09419.

Dillard, R. S., Hampton, C. M., Strauss, J. D., Ke, Z., Altomara, D., Ferreira, R. C. G., Kiss, G. and Wright, E. R. (2018) 'Biological Applications at the Cutting Edge of Cryo-Electron Microscopy', *Microscopy and Microanalysis*, 24(4), pp. 406–419. doi: 10.1017/S1431927618012382.

Dillon, N. (2004) 'Heterochromatin structure and function', *Biology of the Cell*, 96(8), pp. 631–637. doi: 10.1016/j.biolcel.2004.06.003.

Doležel, J., Bartoš, J., Voglmayr, H. and Greilhuber, J. (2003) 'Nuclear DNA content and genome size of trout and human', *Cytometry Part A*, 51A(2), pp. 127–128. doi: 10.1002/cyto.a.10013.

Dorigo, B., Schalch, T., Kulangara, A., Duda, S., Schroeder, R. R. and Richmond, T. J. (2004) 'Nucleosome Arrays Reveal the Two-Start Organization of the Chromatin Fiber', *Science*, 306(5701), pp. 1571–3.

Duijn, P. Van, Prooijen-Knegt, A. C. van and Ploeg, M. van der (1985) 'The involvement of nucleosomes in Giemsa staining of chromosomes: A new hypothesis on the banding mechanism', *Histochemistry: Springer-Verlag*, 82, pp. 363–376.

Durante, M. and Formenti, S. C. (2018) 'Radiation-induced chromosomal aberrations and immunotherapy: Micronuclei, cytosolic DNA, and interferon-production pathway', *Frontiers in Oncology*, 8:192, pp. 1–9. doi: 10.3389/fonc.2018.00192.

Earnshaw, W. C. and Laemmli, U. K. (1983) 'Architecture of metaphase chromosomes and chromosome scaffolds', *Journal of Cell Biology*, 96(1), pp. 84–

93. doi: 10.1083/jcb.96.1.84.

Earnshaw, W. C. and Mackay, A. M. (1994) ‘Role of nonhistone proteins in the chromosomal events of mitosis’, *The Faseb Journal*, 8(12), pp. 947–956. doi: 10.1096/fasebj.8.12.8088460.

El-Saghire, H., Michaux, A., Thierens, H. and Baatout, S. (2013) ‘Low doses of ionizing radiation induce immune-stimulatory responses in isolated human primary monocytes’, *International Journal of Molecular Medicine*, 32(6), pp. 1407–1414. doi: 10.3892/ijmm.2013.1514.

Ellard, S., Toper, S., Stemp, G. U. I., Parry, E. M., Wilcox, P. and Parry, J. M. (1996) ‘A comparison of conventional metaphase analysis of Giemsa-stained chromosomes with multi-colour fluorescence in situ hybridization analysis to detect chromosome aberrations induced by daunomycin’, *Mutagenesis*, 11(6), pp. 537–546.

Estandarte, A. K., Botchway, S., Lynch, C., Yusuf, M. and Robinson, I. (2016) ‘The use of DAPI fluorescence lifetime imaging for investigating chromatin condensation in human chromosomes’, *Scientific Reports*, 6(31417), pp. 1–12. doi: 10.1038/srep31417.

Falcke, S. E., Rühle, P. F., Deloch, L., Fietkau, R., Frey, B. and Gaipl, U. S. (2018) ‘Clinically relevant radiation exposure differentially impacts forms of cell death in human cells of the innate and adaptive immune system’, *International Journal of Molecular Sciences*, 19(11), pp. 3–6. doi: 10.3390/ijms19113574.

Fan, D. M., Yang, X., Huang, L. M., Ouyang, G. J., Yang, X. X. and Li, M. (2019) ‘Simultaneous detection of target CNVs and SNVs of thalassemia by multiplex PCR and next-generation sequencing’, *Molecular Medicine Reports*, 19(4), pp. 2837–2848. doi: 10.3892/mmr.2019.9896.

Feinendegen, L. E. and Neumann, R. D. (2005) ‘Physics must join with biology in better assessing risk from low-dose irradiation’, *Radiation Protection Dosimetry*, 117(4), pp. 346–356. doi: 10.1093/rpd/nci357.

Feinendegen, L. E., Pollycove, M. and Neumann, R. D. (2007) ‘Whole-body responses to low-level radiation exposure: New concepts in mammalian radiobiology’, *Experimental Hematology*, 35(4 SUPPL.), pp. 37–46. doi:

10.1016/j.exphem.2007.01.011.

Finch, J. T. and Klug, A. (1976) ‘Solenoidal model for superstructure in chromatin’, *Proceedings of the National Academy of Sciences of the United States of America*, 73(6), pp. 1897–1901. doi: 10.1073/pnas.73.6.1897.

Forsburg, S. L. (2004) ‘Eukaryotic MCM Proteins : Beyond Replication Initiation’, *American Society for Microbiology*, 68(1), pp. 109–131. doi: 10.1128/MMBR.68.1.109.

Friedrich, U., Caprani, M., Niebuhr, E., Therkelsen, A. J. and Jørgensen, A. L. (1996) ‘Extreme variant of the short arm of chromosome 15’, *Human Genetics*, 97(6), pp. 710–713. doi: 10.1007/BF02346177.

Fujimichi, Y. and Hamada, N. (2014) ‘Ionizing irradiation not only inactivates clonogenic potential in primary normal human diploid lens epithelial cells but also stimulates cell proliferation in a subset of this population’, *PLoS ONE*, 9(5:e98154). doi: 10.1371/journal.pone.0098154.

Gagula-Palalic, S. and Can, M. (2013) ‘Denver Groups Classification of Human Chromosomes Using CANN Teams’, *Southeast Europe Journal of Soft Computing*, 2(2). doi: 10.21533/scjournal.v2i2.22.

Gasser, S. M., Laroche, T., Falquet, J., Tour, E. B. De and Laemmli, U. K. (1986) ‘Metaphase chromosome structure: Involvement of topoisomerase II’, *Journal of Molecular Biology*, 188(4), pp. 613–629. doi: https://doi.org/10.1016/S0022-2836(86)80010-9.

Gassmann, R., Henzing, A. J. and Earnshaw, W. C. (2005) ‘Novel components of human mitotic chromosomes identified by proteomic analysis of the chromosome scaffold fraction’, *Chromosoma*, 113(7), pp. 385–397. doi: 10.1007/s00412-004-0326-0.

Gil, O. M., Martins, J. O. and Rosário, P. (2020) ‘Use of biological dosimetry to confirm radiation exposure: Case study’, *Radiation Physics and Chemistry*, 171. doi: 10.1016/j.radphyschem.2020.108683.

Goldfeder, R. L., Wall, D. P., Khoury, M. J., Ioannidis, J. P. A. and Ashley, E. A. (2017) ‘Human Genome Sequencing at the Population Scale: A Primer on High-Throughput DNA Sequencing and Analysis’, *American Journal of Epidemiology*,

186(8), pp. 1000–1001. doi: 10.1093/aje/kww224.

Goodpasture, C. and Bloom, S. E. (1975) ‘Visualization of nucleolar organizer regions in mammalian chromosomes using silver staining’, *Chromosoma*, 53(1), pp. 37–50. doi: 10.1007/BF00329389.

Gookin, S., Min, M., Phadke, H., Chung, M., Moser, J., Miller, I., Carter, D. and Spencer, S. L. (2017) ‘A map of protein dynamics during cell-cycle progression and cell-cycle exit’, *Public Library of Science: Biology*, 15(9), pp. 1–25.

Gospodinov, A. and Herceg, Z. (2013) ‘Chromatin structure in double strand break repair’, *DNA Repair*, 12(10), pp. 800–810. doi: 10.1016/j.dnarep.2013.07.006.

Grady, D. L., Ratliff, R. L., Robinson, D. L., Mccanlies, E. C., Meyne, J. and Moyzis, R. K. (1992) ‘Highly conserved repetitive DNA sequences are present at human centromeres’, *Proceedings of the National Academy of Sciences of the United States of America*, 89(5), pp. 1695–1699. doi: 10.1073/pnas.89.5.1695.

Gulston, M., de Lara, C., Jenner, T., Davis, E. and O’Neill, P. (2004) ‘Processing of clustered DNA damage generates additional double-strand breaks in mammalian cells post-irradiation’, *Nucleic Acids Research*, 32(4), pp. 1602–1609. doi: 10.1093/nar/gkh306.

Harris, P., Boyd, E., Young, B. D. and Ferguson-Smith, M. A. (1986) ‘Determination of the DNA content of human chromosomes by flow cytometry’, *Cytogenetics and Cell Genetics*, 41, pp. 14–21.

Harshman, S. W., Young, N. L., Parthun, M. R. and Freitas, M. A. (2013) ‘H1 histones: Current perspectives and challenges’, *Nucleic Acids Research*, 41(21), pp. 9593–9609. doi: 10.1093/nar/gkt700.

Hayat, M. A. and Miller, S. E. (1990) *Negative Staining*. New York: McGraw-Hill Publishing Company.

Heitz, E. (1928) ‘Das Heterochromatin der Moose’, *Jahrbücher für wissenschaftliche Botanik.*, 69, pp. 762–818.

Hémonnot, C. Y. J. and Köster, S. (2017) ‘Imaging of Biological Materials and Cells by X-ray Scattering and Diffraction’, *American Chemical Society: Nanoscience, Nanotechnology*, 11(9), pp. 8542–8559. doi:

10.1021/acsnano.7b03447.

Henderson, A. S., Warburton, D. and Atwood, K. C. (1972) 'Location of ribosomal DNA in the human chromosome complement.', *Proceedings of the National Academy of Sciences of the United States of America*, 69(11), pp. 3394–3398. doi: 10.1073/pnas.69.11.3394.

Heylmann, D., Rödel, F., Kindler, T. and Kaina, B. (2014) 'Radiation sensitivity of human and murine peripheral blood lymphocytes, stem and progenitor cells', *Biochimica et Biophysica Acta - Reviews on Cancer*, 1846(1), pp. 121–129. doi: 10.1016/j.bbcan.2014.04.009.

Hiorns, L. R., Bradshaw, T. D., Skelton, L. A., Yu, Q., Kelland, L. R. and Leyland-Jones, B. (2004) 'Variation in RNA expression and genomic DNA content acquired during cell culture', *British Journal of Cancer*, 90(2), pp. 476–482. doi: 10.1038/sj.bjc.6601405.

Hockings, C., Poudel, C., Feeney, K., Novo, C., Hamouda, M., Mela, I., Fernandez-Antoran, D., Vallejo-Ramirez, P., Rugg-Gunn, P., Chalut, K., Kaminski, C. and Kaminski-Schierle, G. (2020) 'Illuminating chromatin compaction in live cells and fixed tissues using SiR-DNA fluorescence lifetime', *BioRxiv- the preprint server for Biology*, pp. 1–11. doi: 10.1101/2020.05.02.073536.

Howells, M., Jacobsen, C., Warwick, T. and Van den Bos, A. (2006) 'Principles and Applications of Zone Plate X-Ray Microscopes', in Hawkes P.W. and Spence, J. C. H. (eds) *Science of Microscopy*. New York (NY): Springer, pp. 835–926. doi: 10.1016/s1369-7021(06)71581-4.

Howells, M. R., Beetz, T., Chapman, H. N., Cui, C., Holton, J. M., Jacobsen, C. J., Kirz, J., Lima, E., Marchesini, S., Miao, H., Sayre, D., Shapiro, D. A., Spence, J. C. H. and Starodub, D. (2009) 'An assessment of the resolution limitation due to radiation-damage in X-ray diffraction microscopy', *Journal of Electron Spectroscopy and Related Phenomena*, 170(1–3), pp. 4–12. doi: 10.1016/j.elspec.2008.10.008.

Hozier, J. C., Furcht, L. T. and Wendelshafer-grabb, G. (1981) 'Structure of Human Chromosomes Visualized at the Electron Microscopic Level', *Chromosoma*, 64, pp. 55–64. doi: https://doi.org/10.1007/BF00285749.

Huang, X., Nelson, J., Kirz, J., Lima, E., Marchesini, S., Miao, H., Neiman, A. M., Shapiro, D., Steinbrener, J., Stewart, A., Turner, J. J. and Jacobsen, C. (2009) 'Soft X-Ray Diffraction Microscopy of a Frozen Hydrated Yeast Cell', *Physical Review Letters*, 103(19). doi: 10.1103/PhysRevLett.103.198101.

Huang, X. shuang, Li, X., Tan, C., Xiao, L., Jiang, H. ou, Zhang, S. fang, Wang, D. mei and Zhang, J. xiang (2010) 'Genome-wide scanning reveals complex etiology of oculo-auriculo-vertebral spectrum', *Tohoku Journal of Experimental Medicine*, 222(4), pp. 311–318. doi: 10.1620/tjem.222.311.

Humphray, S. J., Oliver, K., Hunt, A. R., Plumb, R. W., Loveland, J. E., Howe, K. L., Andrews, T. D., Searle, S., Hunt, S. E., Scott, C. E., Jones, M. C., Ainscough, R., Almeida, J. P., Ambrose, K. D., Ashwell, R. I. S., Babbage, A. K., Babbage, S., Bagguley, C. L., Bailey, J., Banerjee, R., Barker, D. J., Barlow, K. F., Bates, K., Beasley, H., Beasley, O., Bird, C. P., Bray-Allen, S., Brown, A. J., Brown, J. Y., Burford, D., Burrill, W., Burton, J., Carder, C., Carter, N. P., Chapman, J. C., Chen, Y., Clarke, G., Clark, S. Y., Clee, C. M., Clegg, S., Collier, R. E., Corby, N., Crosier, M., Cummings, A. T., Davies, J., Dhami, P., Dunn, M., Dutta, I., Dyer, L. W., Earthrowl, M. E., Faulkner, L., Fleming, C. J., Frankish, A., Frankland, J. A., French, L., Fricker, D. G., Garner, P., Garnett, J., Ghori, J., Gilbert, J. G. R., Glison, C., Grafham, D. V., Gribble, S., Griffiths, C., Griffiths-Jones, S., Grocock, R., Guy, J., Hall, R. E., Hammond, S., Harley, J. L., Harrison, E. S. I., Hart, E. A., Heath, P. D., Henderson, C. D., Hopkins, B. L., Howard, P. J., Howden, P. J., Huckle, E., Johnson, C., Johnson, D., Joy, A. A., Kay, M., Keenan, S., Kershaw, J. K., Kimberley, A. M., King, A., Knights, A., Laird, G. K., Langford, C., Lawlor, S., Leongamornlert, D. A., Leversha, M., Lloyd, C., Lloyd, D. M., Lovell, J., Martin, S., Mashreghi-Mohammadi, M., Matthews, L., McLaren, S., McLay, K. E., McMurray, A., Milne, S., Nickerson, T., Nisbett, J., Nordsiek, G., Pearce, A. V., Peck, A. I., Porter, K. M., Pandian, R., Pelan, S., Phillimore, B., Povey, S., Ramsey, Y., Rand, V., Scharfe, M., Sehra, H. K., Shownkeen, R., Sims, S. K., Skuce, C. D., Smith, M., Steward, C. A., Swarbreck, D., Sycamore, N., Tester, J., Thorpe, A., Tracey, A., Tromans, A., Thomas, D. W., Wall, M., Wallis, J. M., West, A. P., Whitehead, S. L., Willey, D. L., Williams, S. A., Wilming, L., Wray, P. W., Young, L., Ashurst, J. L., Coulson, A., Blöcker, H., Durbin, R., Sulston, J. E., Hubbard, T., Jackson, M. J., Bentley, D. R., Beck, S., Rogers, J. and Dunham, I.

(2004) ‘DNA sequence and analysis of human chromosome 9’, *Nature*, 429(6990), pp. 369–374. doi: 10.1038/nature02465.

Inaga, S., Katsumoto, T., Tanaka, K., Kameie, T., Nakane, H. and Naguro, T. (2007) ‘Platinum blue as an alternative to uranyl acetate for staining in transmission electron microscopy’, *Archives of Histology and Cytology*, 70(1), pp. 43–49. doi: 10.1679/aohc.70.43.

Ishizuka, T., Liu, H. S., Ito, K. and Xu, Y. (2016) ‘Fluorescence imaging of chromosomal DNA using click chemistry’, *Scientific Reports*. Nature Publishing Group, 6: 33217, pp. 1–10. doi: 10.1038/srep33217.

Jackson, M. S., Rocchi, M., Thompson, G., Hearn, T., Crosier, M., Guy, J., Kirk, D., Mulligan, L., Ricco, A., Piccininni, S., Marzella, R., Viggiano, L. and Archidiacono, N. (1999) ‘Sequences flanking the centromere of human chromosome 10 are a complex patchwork of arm-specific sequences, stable duplications and unstable sequences with homologies to telomeric and other centromeric locations’, *Human Molecular Genetics*, 8(2), pp. 205–215. doi: 10.1093/hmg/8.2.205.

Jain, A. K., Singh, D., Dubey, K., Maurya, R. and Pandey, A. K. (2017) ‘Chromosomal Aberrations’, in Kumar, A., Dobrovolsky, V., Dhawan, A., and Shanker, R. (eds) *Mutagenicity:Assays and Applications*. 1st edn. Ahemdabad, India: Academic Press, pp. 69–83.

Jalal, S. M. and Law, M. E. (1999) ‘Utility of multicolor fluorescent in situ hybridization in clinical cytogenetics’, *Genetics in Medicine*, 1(5), pp. 181–186. doi: 10.1097/00125817-199907000-00003.

Kaddour, A., Colicchio, B., Buron, D., Maalouf, E. El, Laplagne, E., Ricoul, M., Lenain, A., Hempel, W. M., Morat, L., Jawhari, M. Al, Cuceu, C., Heidingsfelder, L., Jeandidier, E., Deschênes, G., May, M. El, Girinsky, T. and Bennaceur-griscelli, A. (2017) ‘Transmission of Induced Chromosomal Aberrations through Successive Mitotic Divisions in Human Lymphocytes after In Vitro and In Vivo Radiation’, *Scientific reports*, 7: 3291, pp. 1–11. doi: 10.1038/s41598-017-03198-7.

Kapuscinski, J. (1995) ‘DAPI: A DMA-Specific fluorescent probe’, *Biotechnic and Histochemistry*, 70(5), pp. 220–233. doi: 10.3109/10520299509108199.

Karg, T. J. and Golic, K. G. (2018) ‘Photoconversion of DAPI and Hoechst dyes to green and red emitting forms after exposure to UV excitation’, *Chromosoma*, 127(2), pp. 235–245. doi: 10.1007/s00412-017-0654-5.

Kielkopf, C. L., White, S., Szewczyk, J. W., Turner, J. M., Baird, E. E., Dervan, P. B. and Rees, D. C. (1998) ‘A structural basis for recognition of A.T and T.A base pairs in the minor groove of B-DNA.’, *Proceedings of the National Academy of Sciences of the United States of America*, 282(5386), pp. 111–115. doi: 10.1126/science.282.5386.111.

Korenberg, J. R. and Engels, W. R. (1978) ‘Base ratio, DNA content, and quinacrine-brightness of human chromosomes’, *Proceedings of the National Academy of Sciences of the United States of America*, 75(7), pp. 3382–3386.

Kosyakova, N., Grigorian, A., Liehr, T., Manvelyan, M., Simonyan, I., Mkrtchyan, H., Aroutiounian, R., Polityko, A. D., Kulpanovich, A. I., Egorova, T., Jaroshevich, E., Frolova, A., Shorokh, N., Naumchik, I. V., Volleth, M., Schreyer, I., Nelle, H., Stumm, M., Wegner, R. D., Reising-Ackermann, G., Merkas, M., Brecevic, L., Martin, T., Rodríguez, L., Bhatt, S., Ziegler, M., Kreskowski, K., Weise, A., Sazci, A., Vorsanova, S., Cioffi, M. D. B. and Ergul, E. (2013) ‘Heteromorphic variants of chromosome 9’, *Molecular Cytogenetics*, 6(1), pp. 1–11. doi: 10.1186/1755-8166-6-14.

Lachner, M., O’Carroll, D., Rea, S., Mechtler, K. and Jenuwein, T. (2001) ‘Methylation of histone H3 lysine 9 creates a binding site for HP1 proteins’, *Nature*, 410, pp. 116–120. doi: https://doi.org/10.1038/35065132.

Lakowicz, J. R. (2006a) ‘Fluorescence Lifetime Imaging Microscopy’, in *Principles of Fluorescence Spectroscopy*. 3rd edn. Boston, MA: Springer, pp. 741–755.

Lakowicz, J. R. (2006b) ‘Introduction to Fluorescence’, in *Principles of Fluorescence Spectroscopy*. 3rd edn. Boston, MA: Springer, pp. 1–26.

Lakowicza, J. R., Chereka, H., Gryczynskia, I., Joshia, N. and Johnson, M. L. (1987) ‘Analysis of fluorescence decay kinetics measured in the frequency domain using distributions of decay times’, *Biophysical Chemistry*, 28(1), pp. 35–50. doi: 10.1016/j.physbeh.2017.03.040.

Lander ES, Linton LM, Birren B, Nusbaum C, Zody MC, Baldwin J, Devon K, Dewar K, Doyle M, FitzHugh W, Funke R, Gage D, Harris K, Heaford A, Howland J, Kann L, Lehoczky J, LeVine R, McEwan P, McKernan K, Meldrim J, Mesirov JP, Miranda C, Morris W, Naylor J, S. J. I. H. G. S. C. (2001) 'Initial sequencing and analysis of the human genome', *Nature*, 409(6822), pp. 860–921.

Langlois, R. G., Yu, L. C., Gray, J. W. and Carrano, A. V. (1982) 'Quantitative karyotyping of human chromosomes by dual beam flow cytometry', *Proceedings of the National Academy of Sciences of the United States of America*, 79, pp. 7876–7880. doi: 10.1073/pnas.79.24.7876.

Laptenok, S., Mullen, K. M., Borst, J. W., Stokkum, I. H. M. va., Apanasovich, V. V and Visser, A. J. W. . (2007) 'Fluorescence Lifetime Imaging Microscopy (FLIM) Data Analysis with TIMP', *Journal Of Statistical Software*, 18(8), pp. 1–20. doi: 10.18637/jss.v069.i12.

Larabell, C. A. and Nugent, K. A. (2010) 'Imaging Cellular Architecture with X-rays', *Current Opinion in Structural Biology*, 20(5), pp. 623–31. doi: 10.1038/jid.2014.371.

Lee, K. F., Weng, J. T. Y., Hsu, P. W. C., Chi, Y. H., Chen, C. K., Liu, I. Y., Chen, Y. C. and Wu, L. S. H. (2014) 'Gene expression profiling of biological pathway alterations by radiation exposure', *BioMed Research International*. Hindawi Publishing Corporation, 2014:83408. doi: 10.1155/2014/834087.

Lee, Y., Kim, C., Park, Y. J., Pyun, J. A. and Kwack, K. B. (2016) 'Next generation sequencing identifies abnormal Y chromosome and candidate causal variants in premature ovarian failure patients', *Genomics*. Elsevier Inc., 108(5–6), pp. 209–215. doi: 10.1016/j.ygeno.2016.10.006.

Leenhouts, H. P. and Chadwick, K. H. (1989) 'The molecular basis of stochastic and nonstochastic effects', *Health Physics*, 57 Suppl 1, pp. 343–348. doi: 10.1097/00004032-198907001-00048.

Levan, A., Fredga, K. and Sandberg, A. A. (1964) 'Nomenclature for Centromeric Position on Chromosomes', *Hereditas*, 52(2), pp. 201–220. doi: 10.1111/j.1601-5223.1964.tb01953.x.

Lewis, C. D. and Laemmli, U. K. (1982) 'Higher order metaphase chromosome

structure: Evidence for metalloprotein interactions', *Cell*, 29(1), pp. 171–181. doi: 10.1016/0092-8674(82)90101-5.

Liang, X., Gu, J., Yu, D., Wang, G., Zhou, L., Zhang, X., Zhao, Y., Chen, X., Zheng, S., Liu, Q., Cai, L., Cui, J. and Li, W. (2016) 'Low-dose radiation induces cell proliferation in human embryonic lung fibroblasts but not in lung cancer cells: Importance of ERK1/2 and AKT signaling pathways', *Dose-Response*, 14(1), pp. 1–10. doi: 10.1177/1559325815622174.

Lin, C. C., Wu, L. S. H. and Lee, K. F. (2019) 'The Potential Effect of Different Doses of Ionizing Radiation on Genes and Disease', *Dose-Response*, 17(2), pp. 1–10. doi: 10.1177/1559325819843375.

Lin, Y. W. (2020) 'Uranyl binding to proteins and structural-functional impacts', *Biomolecules*, 10(3), pp. 1–16. doi: 10.3390/biom10030457.

Linet, M. S., Slovis, T. L., Miller, D. L., Kleinerman, R., Lee, C., Rajaraman, P. and Gonzalez, A. B. De (2012) 'Cancer Risks Associated With External Radiation From Diagnostic Imaging Procedures', *CA: A Cancer Journal for Clinicians*, 62(2), pp. 75–100. doi: 10.3322/caac.21132.

Llères, D., James, J., Swift, S., Norman, D. G. and Lamond, A. I. (2009) 'Quantitative analysis of chromatin compaction in living cells using FLIM–FRET', *The Journal of Cell Biology*, 187(4), pp. 481–496. doi: 10.1083/jcb.200907029.

Lohka, M. J. F. in vitro of S. P. and M. C. I. by A. O. C. A. (s): M. J. . Lo and Masui, Y. (1983) 'Formation in vitro of sperm pronuclei and mitotic chromosomes induced by amphibian ooplasmic components', *Science*, 220(4598), pp. 719–721. doi: 10.1126/science.6601299. PMID: 6601299.

Lomax, M. E., Folkes, L. K. and Neill, P. O. (2013) 'Biological Consequences of Radiation-induced DNA Damage : Relevance to Radiotherapy', *Clinical Oncology*, 25(10), pp. 578–585. doi: 10.1016/j.clon.2013.06.007.

Lowe, D. J., Herzog, M., Mosler, T., Cohen, H., Felton, S., Beli, P., Raj, K., Galanty, Y. and Jackson, S. P. (2020) 'Chronic irradiation of human cells reduces histone levels and deregulates gene expression', *Scientific Reports*, 10(1), pp. 1–16. doi: 10.1038/s41598-020-59163-4.

Luger, K., Mäder, A. W., Richmond, R. K., Sargent, D. F. and Richmond, T. J.

(1997) ‘Crystal structure of the nucleosome ˚ resolution core particle at 2 . 8 A’, *Nature*, 389, pp. 251–260. doi: https://doi.org/10.1038/38444.

M’Kacher, R., El Maalouf, E., Terzoudi, G., Ricoul, M., Heidingsfelder, L., Karachristou, I., Laplagne, E., Hempel, W. M., Colicchio, B., Dieterlen, A., Pantelias, G. and Sabatier, L. (2015) ‘Detection and Automated Scoring of Dicentric Chromosomes in Nonstimulated Lymphocyte Prematurely Condensed Chromosomes after Telomere and Centromere Staining’, *International Journal of Radiation Oncology Biology Physics*. The Authors, 91(3), pp. 640–649. doi: 10.1016/j.ijrobp.2014.10.048.

Madian, N. and Jayanthi, K. B. (2014) ‘Analysis of human chromosome classification using centromere position’, *Measurement: Journal of the International Measurement Confederation*, 47(1), pp. 287–295. doi: 10.1016/j.measurement.2013.08.033.

Madon, P. F., Athalye, A. S. and Parikh, F. R. (2005) ‘Polymorphic variants on chromosomes probably play a significant role in infertility’, *Reproductive BioMedicine Online*. Reproductive Healthcare Ltd, Duck End Farm, Dry Drayton, Cambridge CB23 8DB, UK, 11(6), pp. 726–732. doi: 10.1016/S1472-6483(10)61691-4.

Maeshima, K. and Eltsov, M. (2008) ‘Packaging the genome: The structure of mitotic chromosomes’, *Journal of Biochemistry*, 143(2), pp. 145–153. doi: 10.1093/jb/mvm214.

Maeshima, K., Hihara, S. and Eltsov, M. (2010) ‘Chromatin structure: does the 30-nm fibre exist in vivo?’, *Current opinion in cell biology*. Elsevier Ltd, 22(3), pp. 291–7. doi: 10.1016/j.ceb.2010.03.001.

Maeshima, K., Imai, R., Tamura, S. and Nozaki, T. (2014) ‘Chromatin as dynamic 10-nm fibers’, *Chromosoma*, 123(3), pp. 225–237. doi: 10.1007/s00412-014-0460-2.

Magnander, K., Hultborn, R., Claesson, K. and Elmroth, K. (2010) ‘Clustered DNA damage in irradiated human diploid fibroblasts: Influence of chromatin organization’, *Radiation Research*, 173(3), pp. 272–282. doi: 10.1667/RR1891.1.

Mahaney, B. L., Meek, K. and Lees-Miller, S. P. (2009) ‘Repair of ionizing

radiation-induced DNA double strand breaks by non-homologous end-joining', *Biochemistry*, 417(3), pp. 639–650. doi: 10.1038/jid.2014.371.

Maiden, A., Johnson, D. and Li, P. (2017) 'Further improvements to the ptychographical iterative engine', *Optica*, 4(7), pp. 736–745. doi: 10.1364/optica.4.000736.

Maiden, A. M. and Rodenburg, J. M. (2009) 'An improved ptychographical phase retrieval algorithm for diffractive imaging', *Ultramicroscopy*, 109(10), pp. 1256–1262. doi: 10.1016/j.ultramic.2009.05.012.

Manders, E. M. M., Kimura, H. and Cook, P. R. (1999) 'Direct imaging of DNA in living cells reveals the dynamics of chromosome formation', *Journal of Cell Biology*, 144(5), pp. 813–821. doi: 10.1083/jcb.144.5.813.

Marchal, J., Horswell, I., Willis, B., Plackett, R., Gimenez, E. N., Spiers, J., Ballard, D., Booker, P., Thompson, J. A., Gibbons, P., Burge, S. R., Nicholls, T., Lipp, J. and Tartoni, N. (2013) 'EXCALIBUR: A small-pixel photon counting area detector for coherent X-ray diffraction - Front-end design, fabrication and characterisation', *Journal of Physics: Conference Series*, 425(PART 6), pp. 9–14. doi: 10.1088/1742-6596/425/6/062003.

Marci, R., Mallozzi, M., Di Benedetto, L., Schimberni, M., Mossa, S., Soave, I., Palomba, S. and Caserta, D. (2018) 'Radiations and female fertility', *Reproductive Biology and Endocrinology*. Reproductive Biology and Endocrinology, 16(1), pp. 1–12. doi: 10.1186/s12958-018-0432-0.

Marshall, R. R., Murphy, M., Kirkland, D. J. and Bentley, K. S. (1996) 'Fluorescence in situ hybridisation with chromosome-specific centromeric probes: A sensitive method to detect aneuploidy', *Mutation Research - Fundamental and Molecular Mechanisms of Mutagenesis*, 372(2), pp. 233–245. doi: 10.1016/S0027-5107(96)00143-1.

Martin, C. (2002) 'Interactions of ionising radiations with matter', in Martin, C. and DG, S. (eds) *Practical Radiation Protection in Health Care*. Oxford, UK: Oxford University Press, pp. 13–26.

Maser, J., Osanna, A., Wang, Y., Jacobsen, C., Kirz, J., Spector, S., Winn, B. and Tennant, D. (2000) 'Soft X-ray microscopy with a cryo scanning transmission

X-ray microscope : I . Instrumentation, imaging and spectroscopy', *Journal of Microscopy*, 197, pp. 68–79.

Mayall, B. H., Carrano, A. V., Moore, D. H., Ashworth, L. K., Bennett, D. E. and Mendelsohn, M. L. (1984) 'The DNA-based human karyotype', *Cytometry*, 5(4), pp. 376–385. doi: 10.1002/cyto.990050414.

Mazzini, A., Cavatorta, P., Iori, M., Favilla, R. and Sartor, G. (1992) 'The binding of 4′,6-diamidino-2-phenylindole to bovine serum albumin', *Biophysical Chemistry*, 42(1), pp. 101–109. doi: 10.1016/0301-4622(92)80012-T.

Melvin, T., Cunniffe, S. M. T., O'Neill, P., Parker, A. W. and Roldan-Arjona, T. (1998) 'Guanine is the target for direct ionisation damage in DNA, as detected using excision enzymes', *Nucleic Acids Research*, 26(21), pp. 4935–4942. doi: 10.1093/nar/26.21.4935.

Mendelsohn, M. L., Mayall, B. H., Bogart, E., Moore II, D. H. and Perry, B. H. (1973) 'DNA Content and DNA-Based Centromeric Index of the 24 Human Chromosomes', *Science*, 179(4078), pp. 1126–1129.

Meyne, J., Bartholdi, M. F., Travis, G. and Cram, L. S. (1984) 'Counterstaining human chromosomes for flow karyology', *Cytometry*, 5, pp. 580–583.

Miao, J., Sandberg, R. R. L. and Song, C. (2012) 'Coherent X-Ray Diffraction Imaging', *IEEE Journal Of Selected Topics In Quantum Electronics*, 18(1), pp. 399–410. doi: 10.1109/JSTQE.2011.2157306.

Moralli, D., Yusuf, M., Mandegar, M. A., Khoja, S., Monaco, Z. L. and Volpi, E. V. (2011) 'An Improved Technique for Chromosomal Analysis of Human ES and iPS Cells', *Stem Cell Reviews and Reports*, 7(2), pp. 471–477. doi: 10.1007/s12015-010-9224-4.

Morgan, David O. (2007) *The Cell Cycle: Principles of Control*. Oxford: New Science Press Ltd.

Muehlbauer, P. A. and Schuler, M. J. (2005) 'Detection of numerical chromosomal aberrations by flow cytometry : A novel process for identifying aneugenic agents', *Mutation Research*, 585, pp. 156–169. doi: 10.1016/j.mrgentox.2005.05.002.

Nair, S., Engelbrecht, M., Miles, X., Ndimba, R., Fisher, R., du Plessis, P.,

Bolcaen, J., Nieto-Camero, J., de Kock, E. and Vandevoorde, C. (2019) 'The impact of dose rate on DNA double-strand break formation and repair in human lymphocytes exposed to fast neutron irradiation', *International Journal of Molecular Sciences*, 20(21). doi: 10.3390/ijms20215350.

Nakano, T., Xu, X., Salem, A. M. H., Shoulkamy, M. I. and Ide, H. (2017) 'Radiation-induced DNA–protein cross-links: Mechanisms and biological significance', *Free Radical Biology and Medicine*, 107(November 2016), pp. 136–145. doi: 10.1016/j.freeradbiomed.2016.11.041.

Nasmyth, K. (2010) 'Segregating Sister Genomes : The Molecular Biology of Chromosome Separation', *Science*, 297(5581), pp. 559–565. doi: 10.1126/science.1074757.

Natarajan, A. T. and Boei, J. J. W. A. (2003) 'Formation of chromosome aberrations: Insights from FISH', *Mutation Research*, 544(2–3), pp. 299–304. doi: 10.1016/j.mrrev.2003.09.005.

Newman, H. C., Prise, K. M., Folkard, M. and Michael, B. D. (1997) 'DNA double-strand break distributions in X-ray and α-particle irradiated V79 cells: Evidence for non-random breakage', *International Journal of Radiation Biology*, 71(4), pp. 347–363. doi: 10.1080/095530097143978.

Nicetto, D. and Zaret, K. (2019) 'Role of H3K9me3 Heterochromatin in Cell Identity Establishment and Maintenance', *Current Opinion in Genetics & Development*, 55(2), pp. 1–10. doi: 10.1016/j.gde.2019.04.013.

Nishibuchi, G. and Déjardin, J. (2017) 'The molecular basis of the organization of repetitive DNA-containing constitutive heterochromatin in mammals', *Chromosome Research*, 25(1), pp. 77–87. doi: 10.1007/s10577-016-9547-3.

Nishino, Y., Takahashi, Y., Imamoto, N., Ishikawa, T. and Maeshima, K. (2009) 'Three-dimensional visualization of a human chromosome using coherent X-ray diffraction', *Physical Review Letters*, 102(1), pp. 8–11. doi: 10.1103/PhysRevLett.102.018101.

Ojima, M., Ito, M., Suzuki, K. and Kai, M. (2015) 'Unstable Chromosome Aberrations Do Not Accumulate in Normal Human Fibroblast after Fractionated X-Irradiation', *PLoS ONE*, 10(2), pp. 1–13. doi: 10.1371/journal.pone.0116645.

Olins, A. L. and Olins, D. E. (1974) ‘Spheroid Chromatin Units (v Bodies)’, *Science*, 183(4122), pp. 330–332.

Ono, T., Losada, A., Hirano, M., Myers, M. P., Neuwald, A. F. and Hirano, T. (2003) ‘Differential contributions of condensin I and condensin II to mitotic chromosome architecture in vertebrate cells’, *Cell*, 115(1), pp. 109–121. doi: 10.1016/S0092-8674(03)00724-4.

Ou, H. D., Phan, S., Deerinck, T. J., Thor, A., Ellisman, M. H. and O’Shea, C. C. (2017) ‘ChromEMT: Visualizing 3D chromatin structure and compaction in interphase and mitotic cells’, *Science*, 357(6349:eaag0025). doi: 10.1126/science.aag0025.

Ouchi, N. B. (2015) ‘On the Dynamical Approach of Quantitative Radiation Biology’, in Nenoi, M. (ed.) *Evolution of Ionizing Radiation Research*. IntechOpen, pp. 41–62.

Palmer, C. G. and Funderburk, S. (1965) ‘Secondary constrictions in human chromosomes.’, *Cytogenetics*, 4(4), pp. 261–276. doi: 10.1159/000129863.

Park, Y., Peoples, A. R., Madugundu, G. S., Sanche, L. and Wagner, J. R. (2013) ‘Side-by-side comparison of DNA damage induced by low-energy electrons and high-energy photons with solid TpTpT trinucleotide’, *Journal of Physical Chemistry B*, 117(35), pp. 10122–10131. doi: 10.1021/jp405397m.

Pfeiffer, P., Goedecke, W. and Obe, G. (2000) ‘Mechanisms of DNA double-strand break repair and their potential to induce chromosomal aberrations’, *Mutagenesis*, 15(4), pp. 289–302. doi: 10.1093/mutage/15.4.289.

Phengchat, R., Takata, H., Morii, K., Inada, N., Murakoshi, H., Uchiyama, S. and Fukui, K. (2016) ‘Calcium ions function as a booster of chromosome condensation’, *Scientific Reports*, 6(1), p. 38281. doi: 10.1038/srep38281.

Pinkel, D., Segraves, R., Sudar, D., Clark, S., Poole, I., Kowbel, D., Collins, C., Kuo, W. L., Chen, C., Zhai, Y., Dairkee, S. H., Ljung, B. M., Gray, J. W. and Albertson, D. G. (1998) ‘High resolution analysis of DNA copy number variation using comparative genomic hybridization to microarrays’, *Nature Genetics*, 20(2), pp. 207–211. doi: 10.1038/2524.

Pinkel, D., Straume, T. and Gray, J. W. (1986) ‘Cytogenetic analysis using

quantitative, high-sensitivity, fluorescence hybridization', *Proceedings of the National Academy of Sciences of the United States of America*, 83(9), pp. 2934–2938.

Piovesan, A., Pelleri, M. C., Antonaros, F., Strippoli, P., Caracausi, M. and Vitale, L. (2019) 'On the length, weight and GC content of the human genome', *BMC Research Notes*, 12(1), pp. 1–7. doi: 10.1186/s13104-019-4137-z.

Pita, M., Gosálvez, J., Gosálvez, A., Nieddu, M., López-Fernández, C. and Mezzanotte, R. (2010) 'A highly conserved pericentromeric domain in human and gorilla chromosomes', *Cytogenetic and Genome Research*, 126(3), pp. 253–258. doi: 10.1159/000251962.

Pollycove, M. and Feinendegen, L. E. (2001) 'Biologic responses to low doses of ionizing radiation: Detriment versus hormesis. Part 2. Dose responses of organisms.', *Journal of nuclear medicine*, 42(9).

Prosser, J., Frommer, M., Paul, C. and Vincent, P. C. (1986) 'Sequence relationships of three human satellite DNAs', *Journal of Molecular Biology*, 187(2), pp. 145–155. doi: 10.1016/0022-2836(86)90224-X.

Rahman-Roblick, R., Hellman, U., Becker, S., Bader, F. G., Auer, G., Wiman, K. G. and Roblick, U. J. (2008) 'Proteomic identification of p53-dependent protein phosphorylation', *Oncogene*, 27(35), pp. 4854–4859. doi: 10.1038/onc.2008.124.

Rau, C., Wagner, U. H., Vila-Comamala, J., Bodey, A., Parson, A., García-Fernández, M., De Fanis, A., Pešić, Z., Zanette, I. and Zdora, M. (2016) 'Micro- and nano-imaging at the diamond beamline I13L-imaging and coherence', in *AIP Conference Proceedings*. New York (NY), United States: AIP Publishing, pp. 030008–1–030008–5. doi: 10.1063/1.4952831.

Redon, R. and Carter, N. P. (2009) 'Comparative Genomic Hybridization: microarray design and data interpretation', *Methods in Molecular Biology*, 529(2), pp. 37–49. doi: 10.1007/978-1-59745-538-1.

Reisz, J. A., Bansal, N., Qian, J., Zhao, W. and Furdui, C. M. (2014) 'Effects of ionizing radiation on biological molecules - mechanisms of damage and emerging methods of detection', *Antioxidants and Redox Signaling*, 21(2), pp. 260–292. doi: 10.1089/ars.2013.5489.

Renshaw, M. J., Ward, J. J., Kanemaki, M., Natsume, K., Nédélec, F. J. and Tanaka, T. U. (2010) 'Condensins promote chromosome recoiling during early anaphase to complete sister chromatid separation', *Developmental Cell*, 19(2), pp. 232–244. doi: 10.1016/j.devcel.2010.07.013.

Ried, T., Schröck, E., Ning, Y. and Wienberg, J. (1998) 'Chromosome painting: A useful art', *Human Molecular Genetics*, 7(10), pp. 1619–1626. doi: 10.1093/hmg/7.10.1619.

Robinson, I. (2015) 'Coherent three-dimensional X-ray cryo-imaging', *International Union of Crystallography (IUCr) Journal*, 2(1976), pp. 477–478. doi: 10.1107/S2052252515015109.

Robinson, I., Yang, Y., Zhang, F., Lynch, C., Yusuf, M. and Cloetens, P. (2016) 'Nuclear incorporation of iron during the eukaryotic cell cycle', *Journal of Synchrotron Radiation*, 23(6), pp. 1490–1497. doi: 10.1107/S1600577516012807.

Robinson, I., Yusuf, M., Schwenke, J., Estandarte, A., Zhang, F., Bhella, G., Parmar, N., Clark, J., Song, C., Nam, D., Ratnasari, G., Kaneyoshi, K., Takata, H. and Fukui, K. (2015) 'Damage-free imaging of human chromosomes', *Chromosome Science*, 18, pp. 69–72.

Robinson, P. J. J., Fairall, L., Huynh, V. A. T. and Rhodes, D. (2006) 'EM measurements define the dimensions of the "30-nm" chromatin fiber: Evidence for a compact, interdigitated structure', *Proceedings of the National Academy of Sciences of the United States of America*, 103(17), pp. 6506–6511. doi: 10.1073/pnas.0601212103.

Rodenburg, J. M., Hurst, A. C., Cullis, A. G., Dobson, B. R., Pfeiffer, F., Bunk, O., David, C., Jefimovs, K. and Johnson, I. (2007) 'Hard-X-ray lensless imaging of extended objects', *Physical Review Letters*, 98(3), pp. 1–4. doi: 10.1103/PhysRevLett.98.034801.

Ronne, M., Andersen, O. and Erlandsen, M. (1979) 'Effect of colcemid exposure and methanol acetic acid fixation on human metaphase chromosome structure', *Hereditas*, 90(2), pp. 195–201. doi: 10.1111/j.1601-5223.1979.tb01306.x.

Rozgaj, R., Kašuba, V., Šentija, K. and Prlić, I. (1999) 'Radiation-induced

chromosomal aberrations and haematological alterations in hospital workers', *Occupational Medicine*, 49(6), pp. 353–360. doi: 10.1093/occmed/49.6.353.

Ryan, T. L., Pantelias, A. G., Terzoudi, G. I., Pantelias, G. E. and Balajee, A. S. (2019) 'Use of human lymphocyte G0 PCCs to detect intra- And inter-chromosomal aberrations for early radiation biodosimetry and retrospective assessment of radiation-induced effects', *PLoS ONE*, 14(5), pp. 1–18. doi: 10.1371/journal.pone.0216081.

Ryu, T. H., Kim, J. H. and Kim, J. K. (2016) 'Chromosomal Aberrations in Human Peripheral Blood Lymphocytes after Exposure to Ionizing Radiation', *Genome Integrity*, 7: 5, pp. 3–5. doi: 10.4103/2041-9414.197172.

Sahin, F. I., Yilmaz, Z., Yuregir, O. O., Bulakbasi, T., Ozer, O. and Zeyneloglu, H. B. (2008) 'Chromosome heteromorphisms: An impact on infertility', *Journal of Assisted Reproduction and Genetics*, 25(5), pp. 191–195. doi: 10.1007/s10815-008-9216-3.

Saksouk, N., Simboeck, E. and Déjardin, J. (2015) 'Constitutive heterochromatin formation and transcription in mammals', *Epigenetics and Chromatin*, 8(1), pp. 1–17. doi: 10.1186/1756-8935-8-3.

Sanchez, L., Martinez, P. and Goyanes, V. (1991) 'Analysis of centromere size in human chromosomes 1, 9, 15, and 16 by electron microscopy', *Genome*, 34(5), pp. 710–713. doi: 10.1139/g91-109.

Sanders, J., Freeman, T., Xu, Y., Golloshi, R., Stallard, M., Martin, R. S., Balajee, A. and McCord, R. P. (2019) 'Radiation-Induced DNA Damage and Repair Effects on 3D Genome Organization', *BioRxiv- the preprint server for Biology*. doi: https://doi.org/10.1101/740704.

Schalch, T., Duda, S., Sargent, D. F. and Richmond, T. J. (2005) 'X-ray structure of a tetranucleosome and its implications for the chromatin fibre', *Nature*, 436(7047), pp. 138–141. doi: 10.1038/nature03686.

Schnerch, D., Yalcintepe, J., Schmidts, A., Becker, H., Follo, M., Engelhardt, M. and Wäsch, R. (2012) 'Cell cycle control in acute myeloid leukemia.', *American journal of cancer research*, 2(5), pp. 508–528.

Schröck, E., Manoir, du S., Veldman, T., Schoell, B., Wienberg, J., Ferguson-

Smith, M. A., Ning, Y., Ledbetter, D. H., Bar-Am, I., Soenksen, D., Garini, Y. and Ried, T. (1996) 'Multicolor Spectral Karyotyping of Human Chromosomes', *American Association for the Advancement of Science*, 273(5274), pp. 494–497.

Schröder, A., Kriesen, S., Hildebrandt, G. and Manda, K. (2019) 'First insights into the effect of low-dose X-ray irradiation in adipose-derived stem cells', *International Journal of Molecular Sciences*, 20(23), pp. 1–13. doi: 10.3390/ijms20236075.

Schroer, C. G., Kuhlmann, M., Hunger, M. D., Günzler, T. F., Kurapova, O., Feste, S., Frehse, F., Drakopoulos, M., Somogyi, H. R., Simionovici, A. S., Snigirev, A., Snigireva, I., Schug, C. and Schröder, W. H. (2003) 'Nanofocusing parabolic refractive X-ray lenses', *Applied Physics Letters*, 82(9), pp. 1485–1487. doi: 10.1063/1.1556960.

Schwenke, J., Shemilt, L. A., Wagner, U., Morrison, G. R., Zhang, F., Yusuf, M., Rau, C. and Robinson, I. K. (no date) 'Quantitative phase measurements of human cell nuclei using X-ray ptychography', pp. 1–14.

Schwer, B., Wei, P., Chang, A. N. and Kao, J. (2016) 'Transcription-associated processes cause DNA double-strand breaks and translocations in neural stem / progenitor cells', *Proceedings of the National Academy of Sciences of the United States of America*, 113(8), pp. 2258–2263. doi: 10.1073/pnas.1525564113.

Shaw, M. W. (1973) 'Uses of banding techniques for the identification of human disease of cytogenetic origin', *Environmental Health Perspectives*, 6, pp. 151–156. doi: 10.1289/ehp.7306151.

Shemilt, L. A., Estandarte, A. K. C., Yusuf, M. and Robinson, I. K. (2014) 'Scanning electron microscope studies of human metaphase chromosomes.', *Philosophical transactions. Series A, Mathematical, physical, and engineering sciences*, 372(2010), p. 20130144. doi: 10.1098/rsta.2013.0144.

Shemilt, L., Verbanis, E., Schwenke, J., Estandarte, A. K., Xiong, G., Harder, R., Parmar, N., Yusuf, M., Zhang, F. and Robinson, I. K. (2015) 'Karyotyping human chromosomes by optical and X-ray ptychography methods', *Biophysical Journal*, 108(3), pp. 706–713. doi: 10.1016/j.bpj.2014.11.3456.

Sherrard, A., Bishop, P., Panagi, M., Villagomez, M. B., Alibhai, D. and Kaidi, A.

(2018) ‘Streamlined histone-based fluorescence lifetime imaging microscopy (FLIM) for studying chromatin organisation’, *Biology Open*, 7(3), pp. 1–8. doi: 10.1242/bio.031476.

Shimura, N. and Kojima, S. (2018) ‘The Lowest Radiation Dose Having Molecular Changes in the Living Body’, *Dose-Response*, 16(2), pp. 1–17. doi: 10.1177/1559325818777326.

Sidorenko, P. and Cohen, O. (2016) ‘Single-shot ptychography’, *Optica*, 3(1), pp. 9–14.

Singh, P., Aggarwal, L. M., Parry, S. A. and Raman, M. J. (2018) ‘Radiation dosimetry and repair kinetics of DNA damage foci in mouse pachytene spermatocyte and round spermatid stages’, *Mutagenesis*, 33(3), pp. 231–239. doi: 10.1093/mutage/gey007.

Smith, E. A., McDermott, G., Do, M., Leung, K., Panning, B., Le Gros, M. A. and Larabell, C. A. (2014) ‘Quantitatively imaging chromosomes by correlated cryo-fluorescence and soft X-ray tomographies’, *Biophysical Journal*, 107(8), pp. 1988–1996. doi: 10.1016/j.bpj.2014.09.011.

Spagnol, S. T. and Dahl, K. N. (2016) ‘Spatially Resolved Quantification of Chromatin Condensation through Differential Local Rheology in Cell Nuclei Fluorescence Lifetime Imaging’, *PLoS ONE*, 11(1), pp. 1–19. doi: 10.1371/journal.pone.0146244.

Speicher, M. R., Ballard, S. G. and Ward, D. C. (1996) ‘Karyotyping human chromosomes by combinatorial multi-fluor FISH’, *Nature Genetics*, 12, pp. 368–375.

Spelcher, M. R., Manoir, S. Du, Schröck, E., Holtgreve-grez, H., Schoell, B., Lengauer, C., Cremer, T. and Ried, T. (1993) ‘Molecular cytogenetic analysis of formalin-fixed, paraffin-embedded solid tumors by comparative genomic hybridization after universal DNA-amplification’, *Human Molecular Genetics*, 2(11), pp. 1907–1914. doi: 10.1093/hmg/2.11.1907.

Stachnik, K. (2012) *Ptychographical measurements of biological specimen*. Poland.

Staessen, C., Kirsch-Volders, M. and Susanne, C. (1982) ‘Comparison of two

measuring methods for the evaluation of C-heterochromatin in human chromosomes', *Human Genetics*, 61(1), pp. 68–70. doi: 10.1007/BF00291337.

Stewart, C. C., Cramer, S. F. and Steward, P. G. (1975) 'The response of human peripheral blood lymphocytes to phytohemagglutinin: Determination of cell numbers', *Cellular Immunology*, 16(2), pp. 237–250. doi: 10.1016/0008-8749(75)90115-X.

Strachan, T. and Read, Andrew P. (2004) 'Chromosome structure and function', in *Human Molecular Genetics*. 3rd edn. London and New York: Garland Science: Taylor & Francis Group, pp. 34–36.

Suhling, K., Hirvonen, L. M., Levitt, J. A., Chung, P.-H., Tregidgo, C., Le Marois, A., Rusakov, D. A., Zheng, K., Ameer-Beg, S., Poland, S., Coelho, S., Henderson, R. and Krstajic, N. (2015) 'Fluorescence lifetime imaging (FLIM): Basic concepts and some recent developments', *Medical Photonics*, 27, pp. 3–40. doi: 10.1016/j.medpho.2014.12.001.

Suhling, K., Levitt, J. A., Chung, P.-H., Kuimova, M. K. and Yahioglu, G. (2012) 'Fluorescence Lifetime Imaging of Molecular Rotors in Living Cells', *Journal of Visualized Experiments*, (60), pp. 1–5. doi: 10.3791/2925.

Sullivan, L. L., Chew, K. and Sullivan, B. A. (2017) 'α satellite DNA variation and function of the human centromere', *Nucleus*. Taylor & Francis, 8(4), pp. 331–339. doi: 10.1080/19491034.2017.1308989.

Sumner, A. T. (1982) 'The nature and mechanisms of chromosome banding', *Cancer Genetics and Cytogenetics*, 6(1), pp. 59–87. doi: 10.1016/0165-4608(82)90022-X.

Sumner, A. T., Evans, H. J. and Buckland, R. A. (1971) 'New technique for distinguishing between human chromosomes', *Nature New biology*, 231, pp. 31–32. doi: https://doi.org/10.1038/newbio232031a0.

Swarts, S. G., Gilbert, D. C., Sharma, K. K., Razskazovskiy, Y., Purkayastha, S., Naumenko, K. A. and Bernhard, W. A. (2007) 'Mechanisms of direct radiation damage in DNA, based on a study of the yields of base damage, deoxyribose damage, and trapped radicals in d(GCACGCGTGC)2', *Radiation Research*, 168(3), pp. 367–381. doi: 10.1667/RR1058.1.

Tagarro, I., Fernández-Peralta, A. M. and González-Aguilera, J. J. (1994) 'Chromosomal localization of human satellites 2 and 3 by a FISH method using oligonucleotides as probes', *Human Genetics*, 93(4), pp. 383–388. doi: 10.1007/BF00201662.

Takata, H., Uchiyama, S., Nakamura, N., Nakashima, S., Kobayashi, S., Sone, T., Kimura, S., Lahmers, S., Granzier, H., Labeit, S., Matsunaga, S. and Fukui, K. (2007) 'A comparative proteome analysis of human metaphase chromosomes isolated from two different cell lines reveals a set of conserved chromosome-associated proteins', *Genes to Cells*, 12(3), pp. 269–284. doi: 10.1111/j.1365-2443.2007.01051.x.

Takata, M., Sasaki, M. S., Sonoda, E., Morrison, C., Hashimoto, M., Utsumi, H., Yamaguchi-iwai, Y., Shinohara, A. and Takeda, S. (1998) 'Homologous recombination and non-homologous end-joining pathways of DNA double-strand break repair have overlapping roles in the maintenance of chromosomal integrity in vertebrate cells', *The European Molecular Biology Organization Journal*, 17(18), pp. 5497–5508.

Taylor, E. W. (1965) 'The Mechanism of Colchicine Inhibition of Mitosis', *The Journal of cell biology*, 25, pp. 145–160. doi: 10.1083/jcb.25.1.145.

Terrenoire, E., Halsall, J. A. and Turner, B. M. (2015) 'Immunolabelling of human metaphase chromosomes reveals the same banded distribution of histone H3 isoforms methylated at lysine 4 in primary lymphocytes and cultured cell lines', *BMC Genetics*, 16(1), pp. 1–7. doi: 10.1186/s12863-015-0200-5.

Therman, E. (2012) 'Structure of the Eukaryotic Chromosome and the Karyotype', in *Human Chromosomes: Structure, Behavior, Effects*. 2nd edn. Berlin Heidelberg: Springer-Verlag, pp. 11–23.

Thoma, F., Koller, T. and Klug, A. (1979) 'INVOLVEMENT OF HISTONE H1 IN THE ORGANIZATION OF THE NUCLEOSOME AND OF THE SALT-DEPENDENT SUPERSTRUCTURES OF CHROMATIN', *The Journal of cell biology*, 83(2 Pt 1), pp. 403–27. Available at: http://www.pubmedcentral.nih.gov/articlerender.fcgi?artid=2111545&tool=pmcentrez&rendertype=abstract.

Tjio, J. H. and Levan, A. (1956) 'The Chromosome Number of Man', *Hereditas*,

42(1–2), pp. 1–6. doi: 10.1111/j.1601-5223.1956.tb03010.x.

Tobias, E. (2011) ‘Chromosome aberrations’, in *Essential Medical Genetics*. 6th edn. Singapore: Wiley-Blackwell, pp. 89–111.

Touil, N., Elhajouji, A., Thierens, H. and Kirsch-Volders, M. (2000) ‘Analysis of chromosome loss and chromosome segregation in cytokinesis-blocked human lymphocytes: non-disjunction is the prevalent mistake in chromosome segregation produced by low dose exposure to ionizing radiation’, *Mutagenesis*, 15(1), pp. 1–7. doi: 10.1093/mutage/15.1.1.

Truong, K., Bradley, S., Baginski, B., Wilson, J. R., Medlin, D., Zheng, L., Wilson, R. K., Rusin, M., Takacs, E. and Dean, D. (2018) ‘The effect of well-characterized, very low-dose x-ray radiation on fibroblasts’, *PLoS ONE*, 13(1), pp. 1–16. doi: 10.1371/journal.pone.0190330.

Uchiyama, S., Kobayashi, S., Takata, H., Ishihara, T., Hori, N., Higashi, T., Hayashihara, K., Sone, T., Higo, D., Nirasawa, T., Takao, T., Matsunaga, S. and Fukui, K. (2005) ‘Proteome analysis of human metaphase chromosomes’, *Journal of Biological Chemistry*, 280(17), pp. 16994–17004. doi: 10.1074/jbc.M412774200.

Verma, R. S., Luke, S., Brennan, J. P., Mathews, T., Conte, R. a and Macera, M. J. (1993) ‘Molecular topography of the secondary constriction region (qh) of human chromosome 9 with an unusual euchromatic band.’, *American journal of human genetics*, 52, pp. 981–6. Available at: http://www.pubmedcentral.nih.gov/articlerender.fcgi?artid=1682060&tool=pmcentrez&rendertype=abstract.

Voisin, P. (2015) ‘Standards in biological dosimetry: A requirement to perform an appropriate dose assessment’, *Mutation Research - Genetic Toxicology and Environmental Mutagenesis*. Elsevier Ltd, 793, pp. 115–122. doi: 10.1016/j.mrgentox.2015.06.012.

Wako, T., Yoshida, A., Kato, J., Otsuka, Y., Ogawa, S., Kaneyoshi, K., Takata, H. and Fukui, K. (2020) ‘Human metaphase chromosome consists of randomly arranged chromatin fibres with up to 30-nm diameter’, *Scientific Reports*, 10(1), pp. 1–6. doi: 10.1038/s41598-020-65842-z.

Wang, C. and Bai, C. (2006) ‘Single Molecule Fluorescence Imaging and Spectrocopy: Far-Field studies’, in *Single Molecule Chemistry and Physics-An Introduction*. 1st edn. Beijing, China: Springer-Verlag Berlin Heidelberg, pp. 183–190.

Wanner, G. and Formanek, H. (1995) ‘Imaging of DNA in human and plant chromosomes by high-resolution scanning electron microscopy’, *Chromosome Research*, 3(6), pp. 368–374. doi: 10.1007/BF00710018.

Woodcock, C. L. F., Frado, L. Y. and Rattner, J. B. (1984) ‘The Higher-order Structure of Chromatin : Evidence for a Helical Ribbon Arrangement’, *The Journal of Cell Biology*, 99(1 pt 1), pp. 42–52. doi: 10.1083/jcb.99.1.42.

Woodcock, C. L. and Ghosh, R. P. (2010) ‘Chromatin Higher-order Structure and Dynamics’, pp. 1–25.

Xu, X. and Wu, M. (1983) ‘Electron microscopy of G-banded human mitotic chromosomes’, *Chromosoma*, 88(3), pp. 237–240. doi: 10.1007/BF00285626.

Yahav, G., Hirshberg, A., Salomon, O., Amariglio, N., Trakhtenbrot, L. and Fixler, D. (2016) ‘Fluorescence Lifetime Imaging of DAPI- Stained Nuclei As a Novel Diagnostic Tool for the Detection and Classification of B-Cell Chronic Lymphocytic Leukemia’, *Cytometry Part A*, 89A(6), pp. 644–652. doi: 10.1002/cyto.a.22890.

Yamamoto, Y. and Shinohara, K. (2002) ‘Application of X-ray microscopy in analysis of living hydrated cells’, *Anatomical Record*, 269(5), pp. 217–223. doi: 10.1002/ar.10166.

Yan, H., Nazaretski, E., Lauer, K., Huang, X., Wagner, U., Rau, C., Yusuf, M., Robinson, I., Kalbfleisch, S., Li, L., Bouet, N., Zhou, J., Conley, R. and Chu, Y. S. (2016) ‘Multimodality hard-x-ray imaging of a chromosome with nanoscale spatial resolution’, *Scientific Reports*, 6, pp. 1–7. doi: 10.1038/srep20112.

Young, A. T. (1981) ‘Rayleigh Scattering’, *Applied optics*, 20(4), pp. 533–535. doi: https://doi.org/10.1364/AO.20.000533.

Yusuf, M., Bauer, D. L. V., Lipinski, D. M., MacLaren, R. E., Wade-Martins, R., Mir, K. U. and Volpi, E. V. (2011) ‘Combining M-FISH and Quantum Dot technology for fast chromosomal assignment of transgenic insertions’, *BMC*

Biotechnology, 11:121, pp. 1–10. doi: 10.1186/1472-6750-11-121.

Yusuf, M., Chen, B., Hashimoto, T., Estandarte, A. K., Thompson, G. and Robinson, I. (2014) 'Staining and embedding of human chromosomes for 3-D serial block-face scanning electron microscopy', *BioTechniques*, 57(6), pp. 302–307. doi: 10.2144/000114236.

Yusuf, M., Kaneyoshi, K., Fukui, K. and Robinson, I. (2019) 'Use of 3D imaging for providing insights into high-order structure of mitotic chromosomes', *Chromosoma*, 128(1), pp. 7–13. doi: 10.1007/s00412-018-0678-5.

Yusuf, M., Leung, K., Morris, K. J. and Volpi, E. V. (2013) 'Comprehensive cytogenomic profile of the in vitro neuronal model SH-SY5Y', *Neurogenetics*, 14(1), pp. 63–70. doi: 10.1007/s10048-012-0350-9.

Yusuf, M., Millas, A. L. G., Estandarte, A. K. C., Bhella, G. K., McKean, R., Bittencourt, E. and Robinson, I. K. (2014) 'Platinum blue staining of cells grown in electrospun scaffolds', *BioTechniques*, 57(3). doi: 10.2144/000114206.

Yusuf, M., Parmar, N., Bhella, G. K. and Robinson, I. K. (2014) 'A simple filtration technique for obtaining purified human chromosomes in suspension', *BioTechniques*, 56(5), pp. 257–261. doi: 10.2144/000114168.

Yusuf, M., Zhang, F., Chen, B., Bhartiya, A., Cunnea, K., Wagner, U., Schwenke, J. and Robinson, I. K. (2017) 'Procedures for cryogenic X-ray ptychographic imaging of biological samples', *International Union of Crystallography (IUCr) Journal*, 4, pp. 147–151. doi: 10.1107/S2052252516020029.

Zhang, F., Vila-Comamala, J., Diaz, A., Berenguer, F., Bean, R., Chen, B., Menzel, A., Robinson, I. K. and Rodenburg, J. M. (2013) 'Translation position determination in ptychographic coherent diffraction imaging', *Optics Express*, 21(11), p. 13592. doi: 10.1364/OE.21.013592.

Zhang, Y., Máté, G., Müller, P., Hillebrandt, S., Krufczik, M., Bach, M., Kaufmann, R., Hausmann, M. and Heermann, D. W. (2015) 'Radiation induced chromatin conformation changes analysed by fluorescent localization microscopy, statistical physics, and graph theory', *PLoS ONE*, 10(6), pp. 1–23. doi: 10.1371/journal.pone.0128555.

8. List of Glossary used in this thesis

Auto-fluorescence	Emission of light that naturally occurs within the biological structures
Chromosomal aberrations	Chromosomal aberrations can be classified as numerical or structural damage to the chromosome
Chromosome spread	A complete set of 46 human metaphase chromosomes in one frame
Coherence	A property of waves having a constant phase and frequency
Constitutive heterochromatin	Remains compact, gene-poor and enriched with repetitive and late replicating DNA sequences.
DNA content (2C)	The amount of DNA contained by 2N chromosomes
Facultative heterochromatin	Show temporal and spatial active and inactive behaviour of transcription
Fluorescence lifetime	The amount of time a fluorophore remains on an average in its excited state before returning to the ground state by emitting a photon
Fluorescence lifetime imaging microscopy (FLIM)	FLIM is a technique that can map the molecular environment of fluorophore and can act as a reporter to photophysical events at a nanosecond time scale
G0 stage	Quiescent state of the cell cycle
Heterochromatin region	The region consists of highly packed repetitive DNA
Heteromorphic	Chromosome pair with difference in heterochromatin appearance/shape/staining present close to the pericentromeric region
Hormesis	Hormesis is an “adaptive process” that occurs at a low-level stress to protect the cells/genetic material from upcoming severe stress (Arumugam *et al.*, 2006)
Ionising radiation	High energy radiation given off from radioactive materials. The interaction with DNA directly releases electrons from the atoms and bonds and can break strands of DNA

Karyotype	Chromosomes are arranged according to many parameters that include their size, shape, and amount of genetic material
Long lifetime	The region (blue pseudo colour) where DAPI fluorophore decay slow
Metaphase chromosomes	Chromosomes align to the equator of the cell and the chromosomes are at their most condensed state
M-FISH	M-FISH is a fluorescence technique that uses computer-generated pseudo colours from a coding scheme, which analyses the fluorescence from various combinations of five paints (probes) and uses DAPI as a counterstain
Non-heterochromatic regions/euchromatin	The region of a chromosome apart from its centromere has been mentioned as non-heterochromatic regions.
Non-heteromorphic chromosomes	Human chromosomes apart from chromosomes 1, 9, 15, 16 and Y present in a single nucleus are mentioned as non-heteromorphic chromosomes
Photo-bleaching	Complete decayed of fluorophore
Ptychography	A technique in which an object is illuminated and scanned in a stepwise fashion to produce an array of partially overlapped probe spots onto the object
Satellite DNA	Tandemly repeated sequences of DNA present in the chromosomes
Short lifetime	The region (red pseudo colour) where DAPI fluorophore decay fast